HYDRO-MECHANICAL NETWORK MODELLING OF POROUS GEOMATERIALS

IGNATIOS ATHANASIADIS

DIVISION OF INFRASTRUCTURE AND ENVIRONMENT
SCHOOL OF ENGINEERING

UNIVERSITY OF GLASGOW

Submitted in fulfilment of the requirements for the degree of Doctor of Philosophy

FEBRUARY 2017

Abstract

The microstructure of porous geomaterials strongly influences macroscopic hydro-mechanical properties, such as fluid retention, conductivity and stiffness. These properties are of importance for predicting the performance of many engineering applications, such as waste barriers and flood defence embankments. Predicting these properties with confidence requires a thorough understanding of processes at the microscale and their effect on macroscopic phenomenological properties. For unsaturated geomaterials, providing this understanding requires still further research. In this study, network models representing processes in the pore structure and solid skeleton were developed with the aim to improve the required understanding to link processes at the micro-scale to macroscopic properties. The objectives were to develop a new coupled hydro-mechanical network model, with main application the improvement of understanding of the influence of microstructure on the retention behaviour and conductivity of porous geomaterials, the mechanical response in the form of the elastic stiffness, and their interaction. The model is valid for investigation of transport and mechanical aspects geomaterials such as concrete, rocks, sand and clay soils with length scales of the pore radii spanning from sub-μm to mm.

In the present network models, the microstructure of the material is idealised by means of a network of voids for the transport response and a network of grains/particles representing the solid skeleton response. For the transport network, the void structure is idealised by spheres representing large voids and pipes for the interconnecting narrow throats. The structural network of grains is modelled by rigid polyhedra connected by springs which contain information related to the constitutive response of the skeleton. The geometry of the networks is determined by dual irregular Delaunay and Voronoi tessellations based on random sets of points. For the transport network, the spheres and pipes were placed on the Voronoi polyhedral vertices and along the ridges, respectively. The mechanical elements were placed on the edges of the Delaunay tetrahedra. In addition to the irregular arrangement of elements, microstructural heterogeneity was introduced by assigning the radii of the spheres and pipes as well as the polyhedra contact areas from probability distributions. New techniques to provide Periodic Boundary Conditions for representative cells generated by the irregular networks were developed. Another new feature of the model is a pore scaling technique which improves the modelling of the retention behaviour.

For being able to perform simulations of representative cells of the coupled networks, the model was implemented in a finite element framework. The correct development and implementation of the network models was verified by comparison with a range of analytical solutions. Furthermore, a sensitivity study was performed to investigate the qualitative macroscopic response of the material in the form of retention behaviour, conductivity and stiffness for important model parameters. For the influence of the cell size on the macroscopic

properties, it was found that for large cell sizes, the macroscopic response of the model is independent of a change of the cell size. For all macroscopic properties investigated, the mean converges to a representative value. Furthermore, the standard deviation approaches zero for large cells for almost all cases. Only for a small range of very low conductivities for highly unsaturated conditions, the standard deviation did not decrease with increasing cell size, which was attributed to the occurrence of percolation. In addition to the verification part, a calibration strategy was developed for the transport part of the model. Then, the model was used to predict the relative conductivity of unsaturated geomaterials reported in the literature. The agreement between the numerical prediction and the experimental results for degree of saturation and relative permeability was found to be very good. The model presented possibility to predict evolution of relative permeability when calibrated to match retention experimental data.

Acknowledgements

The research findings reported in the present thesis were undertaken and completed in the Infrastructure and Environmental Research Division within the School of Engineering of the University of Glasgow from December 2012 to June 2016. I would like to acknowledge the financial support received for the completion of the present thesis received from the U.K. Engineering and Physical Sciences Research Council (EPSRC) under Grant EP/I036427/1 and funding from Radioactive Waste Management Limited (RWM), a wholly-owned subsidiary of the Nuclear Decommissioning Authority.

I would like to thank Doctor Peter Grassl and Professor Simon Wheeler for their constant guidance, advice and patient support throughout the process of the present thesis completion. I really enjoyed and appreciated their clear explanation of complex numerical and physical processes as well as their knowledge transfer. They strongly contributed to my personal improvement.

Furthermore, I would like to specially acknowledge Dimitris' and Maria's great help in both practical and PhD related issues during my arrival in Glasgow. Dimitris' help in my initial steps in coding is much appreciated. I would also like to thank my colleagues Caroline, Ross, Alan, Ali, Greame, Xue, Michael, Euan M., James and Ahmed, who already inhabited office No. 604 in Rankine Building in my arrival, for their help in my integration in the office community and contributed to everyday issues. I also thank my colleagues that later arrived in the office, Eri, Yiannis, Andrea, Zahur, Remi, Euan R., Pradeep, Assad, Petr, Victor and Thomas for the nice chats we had during tea and launch breaks.

I wish to thank my old friends Savvas and Petros for their moral support throughout my studies. Also many thanks to Andreas, Sotiris and Thomas, for the exciting table football Friday nights during my PhD years. Special thanks to Sotiris and Professor Paul Younger for their great support towards the final semester of my thesis completion.

Immense thanks to my parents Yiannis and Sabina and my brothers Angelos and Andreas, who have morally supported me throughout my life and set the basis to pursue this PhD. Finally, and most importantly, I want to thank my girlfriend Sotiria for her every-day support starting long before my journey to Glasgow.

Table of Contents

Nomenclature

Abbreviations

BCC Body Centred Cubic

CDF Cumulative Distribution Function

CFD Computational Fluid Dynamics

DDA Discontinuous Deformation Analysis

DEM Discrete Element Method

FCC Face Centred Cubic

GCM Glasgow Coupled Model

FEM Finite Element Method

HCP Hexagonal Close Packing

MCC Modified Cam Clay

OOFEM Object Oriented Finite Element Method

PBCs Periodic Boundary Conditions

PDF Probability Density Function

PFV Pore-scale Finite Volume

RBSM Rigid Body Spring Model

RRM Rolling Resistance Model

RVE Representative Volume Element

Greek symbols

α Microstructural evolution rate of change

$\boldsymbol{\alpha_e}$ Pipe element conductivity matrix

β_i Rotational displacement of the i-th mechanical node perpendicular to the element

γ Surface tension of the drying-wetting fluid interface [N/m]

γ_1 Ratio of the mechanical element tangent modulus to element normal modulus

γ_2 Ratio of the mechanical element rotational modulus to element normal modulus

γ_{SD} Surface tension of the solid-drying fluid interface [N/m]

γ_{SW} Surface tension of the solid-wetting fluid interface [N/m]

ΔZ Difference in elevation [m]

$\Delta\lambda$ Change of plastic multiplier

$\Delta\lambda^{(h)}$ Change of plastic multiplier at the h-th step of the analysis

ΔF Inter-particle force increase due to meniscus water bridge generation [N]

Δp_{f} Pressure difference [Pa]

$\Delta P_x, \Delta P_y, \Delta P_z$ Pressure differences along x, y, z axes [Pa]

$\boldsymbol{\varepsilon}$ Total strain vector

$\boldsymbol{\varepsilon}_{\mathrm{p}}$ Plastic strain vector

$\boldsymbol{\varepsilon}_{\hat{\mathrm{t}}}$, $\boldsymbol{\varepsilon}_{\hat{\mathrm{s}}}$, $\boldsymbol{\varepsilon}_{\hat{\mathrm{t}}}$ The normal and the two shear strains for the mechanical element

$\dot{\boldsymbol{\varepsilon}}_{\mathrm{p}}$ Rate of change of plastic strain vector of the mechanical element

$\dot{\boldsymbol{\varepsilon}}^{h}$ Total strain vector of the mechanical element at the h-th step of the analysis

$\varepsilon_{\hat{n}\mathrm{p}}$ Normal plastic strain of the mechanical element

ζ Mean of the underlying Gauss distribution of a lognormal distribution

Θ Constant for the evaluation of the stress tensor of an FCC structural at failure

θ Contact angle [^{o}]

θ_i Nodal rotation

ι Non dimensional hydraulic gradient

κ Permeability of the geomaterial [m^2]

κ_0 Permeability of the saturated geomaterial [m^2]

λ Plastic multiplier

$\dot{\lambda}$ Rate of change of plastic multiplier

μ Dynamic viscosity [Pa s]

ν Poisson's ratio

ξ Arbitrary constant

o Parameter in the incremental strain tensor

ρ Fluid density [kg/m^3]

ρ_0 Saturated vapour density [kg/m^3]

σ Standard deviation of the underlying Gaussian distribution of a lognormal distribution

$\boldsymbol{\sigma}$ Stress vector [Pa]

$\boldsymbol{\sigma}_{\mathrm{tot}}$ Tensor of the total stresses [Pa]

$\boldsymbol{\sigma}^*$ Modified Bishop stress tensor [Pa]

$\boldsymbol{\sigma}'$ Effective stress tensor [Pa]

$\boldsymbol{\sigma}''$ Modified effective stress tensor [Pa]

$\boldsymbol{\sigma}_{\mathrm{tot}}$ Total stress tensor [Pa]

σ_{11},σ_{22},σ_{33} The three normal principal stresses [Pa]

σ_{n} Normal stress of a mechanical element [Pa]

σ_{net} Net stress [Pa]

σ_{m} Mean of the principal stresses [Pa]

$\sigma_{\hat{n}}$ Normal stress of the mechanical element [Pa]

$\sigma_{\hat{s}}$ First tangential stress of the mechanical element [Pa]

$\sigma_{\hat{t}}$ Second tangential stress of the mechanical element [Pa]

$\sigma^{(tr)}$ Trial stress vector [Pa]

τ Resultant of the tangential stresses [Pa]

υ Volume flux [m^3/s]

$\Phi()$ Lognormal Cumulative Distribution Function

ϕ Friction angle [^{o}]

χ Weighting factor for the Bishop stress

ψ Parameter in the incremental strain tensor

$\Omega()$ Lognormal Cumulative Distribution Function

ω_i Rotational displacement of the i-th mechanical node coaxial to the element

Roman symbols

A_{p} Pipe cross-section area [m^2]

A_{mech} Area of a mechanical element [m^2]

a, b, c Edge lengths of a cell along x, y and z [m]

a_{Lin} The slope of a cumulative linear distribution function [m^{-1}]

a_{mech} The slope of the Cumulative Distribution Function of the mechanical elements cross-section radii [m^{-1}]

a_{p} The slope of the Cumulative Distribution Function of the pipes cross-section radii [m^{-1}]

a_{s} The slope of the Cumulative Distribution Function of the spheres cross-section radii [m^{-1}]

$\mathbf{B}$ Matrix relating the midpoint displacement discontinuity to the nodal displacements of a mechanical element

$\mathbf{B}_1$ First sub-matrix of $\mathbf{B}$

$\mathbf{B}_2$ Second sub-matrix of $\mathbf{B}$

$\mathbf{B}_{\mathrm{r}}$ Matrix relating mechanical element nodal rotations to midpoint rotational jumps

$\mathbf{B}^*$ Sub-matrix of $\mathbf{B}_2$

b The length of one of the edges of the tessellated rectangular domain

b_{Biot} Biot coefficient

b_{Lin} Intersection point of the extension of a cumulative of a linear distribution function with the probability axis

b_{m} Intersection point of the extension of the Cumulative Distribution Function of the mechanical elements cross-section radius with the probability axis

b_{p} Intersection point of the extension of the Cumulative Distribution Function of the pipes cross-section radii with the probability axis

b_{s} Intersection point of the extension of the Cumulative Distribution Function of the spheres radii with the probability axis

C Mechanical element mid-point

C′ Mechanical element mid-point corresponding to the left hand rigid arm

C″ Mechanical element mid-point corresponding to the right hand rigid arm

c_{circ} Circumference of the pipe element cross-section [m]

$\mathrm{COV_L}$ The coefficient of variation of an arbitrary lognormal distribution

$\mathrm{COV^{mech}}$ The coefficient of variation of the lognormal distribution of mechanical elements cross-section radii

$\mathrm{COV^p}$ The coefficient of variation of the lognormal distribution of pipes cross-section radii

$\mathrm{COV^s}$ The coefficient of variation of the lognormal distribution of spheres radii

$\mathbf{D}_{\mathrm{el}}$ Elastic stiffness matrix [Pa]

$\mathbf{D}_{\mathrm{ep}}$ Elastic elasto-plastic tangent stiffness matrix [Pa]

$\mathbf{d}_e$ Vector of the nodal degrees of freedom of one element

$\mathbf{d}'$ Displacement vector of the mechanical element mid-point corresponding to the left hand rigid arm

$\mathbf{d}''$ Displacement vector of the mechanical element mid-point corresponding to the right hand rigid arm

D_{v} Molecular diffusivity of vapour in air [m^2/s]

d_{min} Minimum spacing of generated points [m]

$\mathbf{E}_{\mathrm{AVE}}$ Vector of the average engineering strains

E Mechanical element normal modulus

E_e Mechanical element normal modulus

E_{macro} Young's modulus of a numerical cell

E_{x}, E_{y}, E_{z} The three normal average engineering strains

E_{yx}, E_{zx}, E_{yx} The three shear average engineering strains

erf() The error function

$\mathbf{f_e}$ Pipe nodal flow rate vector

$\boldsymbol{f_\sigma}$ The vector equal to $\partial f/\partial \boldsymbol{\sigma}$

f Plasticity yield function

$\dot{f}$ Time derivative of the yield function

G_{macro} Shear modulus of a periodic cell Pa

g Gravitational acceleration [$\mathrm{m/s}^2$]

$H()$ Heaviside step function

$\mathbf{I}$ Identity matrix

I_1 First principal moment of inertia of the mechanical element cross-section [m^4]

I_2 Second principal moment of inertia of the mechanical element cross-section [m^4]

I_{p} Polar moment of inertia of the mechanical element cross-section [m^4]

$\mathbf{K}$ Structural element stiffness matrix

$\mathbf{K}_{11}$, $\mathbf{K}_{22}$, $\mathbf{K}_{21}$, $\mathbf{K}_{12}$ Sub-matrices of the structural element stiffness matrix [N/m]

$\mathbf{K}_{\mathrm{r}}$ Rotational stiffness matrix of the structural element [N m]

$\mathbf{K}'_{\mathrm{r}}$ Sub-matrix of the rotational stiffness matrix of the structural element [N m]

$\mathbf{k}$ Sub-matrix of the transformation matrix $\mathbf{T}$ for the mechanical periodic element [N/m]

$\mathbf{k}_{21}$, $\mathbf{k}_{22}$ Sub-matrices of $\mathbf{k}$

$\mathbf{k}_{\mathrm{spring}}$ Matrix of zero sized spring of a mechanical element

k_{D} Darcy conductivity [m/s]

$K_{\hat{n}}$ Normal stiffness of mechanical element

K_{p} Mechanical element polar rotational stiffness

K_{r1}, K_{r2} First and second mechanical element rotational stiffnesses

$K_{\hat{s}}$, $K_{\hat{t}}$ First and second mechanical element tangential stiffnesses

k_{CELL} Conductivity of a cell

$k_{\mathrm{CELL,0}}$ Conductivity of a saturated cell with no microstractural evolution

k_{l} Liquid fluid conductivity of a pipe element [s]

k_{pipe} Pipe conductivity [s]

k_{v} Vapour conductivity of a pipe element[s]

k_{x}, k_{y}, k_{z} Integer denoting the direction of shift of points towards the x, y and z direction

L Arbitrary length used to determine gradients [m]

l_e Element length [m]

l_{BCC} The edge length of a BCC [m]

l_{CELL} The edge length of a periodic cell [m]

l_{p} Pipe length [m]

$\mathbf{M}$ Translation matrix

M Water molecular weight [kg/mol]

m Number of spheres in the cell

m_{seed} Number of seeding spheres

m_{w} Number of spheres filled with wetting fluid in the network model

N Non-integer number of pores according to scaling technique

n Current porosity

n_0 Initial porosity

N_{con} Number of neighbouring spheres of a sphere

N_{wn} Number of neighbour spheres filled with wetting fluid

$\hat{n}$ Mechanical element local axis coaxial to the element

$\mathbf{P}_{\mathrm{f}}$ Pressure vector of a pipe element [Pa]

P_{c} Capillary suction [Pa]

$P_{\mathrm{c}}^{r_{\mathrm{pm}}}$ Capillary suction corresponding to r_{pm} [Pa]

$P_{\mathrm{c}}^{r_{\mathrm{sm}}}$ Capillary suction corresponding to r_{sm} [Pa]

$P_{\mathrm{c}}^{\mathrm{T}(h+1)}$ Target capillary suction at step $h+1$ [Pa]

P_{c0} Network suction value that a sphere or pipe fills with water [Pa]

P_{cD} Minimum capillary suction that a sphere can be filled with drying fluid [Pa]

P_{cW} Maximum capillary suction that a sphere can be filled with wetting fluid [Pa]

$P()$ Cumulative linear probability function

P^{-1} Inverse of the cumulative linear probability function

p_{dry} Pressure of the drying fluid [Pa]

p_{f} Fluid pressure [Pa]

p_{wet} Pressure of the wetting fluid [Pa]

$\bar{p}$ Mean net stress [Pa]

Q Mass flow rate through a pipe cross-section [kg/s]

Q_{CELL} Mass flow rate through a numerical cell [kg/s]

q Mass flow rate per unit area through a geomaterial [kg/m^2/s]

q_{CELL} Flux through the area of a cell [kg/m^2/s]

$\mathbf{r}$ Vector of nodal rotations of both nodes of a mechanical element

$\mathbf{r}_{\mathrm{C}}$ Vector of rotational jump of mechanical element midpoint

R Universal gas constant [J/mol/K]

$\mathbf{r}_i$, $\mathbf{r}_j$ Vector rotations of nodes i and j

R_1, R_2 The two principal curvature radii of a fluid-fluid interface [m]

r Arbitrary radius [m]

r_1, r_2 The two principal curvature radii of a meniscus water bridge between two identical particles [m]

r_{s0} The initial radius of a sphere [m]

r_{s} The radius of the pores represented by a sphere [m]

r_{p} Pipe radius [m]

r_{part} Particle radius [m]

r_{m} Mean of a lognormal distribution [m]

r_0 Initial value of either a pipe or sphere [m]

r_{mechm} The mean value of mechanical contact areas [m]

r_{pm} The mean value of the pipe radii distribution [m]

r_{sm} The mean value of the sphere radii distribution [m]

r_{min} Minimum value of the radius of either a pipe or a sphere [m]

$r_{\mathrm{mech}}^{\mathrm{max}}$ Maximum radius of the mechanical cross section lognormal distribution [m]

$r_{\mathrm{mech}}^{\mathrm{min}}$ Minimum radius of the mechanical cross section lognormal distribution [m]

$r_{\mathrm{s}}^{\mathrm{max}}$ Maximum radius of the spheres lognormal distribution [m]

$r_{\mathrm{s}}^{\mathrm{min}}$ Minimum radius of the pipe lognormal distribution [m]

$r_{\mathrm{p}}^{\max}$ Maximum radius of the pipe lognormal distribution [m]

$r_{\mathrm{p}}^{\min}$ Minimum radius of the pipe lognormal distribution [m]

r^{mech} Radius of the mechanical element cross section [m]

$r^{\max}$ Maximum of a truncated lognormal distribution [m]

$r^{\min}$ Minimum of a truncated lognormal distribution [m]

S_{r} Degree of saturation

s Standard deviation of a lognormal distribution

s^* Modified suction [Pa]

$\hat{s}$ Mechanical element local axis perpendicular to the element

$\mathbf{T}_{\mathrm{m}}$ Transformation matrix for mechanical periodic elements

$\mathbf{T}_{\mathrm{t}}$ Transformation matrix for transport periodic elements

T Temperature [K]

$\hat{t}$ Mechanical element local axis perpendicular to the element

$\mathbf{u}$ Vector of nodal translations of a mechanical element [m]

$\mathbf{u}_{\mathrm{c}}$ Vector of the displacement discontinuity at the midpoint of a mechanical element [m]

$\mathbf{u}_i$, $\mathbf{u}_j$ Vector translation of nodes i and j [m]

$\mathbf{u}_{\mathrm{e}}$ Vector of the nodal displacements of a mechanical element [m]

u_i Translational displacement of the i-th mechanical node coaxial to the element [m]

V_{f} Volume of fluid under consideration [m^3]

V_{v} The volume represented by each sphere [m^3]

V_{void} Total volume of voids of a geomaterial [m^3]

$V_{\mathrm{sW}i}$ Volume of the i-th sphere filled with wetting fluid [m^3]

$V_{\mathrm{s}i}$ Volume of the i-th sphere in the network [m^3]

v_i Translational displacement of the i-th mechanical node perpendicular to the element [m]

w_i Translational displacement of the i-th mechanical node perpendicular to the element [m]

$\mathbf{x}$ Point coordinate vector [m]

$\mathbf{x}'$ Image point coordinate vector of the translated points for the generation of the periodic cell [m]

x, y, z Global Cartesian axes [m]

Chapter 1

Introduction

1.1 Background

Porous materials, such as soil, concrete and rock, are used in a variety of engineering applications where two pore fluids are present. Fluid transport, fluid retention and fluid-solid interaction, that govern the performance and durability of the materials, are dependent on their microstructure. Foundations, earthworks, oil recovery, supercritical CO_2 underground sequestration, underground nuclear waste disposal schemes and concrete structures are examples of engineering applications where such materials are used. Incorrect prediction of the material behaviour can lead to economical or environmental damages. Numerous experiments and numerical investigations have therefore been undertaken by many different researchers with the aim of understanding the dependence of the macroscopic material properties on the microstructure. Recent developments achieved significant improvements towards this direction by detecting individual phenomena occurring at lower scales (any scale below the continuum scale). However, these techniques are time consuming and cannot yet directly connect all the individual phenomena that are occurring simultaneously to the overall material behaviour.

To this end, numerical models that are able to reproduce the macroscopic behaviour based on the most important processes occurring at lower scales are considered to be attractive. They offer a tool to understand the connection between the lower and higher scales and to produce reliable quantitative results. To achieve this, the pore structure and solid particles are idealised in order to represent the microstructure. The main processes taken into account are particle-particle mechanical interactions, fluid-fluid interface displacements, pressure driven flow, changes in the pore volumes due to irreversible mechanical changes, forces exerted on particles due to the generation of water menisci bridges around the contact of two particles

and particle breakage.

The model types that are commonly used for investigating the influence of microstructure on macroscopic transport and mechanical properties are network and discrete or lattice element models, respectively. In the present work the network and lattice element approaches are used. Network models are based on an idealisation of the pore network by an equivalent one, consisting of pipes and spheres. The lattice elements are used as an idealisation of the contacts of the solid particles. Despite the large volume of literature on both approaches, few published papers consider hydro-mechanical coupling at the capillary scale (see Section 2.1) by combining the two approaches. Also, little has been published on the calibration of network and lattice models. Calibration is an essential task that should provide an objective technique for the choice of model input parameters. Hence, this process is important to investigate the emergent macroscopic properties of the idealised microstructures.

1.2 Aim & objectives

The aim of the present thesis is to develop a hydro-mechanical model for porous geomaterials, such as concrete, rocks, sand and clay soils with length scales of the pore radii spanning from sub-μm to mm, containing two pore fluids based on idealisation of the material microstructure, in order to predict macroscopic behaviour (see Section 2.1) of those materials and to improve understanding of the roles of various capillary scale phenomena in influencing macroscopic behaviour.

The main objectives of the thesis are

- Development of a new framework of a transport and structural network model for transport and mechanical modelling of porous geomaterials containing two pore fluids.

- Generation of irregular network geometries to allow production of results unaffected by boundaries. These network geometries are considered to generate numerical specimens, from now on referred as cells, for the analysis of the macroscopic behaviour of porous geomaterials.

- Introduction of new Periodic Boundary Conditions (PBCs) (see Section 3.7) for hydro-mechanical network analyses. The introduction of PBCs allows for analysing cells of much smaller size than specimens used for boundary value problems in experiments.

The new techniques associated with the PBCs are related to the initiation of the transport analyses and the preservation of network irregularity.

- New pore scaling approach to improve the retention response of the transport network. This new approach allows for simulating realistic fluid retention response of materials with a significant range of void sizes without needing to explicitly model very large number of smaller voids to use a computationally manageable number of spheres.

- Demonstration that the response of cells consisting of transport and mechanical networks are representative, i.e. independent of size for a wide range of conditions.

- Development of the coupling of the mechanical and transport approaches based on physical processes occurring at a capillary scale.

- Accounting for spatial configurations of two pore fluids and how these configurations changes during wetting and drying processes.

- Evaluation of changes to configurations of two pore fluids caused by any changes of pore dimensions.

- Development of a new calibration strategy for the transport network based on easily obtainable experimental input.

1.3 Assumptions

The present work is focused on modelling the influence of the microstructure of porous materials on their transport, fluid retention and mechanical properties. A coupled hydro-mechanical model was developed combining the transport network and mechanical lattice approaches. Heat transfer and chemical reactions are not included.

The microstructure geometry is generated based on a 3D dual Voronoi-Delaunay tessellation of the domain. The Voronoi polyhedra are used as an idealisation of the solid particles and voids are assumed to be located on the polyhedra vertices and along their edges. For the mass transport model, only capillary pores are modelled i.e. the pore spaces where capillary forces

are dominating over molecular and geochemistry effects (see Section 2.1). The material pore structure is modelled by a network of cylindrical pipes connecting voids, with the spheres representing the larger voids and the pipes representing inter-connecting throats. The locations of pipes and spheres are determined by the Voronoi edges and vertices, respectively. For modelling geomaterials with a range of void sizes a new approach is proposed here where each sphere represents a non-integer number of equal sized spheres. For the mechanical model, the solid particle interaction is modelled by lattice elements placed along the Delaunay edges. For the generation of heterogeneity, random distributions of the radii of spheres, pipes and mechanical contact areas are chosen. The material is considered to be periodic. Based on this assumption and with the aim to preserve the heterogeneity, special PBCs are introduced.

The transport model presented in Section 3.4 was developed to simulate the movement of two immiscible pore fluids (with one being the wetting fluid and the other being the drying fluid as defined in Section 2.3.1) with incompressible flow. For the evaluation of the overall cell conductivity, the wetting fluid is considered to be liquid and the drying one is considered to be gas. Laminar flow is considered for the liquid phase flow and the gas phase moves only due to diffusion. Also, the two pore fluids are considered to be Newtonian, and for the liquid phase they flow according to Hagen-Poisseuille equation. Moreover, the model does not include features of capillary scale experimental observations presented in Section 2.3.1. More specifically, contact angle hysteresis, pinning, snap-off, trapping and liquid water films are not considered. No possibility of trapping of the non-intruding fluid is considered, because there is no consideration of whether there is appropriate connectivity to provide an exit route for the non-intruding fluid. Furthermore, the moisture transport is not influenced by temperature.

Moreover, the mechanical model presented in Sections 3.5 was developed on the main assumption that the porous geomaterial is an assembly of rigid particles with their deformability lumped in zero size springs located at their contact areas. Contacts between pairs of particles are allowed to be cancelled and reformed. However, particles that do not initially share a contact are not allowed to form a new contact during the analyses. The non-linear interaction between particles is modelled by a simple friction law. Also, particle crushing is not taken into account.

For the coupling of the transport and mechanical networks presented in Section 3.6, the coupled approach is based on the assumption that each mechanical contact is created by two perfectly spherical particles with equal radii. Also, when all the spheres surrounding a contact are filled with air, a water meniscus bridge is assumed to be created and an additional force is subjected to the contact (see Section 2.3.3). The additional force is assumed to be constant with varying capillary suction (see Section 2.3.3). From the transport network, only the pipes are affected by the mechanical model in case of plastic flow. Elastic deformations do not affect transport.

1.4 Novelties

In this section, discussion is presented regarding the novelties related to the framework proposed in this thesis and its code implementation.

Network modelling approach was chosen to understand influence of microstructure of porous geomaterials on fluid retention, conductivity and mechanical behaviour. To achieve this, the objectives presented in Section 1.2 were set and the model presented in Chapter 3 and 7 was developed by extending network and lattice modelling approaches found in the literature.

Transport networks consisted of spheres and pipes is a widely used modelling approach, as will be presented in Section 2.3.3. Furthermore, structural networks consisted of mechanical elements as well as simple friction laws have already been proposed. However, this is the first time that a fully periodic transport network was presented (see Sections 3.1 and 3.2) that also created the necessity for development of network initiation approach (see Section 3.8.2). The pore scaling approach presented in Section 3.4.4 is also novel. Furthermore, a completed framework for coupling of transport networks consisted of spheres connected by pipes with mechanical network has not been proposed before. This coupling as well as the extension of microstructural changes model presented in Chapter 7 resulted to the necessity of the development of novel algorithm related fluid stable configuration search (see Section 3.8.2). Moreover, a fully periodic coupled transport and mechanical network is proposed with periodic boundary conditions.

The model presented in Chapter 3 and 7 was implemented by extending existing software packages. More specifically, network generation was implemented as an extension of code initially developed by one of the supervisors of the present thesis, Dr. Peter Grassl. Furthermore, implementation of various material models, elements and solution algorithms were implemented in the open source software OOFEM (Object Orientated Finite Element Method) (Patzák, 2012). Each extension is presented in more detail in the list below

- Extension of already existing 3D non-periodic fully coupled Voronoi/Delaunay network generator for inputs used in numerical analyses. The extension includes generation of fully coupled periodic Voronoi/Delaunay networks (see Sections 3.1 and 3.2) and assignment of sphere, pipe and mechanical cross-section radii (see Section 3.3).

- Extension of already implemented continuum based mechanical and transport lattice elements with polygonal cross-section areas to circular cross-section area mechanical (see Section 3.4.5) and transport pipe elements (see Section 3.5.3), respectively.

- Extension of classic usage of nodes in the finite element framework with solely degrees of freedom to nodes that carry also the microstructural information of radius of larger pores that also perform the pore volume scaling approach presented in Section 3.4.4.

- Implementation of transport material model (see Section 3.4.6).

- Implementation of plasticity model of a simple friction law (see Section 3.5.4 and 3.8.3).

- Implementation of the influence of transport on mechanical model (see Section 3.6.2) and mechanical on transport model (see Section 3.6.3).

- Extension of 2D periodic single mechanical elements to 3D coupled periodic transport (see Section 3.7.2) and mechanical (see Section 3.7.3) elements.

- Implementation of the network initiation and configuration check algorithms (see Section 3.8.2).

- Extension of the discrete transport element and nodes that carry information of associated sphere radii of non-reactive flow presented in Chapter 3 to the reactive flow model presented in Chapter 7.

1.5 Outline

The thesis is divided into 9 chapters. In Chapter 2, the literature review is presented. The physical hydro-mechanical phenomena occurring in porous materials containing two pore fluids are described, with the main focus on phenomena occurring at the capillary pore scale. Moreover, the state of the art of discrete modelling approaches is summarised.

In Chapter 3, the modelling approach used in the subsequent chapters is presented. Initially, the idealisation of the pore scale microstructure with the aid of the network approach is described. The transport and mechanical models are highlighted separately and then their interaction is presented. The implementation of PBCs to analyse the micromechanical problems is then explained. Furthermore, a detailed description of the model implementation is given.

In Chapter 4, the model verification is presented. Simple tests are performed for verifying the correct implementation of the transport model for fluid retention and conductivity. The mechanical model is verified by comparing the model results to analytical ones presented in the literature for elastic and plastic behaviour. The hydro-mechanical coupling is also verified through some simple tests.

In Chapter 5, a parametric investigation of the transport model is presented. This includes investigation of the influence of the pore and pipe radii distribution input parameters on the variation of fluid retention and conductivity changes with capillary suction.

In Chapter 6, the influence of the cell size on the macroscopic behaviour (conductivity, fluid retention and Young's modulus) is investigated. For each cell size, 100 analyses were performed and the mean and standard deviation were evaluated for each macroscopic quantity.

In Chapter 7, the influence of microstructural changes during wetting (swelling of the "particles") on the macroscopic quantities of porosity, degree of saturation and conductivity are presented. This swelling of the "particles" is considered to be at confined conditions and takes place only when the particles come in contact with water. Since swelling is confined the void volumes are reduced. In the present model, confined swelling is represented by the volume changes of pores spaces only. The changes of the macroscopic properties are presented for changing capillary suctions. The numerical results were compared to analytical ones for almost fully dry and almost fully wet conditions.

In Chapter 8, a strategy to calibrate the model parameters is proposed and comparisons to experimental results are presented. For the transport model, wetting and drying retention results are used as a tool to choose the model parameters. For the technique verification, the calibration is applied to match mercury intrusion and extrusion experimental results reported in the literature. Thereafter, validation of the calibration technique is explored by means of comparison of the predicted relative permeability to experimental results reported in the literature.

In Chapter 9, conclusions emerging from the present work are discussed along with recommendations for future work.

Chapter 2

Literature review

This chapter presents a review of the literature relevant to this thesis i.e. for numerical modelling of porous geomaterials with two pore fluids at the capillary pore scale. The length scales of observation are presented for the types of geomaterials of interest (rock, concrete, sand, silt and clay). For the two largest scales amongst those presented (continuum scale and capillary scale), observations and models are presented concerning the transport, mechanical and coupled hydro-mechanical behaviour. Particular focus is given to the theoretical, experimental and numerical studies for the capillary pore scale rather than the continuum scale.

2.1 Scales in porous materials

Three main material phases exist in geomaterials with two pore fluids: either two immiscible liquid phases and a solid one, or a liquid, a gas and a solid phase. In these materials, different structures are observed at different length scales, where different processes are evident at each one (Scheibe et al., 2015). A schematic representation of these structures is presented in Figure 2.1. At the highest scale that is presented in Figure 2.1d the material is considered to be continuous and no consideration is given to individual solid particles or individual void spaces containing pore fluids. However, the perspective of a continuous material falls as soon as lower scales are considered.

One scale below, the three phases are now distinguishable as schematically presented in Figure 2.1c. At this scale the porous material consists of an arrangement of solid "particles" and pore spaces, with the pore spaces of a range of sizes over which capillary forces dominate rather than molecular forces. These type of voids are called capillary pores. At this scale,

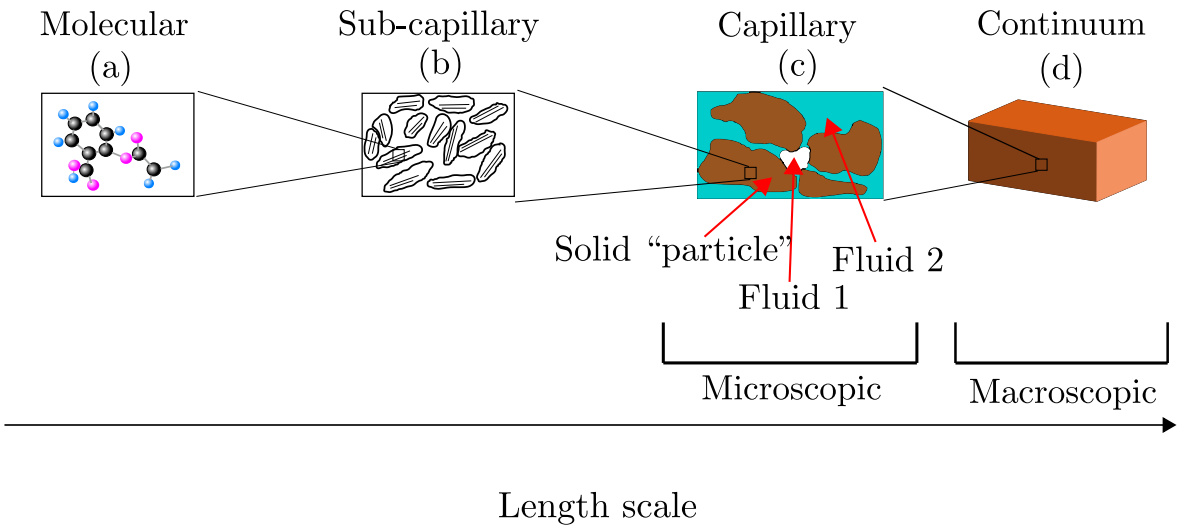

Figure 2.1: Schematic presentation of some of the length scales of porous geomaterials: (a) molecular, (b) sub-capillary, (c) capillary and (d) continuum scale.

each of the two pore fluids can be considered locally as a continuum at a fluid pressure p_f with surface tension occurring at the interface between the two fluids, leading to the generation of capillary forces. Furthermore, forces are exerted on the "particles" at their contacts with other "particles". There are also forces on the surfaces of "particles" due to the fluid pressure in adjacent voids.

The "particles" described above at the capillary scale can take different forms in different geomaterials. In sands, the particles at the capillary scale will be the individual sand grains. However, in clays, the "particles" occurring at the capillary scale will actually be aggregations of many individual clay particles. In these types of materials, examination within one of these aggregates at a lower sub-capillary scale (see Figure 2.1b) shows the arrangement of the individual clay particles (also known as clay platelets) separated by intra-aggregate voids, that are seen in Figure 2.1c. At the scale of these individual clay platelets and intra-aggregate voids, molecular forces are likely to dominate rather than the capillary forces (i.e. the geochemistry becomes crucial). There are many geomaterials, such as compacted bentonite, where both the length scales shown in Figures 2.1b and 2.1c exist (Gens and Alonso, 1992). In contrast there are some geomaterials (e.g. sands and sandstones) where only the capillary scale exists and others (e.g. some natural clays) where only the sub-capillary scale exists.

The next scale of observation is the molecular scale (see Figure 2.1a), within the solid particles, within each of the two fluids or within the complex boundary regions between any two of these three phases. At this scale, molecular forces dominate and a modelling approach known as molecular dynamics is usually adapted (Kresse and Hafner, 1994).

Additionally, the scale separation can continue towards lower scales such as atomic and sub-atomic level. New types of interactions are driving the processes evident at these levels.

These scales are not included in Figure 2.1 since they are further beyond our focus than those presented in Figure 2.1a and b.

The present thesis focuses on the two highest length scales presented in Figures 2.1c and d (the capillary scale and the continuum scale), and the model developed in the thesis represents behaviour at the capillary scale. For abbreviation purposes, the continuum scale will be referred to from now on as the "macroscopic scale" (Figure 2.1d) and the capillary scale will be referred to as the "microscopic scale" (Figure 2.1c). It is important therefore to understand that the use of the terms "microscopic scale" or "microstructure" in the reminder of this thesis does not necessarily imply structures with dimensions of a few micrometers and explicitly excludes structures at the sub-capillary scale that might be implied by the term "microstructure" in many other publications.

The present work focuses on the modelling of the pore-particle structure at capillary scale by means of the network model. The approach is based on capturing the most important capillary pore level events. The aim is to investigate the macroscopic material behaviour as an emergent result from interaction of the capillary pore level events. In Sections 2.2.1, 2.2.2 and 2.2.3 a brief discussion is presented concerning the main macroscopic observations and the corresponding continuum models. Literature related to pore-scale theoretical, experimental and numerical investigations is presented in more detail in Sections 2.3.1, 2.3.2 and 2.3.3.

2.2 Macroscopic observations and modelling in porous materials with two pore fluids

2.2.1 Transport

In the present thesis, the term transport encompasses both mass transport of fluids through a porous geomaterial and retention/storage of fluids within them. In this section, initially the macroscopic retention observations are presented and then the transport observations are presented.

The quantity most commonly used for describing the retention of a fluid within a porous geomaterial is the degree of saturation S_{r} defined as

$$S_{\mathrm{r}} = \frac{V_{\mathrm{f}}}{V_{\mathrm{void}}} \tag{2.1}$$

where V_{f} is the volume of the fluid under consideration retained by the geomaterial and V_{void} is its total void volume.

The variation of the degree of saturation in a porous geomaterial is linked to the variations of capillary suction P_{c} that appears in the presence between an interface of two immiscible fluids. The capillary suction is defined as

$$P_{\mathrm{c}} = p_{\mathrm{dry}} - p_{\mathrm{wet}} \tag{2.2}$$

where p_{wet} and p_{dry} are the pressures in the two fluids. The symbol p_{wet} refers to the wetting fluid and p_{dry} to the drying fluid, where these terms are explained in Section 2.3.1. Here it should be noted that in the present thesis the Cauchy stress tensor $\boldsymbol{\sigma}$, has a tension positive sign convention but the fluid pressure p_{wet} or p_{dry} is defined as compression positive.

When the two fluids co-exist in the porous geomaterial, p_{dry} is always larger than p_{wet} (see Section 2.3.1), hence P_{c} is always positive. When P_{c} increases, drying fluid advances, wetting fluid recedes and the geomaterial is undergoing a drying process, whereas when P_{c} decreases, the wetting fluid advances drying fluid recedes and the geomaterial is wetting. A more detailed description of these processes is given later in Section 2.3.1, where the microscopic observations are presented.

In experiments, wetting and drying of porous geomaterials are driven by changes in P_{c}. The relationship of S_{r} versus P_{c} is non-linear as schematically presented in Figure 2.2a for a wetting fluid. This relationship is known as a retention curve. For the black drying curve in Figure 2.2a, the geomaterial begins from fully saturated conditions at $S_{\mathrm{r}} = 1$. If the geomaterial is subjected to drying, S_{r} decreases while P_{c} increases. If the drying is continued to very high values of P_{c}, the geomaterial will approach a fully dry condition ($S_{\mathrm{r}} = 0$). During wetting from a fully dry condition ($S_{\mathrm{r}} = 0$), the value of S_{r} increases as P_{c} is reduced. On wetting, the value of S_{r} may approach 1 as P_{c} approaches 0 (see Figure 2.2a), indicating that no drying fluid remains in the pores. However, there are cases where the drying fluid can be trapped and S_{r} is not returned back to 1 (Poulovassilis, 1962). The drying and wetting paths followed on drying from $S_{\mathrm{r}} = 1$ or wetting from $S_{\mathrm{r}} = 0$ are called the primary drying and primary wetting curves, respectively. The primary drying curve and primary wetting curve do not coincide (see Figure 2.2a), a phenomenon known as retention hysteresis (Leverett, 1941).

If a reversal of capillary suction change occurs at values of S_{r} between 0 and 1, a different retention curve would be produced. This is schematically presented with the red curves in Figure 2.2a, where the upper one presents a drying path if a preceding wetting stops at $S_{\mathrm{r}} < 1$ and the lower one presents a wetting path if a preceding drying stopped at $S_{\mathrm{r}} > 0$. This type

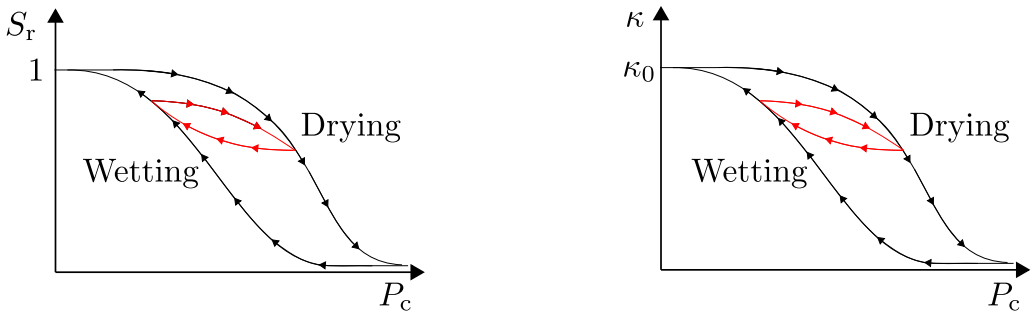

Figure 2.2: Schematic presentation of the variations of macroscopic quantities of porous geomaterials during drying and wetting: (a) degree of saturation S_r versus capillary suction P_c and (b) permeability κ versus P_c.

of curve is known as a scanning curve (Poulovassilis, 1962) and it is different depending on the point where the preceding drying or wetting process was stopped. Therefore, at a given value of P_c a range of values of S_r are possible for a given geomaterial, falling between the primary drying curve and the primary wetting curve.

Before the discussion of the different mass transport mechanisms, it is helpful to give a few more details for the compositions of the two immiscible fluids. Each of these fluids can consist of more than one species since they can be a mixture of two miscible fluids or they can include dissolved species. Consider the example of a geomaterial containing gaseous air and liquid-water. The gas phase (air) consists of oxygen, nitrogen, water vapour and other species and the liquid phase (water) consists of water molecules and other species such as oxygen and nitrogen that are dissolved within it. All these species are able to move within the individual fluid phase or they may even move between the two fluids by changing phase. The different mechanisms that are responsible for these movements are now going to be discussed by considering the same example of a gaseous air and liquid water system.

The main mass transport mechanisms for the pore fluids are pressure driven flow, diffusion and advection (Massmann and Farrier, 1992). The pressure driven flow is generated due to a pressure gradient in the given fluid and it can occur both in liquid water and gaseous air. Diffusion is the mass flow that is initiated due to a concentration gradient of a species. For instance, a concentration gradient of water vapour can generate movement of water vapour within the gas phase or a concentration gradient of dissolved nitrogen can generate movement of nitrogen molecules within the liquid phase.

Finally, advection is the secondary movement of a species due to the primary movement of a phase consisting of another species. For example, water vapour can be transported due to a movement of the gas phase (carrying the water vapour with it) due to a gradient of gas pressure, even when there is no gradient of concentration of water vapour. Another example

of advection is when dissolved oxygen is carried along by flow of the liquid phase (caused by a gradient of liquid pressure) even when there is no gradient in the concentration of dissolved oxygen. Advection is the main source of transport of chloride within concrete structures since it is advected by water that moves from wetter to dryer regions, carrying the chloride ions and then depositing them at the far-most location where the water front can reach.

Pressure driven flow is the main mass transport mechanism taken into account in this thesis and will be described now in greater detail. The pressure driven flow of a fluid through a porous geomaterial is described by Darcy's law (Jerauld and Salter, 1990)

$$q = \frac{\rho\kappa}{\mu}\frac{\Delta p_{\mathrm{f}}}{L} \tag{2.3}$$

q is the mass flow rate per unit area, ρ is the fluid density, κ is the permeability of the geomaterial, μ is the fluid viscosity and Δp_{f} is the drop in fluid pressure over a length L. The permeability κ of the geomaterial is a measure of how easy it is for a fluid to flow through the geomaterial, irrespective of the fluid properties ρ and μ. Equation (2.3) ignores any differences of elevation (i.e. either horizontal flow is assumed or for a difference of elevation ΔZ, $\rho g \Delta Z$, where g is the gravitational acceleration, is considered to be negligible compared to Δp_{f}).

In (2.3), the product $\mu\kappa/\rho$ relates q with $\Delta p_{\mathrm{f}}/L$. Another expression also used to relate q with $\Delta p_{\mathrm{f}}/L$ is

$$q = k\frac{\Delta p_{\mathrm{f}}}{L} \tag{2.4}$$

where k is known as conductivity and its units are of time. The relation between k and κ is

$$k = \frac{\rho\kappa}{\mu} \tag{2.5}$$

Conductivity will be used as the quantity representing the ease of flow through a porous geomaterial for the majority of results presented in this thesis.

It is common to express the fluid flow through geomaterials due to a potential by means of the Darcy's law as

$$\upsilon = k_{\mathrm{D}}\,\iota \tag{2.6}$$

where υ [ms^{-1}] is the volume flux, k_{D} [ms^{-1}] is the Darcy permeability and ι is the non-dimensional hydraulic gradient. The relationship between k and k_{D} is

$$k_{\mathrm{D}} = \mathrm{g}k \tag{2.7}$$

where g is the gravitational acceleration constant ≈ 10. Hence, k_{D} can be evaluated by multiplying all results for k by a factor of 10.

The variation of permeability κ with capillary suction P_{c} is similar to that for S_{r}. Figure 2.2b schematically presents the changes of κ for a wetting fluid for drying and subsequently wetting. When the geomaterial is saturated with wetting fluid, the permeability value is equal the saturated permeability κ_0. The latter value is known as intrinsic permeability for inert geomaterials that do not deform. However, for deformable geomaterials the value of saturated permeability κ_0 is not constant since the void volume changes upon deformation. Hence, κ_0 increases during dilation of a porous geomaterial since the void volume increases and there are larger pathways for the wetting fluid to flow. During compression κ_0 decreases since the void volume decreases and the pathways are narrower, resulting in a reduction of ease of fluid flow. The black curves in Figure 2.2b are for primary wetting and drying where they present hysteresis like the retention curves. If there is trapping of the drying fluid during a wetting path, the value of κ may not return to κ_0 at the end of a primary wetting curve (Poulovassilis, 1962). The scanning curves for permeability (shown in red in Figure 2.2b) take a similar qualitative form to those presented for retention. Hence, for a given value of P_{c} there is a range of possible values of κ for a given geomaterial, depending on the wetting-drying history of the geomaterial.

The qualitative similarities of the permeability curves and the retention curves can be explained by considering the changes of the amount of wetting fluid in the geomaterial for P_{c} changes. As presented in Figure 2.2a, as the geomaterial is dried, S_{r} reduces which means that less wetting fluid is held within the geomaterial and therefore there are fewer pathways for the wetting fluid to move through. This has an explicit impact on κ, with κ reducing as less wetting fluid is able to be transported. The reverse effect happens during wetting, because there is an increase in the pathways available for flow of the wetting fluid and therefore κ increases.

The fact that there are not unique values of S_{r} and κ for each value of P_{c} for a given geomaterial creates a great complexity for the prediction of the transport behaviour of the geomaterial (Romero et al., 1999). The S_{r}-P_{c} and κ-P_{c} relationships can be determined with laboratory tests where P_{c} is controlled for a finite number of drying-wetting cycles. Attempts at capturing the S_{r}-P_{c} and κ-P_{c} relations with analytical expressions have been presented

in the literature (Brooks and Corey, 1964; Van Genuchten, 1980; Fredlund and Xing, 1994). However, models require a calibration exercise of variables without a clear physical meaning in order to match experimental results. Each primary or scanning curve requires a different mathematical expression to capture the geomaterial response. To overcome these drawbacks, other methods have been developed to link the macroscopic transport behaviour to physical properties. These are discussed as part of the review of microscopic behaviour in Section 2.3.1.

2.2.2 Mechanical

The design of numerous engineering applications, such as constructions of dams and buildings, is strongly dependent on the understanding of their mechanical behaviour. In the present section, the mechanical behaviour of geomaterials observed at a macroscopic level is discussed. The mechanical observations described here are going to be for cases with one and two pore fluids along with the proposed stress variables for their mechanical description.

At a macroscopic level, the mechanical behaviour of materials is expressed in terms of relationships between stresses $\boldsymbol{\sigma}$ and strains $\boldsymbol{\varepsilon}$. Early proposals for stress-strain relations were linear elastic and later non-linear elastic (Love, 1927) in terms of total external stresses $\boldsymbol{\sigma}_{\text{tot}}$ and strains $\boldsymbol{\varepsilon}$. It was later found that expressions of this type were inappropriate for porous geomaterials containing a pore fluid under pressure. Terzaghi (1925) proposed that stress-strain relationships for porous geomaterials containing a single pore fluid should be expressed in terms of a new stress variable, the effective stress $\boldsymbol{\sigma}'$ that is given as

$$\boldsymbol{\sigma}' = \boldsymbol{\sigma}_{\text{tot}} + p_{\text{f}}\mathbf{I} \tag{2.8}$$

where $\boldsymbol{\sigma}_{\text{tot}}$ is the total stress tensor, p_{f} is the pressure of the pore fluid and $\mathbf{I}$ is the 3×3 unity tensor.

Equation (2.8) is valid for most types of soils but not for other materials such as concrete and rocks. A modified expression of (2.8) was proposed by Biot (1941) to capture the correct effective stress for all types of porous geomaterials containing a single fluid

$$\boldsymbol{\sigma}' = \boldsymbol{\sigma}_{\text{tot}} + b_{\text{Biot}} p_{\text{f}}\mathbf{I} \tag{2.9}$$

where b_{Biot} is the Biot coefficient and it varies between 0 and 1 for different geomaterials. Equation (2.8) is a special case of (2.9) for the case of $b_{\text{Biot}} = 1$. Skempton (1961) showed

that value of b_{Biot} is determined by the ratio of the individual particle stiffness to the overall geomaterial solid skeleton stiffness rather than the ratio of the inter-particle contact area over the total cross-sectional area of the geomaterial that was previously believed to be the case.

The aforementioned evaluation of stresses in geomaterials hold for the case that the material behaviour lies within the elastic regime and the stress-strain path that the material is subjected is reversible. However, this is not the case for the majority of engineering applications where stress-strain paths are not reversible. The non-reversibility is attributed to two causes, material yielding and material damage.

A variety of plastic models have been proposed to model the plastic behaviour of geomaterials. The main categories of plasticity models are those of perfect plasticity, hardening plasticity and softening plasticity. For perfect plasticity models, yield locus does not change during plastic straining. Some of the most well known perfect plasticity models are Mohr-Coulomb (Shield, 1955) and Drucker-Prager (Drucker and Prager, 1952) models.

Also, for soils saturated only with one type of fluid, more complex plasticity models were developed, for which the yield locus evolves with evolving effective stress states. For instance, this behaviour was successfully described by the Modified Cam Clay (MCC) (Roscoe et al., 1963).

However, the aforementioned models are not able to capture more complex material features such as progressive accumulation of strains and the influence on the dependence of stress path amongst others. Gradual non-linear plastic strain development can be captured by bounding surface models (Dafalias and Herrmann, 1982) or nested yield surface models (Stallebrass and Taylor, 1997). Also, models that capture the evolving anisotropy of plastic behaviour have been developed (Wheeler et al., 2003) where the yield locus is inclined with respect to the principal stress axes, and this yield locus inclination can evolve during plastic straining. Furthermore, models were developed which were able to describe the breakage of bonds between particles (Leroueil and Vaughan, 1990). Here, a yield curve that corresponds to the geomaterial without the bonds is located within the yield curve of the actual bonded material. Finally, models that consider the effect of creep (where strains develop gradually over time while stresses remain constant) and loading rates have been proposed (Yin and Graham, 1999). These models are known as elasto-viscoplastic models since they take into account both elasto-plasticity and creep/load rate effects.

The second mechanical phenomenon that encompasses energy dissipation is damage. In this case, when the stresses exceed the material strength, the material connection is lost and energy is therefore dissipated. Hence, the stresses are reduced with increasing strains and the material is said to soften (Kachanov, 1958; Ortiz, 1985). When the material is unloaded, the strains are fully recovered. Additionally, a combination of the two macroscopic dissipative

phenomena, namely damage and plasticity, can be used to describe more complex material behaviour (Simo and Ju, 1987; Ju, 1989).

All the above models are developed in terms of effective stress. As the investigation of the mechanical behaviour of geomaterials was extended to the case where two pore fluids exist, such as soils under unsaturated conditions, new stress variables needed to be introduced. Initially, a modified effective stress was proposed by Bishop (1960) as

$$\boldsymbol{\sigma}'' = \boldsymbol{\sigma} - [\chi p_{\text{wet}} + (1-\chi) p_{\text{dry}}]\mathbf{I} \tag{2.10}$$

where $\boldsymbol{\sigma}''$ is the modified effective stress and χ is a weighting factor. However, this stress variable was shown to be incapable of describing the yield behaviour of unsaturated soils, including phenomena such as the possible occurrence of "collapse compression" during wetting (Jennings and Burland, 1962). Subsequent research showed that two independent stress variables are required to describe the behaviour of soils under unsaturated conditions (Fredlund and Morgenstern, 1977) i.e. soils containing two pore fluids. A widely used pair of stress variables is the net stress $\boldsymbol{\sigma}_{\text{net}}$ and the capillary suction P_{c} (see 2.2), where $\boldsymbol{\sigma}_{\text{net}}$ is defined by

$$\boldsymbol{\sigma}_{\text{net}} = \boldsymbol{\sigma} - p_{\text{dry}}\mathbf{I} \tag{2.11}$$

The volumetric behaviour of unsaturated soils present complexities. Figure 2.3 shows qualitatively two normal compression line in the porosity n versus mean net stress $\bar{p}$ (the average of the normal net stresses) space for two soil specimens with constant capillary suctions $P_{\text{c}} = 0$ and P_{c1}. Two paths are denoted with letters A and B for the changes of porosity n at constant $\bar{p}$ and decreasing P_{c}, that corresponds to wetting. At path A, the soil under consideration begins from a condition on the elastic branch (the branch of low inclination) of the normal compression line for $P_{\text{c}} = P_{\text{c1}}$ and ends at the elastic branch of the normal compression line for $P_{\text{c}} = P_{\text{c1}}$. At path B, the soil under consideration begins from a condition on the plastic branch (the branch of high inclination) of the normal compression line for $P_{\text{c}} = P_{\text{c1}}$ and ends at the plastic branch of the normal compression line for $P_{\text{c}} = P_{\text{c1}}$. For wetting at $\bar{p}$ low values (path A), n, and hence the overall volume, increases elastically (see path A in Figure 2.3) which is equivalent to a decrease of effective stress in a saturated soil. For wetting at high $\bar{p}$ values (path B), n decreases in a plastic manner (see path B in Figure 2.3), which is equivalent to an increase of effective stress in a saturated soil. Therefore the increase of the wetting fluid in the soil has two potential effects since for a range of $\bar{p}$ values the soil behaves similar as unloading a saturated soil and for other $\bar{p}$ values the soil behaves as loading a saturated soil.

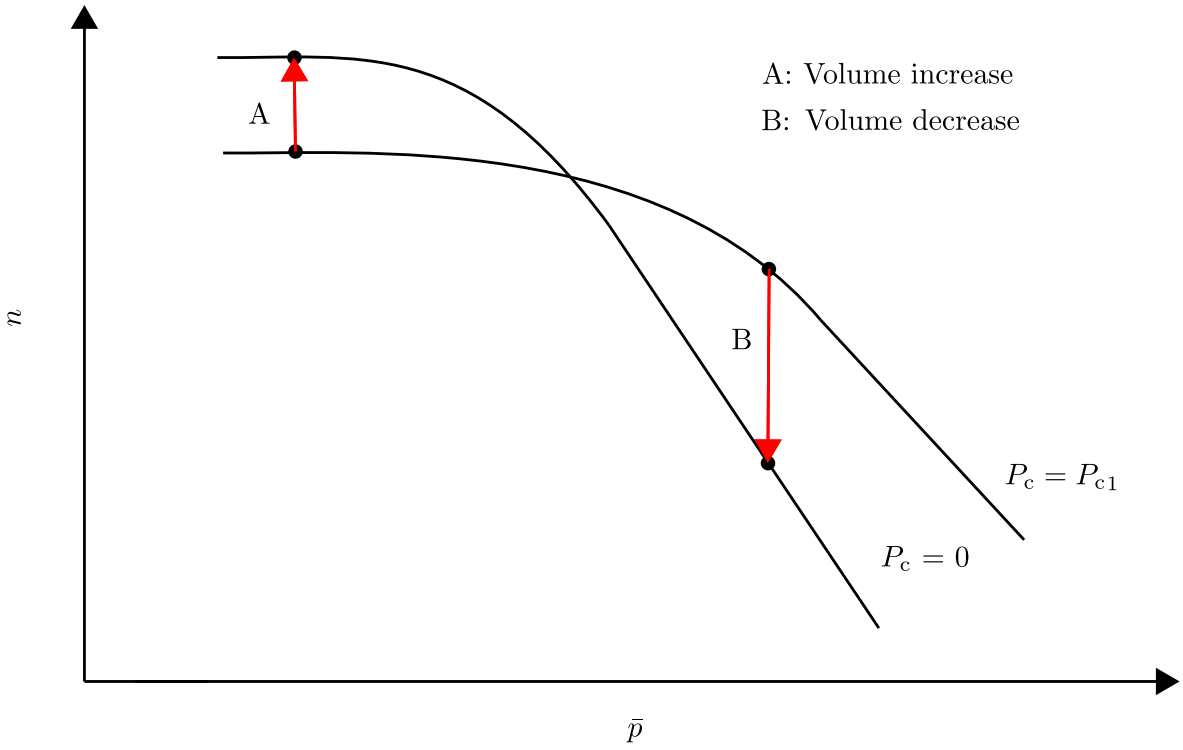

Figure 2.3: Qualitative presentation of volume changes of unsaturated soil during wetting: normal compression lines in porosity n versus mean net stress $\bar{p}$ space for wetting at low $\bar{p}$ and wetting at high $\bar{p}$.

Fredlund et al. (1978) showed that shear strength of unsaturated soils is depended on net stress and capillary suction. Subsequent laboratory experiments showed that shear strength varies non-linearly with increase of capillary suction (Gan et al., 1988). Therefore, capillary suction influences both volumetric and deviatoric behaviour in a non-linear fashion.

The first complete constitutive model for unsaturated soils was presented by Alonso et al. (1990) known as Barcelona Basic Model (BBM). BBM is expressed in terms of $\boldsymbol{\sigma}_{\text{net}}$, P_c and deviatoric stress. This model is one of the most widely used elasto-plastic constitutive models for unsaturated soils and is able to capture swelling and collapse upon wetting and the influence of capillary suction on shear strength. Many subsequent constitutive model employing net stresses and capillary suction have been developed (Wheeler and Sivakumar, 1995). Some of the BBM limitations arise from the particular choice of the uncoupled stress variables. The coupling of stress variables is going to be discussed in Section 2.2.3.

2.2.3 Hydro-mechanical

The hydro-mechanical interaction of porous materials is a topic that has received considerable attention due to its application to a variety of fields such as hydraulic fracturing, slope and foundation stability, nuclear waste disposal schemes and others. Here interaction encompasses

coupling in both directions: the influence of mechanical deformation on fluid transport and retention and also the influence of pore fluid pressures and pore fluid retention (the degree of saturation) on mechanical behaviour.

Pore fluid pressure p_{f} is a common variable in both mechanical and transport behaviour, i.e. appears in mechanical effective stress (2.8 and gradients of p_{f} drive fluid flow (2.3)). Therefore, throughout a hydro-mechanical analysis, information for p_{f} must be exchanged between the mechanical and the transport analyses.

Mechanical straining can cause changes of porosity n, which implies a change of fluid storage capacity and conductivity in transport analysis. Porosity changes, caused by mechanical straining can cause changes of fluid conductivity within transport analysis. This includes homogeneous changes of porosity in many geomaterials, but also the influence of opening or closing of contacts in some geomaterials (Ma, 2015).

From the above, it can be seen that transport and mechanical behaviour must be solved simultaneously for coupled hydro-mechanical analyses. For geomaterials containing a single fluid, information of changes of p_{f} and n must be exchanged between the two behaviours.

Additional parameters are involved in single transport or mechanical analyses of geomaterials with two pore fluids. Pore fluid pressures of the drying fluid p_{dry} and the wetting fluid p_{wet} are common variables in both mechanical and transport/retention behaviour (they appear in mechanical stress state variables, such as $\boldsymbol{\sigma}_{\mathrm{net}}$ in (2.11) and P_{c} in (2.2) , gradients of p_{dry} and p_{wet} also control retention behaviour (through P_{c}). The changes of the above additional parameters are related to each other as well as the changes of the governing parameters of hydro-mechanical analysis of geomaterials containing a single fluid. This is extra information that needs to be exchanged throughout hydro-mechanical analysis of geomaterials with two pore fluids.

Changes of porosity, due to mechanical straining, cause a change of total available fluid storage capacity. Retention behaviour is now required to be examined to present how this storage capacity is divided between the two pore fluids. Changes of porosity, caused by mechanical straining, are found to affect the retention curves of S_{r} versus P_{c}. For example, Figure 2.4 shows a mathematical expression proposed by Gallipoli et al. (2003) fitted to the experimental data of Wheeler and Sivakumar (1995), corresponding to primary wetting curves for a compacted Speswhite kaolin. Furthermore, changes of n as well as changes of S_{r} (where the latter is caused by changes of P_{c}) cause changes of conductivity for each fluid (see Section 2.2.1).

Recent research suggests that changes of S_{r} cause changes of mechanical behaviours which cannot be explained solely in terms of accompanying changes of P_{c}. This is important,

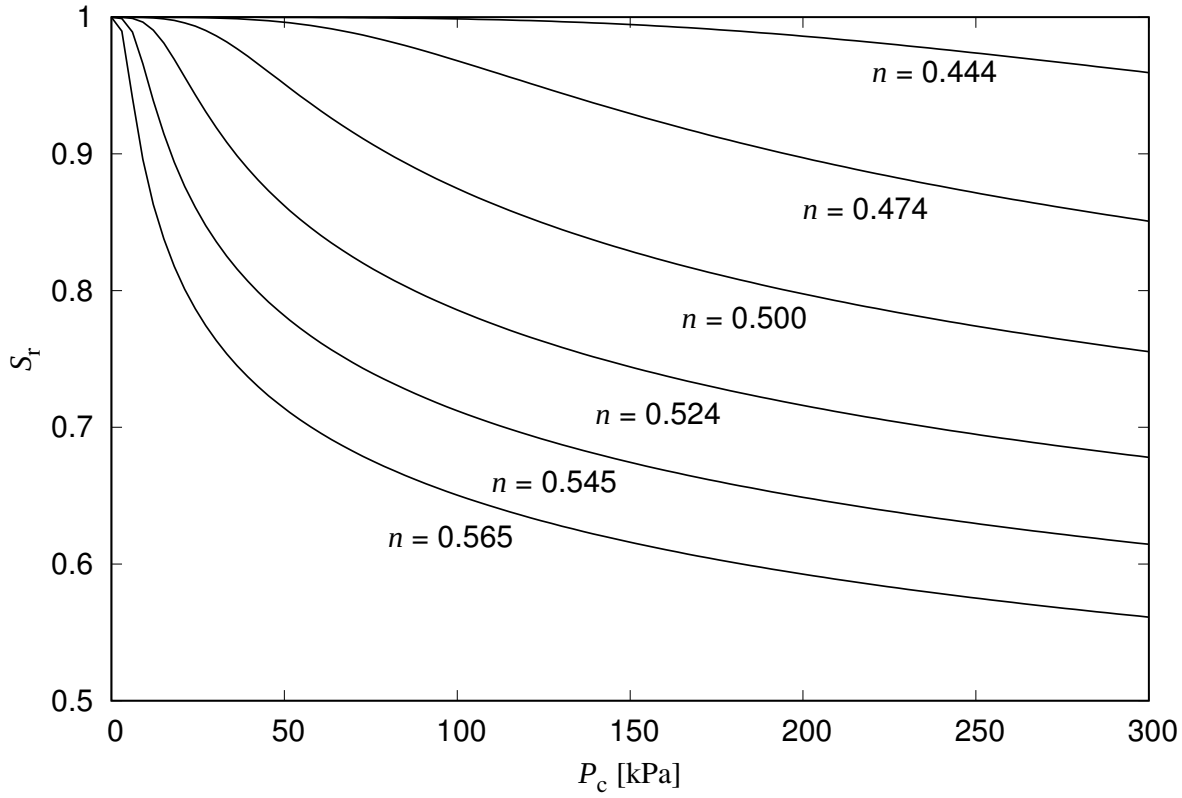

Figure 2.4: Retention curves for primary wetting based on a fitted mathematical expression: degree of saturation S_r versus capillary suction P_c for various porosities n (Gallipoli et al., 2003).

because hydraulic hysteresis means that, for a given geomaterial, there is not a one-to-one relationship between S_r and P_c (see Figure 2.2a). This means that it can be difficult (perhaps impossible) to represent all features of mechanical behaviour when interpreted solely in terms of net stresses and capillary suction. This has led several authors to develop mechanical constitutive models for unsaturated soils applying alternative pairs of stress state variables. For example, Wheeler et al. (2003) developed a model in terms of "Bishop's stress" $\boldsymbol{\sigma}^*$ and "modified suction" s^*, defined as follows

$$\boldsymbol{\sigma}^* = \boldsymbol{\sigma} - [S_r p_{wet} + (1 - S_r) p_{dry}]\mathbf{I} \tag{2.12}$$

$$s^* = nP_c \tag{2.13}$$

The constitutive model of Wheeler et al. (2003) (now known as the Glasgow Coupled Model (GCM)) is a coupled model covering both mechanical behaviour and retention behaviour.

2.3 Microscopic observations and modelling

2.3.1 Transport

The microscopic phenomena occurring at the capillary pore scale during fluid transport and during drying and wetting processes (retention) are discussed in this section. Individual phenomena, as well as interactions of the phenomena, and their role in the macroscopic transport and retention behaviour are presented through analytical, numerical and experimental investigations presented in the literature.

One of the most important features of porous materials that affects microscale transport phenomena is the pore geometry. As can be observed in Figure 2.1, the pore network consists of individual void spaces (pore bodies) between the particles which are inter-connected by narrower paths (pore throats). Additionally, the pore walls, formed by the surfaces of the solid particles, are in general non-smooth, with nooks and crevices within the pore walls.

In the majority of engineering applications on geomaterials the pore fluid velocities are very small, resulting in very small values of Reynolds number. Therefore, when only one fluid is present within two voids and their narrower connecting throat, laminar flow through the throat can be assumed if any fluid pressure gradient is applied. The throat can be idealised as a capillary pipe with a circular cross-section of radius r and the mass flow rate Q through this cross-section can evaluated from the Hagen-Poisseuille equation (Yiotis et al., 2005a)

$$Q = \frac{\rho}{\mu}\frac{\pi r^4}{8}\frac{\Delta p_{\mathrm{f}}}{L} \tag{2.14}$$

The mass flow rate Q can also be written in terms of the cross-section A_{p} and the pipe conductivity k_{pipe}

$$Q = k_{\mathrm{pipe}} A_{\mathrm{p}} \frac{\Delta p_{\mathrm{f}}}{L} \tag{2.15}$$

Comparison of (2.15) and (2.14) shows that the pipe conductivity k_{pipe} is given by

$$k_{\mathrm{pipe}} = \frac{\rho}{\mu}\frac{r^2}{8} \tag{2.16}$$

The Hagen-Poisseuille equation, in which (2.14) and (2.16) are based, assumes that the fluid under consideration is incompressible and that there is no slip between the fluid and the walls of the pipe i.e. the fluid velocity is zero at the pore walls. In addition, (2.14) assumes that elevation effects are negligible comparing to the pressure gradient Δp_{f} similar to (2.3).

When two immiscible fluids meet, an interface is generated, with a surface tension γ (force per unit length of interface) acting tangentially to the interface (Marchand et al., 2011). If the interface is curved, there must be a difference between the values of the two fluid pressures p_{dry} and p_{wet}. Force equilibrium perpendicular to the interface shows that the capillary suction P_{c} (where $P_{\mathrm{c}} = p_{\mathrm{dry}} - p_{\mathrm{wet}}$, as shown in (2.2)) is related to the surface tension γ and principal radii of the curvature R_1 and R_2 by the interface based on the Laplace formula (De Gennes et al., 2004)

$$P_{\mathrm{c}} = \gamma(\frac{1}{R_1} + \frac{1}{R_2}) \tag{2.17}$$

where R_1 and R_2 are positive when measured on the side of the drying fluid (see Figure 2.5).

Contact angle

When the fluid-fluid interface meets a solid phase (such as a solid particle within a geomaterial) at equilibrium conditions, a contact angle θ must be satisfied between the fluid-fluid interface and the solid material (Figure 2.6). The value of this contact angle θ depends upon the two fluids and the solid and is expressed by Young's equation (De Gennes et al., 2004)

$$\cos\theta = \frac{\gamma_{\mathrm{SD}} - \gamma_{\mathrm{SW}}}{\gamma} \tag{2.18}$$

where θ is considered acute and γ_{SW} and γ_{SD} are the surface tensions of the solid-wetting fluid and solid-drying fluid interfaces, respectively. For the same two fluids, different values of contact angle will be observed for different solids. The fluid with the highest fluid-solid surface tension is the drying one. Hence, the fluid that lies on the side of the angle θ is the wetting fluid and the other is the drying one (see Figure 2.6). The shape of the fluid-fluid interface is adjusted in such a way that the contact angle is satisfied at all points where the fluid-fluid interface meets a solid boundary. For a given fluid-fluid interface and capillary suction P_{c}, the total curvature, $1/R_1 + 1/R_2$, will have the same value at all points on the interface (see (2.17)), but the individual values of R_1 and R_2 will vary over the interface to

form a shape that is able to satisfy the required contact angle at all points of contact with solid particles.

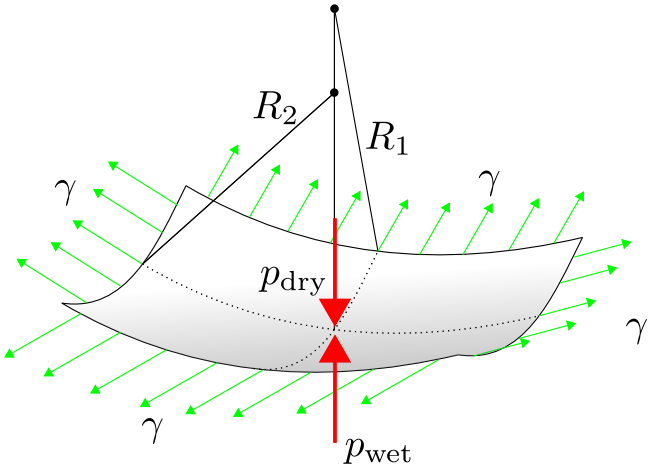

Figure 2.5: Schematic representations of a curved interface generated by two immiscible fluids: the two principal radii of curvature R_1 and R_2, surface tension γ with green arrows and the drying and wetting fluid pressures with red ones.

The value of the contact angle generated between the fluid-fluid interface and the solid is one of the key input parameters in the model presented in this thesis. Solid surfaces can be considered as perfectly smooth or the role of asperities can be taken into account depending on the length scale that is observed. Contact angles are generally measured under the assumption that the surface is smooth, and the contact angle is then the angle generated between the tangent plane to the solid surface and the tangent plane to the fluid-fluid interface at any point on the line of contact (the triple line). Figure 2.6 shows the ideal case, with the fluid-fluid interface contacting with a smooth flat solid surface. However, when the triple line is observed at lower scale, the line of intersection of the fluid-fluid interface and the solid may be passing over asperities on the solid surface. In this case the contact angle should strictly be measured relative to the local tangent to the asperity surface. This means that the measured value of contact angle may strongly depend on the level of resolution of the observation equipment.

When the fluid-fluid interface is moving (during a process of wetting or drying), the measured contact angle is different to the value measured for quasi-static conditions, with larger values of contact angle measured during wetting and smaller values measured during drying. This is known as hysteresis of the contact angle. A variety of factors contribute to contact angle hysteresis, as explained by Bormashenko (2013). A change of contact angle (and hence a change of the geometry of the fluid-fluid interface) while there is no movement of the contact line of the fluid-fluid interface with the solid is known as pinning. This phenomenon of pinning may be attributable to the contact line (triple line) moving very slightly over the surfaces of asperities (only visible at the smaller scale) or it may be due to solid surface energy effects, as claimed by Bormashenko (2013). The higher the solid surface energy, the more prominent pinning is. Chemical heterogeneity of the solid surface may also be a significant factor (Marmur, 1994).

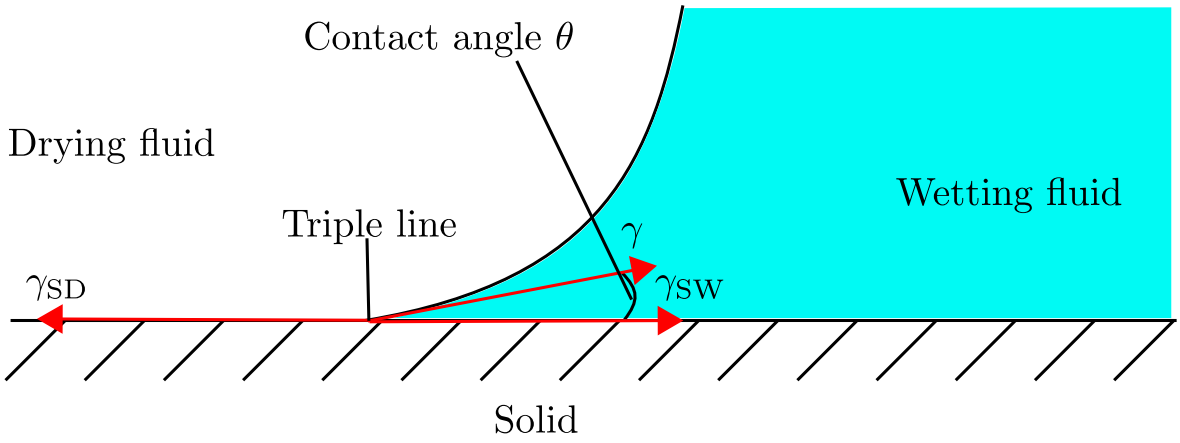

Figure 2.6: Schematic presentation of contact of the solid with the fluid-fluid interface: a contact angle θ is generated between the interface and the solid.

Conventionally, contact angle measurements are conducted by placing a droplet of one fluid within the other fluid on a solid surface and then measuring the angle generated, without taking any account of asperities. For rough surfaces, contact angle measurements performed in this way are sensitive to the measuring technique (Fetzer and Ralston, 2011) and to the droplet volume (Drelich et al., 1996).

The vast majority of porous geomaterials possess pore walls that are chemically heterogeneous and rough. Hence the measurement of the contact angle in applying the traditional measurement techniques would not be suitable. Direct measurement of the contact angle using $\mu-$CT scanning, as described by, for example Andrew et al. (2014a) who applied this technique to water and supercritical CO_2 in sandstone. The hysteresis of contact angle observed by Andrew et al. (2014a) was attributed to the heterogeneity of the pore walls. They also state that the wide range of measured values of contact angle may be due to ambiguities in the post processing of the image data. The ability to measure contact angles at scales two orders of magnitude below those seen in $\mu-$CT was presented by Schmatz et al. (2015). Measurements at this very low scale in a sandstone oil reservoir material were performed and it was found that oil is prone to adhere on clay surfaces irrespective of the surface roughness.

Fluid-fluid interface movement phenomena

During drying and wetting processes there are changes to the arrangement of the two pore fluids within the pore spaces and hence movements of the fluid-fluid interfaces. Drying and wetting are conducted when a drying or a wetting fluid is advancing within the pore space, respectively. The capillary pore scale fluid-fluid interface movement phenomena are related to the type of process that is undertaken within a pore, either drying or wetting. The main categories of fluid-fluid interface movement phenomena occurring during wetting or drying

are: piston-like fluid-fluid interface displacements, Haines' jumps, formation of thin films of wetting fluid, snap-off and contact angle hysteresis (Jerauld and Salter, 1990).

Piston-like displacement is the smooth movement of the fluid-fluid interface within a pore throat (Ryazanov et al., 2009) which can be considered a reversible process (Morrow, 1970). However, there are cases where this interfaces are unable to move slowly along the pore walls and instead they pin. As capillary suction changes, the pinned interface changes shape and ultimately becomes unstable. At this point, a rapid movement of the fluid-fluid interface occurs to a new location and geometry, where the interface is once more stable (Moebius and Or, 2012). These abrupt displacements of the fluid-fluid interface are known as Haines' jumps after Haines (1930) who was the first to report them. It has been reported that when a Haines' jump occurs, a series of such jumps happen, proceeded by an oscillation of the interface (Moebius and Or, 2012; Berg et al., 2013). By combining measurement of the inter-facial areas, pressure changes and solving the Helmholtz free energy balance equation it was found that energy is dissipated during the jumps (Ferrari and Lunati, 2014; DiCarlo et al., 2003). Both numerical (Ferrari and Lunati, 2014) and acoustic emission (DiCarlo et al., 2003) experiments confirmed the dissipative nature of the bursts of fluids abruptly invading pore voids during Haines' jumps.

The snap-off phenomenon is when wetting fluid blocks a capillary pore throat between two voids filled with drying fluids, thus breaking the continuity. In this case, thin films of wetting fluid are retained along the nooks and crevices of pore throats, since the wetting fluid still fills the narrower voids. In Figure 2.7, a simple case is presented where a pore throat resulting from the contact of three identical spheres. In Figure 2.7a, the 2D throat cross-section is presented being filled with both wetting and drying fluids and its 3D longitudinal extension is presented in Figure 2.7b. At this point in the process, there is still continuity of the drying fluid through the throat. However, subsequent variations of capillary suction mean that the radius of the fluid-fluid interfaces in the throat will fluctuate. During reductions of capillary suction, the radius of the interfaces increases and this means that the wetting-drying fluid interfaces located along the nooks moves towards the the centre of the triangle-like throat cross-section presented in Figure 2.7a. When the three wetting-drying fluid interfaces meet, the interfaces collapse, the throat is filled with wetting fluid and the continuity of the drying fluid is interrupted.

Roof (1970) proposed analytical expressions involving the ratio of throat radius and the distance from the fluid-fluid interface to the throat for predicting whether a snap-off event would occur during drying and compared these predictions to experimental results from tests on a single throat in glass. Also, Raeini et al. (2014a) presented numerical results where for the right conditions, snap-off can happen during wetting as well. In Raeini et al. (2014a), wetting fluid advanced through a throat to occupy a neighbouring chamber that was filled with non wetting fluid and once the chamber was filled with wetting fluid, drying fluid entered

the throat creating an interruption of the continuity of the wetting fluid. These snap-off events during wetting were also captured with the aid of X-ray microtomography by Andrew et al. (2014b). The occurrence of the snap-off phenomenon has been attributed to the ratio of a sphere to pipe radius (Mohanty et al., 1987; Mahmud and Nguyen, 2006).

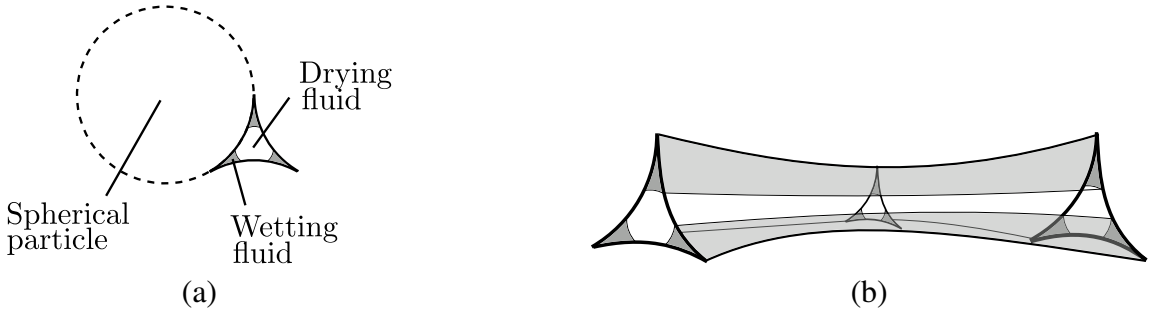

Figure 2.7: Concave pore throat generated by three spherical particles where wetting fluid is located along its nooks: (a) 2D schematic presentation of the throat cross-section with one of the particles that surround it and (b) 3D extension of the same throat.

For the better understanding of the influence of individual pore level events on the macroscopic behaviour of porous materials, such as the variation of degree of saturation and fluid conductivity with capillary suction, experimental investigations have been carried out in idealised transparent networks (Morrow, 1970; Dullien et al., 1986; Lenormand et al., 1983; Chen and Koplik, 1985). One of the macroscopic quantities that was of interest in these studies on transparent networks was the residual saturation, which is the remaining volume of wetting fluid when a pore network is dried to very high values of capillary suction. Morrow (1970) reported a small influence of surface tension, fluid viscosity, contact angle, fluid density and the pore characteristics on the minimum degree of saturation of the wetting fluid that remains in the porous material during a drying process. The reason for a value of residual saturation greater than zero is that wetting fluid can be trapped within pores that are entirely surrounded by larger ones that become filled with drying fluid during drying, meaning that there is no escape route for the trapped wetting fluid (at least by pressure driven flow of the wetting fluid). Residual degree of saturation of wetting fluid should be zero if sufficient time is allowed for the wetting fluid to be transported out of the network by diffusion. Dullien et al. (1986) reported that values of residual saturation reached were lower than those reported in the contemporary literature but also that degree of saturation would keep reducing for increasing capillary suction. They attributed this to the wetting fluid forming a continuous network through the edges on the pore surfaces leading to a continuous reduction of its volume held by the porous material. Similar results were reported by Lenormand et al. (1983) and Chen and Koplik (1985), who also observed that the wetting fluid could be trapped within pore throats due to snap-off events. They also reported that the frequency of snap-off occurrence would decrease with increasing drying fluid flux and lower ratios of sphere radius to pipe radius.

Network modelling

Despite the very important insights provided by the laboratory experiments on artificial transparent networks, it is difficult to investigate a wide range of pore geometries and wetting-drying scenarios with them. To this end, numerical network models, have been used to provide improved understanding of porous geomaterials containing two pore fluids. Fatt (1956) was the first to propose a numerical network model for porous materials containing two pore fluids. In network models, the pores are generally idealised as spheres or chambers and the narrower connecting throats are idealised by pipes of different cross sectional geometries. Simple fluid-fluid interface displacement rules and idealised network geometries are used to investigate the influence of the fluid-fluid interface movement phenomena and pore arrangements on the macroscopic behaviour of the geomaterial.

The criteria for the choice of configuration of the two fluids, i.e. the type of fluid that is located within each sphere/chamber and pipe of the network, was the Young-Laplace equation (see (3.12) in Section 3.4.3). For the choice of the fluid configuration, the sphere/chamber radius was used in (3.12) and for the wetting path the radius of the pipe. Other fluid-fluid interface displacement phenomena were also included such as Haines' jumps, snap-off, formation of wetting fluid streams along nooks and craves and trapping.

The influence of spatial correlation in degree of saturation and trapping have been investigated in Tsakiroglou and Payatakes (1991), Mani and Mohanty (1999) and Knackstedt et al. (2001). There are two types of correlation, namely sphere to sphere radii correlation and sphere to pipe correlation. For sphere to sphere correlation, radii values are assigned to the location of the spheres in order to have neighbouring spheres of similar sizes. For sphere to pipe correlation, radii of pipes are assigned in such a way that the larger pipes are connected to the larger spheres and inversely the smaller pipes are connected to the smaller spheres of the network. Tsakiroglou and Payatakes (1991) studied the influence of uncorrelated networks, sphere to pipe and sphere to sphere correlation on mercury intrusion and extrusion curves and residual mercury saturation. The mercury intrusion and extrusion curves correspond to drying and wetting, respectively. Here, mercury is the drying fluid. When spatial correlation was applied, the high capillary suction sections of the mercury intrusion retention curves showed higher values of degree of saturation of mercury than when no correlation was applied. This means that, higher capillary suction values were required to saturate the network with drying fluid when spatial correlation was applied. Furthermore, spatial correlation reduced predicted values of residual mercury saturation. However, widening of the capillary suction range over which most of variation of degree of saturation occurred was still not large enough to match experimental results. Knackstedt et al. (2001) presented similar conclusions by applying long range correlations with fractal Browninan motion. They used this approach to reproduce results of constant mercury intrusion rate experiments. Similar work presented

by Mani and Mohanty (1999) indicated that for the same pore size distribution very different predictions of retention behaviour were obtained.

The pore filling rules in network models are commonly based on the Young-Laplace equation in (3.12) in Section 3.4.3. Chapman et al. (2013) recently performed experiments and Lattice Boltzmann simulations to investigate the validity of the rules. In the Lattice Boltzmann method, the fluids are represented by groups of particles and their motion is determined by the solution of the advection-diffusion equation (Ferreol and Rothman, 1995). In Chapman et al. (2013), a small network consisting of 4 pore throats and 1 junction was investigated. The study revealed that the rules on the Young-Laplace equation does not always predict the correct capillary suction at which a given part of a network will be filled with a wetting fluid. However, Chapman et al. (2013) presented also results for 4 pipes connected to a chamber rather than a junction. In the latter case, the results were in better agreement with the rules based on the Young-Laplace equation. Therefore, it can be concluded that the basic rules used in the pore networks capture the basic physical phenomena occurring at geometries involving the connection of pipes through a chamber/sphere.

Pore network models have also been widely used for the prediction of oil recovery engineering applications where oil is the drying and water is the wetting fluid. Substantial research has been undertaken to investigate the influence of snap-off for these applications. Snap-off is an important phenomenon for oil recovery applications since it results in a disconnection of the routes of oil within the pore spaces. This leads to an irrecoverable entrapment of oil and reduces the achievable oil flow rate.

Jerauld and Salter (1990) investigated the influence of pore size distribution, as well as pore size spatial correlation and the ratio of sphere radius to adjacent pore throat radius, which was used to determine the occurrence of snap-off events during wetting on oil-water retention hysteresis and relative permeability hysteresis. The ratio of sphere radius to adjacent pore throat radius was found to be of major importance in controlling the hysteresis behaviour. It was also found that both wetting and retention curves (rather than only one of them) are required in order to provide significant information on the pore structure. Jerauld and Salter (1990) also found that the correlation of pore to throat sizes influences the drying fluid spatial distribution and therefore relative permeability. Tsakiroglou and Payatakes (1990) investigated the influence of pore radius to throat radius ratio, radii distributions and the network coordination number (number of pipes connected to a sphere) on mercury intrusion and extrusion simulations. For drying, they found that the retention curve was mainly dependent on the throat size distribution and secondly on the coordination number and the contact angle. Also, retention hysteresis and the volume of any trapped drying fluid increased with increasing ratio of sphere and pipe radii.

Yiotis et al. (2005b) incorporated a mathematical model to take into account the effect of

films on drying rate into a network approach. It was found that for capillary driven flows during drying, significant mass transport is conducted through the films, which enhances the rate of drying. Man and Jing (2000) presented a network model that takes into account the shape of the grain boundaries for the pore throat generation. A method for the calculation of the thickness of the wetting fluid films generated at the crevices of the idealised star-like shapes of the grain boundaries was proposed in order to qualitatively capture the low degree of saturation changes for large capillary suction changes towards the end of a drying process. Reeves and Celia (1996) used bi-conical pore throat shapes within a network model in order to qualitatively investigate fluid retention with respect to the variation of the total fluid-fluid inter-facial surface area within a volume element. It was found that the interface area changes non-monotonically during both drying and wetting. Also, the surface generated in the capillary suction-degree of saturation-interface area space differ for the wetting scanning curves from those of with the drying scanning curves. Scanning retention curves were generated for drying and wetting starting from different values of degrees of saturation. The evolution of the inter-facial surface area strongly depends on the initial degree of saturation and type of process (drying or wetting) the network is subjected to.

The majority of previous studies with network models performed to improve the qualitative understanding of the influence of microscale transport phenomena on the macroscopic transport and retention properties of porous geomaterials. Fewer publications have focused on the quantitative reproduction of the transport retention behaviour of such materials. Matthews et al. (1995) proposed a calibration procedure for network modelling of mercury intrusion and extrusion in sandstone. This calibration approach was then extended by Johnson et al. (2003), where the main objective was to deduce the material microstructure (i.e. the physical characteristics of a network model) from experimental fluid retention curves and then evaluate the conductivity. Later this calibration approach of Johnson et al. (2003) was used in Campos et al. (2015) to use the resulting network model to investigate CO_2 storage capability of sandstones due to trapping. The calibration process in those studies is time consuming and involves the post-processing of information acquired from mercury intrusion porosimetry experiments and electron microscopy measurements. Nevertheless, this calibration approach improved the strategy to choose the network input parameters.

Network models presented in the literature use very idealised geometries for the network structure. The geometry and the connectivity of the pores is as important as the rules for the displacements of the fluid-fluid interfaces for capturing realistic permeability and saturation curves. To this end, an initial attempt of reproducing realistic network structures was proposed by Bakke and Øren (1997) and Øren et al. (1998). The technique was based on the idea that 2D thin section images of a real porous material scan can be used to infer representative 3D information. An algorithm was developed for reproducing the physical processes of sandstone formation such as sedimentation. During the formation process, porosity deduced from random 2D sections of the model were compared to real 2D images

of the material. The artificial geometry chosen was then the one that corresponded to the minimum difference between the model and the real 2D sections. The irregular real pore wall geometries were then captured in the form of voxel arrangements. From information of the voxel arrangements, an equivalent network consisting of pore bodies and throats was generated based on thinning algorithms (Thovert et al., 1993). A good match of relative permeability and retention variation with capillary suction was presented for a sandstone with a relatively narrow range of void sizes.

As $\mu-$CT scanning improved and the representation of the 3D pore network in voxel structures became easier, algorithms developed for the generation of equivalent pore network came more in use. The main groups of these algorithms are the medial axis (Baldwin et al., 1996) based method and the maximal ball method (Silin and Patzek, 2006). The former one is based on the generation of a median axis between the pore walls. Pore bodies are generated where two or more axes meet. The latter involves the search of the maximal ball that can be inscribed within the pore walls (Silin and Patzek, 2006; Dong and Blunt, 2009). Blunt et al. (2013) presented a good match of relative permeability predictions from a network generated using the maximal ball method with corresponding experimental data.

Additionally, the voxel structures can by used for direct Computational Fluid Dynamics (CFD) modelling with the use of finite volumes method by directly solving the Navier-Stokes equations (Raeini et al., 2014b). With this approach, the impact of the complex pore geometry on changes of contact angle and conductivity can be further investigated.

Percolation theory, which is part of the probability theory devoted to the study of random media (Grimmett, 1997), has also been used to analyse random networks. The main objective of this statistical tool is to determine the critical value of the proportion of spheres and pipes that need to include a different property to connect two opposite sides of the network with a continuous rout of a certain species. The percolation theory was initially proposed by Chatzis and Dullien (1977) as a means to statistically describing the fluid displacements in two pore fluid porous materials by making the connection of bond to the throats and sites to pore bodies. An initial mathematical percolation tool was then presented by Golden (1980) to describe conductivity hysteresis. At this point the theory of percolation was enriched by introducing the concept of invasion percolation in Lenormand and Bories (1980) and Wilkinson and Willemsen (1983). In these studies, spheres and pipes changed conditions based on their neighbours and trapping rules, which is different from random choices done in Monte Carlo simulations.

2.3.2 Mechanical

Many porous materials can be seen as packing of individual particles. The contacts between particles transmit forces creating force chains throughout the material. When the voids of the material are filled with a single fluid at zero pressure, these forces chains are entirely responsible for carrying the external forces applied on the material. In order to predict the mechanical behaviour of porous geomaterials, understanding of the interactions between particles is of great importance. This section reviews the experimental, analytical and numerical work found in the literature for the understanding of inter-particle interactions and their influence on the macroscopic behaviour of porous geomaterials containing a single pore fluid at zero pressure (i.e. in the absence of any coupling to hydraulic effects).

The understanding of the overall mechanical behaviour of geomaterials has been widely enhanced by physical experiments involving observations at the scale of individual particles and pore spaces. Computational models that simulate individual particle interactions within geomaterials have also provided information on the influence of individual particle interactions on the macroscopic mechanical behaviour. These numerical models are known as discrete models and there are three main families that have been proposed and developed. The first family is that of Discrete Element Method (DEM) proposed by Cundall and Strack (1979), which was the first algorithm for the numerical modelling of particulate materials at the level of individual particle interactions that allowed new inter-particle contacts to form in the course of an analysis. The second family of discrete models is known as Rigid Body Spring Model (RBSM) first proposed by Kawai (1978) . In RBSM, the material is considered to be an assembly of rigid particles (of polygonal shape in 2D and polyhedral shape in 3D) with their deformability being lumped in zero sized springs located at the contact areas between two particles. Furthermore, only the initial contacts that are specified at the beginning of a simulation are taken into account. New contacts are not generated throughout an analysis. The third and last family is that of Discontinuous Deformation Analysis (DDA) first proposed by Shi (1992). In DDA, each discrete element (of polygonal shape in 2D and polyhedral shape in 3D) is allowed to strain in a linear fashion as well as to form new contacts other than those determined at the beginning of an analysis. In this section, experimental and numerical contributions are presented, which involve the investigation of microscopic mechanical phenomena.

The main microscopic mechanical behaviour of interest is the inter-particle contact behaviour. Two loading directions, namely normal and tangential to the contact area of two particles called shear and normal loading, respectively, were investigated in Cole et al. (2010), Cavarretta et al. (2010) and Senetakis et al. (2013). Initial interest was oriented to the shear and normal behaviour, including the roles the environmental conditions and the geometry of the contacts. Experimental investigation of normal compression of single glass particles places between

two platens suggested that for first loading at low normal forces the irreversible platen displacements behaviour was due to the breakage of the particle asperities (Cavarretta et al., 2010). Also, it has been suggested that the friction coefficient at an individual inter-particle contact is not affected by dynamic or static loading, the direction of the shearing force or the type of surrounding the particle contact (Senetakis et al., 2013). Furthermore, experiments involving normal loading of a contact between two individual particles showed that only first loading presents a Herzian behaviour (where the contact force normal to the inter-particle contact area is proportional to the normal inter-particle displacement in the power of 1.5) of the particles (Cole et al., 2010). Numerical investigation with DEM also suggested that a linear spring contact is adequate to simulate particle interactions (Di Renzo and Di Maio, 2004).

Particle shape is a factor that influence the macroscopic mechanical behaviour of geomaterials (Cho et al., 2007). DEM analyses have indicated that particles with sharp edges result in higher values of a shear strength and the occurrence of larger voids in the failure zone than for the case of spherical particles (Hosseininia, 2012). This higher strength is caused by the locking of the particles due to their irregular shapes. DEM approaches that attempt to represent particles of irregular shape generally use clusters of overlapping spheres to represent individual particles (Garcia et al., 2009) or use polyhedral shapes (Pena et al., 2008). More recently, Andrade et al. (2012) used an isoparametric representation of real particle geometries within DEM.

Another aspect of contact behaviour that has been addressed is the rotational resistance. Oda et al. (1982) and Iwashita and Oda (1998) argued that large voids observed within shear bands in 2D spherical experiments on granular materials could not be reproduced by contemporary DEM simulations due to the absence of a rolling resistance at particle contacts. The 2D experiments were conducted using oval and circular shaped particles, hence no locking could be expected. Iwashita and Oda (1998) presented a Rolling Resistance Model (RRM) within the DEM framework that could reproduce the occurrence of large voids within shear bands. However, the first RRM was presented earlier in the literature by Petrinic (1996). This provided a strong indication that rolling resistance is a physical quantity that has a potential impact on the macroscopic behaviour of geomaterials.

An improved RRM that took into account the underlying configuration of the particle-particle interaction and satisfies the local equilibrium was proposed by Jiang et al. (2005). This model gave higher and more realistic values of the apparent internal friction angle than previous DEM models. Furthermore, the apparent friction angle and the inclination of the shear band were found to increase with increasing rolling resistance (Mohamed and Gutierrez, 2010). Also, the thickness of the shear band was found to decrease with increase of rolling resistance and the dilation angle was found to vary in a non-monotonic fashion with increase of rolling resistance. An assessment of the RRM was presented by Ai et al. (2011) where another,

more generalised, form of a RRM was presented with an elastic-plastic spring dash pot. In validation tests, Ai et al. (2011) found that their new form of RRM was more successful than previous versions, since it was able to correctly capture the dissipative energy for both quasi-static and dynamic conditions. A recent theoretical study (Wang et al., 2015) on the relative motion of two spheres of different sizes concluded that there is a unique way of defining the rolling resistance, which avoids contradictions found in models previously presented in the literature. Experimental measurement of rolling resistance has been undertaken in materials such as pharmaceutical tablets (Ketterhagen et al., 2010). There are no publications covering equivalent tests on particles from geomaterials, despite numerical results suggesting that the rolling resistance influences the material strength and plastic behaviour strongly.

McDowell and Bolton (1998) investigated experimentally the tensile strength of particles of various sizes and mineralogy and interpreted their results by means of Weibull brittle fracture statistics. Single particles were placed between two polished platens and the reaction force on the apparatus was measured for increasing vertical displacements. Non-monotonic variations of forces were caused by the splitting of a particle (hence reducing the applied force for the applied displacement). The mean particle tensile strength was fitted to a fractal power of the particle diameter. A rule for the volumetric change at geomaterials based on the fractal evolution of the particle size, was proposed. It was found to present a good match with experimental data. The findings were supported by results obtained with the DEM method by Cheng et al. (2003) who presented a model for sand behaviour, where each particle was made of a number of smaller spheres and the contact bonds between these individual spheres could break to represent particle splitting. It was found that the sand particles within a granular material exhibit higher compression strengths than the values observed in a two platen test on an individual particles, because of the high coordination number. A quasi critical state was reproduced in the DEM studies of Cheng et al. (2003), i.e. the deviatoric stress and porosity would stay relatively unchanged with increasing deviatoric strain. This was attributed to the rearrangement of the broken agglomerates to form a stable arrangement of particles of higher strength (i.e. particle splitting ceased).

RBSM or DDA modelling has been widely used for the analysis of geomaterials involving very large particles such as rockfill or joined rock masses (where the particles are the rock blocks). Kawai (1980) integrated RBSM in the Finite Element Method (FEM) for modelling inelastic structural behaviour of rock masses (consisting of rock blocks). Thereafter, Hamajima et al. (1985) used this approach to model rock behaviour of both intact and fractured material. Different material laws for the physical discontinuities and the intact regions were used by Hamajima et al. (1985) to capture different local behaviour. Mesh dependency was investigated and analyses were found to be in agreement with experimental results in biaxial and uniaxial compression. 2D arc and tunnel block structures were modelled by Tor and Yoshida (1991). The same authors compared dynamic analyses of simple structures to experiments and good qualitative agreement was observed. A comprehensive review of

the model formulation of DDA and its validation can be found in MacLaughlin and Doolin (2006).

It should be noted that RBSM has been very widely used for fracture analysing from a continuum point of view. The continuum application of RBSM involves the consideration of the geomaterial as continuum that can exhibit a discrete behaviour at the locations of crack formations. The continuum is discretised using rigid bodies with springs between the rigid bodies to describe elastic, plastic and fracture behaviour (Bolander and Saito, 1998). This approach has been used for modelling of fracture in Bolander and Berton (2004). The Rigid Body Spring Models are closely related, and in some cases almost identical, to lattice approaches for fracture and transport used in Herrmann et al. (1989), Schlangen and van Mier (1992), Saduki and van Mier (1997), Grassl et al. (2010) and Grassl and Jirásek (2010). The extension of these type of models is presented in the present thesis for modelling the mechanical interaction of particles.

Various authors have undertaken theoretical work on the influence of particle interaction on macroscopic behaviour by considering idealised regular structures of disks or spheres. The macroscopic strength of Face Centred Cubic (FCC) packing of uniform rigid spheres was initially investigated by Rennie (1959) and Parkin (1965) for the case where the stresses are free to rotate about the intermediate principal strain-increment direction. A general solution was subsequently presented by Thornton (1979). It was found that inter-particle slippage is associated with non-coaxiality of the stress and strain increment tensors. As a consequence, a failure under lower stress ratios was observed. The macroscopic Young's modulus and Poisson's ratio were investigated by Griffiths and Mustoe (2001) for a 2D Hexagonal Close Packing (HCP) of disks idealised by lattice elements with normal and shear stiffnesses. The macroscopic stress was related to the element stiffnesses by differentiating the elastic strain density stored at each node over the macroscopic strain. Wang and Mora (2008) extended this theoretical work to a 3D HPC and FCC. They also evaluated the shear modulus for both packings as well as the rotational stiffness of the FCC packing. The proof approach was the same as in the one in the 2D case but in this case the strain energy stored in an elementary cell was used to evaluate the elastic strain density. The numerical results were compared to the analytical expressions. In the 3D case the numerical analyses were performed with Neumann boundary conditions and a large number of spheres was required to approach the theoretical solution.

Macroscopic constitutive models can also be verified by discrete numerical models with simple contact laws. The Lade-Duncan failure criterion (Lade and Duncan, 1975) was verified by Thornton (2000) for loading conditions that are difficult to be experimentally reproduced. Also, the mean coordination number at the critical state was found to be independent of the initial density of the packing. Thornton (2000) argued that increase of the inter-particle friction coefficient does not significantly contribute to the energy dissipation during yielding.

While the applied load is increasing, chains of particles carry the majority of the loading. When yielding occurs, the regions between these chains are those that are most likely to be unloaded and hence the energy dissipated, proportional to the force acting on the sliding particles, is relatively small.

Various authors have worked on the evaluation of the homogenisation of the discrete particle interactions within a test volume. The first expression was proposed by Drescher and De Jong (1972) for deducing the macroscopic stress acting on a control volume from the forces acting on its boundaries. Christoffersen et al. (1981) proposed an expression based on the assumption of no moment transmission at particle contacts, where the macroscopic stress tensor is evaluated by the sum of the contact forces within the control volume. The above approaches yielded symmetric stress tensors since moment transfer between particles was neglected. Bardet and Vardoulakis (2001) defined the stress tensor by taking into account only contact forces. Two different formulations where presented. For the first formulation, the average stress tensor is defined as the particle assembly volume average of the sum of the average stress tensors of all particles weighted by the volume of each particle. The second formulation involved a virtual work formulation of the average stress tensor. For the first formulation, when contact moments are neglected, the stress tensor is always symmetric for static conditions i.e. when the momentum that particles carry when moving from one location to the other is not taken into account. However, for the second formulation it was found that the average stress tensor is non-symmetric in the absence of contact moments when a particle assembly is loaded by an external moment. The non-symmetry reduces with increasing ratio of the volume over the total surface area of the particle assembly.

A numerical modelling framework known as computational homogenisation has been developed for the investigation of the macroscopic properties of heterogeneous materials (Guedes and Kikuchi, 1990). The macroscopic properties are investigated by considering a cell that is much larger than the length scale of the heterogeneities as well as much smaller than the length scale of the macroscopic boundary value problem. This principle is known as separation of scales. An additional assumption that is widely used is the concept of geometrical as well as displacement periodicity. One of the first derivations of periodic geometric and boundary conditions were presented by Anthoine (1995) and this was then applied to masonry structures. These Periodic Boundary Conditions can be imposed using Lagrange multipliers (Miehe and Koch, 2002) or by using three or four driving nodes and linking the displacements of pairs of nodes located at opposite edges or faces in the 2D or 3D case, respectively (Kouznetsova et al., 2001). For each pair of nodes, the displacement of one node is equal to the displacement of its opposite one plus a displacement value dictated by the average strain tensor applied to the microstructure. An alternative approach for applying Periodic Boundary Conditions that avoids the necessity of having nodes on the boundaries (which would generate geometrical regularity towards the boundaries) was subsequently presented by Grassl and Jirásek (2010).

Elastic analyses with Periodic Boundary Conditions (PBCs) lead a convergence to the macroscopic elastic modulus for smaller cell sizes than in the case of Neumann and Dirichlet boundary conditions. A cell size that is large enough to capture the macroscopic average properties correctly and small enough to be numerically efficient is known as a Representative Volume Element (RVE) (Zhang et al., 2000). Gitman et al. (2007) performed a numerical investigation of the response of a heterogeneous microstructure involving damage and concluded that an RVE does not exist for inelastic materials. The implementation of PBCs in the computational homogenisation framework did not initially take into account strain gradients (Miehe and Koch, 2002; Kouznetsova et al., 2001) known as first order computational homogenisation. An extension for including second order effects was proposed by Kouznetsova et al. (2002). The capturing of the size effect was presented by investigating the influence of the cell size of identical microstructures on the macroscopic stress-strain behaviour.

PBCs can be applied to microstructures of either periodic or non-periodic geometries. For the present thesis, the PBCs developed (presented in Section 3.7) are applicable only to microstructures with periodic geometries.

2.3.3 Hydro-mechanical

The interaction of hydraulic and mechanical phenomena are discussed in the present section from the microscale point of view. Initially, the influence of the mechanical deformation on fluid retention and transport at the capillary pore scale is presented. Then, the discussion moves to the effects of one or two pore fluids within the pores on the geomaterial particles.

The mechanical phenomena include the exertion of forces on the particles of geomaterials. These forces produce a relative movement of the particles that consequently produce changes in the dimensions of pores and throats. The transport and retention properties of the geomaterial are therefore affected for both saturated and unsaturated conditions by mechanical loading. When the void dimensions change as a consequence of mechanical deformation, the storage capacity of the geomaterial is affected. When voids change in volume, the space available for a fluid to be stored in the porous medium changes as well. Also, the changes of pores and throats influence the capillary suction at which wetting or drying of voids occurs (Sweijen et al., 2016), i.e. at which a change of the retention behaviour occurs. Furthermore, changes of pore and throat dimensions influence the ease of fluid movement. Thus, the conductivity is affected. This has been investigated by means of DEM coupled with the Lattice Boltzmann method by Sun et al. (2013) for a sphere assembly that dilates. Also, the generation of fracture planes due to mechanical loading produces significant localised changes of the conductivity of geomaterials (Grassl and Bolander, 2016).

On the other hand, the fluid contained in the pores also influences significantly the behaviour of the particles. In the case where the pores are filled with one fluid, the fluid pressure is exerted on the surface of the particles and transmits mechanical forces that influence the inter-particle contact forces. For instance, Catalano et al. (2014) developed a DEM coupled with the Pore-scale Finite Volume (PFV) method, which is a numerical model for fluid flow through porous materials. The coupling involved the evaluation of the resultant forces exerted on the solid particles due to fluid pressure acting on the particle surface, so that Terzaghi's effective stress principle could be modelled. The DEM-PFV model was validated by comparing a numerical oedometer test to analytical solutions. Also, the influence of fluid pressure on the mechanical response is important for applications of hydraulic fracturing (Shimizu et al., 2011; Eshiet et al., 2013).

For the case of porous material containing two pore fluids, the geometry of the fluid-fluid interfaces located within the pores and throats affects significantly the mechanical particle-particle interactions. The influence of a perfectly symmetrical meniscus water bridge on the contact force between two perfectly smooth identical spheres was studied theoretically by Fisher (1926). Fisher (1926) found that the additional compressive force acting at the contact of two identical smooth spherical particles increases to a finite asymptote with capillary suction increasing (see Section 3.6.2). Kohonen et al. (2004) visualised the meniscus water bridge in arrangements of spheres of same size and studied the average number of meniscus water bridges per sphere with changing water contents. It was found that at low values of water content, where most of the sphere contacts are surrounded by water bridges, the bridges increase the shear stiffness dramatically, whereas this effect decreases as the water content increases and the number of water bridges reduces. Similar behaviour was found through DEM modelling for low water contents (Jiang et al., 2004). As the water content decreased with increasing capillary suction, the number of meniscus water bridges increased and the shear strength increased. Furthermore, the generation of asymmetric meniscus water bridge was found to be due to asperities on the surfaces of the particles (Farmer and Bird, 2015; Butt and Kappl, 2009).

2.4 Purposes of microscale modelling

As discussed in Section 2.1, the macroscopic behaviour of porous geomaterials is the emergent result of processes that occur at lower scales. Understanding the influence of these lower scale processes on the overall material response is valuable when designing for many engineering applications involving geomaterials. In the present thesis, the focus is on numerical microscale modelling.

Despite the increasing amount of published work on numerical microscale modelling, the

vast majority of boundary value problems for engineering applications are modelled using the macroscopic approach. The main reason for this choice is the high computational cost of modelling large boundary value problems with a microscale approach. The large length scale of the engineering applications of interest would encompass an enormous number of individual particles, pore bodies and throats. Therefore, the computational information needed to simulate the whole geotechnical structure would result in impractically time consuming computations. However, this impracticality has been tackled by other numerical approaches that incorporate microscale approaches within the modelling of boundary value problems.

Since the boundary value problems cannot be solved by microscale modelling, the investigation of influence of the microstructure on the overall material response can be analysed by applying proper boundary conditions to a numerical cell with volume much smaller than specimens used in laboratory experiments as presented in Section 2.3.2. These conditions are chosen based on the assumption that the numerical cell is part of a larger region of microstructure that consists of identical cells that all behave similarly. Then, the overall cell behaviour is evaluated based on a so called computational homogenisation scheme. Hence, the link between the two scales can be analysed at the material point level (Thornton, 2000; Athanasiadis et al., 2016).

To connect the microscale and boundary value problem in a numerical framework in an efficient manner, a scheme known as a multiscale approach has been proposed (Kouznetsova et al., 2002). This approach is based on the discretisation of the material, at the macroscopic level, into elements that contain one or more integration points. Then, an individual microscale problem is assigned to each discrete macroscopic constituent. For the approach to be efficient, the macroscopic element must be much larger than the microscale problem. When the element chosen for the microscale problem presents a representative response (its behaviour is invariant to its random generation and to its size increase) then only one cell is assigned to each macroscopic element. Otherwise, a number of microscopic problems are assigned to each element and their average response determines the macroscopic behaviour. Hence, the boundary value problems can be solved by analysing a series of microstructural problems instead of using phenomenological constitutive laws (Miehe et al., 2010; Wang and Sun, 2016).

The present thesis focuses on relating the individual microscopic phenomena to the overall material behaviour. This involves development of a new framework for a hydro-mechanical network model for porous geomaterials describing fluid retention, conductivity and mechanical response at the capillary pore scale. The network model can be used in the future to inform macroscopic constitutive hydro-mechanical relations.

Chapter 3

Model definition

The modelling approach used in this thesis is introduced. The domain discretisation, the mechanical, transport and hydro-mechanical models along with the model parameters used are presented. Furthermore, a new technique is proposed to model Periodic Boundary Conditions (PBCs).

3.1 Point Generation

The domain is discretised by means of an irregular dual Voronoi/Delaunay tessellation. For this purpose, points are initially placed randomly, based on a trial and error approach that ensures a minimum distance d_{min} between the points. A trial point is generated in a cuboid domain (cell) of dimensions a, b and c. When a trial point contravenes the minimum distance requirement to a previously placed point, the trial point is discarded and a new trial point is generated. This point placement is performed until a specified number of consecutive trial points are rejected for contravening the minimum distance criterion. The cell is then considered to be saturated with points down to the specified minimum spacing d_{min}.

To generate periodic cells, new points, called from now on image points, must be generated outside the cell. When a trial point with coordinate vector $\mathbf{x} = (x, y, z)^{\text{T}}$ is accepted, the vector is used to generate 26 image points located outside the rectangular domain. The image points are generated based on the translation rule

$$\mathbf{x}' = \mathbf{M}\mathbf{x} \tag{3.1}$$

where $\mathbf{x}'$ is the coordinate vector of one of the image points, $\mathbf{M}$ is the translation matrix defined as $\mathbf{M} = \text{diag}[1 + k_\text{x}a, 1 + k_\text{y}b, 1 + k_\text{z}c]$ where $k_\text{x}, k_\text{y}, k_\text{z} \in \{-1, 0, 1\}$. The k_x, k_y and k_z coefficients define the direction of the shift from the original point to the image point. The coordinates of the 26 image points are the result of the coordinate translations described by (3.1) for all $k_\text{x}, k_\text{y}, k_\text{z}$ combinations except for the case where $k_\text{x} = k_\text{y} = k_\text{z} = 0$.

A 2D schematic representation of the translation rule is presented in Figure 3.1 for the case of $k_\text{x} = -1$ and $k_\text{y} = 1$. The bold lines denote the borders of the cell within which the initial point $\mathbf{x}$ is generated and the dashed lines denote the two linearly independent translations of the coordinates of $\mathbf{x}$ to generate $\mathbf{x}'$.

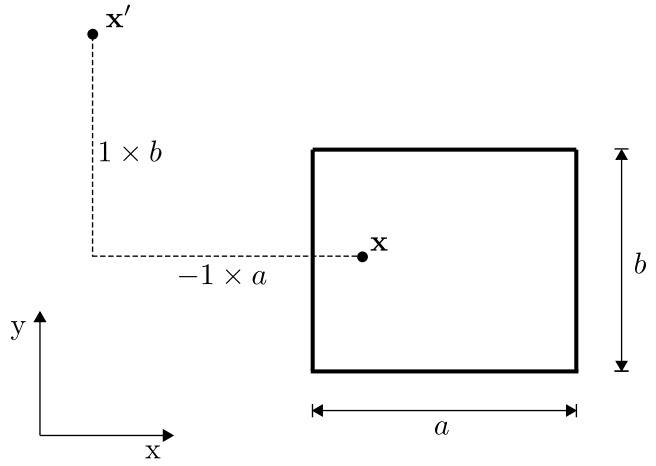

Figure 3.1: Point generation: 2D schematic representation of the generation of point $\mathbf{x}'$ as the result of the translation of point $\mathbf{x}$ according to the translation rule (3.1) for $k_\text{x} = -1$ and $k_\text{y} = 1$.

3.2 Tessellation and discretisation

The points generated are used for the determination of 3D Delaunay and Voronoi graphs (defined below) that are used to determine the geometry of the domain discretisation. 3D Voronoi graphs are sets of convex polyhedra known as Voronoi polyhedra. Each generated point is associated with a Voronoi polyhedron and lies within it. Each polyhedron is the subset of a 3D space whose points are closer to the generated point that is associated with the polyhedron than all the other generated points. Also, facets of Voronoi polyhedra are subsets of 3D space that is equidistant and has minimum distance to a pair of generated point rather than any other point generated. The Delaunay tetrahedra generated by connecting with straight lines the generated points that are associated with Voronoi polyhedra with common facets. Vornoi tessellation can occur in lower and high dimensions than 3D and more information can be found in Okabe et al. (2000).

At this point it should be mentioned that the majority of analyses presented in this thesis, the dual Voronoi/Delaunay tessellation introduced above was used as the geometry of the domain discretisation. However, a dual cubic tessellation (where two cubic networks partition the domain) was used in Sections 3.6.2 and 3.6.3 to verify that the coupling of the transport and mechanical model was implemented correctly.

A 2D schematic example of the dual tessellation is presented in Figure 3.2. The random points on which the domain is tessellated are presented in Figure 3.2a. The domain is then divided into triangles for the Delaunay tessellation (Figure 3.2b) and into polygons for the Voronoi tessellation (Figure 3.2c). Each Voronoi edge is dual to a Delaunay one. In general, each Voronoi tessellation has a unique dual Delaunay one and vice versa (Okabe et al., 2000).

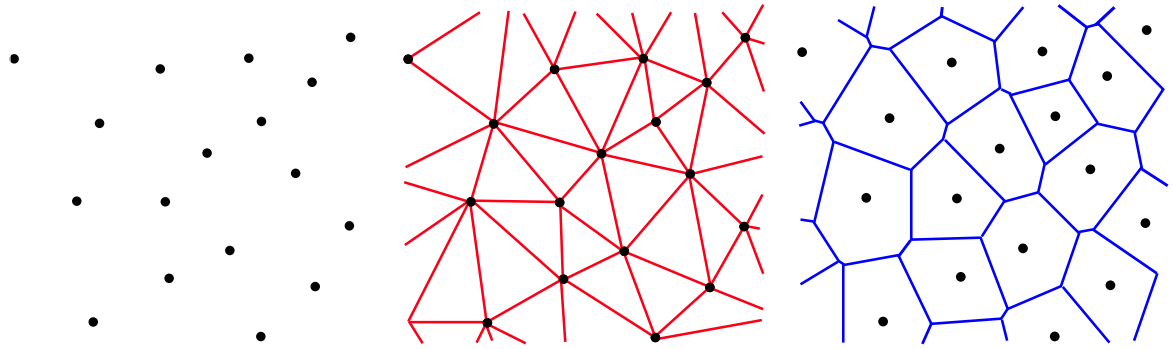

Figure 3.2: 2D dual Voronoi/Delaunay tessellation: (a) randomly placed points, (b) Delaunay tessellation and (c) Voronoi tessellation.

In the 3D case the dual Voronoi/Delaunay tessellation results in two dual sets of Voronoi polyhedra and Delaunay tetrahedra which both fill the space. In Figure 3.3a, a Delaunay tetrahedron is presented along with the associated Voronoi facet of the Delaunay edge $i\,j$. Each Delaunay tetrahedron edge possess an associated Voronoi polyhedron facet, and similarly each Voronoi polyhedron edge possesses an associated Delaunay tetrahedron facet.

The transport elements are line elements with two nodes, with each node having one degree of freedom (the capillary suction), and they are placed along the Voronoi edges (Figure 3.3c). The mechanical elements are line elements placed along the Delaunay edges (Figure 3.3b). Each mechanical element possess two nodes, with each node having six degrees of freedom, three translation and three rotations. The formulation of the transport and mechanical elements are presented in more detail in Sections 3.4.5 and 3.5.3, respectively.

Due to the periodic translation to form image points, a space larger than the basic cell is tessellated. Figure 3.4a schematically presents a tessellated 2D space. The points on which the tessellation is based were generated within the central rectangular cell outlined with thick black lines and then these points were translated to form image points according to the process

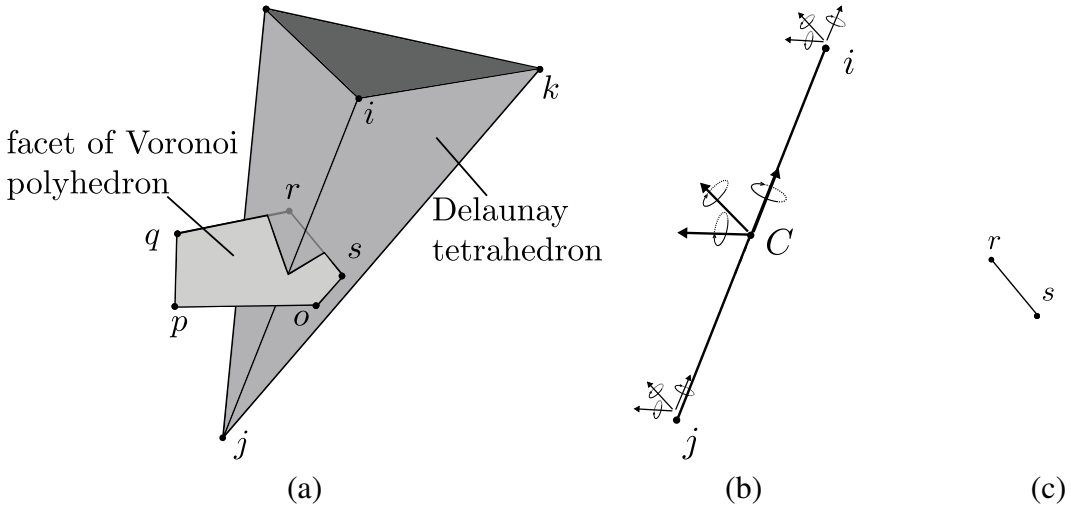

Figure 3.3: Spatial arrangement of the 3D coupled mechanical and transport lattice approach: (a) Delaunay tetrahedron with the dual Voronoi facet corresponding to one Delaunay edge, (b) mechanical element and (c) transport element.

described in Section 3.1. The Delaunay and Voronoi networks are presented with blue and red lines, respectively. All cells contain identical geometries and the domain of interest is denoted by the central cell enclosed with bold lines.

In traditional domain discretisation, the elements lie totally within the boundaries of the periodic cell of interest. However, this does not apply in the present model, for purposes explained in more detail in Section 3.7. Figures 3.4b and 3.4c present the transport and mechanical networks along with the associated edges of each element that correspond to the cell of interest. All edges that have at least one node located in the interior of the cell are used for the domain discretisation. The nodes that are located outside the cell borders are the result of the translation rule (3.1). For instance, the spatial coordinate of node I' result from the translation of the coordinates of node I for $k_{\mathrm{x}} = -1$ and $k_{\mathrm{y}} = 1$.

The Voronoi/Delaunay tessellation and discretisation was chosen to idealise the porous geomaterial microstructure. The material pore structure is modelled by a network of cylindrical pipes connecting spheres, with the spheres representing voids and the pipes representing inter-connecting throats. The spheres are placed on the Voronoi polyhedra vertices and the pipes along the polyhedra edges (Figure 3.5). This is a suitable approach for subsequent hydro-mechanical analyses, where the Voronoi polyhedra represent the porous material particles, which are surrounded by voids and throats (Mason, 1971). Particle interaction can be modelled by placing mechanical elements along the Delaunay edges. A schematic presentation of four Voronoi polyhedra and their corresponding Delaunay edges is presented in Figure 3.5, with each polyhedral particles scaled down in the figure in order to provide a clearer visual impression (in the actual network the particles are in contact).

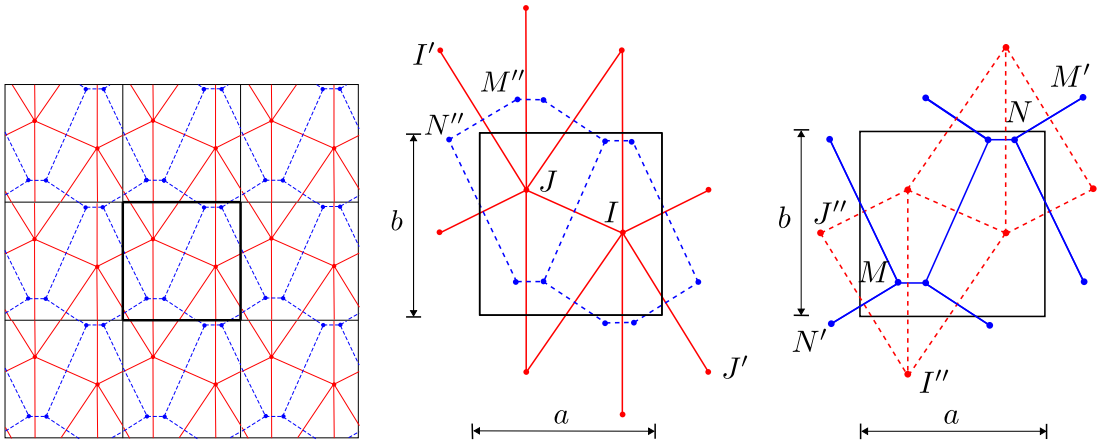

Figure 3.4: 2D periodic dual networks: (a) nine identical cells generated by the translation of the central one according to (3.1), (b) mechanical periodic network of a cell and its corresponding cross-sectional elements and (c) transport network of a cell and its corresponding cross-sectional elements.

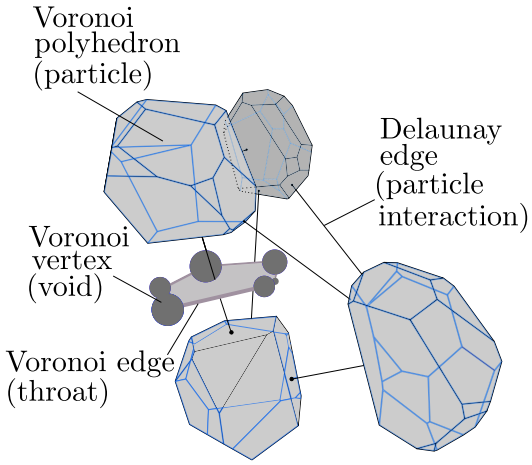

Figure 3.5: Idealisation of physical entities of geomaterial: schematic presentation of physical idealisation of the geomaterial entities, presented in brackets, by the tessellation of the domain.

Inter-particle contacts are considered to take place at the cross-section of the mechanical element. In general, modelling approaches that use the Delaunay tessellation for the determination of the geometry of the mechanical line elements use the associated Voronoi polyhedron facet as contact area (Bolander and Saito, 1998; Berton and Bolander, 2006; Grassl and Jirásek, 2010; Grassl and Bolander, 2016). Here, the Voronoi polyhedra facets are replaced by circular areas with a given radius. Each mechanical element is normal to its associated circular cross-section and the intersection of the elements with its cross-section is located at the centre of the area and at the midpoint of the mechanical element.

The above approach for generation of microstructures was chosen instead of the alternative of extraction of microstructures from real images of porous geomaterials. The latter approach cannot be directly used since direct mapping of a single image to a single of microstructure

geometry cannot offer enough statistically representative microstructural information. However, information for both the actual pore network as well as solid particles geometry provided by post processing large number of images of the same geomaterial could be used to generate distributions of sphere, pipe and particle radii as well as pore connectivity and pipe lengths. Thereafter, these distributions could be used to generate coupled networks.

3.3 Sphere/pipe/contact area radii distributions

Section 3.2 introduced the microstructure idealisation where the material pore structure is modelled by a network of cylindrical pipes connecting spheres and the particle interaction contacts are modelled by mechanical line elements with circular cross-sections. Spheres, pipes and mechanical element cross-section radii are randomly chosen. The assignment of the radii is based on random number generations according to a chosen statistical distribution. The distributions used in the present thesis are the lognormal and the linear ones. The shape, the input parameters and the process of the random radii values generation will be presented.

3.3.1 Lognormal distribution

The lognormal distribution is a continuous distribution of a positive variable. Here, the variable is denoted by r which represents the radius of a pipe, a sphere or a mechanical element cross-section. The logarithm of the lognormal variable exhibits a normal distribution. The parameters that determine the two distributions are linked as

$$\zeta = \ln\left(\frac{r_{\mathrm{m}}}{\sqrt{1+\mathrm{COV}_{\mathrm{L}}^2}}\right) \tag{3.2}$$

$$\sigma = \sqrt{\ln(1+\mathrm{COV}_{\mathrm{L}}^2)} \tag{3.3}$$

where ζ and σ are the mean and the standard deviation of the normal distribution of $\ln r$ and r_{m} and $\mathrm{COV}_{\mathrm{L}}$ are the mean and the coefficient of variation of the lognormal distribution of r. $\mathrm{COV}_{\mathrm{L}}$ is evaluated as

$$\mathrm{COV}_{\mathrm{L}} = \frac{s}{r_{\mathrm{m}}} \tag{3.4}$$

where s is the standard deviation of the lognormal distribution of r. The mathematical expression of the Probability Density Function (PDF) for r is

$$\Omega(r) = \frac{1}{r\sigma\sqrt{2\pi}} e^{-\frac{(\ln r - \zeta)^2}{2\sigma^2}} \tag{3.5}$$

The shape of the PDF is schematically presented in Figure 3.6. The vertical axis presents the frequency that a radius value (the random variable) is generated. Since the random variable values in a lognormal distribution span from 0 to infinity, it was decided to truncate each distribution in order to limit radii to a range that made physical sense. Examples of these imposed minimum and maximum radii, $r^{\min}$ and $r^{\max}$ respectively, where the distribution was truncated, are presented in Figure 3.6. Note that the mean value of the distribution, r_{m}, is greater than the value corresponding to the peak of the PDF curve, because of the asymmetry of the lognormal PDF.

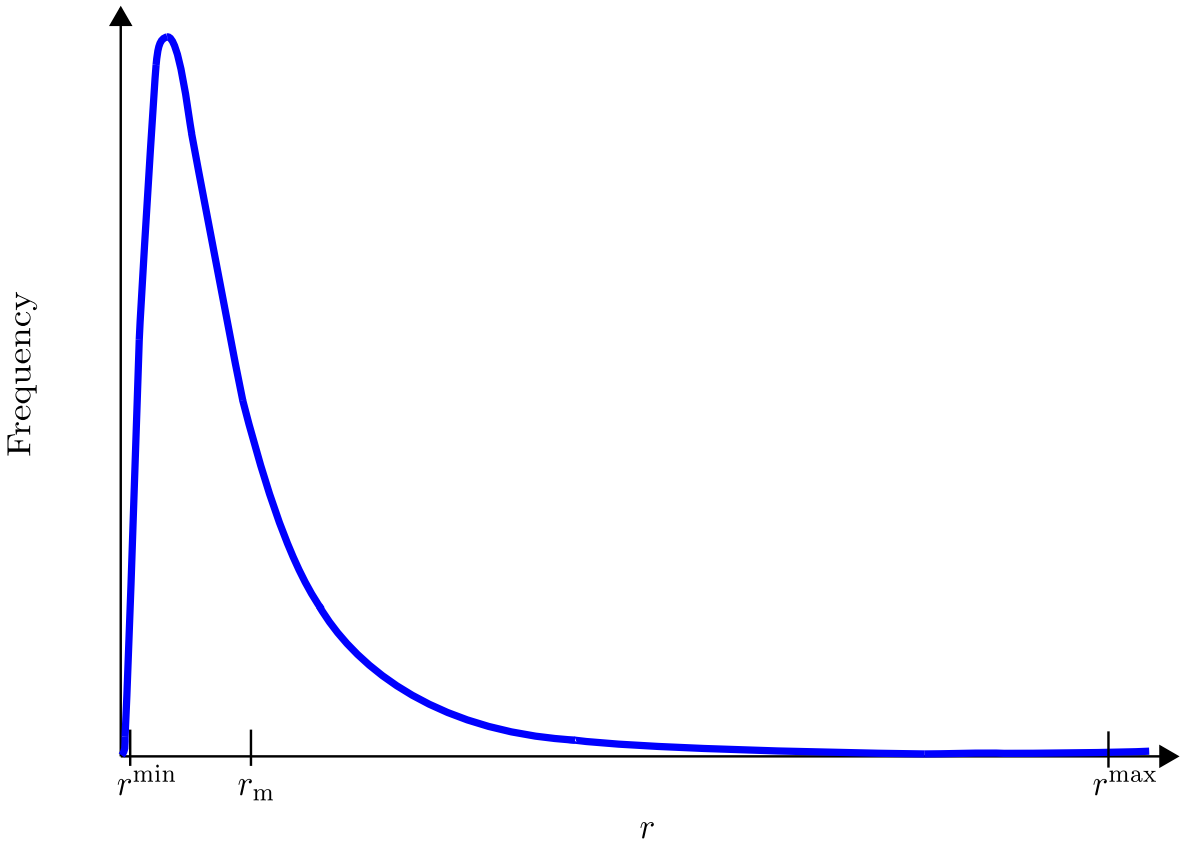

Figure 3.6: Schematic lognormal Probability Density Function: frequency versus radius r, where r_{m} is the mean and the distribution is truncated at $r^{\min}$ and $r^{\max}$.

The generation of a random variable would involve the use of the inverse of the PDF function where the frequency would be given as an input and the random variable as an output. However, with the exception of the peak, two different values of the random variable correspond to each value of frequency. The standard approach for generating random variable values according to

a given distribution is therefore to use of the inverse of the Cumulative Distribution Function (CDF). The lognormal CDF is schematically presented in Figure 3.7. The CDF begins from zero, increases, monotonically and asymptotically approaches a value of 1 as r tends to infinity and is expressed by the function

$$\Phi(r) = \frac{1}{2}\left[1 + \text{erf}\left(\frac{(\ln r - \zeta)}{\sigma\sqrt{2}}\right)\right] \tag{3.6}$$

where erf() denotes the error function defined as

$$\text{erf}(r) = \frac{2}{\sqrt{\pi}} \int_0^r e^{-t^2} \text{d}t \tag{3.7}$$

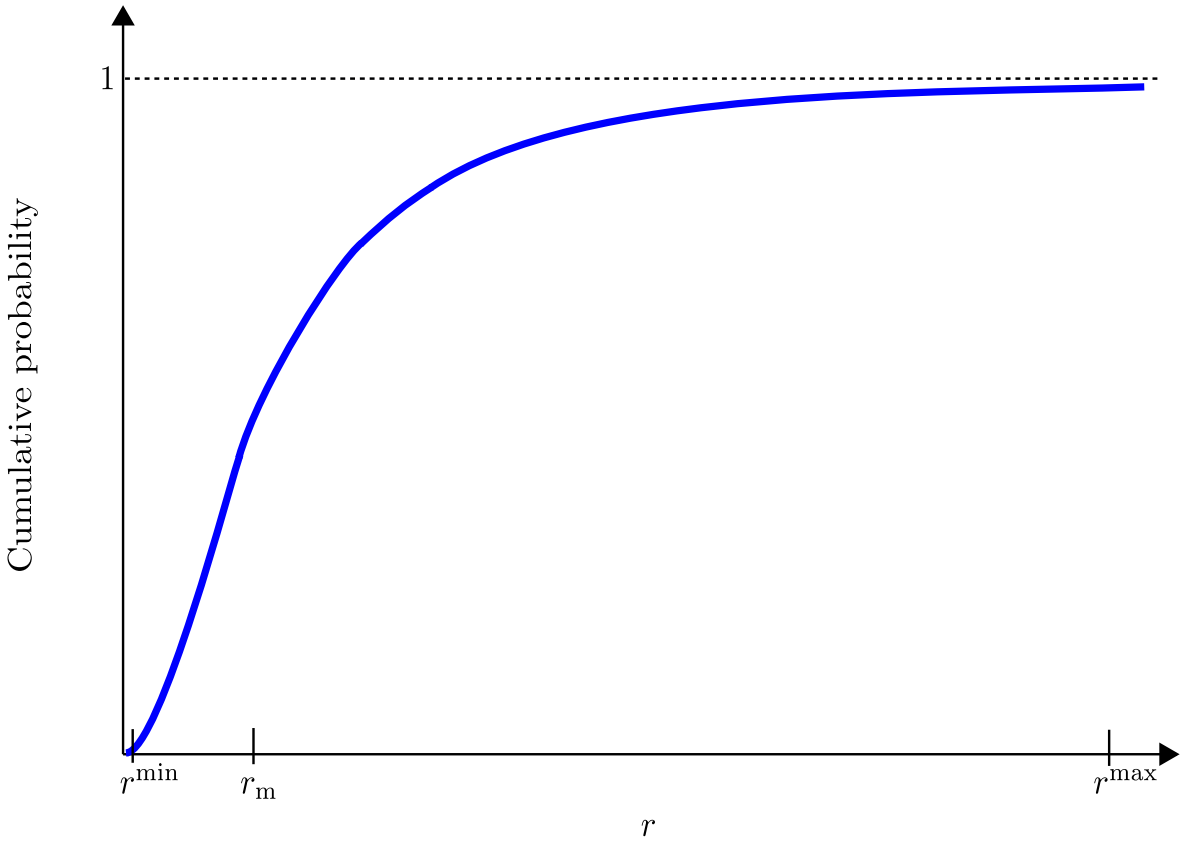

Figure 3.7: Schematic lognormal Cumulative Distribution Function: probability versus radius r and the minimum, maximum and mean $r^{\min}$, $r^{\max}$ and r_{m}, respectively.

The process of the random variable generation for a lognormal distribution is described below.

1. The input parameters concerning the lognormal distribution of r (r_{m} and COV_{L}) and its truncation ($r^{\min}$ and $r^{\max}$) are chosen.

2. Random numbers with a uniform distribution over in the interval (0, 1) are generated using a random number generator algorithm (Knuth, 1982).

3. Each number generated is used as input for the inverse lognormal CDF (inverse of (3.6)) and a corresponding r value is generated.

4. A final check is performed for the generation of the lognormal variable according to the expression below.

$$r = \begin{cases} r^{\min} & \text{if } r \leq r^{\min} \\ r & \text{if } r^{\min} < r < r^{\max} \\ r^{\max} & \text{if } r \geq r^{\max} \end{cases} \tag{3.8}$$

3.3.2 Linear distribution

The linear distribution owes its name to the shape of its CDF (Figure 3.8). The probability of the generation of a radius $P(r)$, varies from 0 to 1, as the variable r varies between minimum and maximum values $r^{\max}$ and $r^{\min}$, respectively. The CDF function is

$$P(r) = a_{\text{Lin}} r - b_{\text{Lin}} \tag{3.9}$$

where $a_{\text{Lin}} = 1/(r^{\max} - r^{\min})$ and $b_{\text{Lin}} = r^{\min}/(r^{\max} - r^{\min})$. The mean r_{m} of the linear distribution is given by

$$r_{\text{m}} = \frac{r^{\min} + r^{\max}}{2} \tag{3.10}$$

The corresponding PDF is presented in Figure 3.9. The PDF curve is a constant of value of $1/(r^{\max} - r^{\min})$ and, as with the lognormal distribution, its inverse cannot be used to generate random variables that follow this distribution. Therefore, the inverse of the CDF is used for this purpose, that is

$$P^{-1} = r = \frac{P + b_{\text{Lin}}}{a_{\text{Lin}}} \tag{3.11}$$

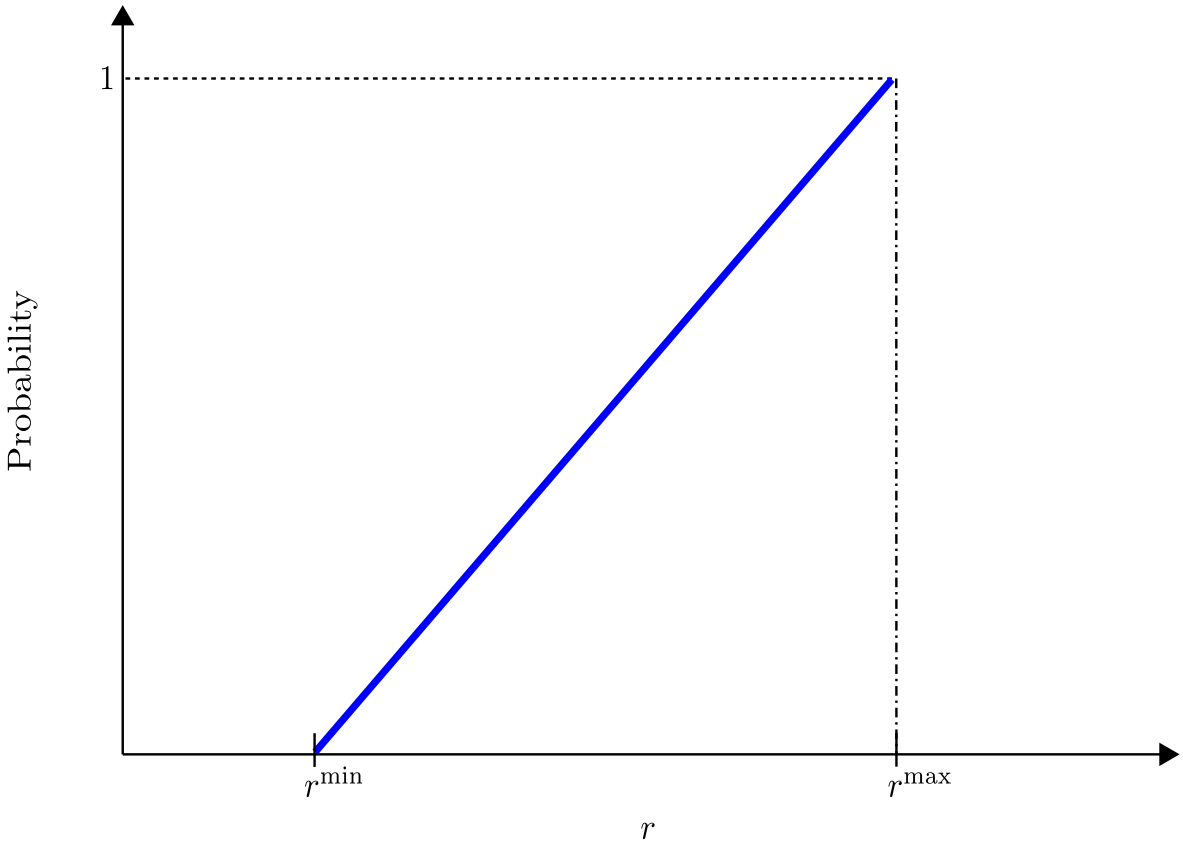

Figure 3.8: Schematic linear Cumulative Distribution Function: probability versus radius r and the minimum and maximum $r^{\min}$ and $r^{\max}$, respectively.

The process of generating random variables that follow the linear distribution is

1. Choose a_{Lin} and b_{Lin} as inputs based on chosen $r^{\min}$ and $r^{\max}$.

2. Generate uniformly distributed random numbers P in the (0,1) interval.

3. Use the random number P in (3.11) to generate the random variable r that follows the linear distribution.

3.3.3 Input parameters

The input parameters for the lognormal distribution are r_{m}, COV_{L}, $r^{\min}$ and $r^{\max}$. The symbols of the lognormal input parameters for the different entities i.e. sphere, pipe and contact area radii are presented in Table 3.1.

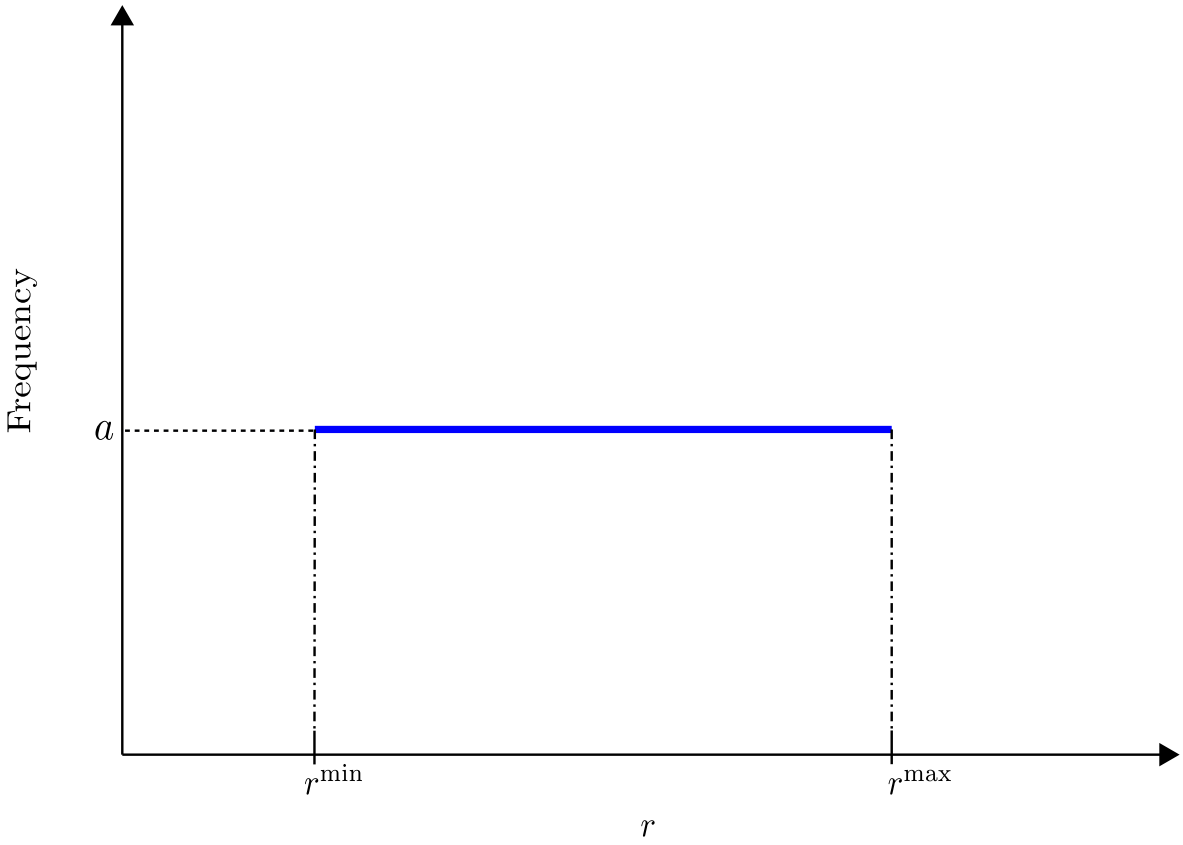

Figure 3.9: Schematic linear Probability Density Function: frequency versus radius r and the minimum and maximum $r^{\min}$ and $r^{\max}$, respectively.

Table 3.1: Lognormal distribution input parameters.

Entity	r_{m}	$\mathrm{COV_L}$	$r^{\min}$	$r^{\max}$
Sphere	r_{sm}	$\mathrm{COV^s}$	$r_{\mathrm{s}}^{\min}$	$r_{\mathrm{s}}^{\max}$
Pipe	r_{pm}	$\mathrm{COV^p}$	$r_{\mathrm{p}}^{\min}$	$r_{\mathrm{p}}^{\max}$
Contact area	r_{mech}	$\mathrm{COV^{mech}}$	$r_{\mathrm{mech}}^{\min}$	$r_{\mathrm{mech}}^{\max}$

For the linear distribution, the input parameters are a_{Lin} and b_{Lin} as presented in (3.11). The corresponding symbols for each entity are presented in Table 3.2.

3.4 Network transport model

3.4.1 Introduction

The network transport model consisting of pipes and spheres is described in this section. This approach was chosen due to its simplicity and computational economy. It able to describe the movement of a fluid-fluid interface between two spheres and the resulting conductivity

Table 3.2: Linear distribution input parameters.

Type of entity	a_{Lin}	b_{Lin}
Sphere	a_{s}	b_{s}
Pipe	a_{p}	b_{p}
Contact area	a_{mech}	b_{mech}

having only two degrees of freedom while other approaches, such as Lattice-Boltzmann (Genty and Pot, 2013) and Finite Volumes (Raeini et al., 2014a), would need to solve for a number of degrees of freedom of at least of two orders of magnitude more. The purpose of the transport model is two-fold. The network model is used to represent retention behaviour of porous geomaterials, showing how degree of saturation S_{r} varies with capillary suction P_{c}. Secondly, the network model is used to represent variation of cell conductivity k_{CELL} for varying S_{r} and P_{c}. For both retention and cell conductivity, the hysteresis are obtained (see Section 2.2.1).

Firstly, the assumptions employed in developing the transport model are presented. The rules used to determine the configuration of the two pore fluids, i.e. determine which spheres are filled with wetting and which with drying fluid, within the network are subsequently presented. Thereafter, the transport element formulation and the relationship between the flow rate and fluid pressure gradient are described. Furthermore, a new methodology is proposed for initiation of wetting or drying in a periodic cell and a new technique is developed for representing large number of the smallest voids within a geomaterial without the need of explicit inclusion of very large numbers of spheres within the network model. Finally, the model parameters are presented.

3.4.2 Assumptions and simplifications

Contact angle hysteresis, pinning, snap-off and trapping and liquid water films presented in Section 2.3.1 are not considered. Also, the two pore fluids are considered to be Newtonian, and to flow according to Hagen-Poisseuille equation. They are immiscible and their flow is incompressible. No possibility of trapping of the non-intruding fluid is considered, because there is no consideration of whether there is appropriate connectivity to provide an exit route for the non-intruding fluid. For the evaluation of the overall cell conductivity, the wetting fluid is considered to be liquid and the drying one is considered to be gas. Laminar flow is considered for the liquid phase flow and the gas phase moves only due to diffusion. Furthermore, the moisture transport is not influenced by temperature.

3.4.3 Rules for filling and emptying spheres and pipes

The transport model was developed to compute the overall mass flow conducted through the network which is the result of the collective flow through the pipe elements previously described. The flow can be evaluated for different values of degree of saturation S_{r} that changes due to wetting or drying of the network. Capillary suction P_{c} is the driving variable for the drying and wetting. For a target P_{c}, the intruding fluid (non-wetting fluid during drying path and wetting fluid during a wetting path) advances to neighbouring spheres and pipes according to filling and emptying rules that are explained below.

The rules that determine the filling and emptying of spheres and pipes within the network are based on the Young-Laplace equation

$$P_{\mathrm{c}} = \frac{2\gamma cos\theta}{r} \tag{3.12}$$

where γ is the surface tension, r is the radius of a pipe or a sphere and θ is the contact angle formed between the fluid-fluid interface and the solid measured on the side of the wetting fluid. Different rules apply during drying or wetting fluid processes.

Furthermore, r in (3.12) is the radius of a pipe during a drying process and the radius of a sphere during a wetting process, to represent the so-called ink bottle effect (Moro and Bohni, 2002). A drying or wetting process is modelled by considering the intruding fluid moving from a void already filled with that fluid to a connected void not previously filled with that fluid, i.e. direct connection to a void already filled with the intruding fluid is imposed as a requirement for a void to fill with the intruding fluid. The drying fluid is the intruding fluid during a drying path, whereas the wetting fluid is the intruding fluid during a wetting path. Figure 3.10a illustrates the situation during a drying process. The hatched area corresponds to the wetting fluid. The drying fluid has already intruded through pipe 1 into sphere A at a value of P_{c} corresponding to the application of (3.12) with r as the radius of pipe 1. As the value of P_{c} is increased further during the drying process, the next consideration is when the drying fluid will intrude further from sphere A along either pipe 2 or pipe 3. Pipe 2 is of larger radius than pipe 3, and therefore the first action to occur is intrusion of the drying fluid along pipe 2 and into sphere B, at a value of P_{c} corresponding to the application of (3.12) with r as the radius of pipe 2. If either pipe 4 or pipe 6 was larger than pipe 2 the intrusion would continue along this pipe into an additional sphere without need for further increase of P_{c}.

Figure 3.10b illustrates an equivalent situation for a wetting process, with the hatched area again representing the wetting fluid. Wetting fluid has already entered sphere A from pipe 1, at a value of P_{c} corresponding to the application of (3.12) with r as the radius of sphere A,

and immediately moved into pipes 2 and 3. As the value of P_c is reduced further during the wetting process, the next consideration is when the wetting fluid will intrude into sphere B or sphere C. As sphere C is smaller than sphere B, the first thing that happens is intrusion of the wetting fluid into sphere C, at a value of P_c corresponding to the application of (3.12) with r as the radius of sphere C, and immediate further movement of the wetting fluid into pipes 5 and 7. If either pipe 5 or pipe 7 connected to an additional sphere that was smaller than sphere C, the wetting fluid would continue into this sphere without need for further decrease of P_c.

In a network, the stability of the configuration is checked. When a phase change of a sphere concludes to an unstable configuration, a new sphere phase change is performed. This is done until stability is reached. The detailed description of the search of stability is described in Section 3.8.2.

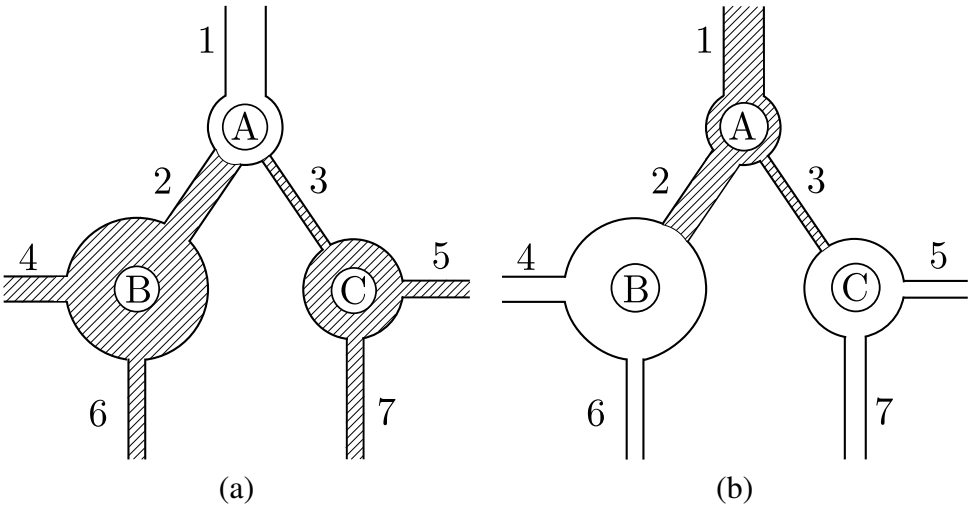

Figure 3.10: A schematic 2D network where hatched areas represent the wetting fluid: (a) network subjected to drying, with the drying fluid entering from pipe 1, (b) network subjected to wetting, with the wetting fluid entering from pipe 1.

With the use of PBCs, it is not possible to start a drying path from a fully saturated condition (S_r = 1) or a wetting path from a fully dry condition (S_r = 0), because there is no external boundary from which to introduce the intruding fluid. Instead, a drying path must start with at least one sphere within the cell already filled with the drying fluid and a wetting path must start with at least one sphere already filled with the wetting fluid.

Realistic modelling of a drying or wetting path is not achieved by starting with only a single sphere filled with the intruding fluid. Due to the low coordination number of 4 (i.e. each sphere has only 4 pipes connecting to it for all analyses presented in this thesis except for those presented in Section 4.3 where the coordination number is 6), an extreme change of P_c might be required for the intruding fluid to break out of this sphere to a neighbouring sphere, because this will depend on only the radii of the 4 pipes in the case of a drying path or the radii of the 4 spheres on the other ends of these pipes in the case of a wetting path.

In order to achieve realistic modelling, drying or wetting paths should start with a small number of spheres m_{seed}, already filled with the intruding fluid and these seeding spheres should not simply be selected at random. Instead, to achieve realistic modelling of a drying path, it should always be preceded by modelling of a previous wetting path finishing with a small number of spheres (the seeding spheres) still filled with the drying fluid. A similar condition applies for realistic modelling of a wetting path, which should always be preceded by modelling of a previous drying path to leave an appropriate number of seeding spheres filled with the wetting fluid.

Investigation of this initiation process allowed an appropriate value to be selected for the number of seeding spheres equal to 1% of the total number of spheres of the network. This value was determined after several trials for different values (of multiples of 1% of m) of m_{seed} and cell sizes for which realistic retention curve shapes with no abrupt degree of saturation changes were produced. A value of m_{seed} = 1% was used in all analyses presented in this thesis except for those presented in Section 4.1.1, 4.3.1 and 4.3.1 where the material had to be fully saturated (hence m_{seed} = 0%) to verify correctness of model implementation.

3.4.4 Pore volume scaling

Practical problems arise when using a network approach for modelling a material with a wide range of pore sizes and where the smaller pores make similar contribution to the total pore volume as the larger pores. In this situation, a network would require a very large number of smaller pores in order to also include a statistically representative number of larger pores. With a standard network, this would require a network with an impractically large number of spheres. In addition, a standard network could not capture the fact that the average centre-to-centre spacing of smaller pores should be much less than the corresponding spacing for larger pores, otherwise adjacent small pores would be unreasonably far apart (suggesting an exceptionally low local porosity) and two adjacent large pores would be impossibly close together (suggesting overlap of the two pores).

In order to avoid these problems, a new approach was introduced, where each sphere within the network represents a scaled number of pores, with this scaling number increasing as the sphere size reduces. In the pore volume scaling technique, each sphere of radius r_{s} is taken to represent not a single pore but a non-integer number N of pores, each of radius r_{s}, where N is given by

$$N = \left(\frac{r_{\text{sm}}}{r_{\text{s}}} \right)^3 \tag{3.13}$$

where r_{sm} is the mean radius of the spheres. Equation (3.13) implies that each sphere of radius smaller than the mean represents more than a single pore, whereas each sphere of radius greater than the mean represents less than one pore. This scaled number of pores means that each sphere represents a volume V_{v} of pores given by

$$V_{\text{v}} = N\frac{4}{3}\pi r_{\text{s}}^3 = \frac{4}{3}\pi r_{\text{sm}}^3 \tag{3.14}$$

which shows that each sphere, whatever its radius, represents the same volume of pores.

The volume of pipes is ignored in calculating the porosity or degree of saturation of the periodic cell and therefore the porosity n of a cubical periodic cell of side length l_{CELL} containing a total of m spheres is simply given by

$$n = \frac{4\pi m r_{\text{sm}}^3}{3l_{\text{CELL}}^3} \tag{3.15}$$

Also since all spheres represent equal volumes the network degree of saturation S_{r} is evaluated as

$$S_{\text{r}} = \frac{m_{\text{w}}}{m} \tag{3.16}$$

where m_{w} is the number of wetting-fluid filled spheres.

The advantage of the pore volume scaling approach is that the network model is able to represent a periodic cell containing a large number of small pores without excessive computational effort. In addition, local values of porosity internally within the periodic cell are realistic, rather than being unreasonably low in regions around smaller spheres and impossibly high in regions around the largest spheres. A disadvantage of the pore volume scaling approach is that modelling of connectivity between pores, which is always imperfectly represented in a network model, may be represented even less realistically than without scaling. This can be illustrated by considering the case of a sphere that is significantly smaller than the mean sphere radius r_{sm}. This sphere represents a substantial number N of pores, rather than a single pore. The scaling technique means that local connectivity between these N pores is overstated, as they are all assumed to be at the same location in the network and are therefore perfectly connected to each other. In contrast, external connectivity between these N pores and other pores is understated, as only 4 pipes connect the single sphere representing all these N pores to other spheres. Reverse arguments apply to pores that are larger than the mean radius.

3.4.5 Element formulation

Formulation of pipe elements is restricted to the sole consideration of a liquid-gas system, where the liquid is the wetting fluid e.g. water-air system. For the remainder of Section 3.4, a water-air system is assumed. The fluid transport through pipes is determined by a mass balance equation. For each pipe, the discrete form of the mass transport differential equation for one pipe is given by

$$\boldsymbol{\alpha}_{\mathbf{e}}\mathbf{P}_{\mathbf{c}} = \mathbf{f}_{\mathbf{e}} \tag{3.17}$$

where $\mathbf{P}_{\mathbf{c}}$ is the vector of the capillary suctions at the nodes of the element, $\mathbf{f}_{\mathbf{e}}$ is the vector of the nodal flow rate and $\boldsymbol{\alpha}_{\mathbf{e}}$ is the conductivity matrix. The conductivity matrix has the form

$$\boldsymbol{\alpha}_{\mathbf{e}} = \frac{\pi r_{\mathrm{p}}^2}{l_{\mathrm{p}}} k_{\mathrm{pipe}} \begin{bmatrix} 1 & -1 \\ -1 & 1 \end{bmatrix} \tag{3.18}$$

where k_{pipe} is the pipe conductivity, r_{p} is the radius of the pipe and l_{p} is the length of the pipe. All the above parameters are geometrical except for k_{pipe}. The conductivity k_{pipe} is a variable that is dependent on the fluid that is conducted through the pipe as well as the pipe radius. The present model is able to evaluate the conductivity of a network with pipes filled with liquid water or water vapour. The determination of k_{pipe} for the specific cases of liquid or vapour filled pipes is presented in the next section.

3.4.6 Pipe element conductivity evaluation

As explained above, the present approach models the water mass transport of a network with pipes filled with water in either its liquid or gas phase. The k_{pipe} material parameter presented in (3.18) will be now substituted by k_{l} and k_{v} in the case of a liquid or vapour filled pipe, respectively. A pipe of a given radius will have one value of conductivity if the water transport is in liquid form and a different (much lower) value of conductivity if the water transport is limited to vapour movements. A liquid water conductivity is assumed when both spheres connected by the pipe are filled with liquid water. In this case, the flow is considered to be in the laminar regime. Thus, following the assumptions and expressions for evaluation of pipe conductivity presented in Section 2.3.1, k_{l} is calculated by the Hagen-Poisseuille equation (Yiotis et al., 2005a)

$$k_{\mathrm{l}} = \frac{\rho}{\mu}\frac{r_{\mathrm{p}}^2}{8} \tag{3.19}$$

where ρ is the density of liquid water and μ the dynamic viscosity. A pipe exhibits a water vapour conductivity when either one or both of the spheres connected by the pipe are gas filled. The mass transport of water vapour is assumed to be driven by diffusion (Maekawa et al., 2008) given by

$$Q = -A_{\mathrm{p}} D_{\mathrm{v}} \frac{\Delta \rho_{\mathrm{v}}}{l_{\mathrm{p}}} \tag{3.20}$$

where Q is the mass flow rate due to vapour diffusion, D_{v} the molecular diffusivity for vapour through air and ρ_{v} is the vapour density. Under equilibrium conditions (across an air/water interface), Kelvin's law (Maekawa et al., 2008) can be applied as

$$\frac{\rho_{\mathrm{v}}}{\rho_0} = \exp\left(\frac{-P_{\mathrm{c}} M}{\rho R T}\right) \tag{3.21}$$

where ρ_0 is the density of the saturated vapour, M the molar mass of water, R the universal gas constant and T the absolute temperature. The vapour density is therefore given by

$$\rho_{\mathrm{v}} = \rho_0 \exp\left(\frac{-P_{\mathrm{c}} M}{\rho R T}\right) \tag{3.22}$$

By differentiating (3.22) the result is

$$\mathrm{d}\rho_{\mathrm{v}} = \frac{-\rho_0 M}{\rho R T} \exp\left(\frac{-P_{\mathrm{c}} M}{\rho R T}\right) \mathrm{d}P_{\mathrm{c}} \tag{3.23}$$

Then, inserting (3.21) into (3.23), the result is

$$\mathrm{d}\rho_{\mathrm{v}} = \frac{-\rho_{\mathrm{v}} M}{\rho R T} \mathrm{d}P_{\mathrm{c}} \tag{3.24}$$

Furthermore, inserting (3.24) into (3.20) the result is

$$Q = -A_{\mathrm{p}} D_{\mathrm{v}} \frac{\rho_{\mathrm{v}}}{\rho} \frac{M}{\rho R T} \frac{\Delta P_{\mathrm{c}}}{l_{\mathrm{p}}} \tag{3.25}$$

A comparison between (3.25) and (2.15) it can be understood that the pipe conductivity can now be evaluated as

$$k = \frac{\rho_{\mathrm{v}}}{\rho} \frac{D_{\mathrm{v}} M}{R T} \tag{3.26}$$

Note that ρ_{v} is a variable (it varies with P_{c} according to (3.22)) and hence k_{pipe} is not strictly constant. However, we can simplify (3.26) by assuming that $\rho_{\mathrm{v}} \approx \rho_0$ (this is reasonable, provided P_{c} is less than 14 MPa see (3.22)). Therefore k_{v} is calculated by

$$k_{\mathrm{v}} = \frac{\rho_0}{\rho} \frac{D_{\mathrm{v}} M}{RT} \tag{3.27}$$

3.4.7 Model parameters

The transport model is based on a number of parameters, same of which are physical and others are non-physical.

The physical constants of the model are fluid density ρ, fluid viscosity μ, contact angle θ, surface tension γ, saturated vapour density ρ_0, water vapour diffusivity D_{v}, absolute temperature T, universal gas constant R and water molecular weight M.

The non-physical parameters are all the parameters related to the pipe and sphere radii distributions presented in Section 3.3.3 as well as the number of spheres m_{seed} used as seed for seeding at the start of a drying or wetting process (Section 3.4.3).

3.5 Mechanical model

3.5.1 Introduction

The mechanical model is developed to idealise the mechanical interaction between the particles within geomaterials. In the mechanical model, the particles are considered as rigid bodies connected by springs that describe both elastic and inelastic interactions. The model assumptions are initially presented. Then, the mechanical element formulation is explained and finally the material laws relating to the inter-particle contact interactions are presented.

3.5.2 Assumptions and simplifications

The mechanical model is developed within the framework of the lattice element approach (Bolander and Saito, 1998). A contact between two particles is allowed to be cancelled and

reformed. However, particles that do not initially share a contact are not allowed to form a new contact during the analyses. Also, particle crushing is not taken into account. The non-linear interaction between particles is modelled by a simple friction law.

3.5.3 Element formulation

The formulation is based on lattice element kinematics presented in Berton and Bolander (2006). The main assumption for the development of the present element is that the porous geomaterial is considered to be an assembly of rigid particles (Figure 3.5) with their deformability lumped in zero size springs (Berton and Bolander, 2006). The deformability of a two particle assembly is then modelled by the mechanical element presented in this section for the case of an elastic material response. For nonlinear responses, an incremental-iterative solution process is used.

The mechanical element presented earlier in Figure 3.3b has two nodes, namely i and j whose degrees of freedom represent particles rigid body motions. The contact of the two rigid particles takes place at a constant circular area with a radius r_{mech}. The same element as that in Figure 3.3b is presented in Figure 3.11 rotated in order to be aligned with its local axis coordinate system $(\hat{n}, \hat{t}, \hat{s})$. The cross-section is omitted in Figure 3.11. The interaction of two rigid particles are represented by two rigid arms $i - \text{C}'$ and $j - \text{C}''$, where C′ and C″ are connected by six (three translational and three rotational aligned with the local coordinate axes) zero sized springs (omitted in Figure 3.11). C′ and C″ are located at the centre of the mechanical element C (not presented) with initial zero distance. When C′ and C″ are moved apart due to displacements of nodes i and j, the springs are elongated or compressed and a reaction force is generated at the nodes of the element. Therefore, the stiffness of the lumped springs is directly related to the stiffness of the element.

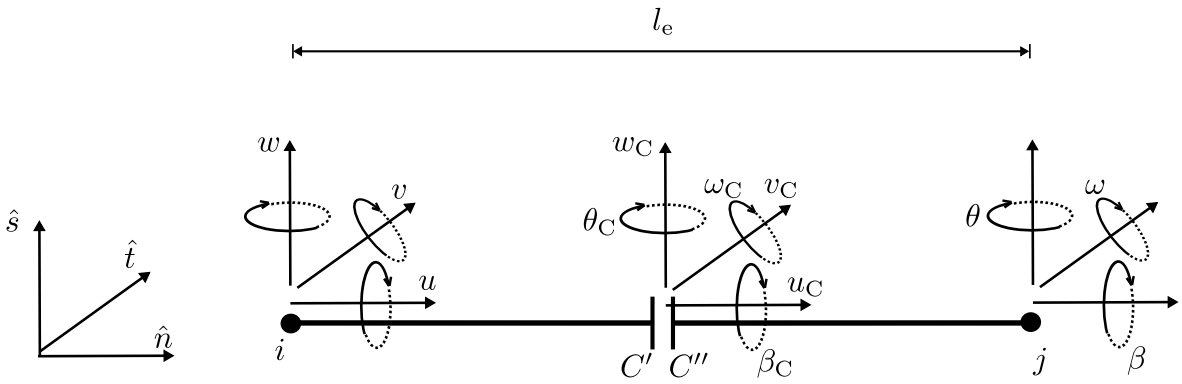

Figure 3.11: Schematic presentation of a mechanical element: nodes i and j, rigid arms $i - C'$ and $j - C''$ and the displacement jump evaluated by the relative distance of C′ and C″.

The stiffness of each spring is related to the element geometry. The spring that is aligned

with the element axis, with stiffness $K_{\hat{n}}$, is related to the element geometry according a beam stiffness formula as

$$K_{\hat{n}} = \frac{EA_{\text{mech}}}{l_e} \tag{3.28}$$

where $A_{\text{mech}} = \pi r_{\text{mech}}^2$ is the element area and E is the normal modulus of the relevant element and l_e the element length. For the tangential stiffnesses $K_{\hat{t}}$ and $K_{\hat{s}}$ a similar expression is used

$$K_{\hat{s}} = K_{\hat{t}} = \frac{\gamma_1 EA_{\text{mech}}}{l_e} \tag{3.29}$$

where γ_1 is the ratio of the element tangential modulus to element normal modulus. The rotational spring stiffnesses are also related to the element geometry using the beam element stiffness formulas. The polar rotational stiffness, for rotations aligned to the element axis, the stiffness is

$$K_{\text{p}} = \frac{\gamma_2 EI_{\text{p}}}{l_e} \tag{3.30}$$

where γ_2 is the ratio of the element rotational modulus to element normal modulus and I_{p} is the polar moment of inertia of the element cross-section. Finally, the first and second rotational stiffnesses K_{r1} and K_{r2}, respectively, are related to the element geometry according to

$$K_{\text{r1}} = \frac{\gamma_2 EI_1}{l_e} \tag{3.31}$$

and

$$K_{\text{r2}} = \frac{\gamma_2 EI_2}{l_e} \tag{3.32}$$

where I_1 and I_2 are the first and second principal moments of inertia of the element cross-section, respectively. For a circular cross-section $I_1 = I_2 = \pi\ r_{\text{mech}}^4/4$ and $I_{\text{p}} = \pi\ r_{\text{mech}}^4/2$.

The element stiffness results from the force needed to be applied for a unit displacement of each node which is the result of the elongation or compression of the springs lumped at the element mid-point. Each nodal displacement is related to the relative displacements of C′ and C″ (displacement jumps). Hence, for the evaluation of the element stiffness, it is useful to find the relation between the nodal displacements and the displacement jumps. This evaluation is presented below.

Each node possesses six degrees of freedom, namely three translations and three rotations. The local degrees of freedom $\mathbf{d}_{\mathrm{e}} = (\mathbf{u}, \mathbf{r})^{\mathrm{T}}$, where $\mathbf{u}$ and $\mathbf{r}$ are the vectors containing the translational and rotational degrees of freedom of nodes i and j, respectively. More specifically, the translation vector consists of two sub-vectors: $\mathbf{u} = (\mathbf{u}_i, \mathbf{u}_j)^{\mathrm{T}}$ where $\mathbf{u}_i = (u_i, v_i, w_i)^{\mathrm{T}}$ and $\mathbf{u}_j = (u_j, v_j, w_j)^{\mathrm{T}}$. Similarly, the rotational sub-vector is formulated as $\mathbf{r} = (\mathbf{r}_i, \mathbf{r}_j)^{\mathrm{T}}$ where $\mathbf{r}_i = (\beta_i, \theta_i, \omega_i)^{\mathrm{T}}$ and $\mathbf{r}_j = (\beta_j, \theta_j, \omega_j)^{\mathrm{T}}$. The translational discontinuities at the centroid of the mechanical element cross section C, $\mathbf{u}_{\mathrm{C}} = (u_{\mathrm{C}}, v_{\mathrm{C}}, w_{\mathrm{C}})^{T}$, are aligned with the local coordinate system $(\hat{n}, \hat{t}, \hat{s})$ and are related to the element nodal translational degrees of freedom as

$$\mathbf{u}_{\mathrm{C}} = \mathbf{B}\mathbf{d}_{e} \tag{3.33}$$

where $\mathbf{B}$ is a linear operator that is used to evaluate the contributions of each unit displacement of the nodal translations and rotations to the translational discontinuity.

The matrix $\mathbf{B}$ is expressed in terms of sub-matrices as

$$\mathbf{B} = \begin{bmatrix} \mathbf{B}_1 & \mathbf{B}_2 \end{bmatrix} \tag{3.34}$$

where

$$\mathbf{B}_1 = \begin{bmatrix} -\mathbf{I} & \mathbf{I} \end{bmatrix} \tag{3.35}$$

and

$$\mathbf{B}_2 = \begin{bmatrix} \mathbf{B}^* & \mathbf{B}^* \end{bmatrix} \tag{3.36}$$

In (3.35) and (3.36), $\mathbf{I}$ is the 3×3 identity matrix and $\mathbf{B}^*$

$$\mathbf{B}^* = \begin{bmatrix} 0 & 0 & 0 \\ 0 & 0 & -l_e/2 \\ 0 & l_e/2 & 0 \end{bmatrix} \tag{3.37}$$

The derivation of matrix **B** is described below.

For the derivation, the mechanical element presented in Figure 3.11 is considered. All the displacements and vectors are presented with respect to the local coordinate system. Two coinciding points C′ and C″ (presented here with a small gap for clarity) are located at the midpoint of the element. The element nodes i and j are connected, through two rigid arms, $i - C'$ and $j - C''$. The displacement of each node generates the rigid motion of its corresponding arm. The relative displacement of C′ and C″ forms the displacement jump evaluated at the midpoint of the element. This relative displacement is calculated by multiplying the **B** matrix with the element's nodal displacements in the local coordinate system.

Let $\mathbf{d}'$ and $\mathbf{d}''$ be the displacement vectors of C′ and C″, respectively, in the local coordinate system. The displacement jump is defined as $\mathbf{d}'' - \mathbf{d}'$. For the derivation of **B** matrix, unit nodal displacements are applied in turn, with the remaining degrees of freedom restrained. When u_i is applied (translation in $\hat{n}$ direction), the displacement of C′ is evaluated as $u_{C'} = u_i$ where all the other displacements are zero. Therefore, the displacement jump is $u_{C''} - u_{C'} = -u_i$. Similarly, when only u_j is applied, $u_{C''} - u_{C'} = u_j$ and therefore the displacement jump along the $\hat{n}$ axis, if both u_i and u_j are applied is evaluated as $u_{C''} - u_{C'} = u_j$.

The translational jumps along the other two axes ($\hat{t}$ and $\hat{s}$) are affected both by the nodal translations (in $\hat{t}$ and $\hat{s}$ directions respectively) and by the nodal rotations (about $\hat{t}$ and $\hat{s}$ axes respectively). The influence of the nodal translations on the translational jumps is represented through the negative and positive identity sub-matrices of **B**, whereas the influence of the nodal rotations about the $\hat{t}$ and $\hat{s}$ axes on the tranlsational jumps in the $\hat{s}$ and $\hat{t}$ directions is represented through the $\mathbf{B}^*$ sub-matrices of **B**.

The translational discontinuities at C are then transformed to element strains as

$$\boldsymbol{\varepsilon} = \mathbf{u}_C / l_e = (\varepsilon_{\hat{\mathrm{n}}}, \varepsilon_{\hat{\mathrm{s}}}, \varepsilon_{\hat{\mathrm{t}}})^{\mathrm{T}} \tag{3.38}$$

where l_e is the element length (Figure 3.11).

The nodal rotations also produce rotational discontinuities between C′ and C″. The expression

that relates the nodal degrees of freedom with the rotational jumps $\mathbf{r}_{\mathrm{C}} = (\beta_{\mathrm{C}}, \theta_{\mathrm{C}}, \omega_{\mathrm{C}})^T$ at the element mid-point is

$$\mathbf{r}_{\mathrm{C}} = \mathbf{B}_{\mathrm{r}} \mathbf{d}_e \tag{3.39}$$

where $\mathbf{B}_{\mathrm{r}}$ is

$$\mathbf{B}_{\mathrm{r}} = \begin{bmatrix} \mathbf{0} & \mathbf{0} & -\mathbf{I} & \mathbf{I} \end{bmatrix} \tag{3.40}$$

Here, $\mathbf{I}$ and $\mathbf{0}$ are the 3×3 unit and zero matrices, respectively. The derivation of (3.40) follows the same principles of two rigid arms as those presented for the derivation of (3.34) - (3.37).

The zero sized spring stiffnesses can be gathered into the diagonal stiffness matrix $\mathbf{k}_{\mathrm{spring}} = \mathrm{diag}[K_{\hat{n}}, K_{\hat{s}}, K_{\hat{t}}, K_{\mathrm{p}}, K_{\mathrm{r1}}, K_{\mathrm{r2}}]$ that relate the spring force vector $\mathbf{q}_{\mathrm{C}}$ to the displacement jumps as

$$\mathbf{q}_{\mathrm{C}} = \mathbf{k}_{\mathrm{spring}} \begin{pmatrix} \mathbf{u}_{\mathrm{C}} \\ \mathbf{r}_{\mathrm{C}} \end{pmatrix} \tag{3.41}$$

These spring forces result in nodal forces

$$\mathbf{q}_{\mathrm{e}} = \begin{bmatrix} \mathbf{B}^{\mathrm{T}} & \mathbf{B}_{\mathrm{r}}{}^{\mathrm{T}} \end{bmatrix}^{\mathrm{T}} \mathbf{q}_{\mathrm{C}} \tag{3.42}$$

The resulting force displacement law is

$$\mathbf{q}_{\mathrm{e}} = \begin{bmatrix} \mathbf{B}^{\mathrm{T}} & \mathbf{B}_{\mathrm{r}}{}^{\mathrm{T}} \end{bmatrix}^{\mathrm{T}} \mathbf{k}_{\mathrm{spring}} \begin{bmatrix} \mathbf{B} \\ \mathbf{B}_{\mathrm{r}} \end{bmatrix} \mathbf{d}_e = \mathbf{K} \mathbf{d}_e \tag{3.43}$$

Thus

$$\mathbf{K} = \begin{bmatrix} \mathbf{B}^{\mathrm{T}} & \mathbf{B}_{\mathrm{r}}{}^{\mathrm{T}} \end{bmatrix}^{\mathrm{T}} \mathbf{k}_{\mathrm{spring}} \begin{bmatrix} \mathbf{B} \\ \mathbf{B}_{\mathrm{r}} \end{bmatrix} \tag{3.44}$$

By rearranging (3.44) the element stiffness matrix in the local coordinate system has the form

$$\mathbf{K} = \begin{bmatrix} \mathbf{K}_{11} & \mathbf{K}_{12} \\ \\ \mathbf{K}_{21} & \mathbf{K}_{22} \end{bmatrix} = \begin{bmatrix} \dfrac{\pi r_{\text{mech}}^2}{l_e}\mathbf{B}_1^{\text{T}}\mathbf{D}_{\text{el}}\mathbf{B}_1 & \dfrac{\pi r_{\text{mech}}^2}{l_e}\mathbf{B}_1^{\text{T}}\mathbf{D}_{\text{el}}\mathbf{B}_2 \\ \\ \dfrac{\pi r_{\text{mech}}^2}{l_e}\mathbf{B}_2^{\text{T}}\mathbf{D}_{\text{el}}\mathbf{B}_1 & \dfrac{\pi r_{\text{mech}}^2}{l_e}\mathbf{B}_2^{\text{T}}\mathbf{D}_{\text{el}}\mathbf{B}_2 + \mathbf{K}_{\text{r}} \end{bmatrix} \tag{3.45}$$

where $\mathbf{K}_{\text{r}}$ is the rotational stiffness matrix denoted as

$$\mathbf{K}_{\text{r}} = \begin{bmatrix} \mathbf{K}'_{\text{r}} & -\mathbf{K}'_{\text{r}} \\ \\ -\mathbf{K}'_{\text{r}} & \mathbf{K}'_{\text{r}} \end{bmatrix} \tag{3.46}$$

Here, the sub-matrix $\mathbf{K}'_{\text{r}}$ is

$$\mathbf{K}'_{\text{r}} = \frac{\gamma_2 E}{l_e}\begin{bmatrix} I_{\text{p}} & 0 & 0 \\ 0 & I_1 & 0 \\ 0 & 0 & I_2 \end{bmatrix} \tag{3.47}$$

In (3.45), $\mathbf{D}_{\text{el}}$ is the 3×3 material stiffness matrix (see Section 3.5.4).

Finally, the element volume is evaluated as the product of the element cross-section area A_{mech} with the element length l_{e}.

3.5.4 Material model

The material model relates the stress vector with the element strains presented in Section 3.5.3 in (3.38). The stress vector $\boldsymbol{\sigma}$, results from the division of the normal and tangantial components of the spring forces vector $\mathbf{q}_{\text{C}}$ with the element cross-section area. For the case of linear elasticity, $\mathbf{D}_{\text{el}}$ in (3.45) is a diagonal tangent stiffness matrix $\mathbf{D}_{\text{el}}$ = diag$[E, \gamma_1 E, \gamma_1 E]$ where γ_1 is the ratio of the shear modulus of the element over the normal Young's modulus E. The stress vector is evaluated as

$$\boldsymbol{\sigma} = (\sigma_{\hat{n}}, \sigma_{\hat{s}}, \sigma_{\hat{t}})^{\text{T}} = \mathbf{D}_{\text{el}}\boldsymbol{\varepsilon} \tag{3.48}$$

where $\boldsymbol{\varepsilon}$ is the total strain vector as defined in (3.38). Many porous materials experience

plastic deformations under mechanical loads, i.e. irreversible strains occur as a consequence of inter-particle slippage or other irreversible phenomena. The stress-strain relationship is then

$$\boldsymbol{\sigma} = \mathbf{D}_{\text{el}}(\boldsymbol{\varepsilon} - \boldsymbol{\varepsilon}_{\text{p}}) \tag{3.49}$$

where $\boldsymbol{\varepsilon}_{\text{p}}$ is the vector of plastic strains. A simple constitutive friction law (Drucker, 1954) that applies only to compressive $\sigma_{\hat{n}}$ and represents the mechanical behaviour at the inter-particle level is presented with a yield function

$$f = \tau + \sigma_{\hat{n}} \tan\phi \tag{3.50}$$

where $\sigma_{\hat{n}}$ is the normal stress, ϕ is the friction angle and τ is the resultant of the two tangential stresses evaluated as $\tau = \sqrt{\sigma_{\hat{t}}^2 + \sigma_{\hat{s}}^2}$. This condition defines the stress state at which the material exhibits plastic flow. The yield function curve is presented in the $\sigma_{\hat{n}}$ - τ space in Figure 3.12. The stress states that satisfy the yield condition $f = 0$ form the yield surface. All sets of stress states which satisfy the condition $f \leq 0$ are called admissible stresses and these are the only states that the material can take.

When the yield condition is satisfied, plastic strains occur according to a flow rule

$$\dot{\boldsymbol{\varepsilon}}_{\text{p}} = \dot{\lambda}\frac{\partial f}{\partial \boldsymbol{\sigma}} = \dot{\lambda}\boldsymbol{f}_{\boldsymbol{\sigma}} \tag{3.51}$$

where $\dot{\boldsymbol{\varepsilon}}_{\text{p}}$ is the rate of change of the plastic strains $\boldsymbol{f}_{\boldsymbol{\sigma}}(\boldsymbol{\sigma}) = \partial f/\partial\boldsymbol{\sigma}$ the vector of the gradient of the yield function $\dot{\lambda}$ is the rate of change of the plastic multiplier. From now on the gradient of the yield function will be denoted as $\boldsymbol{f}_{\boldsymbol{\sigma}}$ (presented in Figure 3.12 at an arbitrary point of the yield surface) for the sake of simplicity. Since the yield function is linear, its gradient is a constant. Therefore, it does not depend on the stress state $\boldsymbol{\sigma}$. Equation (3.51) represents an associative flow rule.

The rate of the plastic multiplier $\dot{\lambda}$ defines the magnitude of the plastic strain and it is possible to be computed by the loading and unloading conditions

$$f \leq 0, \quad \dot{\lambda} \geq 0, \quad \dot{\lambda} f = 0 \tag{3.52}$$

When plastic strains are occurring, the tangent stiffness matrix is not the same as the elastic stiffness matrix $\mathbf{D}_{\text{el}}$ (compare (3.48) with the elastic case of (3.49)). The material stiffness matrix $\mathbf{D}_{\text{el}}$ in (3.49) is not the tangent one in contrast to the elastic case in (3.48). For the case of plastic flow, , the tangent stiffness matrix is known as elasto-plastic stiffness matrix, $\mathbf{D}_{\text{ep}}$. The evaluation of $\mathbf{D}_{\text{ep}}$ is presented below. During plastic flow, the rate of change of the yield function is zero and using the chain rule it can be shown that

$$\dot{f} = \boldsymbol{f}_{\boldsymbol{\sigma}}^{\mathrm{T}} \dot{\boldsymbol{\sigma}} = 0 \tag{3.53}$$

The rate of change of stresses can be evaluated by using (3.49) and (3.51)

$$\dot{\boldsymbol{\sigma}} = \mathbf{D}_{\text{el}}(\dot{\boldsymbol{\varepsilon}} - \dot{\boldsymbol{\varepsilon}}_{\text{p}}) = \mathbf{D}_{\text{el}}(\dot{\boldsymbol{\varepsilon}} - \dot{\lambda} \boldsymbol{f}_{\boldsymbol{\sigma}}) \tag{3.54}$$

By substituting (3.54) into (3.53) and solving for $\dot{\lambda}$

$$\dot{\lambda} = \frac{\boldsymbol{f}_{\boldsymbol{\sigma}}^{\mathrm{T}} \mathbf{D}_{\text{el}} \dot{\boldsymbol{\varepsilon}}}{\boldsymbol{f}_{\boldsymbol{\sigma}}^{\mathrm{T}} \mathbf{D}_{\text{el}} \boldsymbol{f}_{\boldsymbol{\sigma}}} \tag{3.55}$$

By substituting (3.55) in (3.54), the stress-strain law

$$\dot{\boldsymbol{\sigma}} = \mathbf{D}_{\text{el}} \left(\dot{\boldsymbol{\varepsilon}} - \frac{\boldsymbol{f}_{\boldsymbol{\sigma}}^{\mathrm{T}} \mathbf{D}_{\text{el}} \dot{\boldsymbol{\varepsilon}}}{\boldsymbol{f}_{\boldsymbol{\sigma}}^{\mathrm{T}} \mathbf{D}_{\text{el}} \boldsymbol{f}_{\boldsymbol{\sigma}}} \boldsymbol{f}_{\boldsymbol{\sigma}} \right) = \mathbf{D}_{\text{el}} \dot{\boldsymbol{\varepsilon}} - \frac{\mathbf{D}_{\text{el}} \boldsymbol{f}_{\boldsymbol{\sigma}} \boldsymbol{f}_{\boldsymbol{\sigma}}^{\mathrm{T}} \mathbf{D}_{\text{el}}}{\boldsymbol{f}_{\boldsymbol{\sigma}}^{\mathrm{T}} \mathbf{D}_{\text{el}} \boldsymbol{f}_{\boldsymbol{\sigma}}} \dot{\boldsymbol{\varepsilon}} \tag{3.56}$$

is obtained. The rate of stresses can be expressed as a linear transformation of the rate of the total strains as

$$\dot{\boldsymbol{\sigma}} = \mathbf{D}_{\text{ep}} \dot{\boldsymbol{\varepsilon}} \tag{3.57}$$

where $\mathbf{D}_{\text{ep}}$ is

$$\mathbf{D}_{\text{ep}} = \mathbf{D}_{\text{el}} - \frac{\mathbf{D}_{\text{el}} \boldsymbol{f}_{\boldsymbol{\sigma}} \boldsymbol{f}_{\boldsymbol{\sigma}}^{\mathrm{T}} \mathbf{D}_{\text{el}}}{\boldsymbol{f}_{\boldsymbol{\sigma}}^{\mathrm{T}} \mathbf{D}_{\text{el}} \boldsymbol{f}_{\boldsymbol{\sigma}}} \tag{3.58}$$

During plastic flow, the tangent matrix, given by (3.58), is a fully populated one rather than a diagonal matrix, for the elastic case.

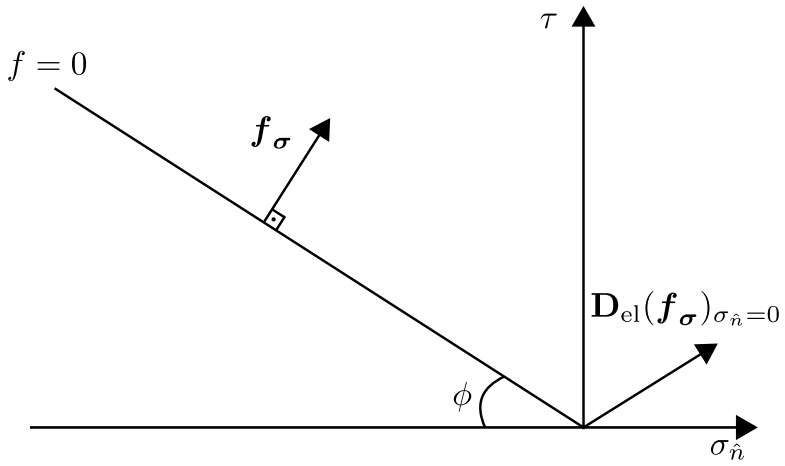

Figure 3.12: Yield function and flow rule: shear τ versus normal stress $\sigma_{\hat{\mathrm{n}}}$, yield function f, friction angle ϕ, flow rule $\boldsymbol{f_\sigma}$ and the product of $\mathbf{D}_{\mathrm{el}}$ and $\boldsymbol{f_\sigma}$ for $\sigma_{\hat{n}} = 0$.

3.5.5 Model parameters

The parameters used for a mechanical elastic analysis are the element normal modulus E, the ratio γ_1 of element tangent modulus to element normal modulus and ratio γ_2 of element rotational modulus to element normal modulus. Finally, for the plasticity model the friction angle ϕ is required.

3.6 Coupled approach

3.6.1 Introduction

The coupling of the mechanical and transport models is described here. The influence of the transport model on the mechanical model is developed based on an analytical expression presented in the literature for the additional inter-particle force produced by a meniscus water bridge. Furthermore, a simplified approach is proposed for taking into account the influence of the plastic mechanical strains on the radii of pipes within the transport network and hence on the conductivity.

3.6.2 Influence of fluid retention in the transport network on inter-particle interaction

The influence of fluid retention in the transport network on inter-particle interaction is modelled by taking into account the influence of the "meniscus water bridge" generation on the inter-particle contact forces. A major assumption, that the present framework is based on, is that no fluid pressure is considered to act on the particles. For the inclusion of the action of fluid pressure on particles a more sophisticated approach must be developed.

The derivation of an expression for the additional compressive normal inter-particle force produced by a meniscus water bridge follows the methodology first presented by Fisher (1926). This applies to the case of two identical smooth spherical particles of radius r_{part} in direct contact, as shown in Figure 3.13a The principal radii of the meniscus water bridge surrounding the inter-particle contact are r_1 and r_2 (Figure 3.13a). Capillary suction P_{c} can be expressed (see (2.17)) in terms of r_1 and r_2 and the surface tension γ as

$$P_{\text{c}} = \gamma \left(\frac{1}{r_1} - \frac{1}{r_2} \right) \tag{3.59}$$

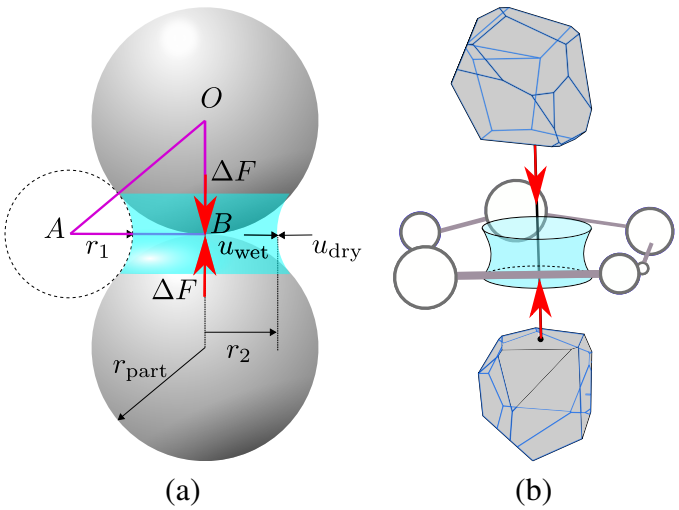

Figure 3.13: Schematic representation of influence of transport on the mechanical part: (a) two identical spherical particles in contact with a fully formed axisymmetric meniscus water bridge that generates an extra force ΔF and (b) two Voronoi polyhedra with their common mechanical element surrounded by drying fluid filled spheres that is the equivalent case of the generation of the meniscus water bridge.

Note the negative sign in (3.59) (compare with (2.17)), because the principal radius r_2 is measured on the water side of the air-water interface. Assuming, for simplicity, that the profile of the meniscus water bridge seen in Figure 3.13a is a circular arc of radius r_1 (as assumed by Fisher (1926)), application of Pythagoras' theorem on triangle OAB in Figure 3.13a, gives after rearrangement

$$r_1 = \frac{r_2^2}{2(r_{\text{part}} - r_2)} \tag{3.60}$$

Equations (3.59) and (3.60) can be combined, to eliminate r_1, to give an expression for r_2/r_{part} (see Hasan (2016))

$$\frac{r_2}{r_{\text{part}}} = \frac{3\gamma}{2r_{\text{part}}P_{\text{c}}}\left[\left(1 + \frac{8r_{\text{part}}P_{\text{c}}}{9\gamma}\right)^{1/2} - 1\right] \tag{3.61}$$

The additional inter-particle normal force ΔF produced by the meniscus water bridge is then given by simple force equilibrium as

$$\Delta F = 2\pi\gamma r_2 + \pi P_{\text{c}} {r_2}^2 \tag{3.62}$$

Inserting r_2 from (3.61) in (3.62) gives (see Hasan (2016))

$$\Delta F = \pi\gamma r_{\text{part}}\left(2 - \frac{3\gamma}{2r_{\text{part}}P_{\text{c}}}\left[\left(1 + \frac{8r_{\text{part}}P_{\text{c}}}{9\gamma}\right)^{1/2} - 1\right]\right) \tag{3.63}$$

Equation (3.63) states how ΔF varies with capillary suction P_{c} for particles of a given radius r_{part} (and a given value of surface tension γ) (Figure 3.14). As capillary suction tends to zero, (3.63) gives

$$(\Delta F)_{P_{\text{c}}=0} = \frac{4}{3}\pi\gamma r_{\text{part}} \tag{3.64}$$

Conversely, as capillary suction tends to infinity, (3.63) gives

$$(\Delta F)_{P_{\text{c}}=\infty} = 2\pi\gamma r_{\text{part}} \tag{3.65}$$

Note that the value of ΔF at $P_{\text{c}} = \infty$ is only 50% greater than the value of ΔF at $P_{\text{c}} = 0$.

Inspection of Figure 3.14 provides useful information for the generation and evolution of additional inter-particle compressive contact force due to meniscus water bridge formation.

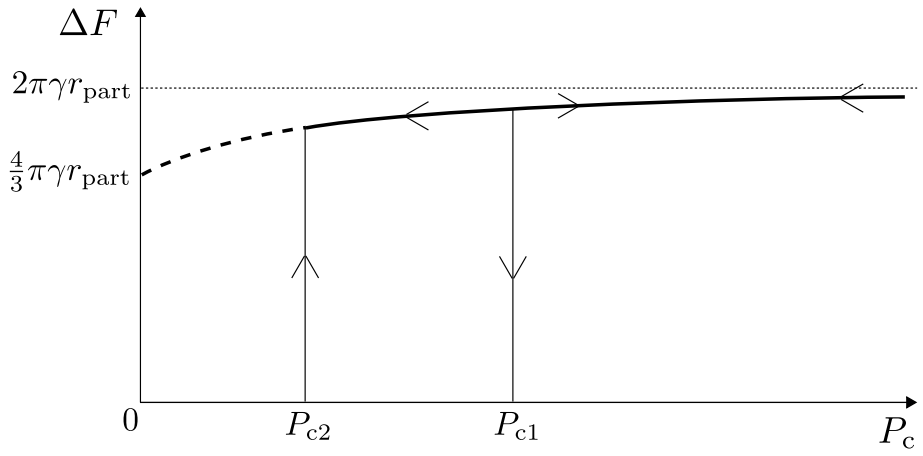

Figure 3.14: Schematic presentation of the evolution of the inter-particle force due to the generation of a meniscus water bridge between two equal spherical particles with radius r_{part}: additional inter-particle force ΔF versus capillary suction P_{c} where P_{c0}.

During drying capillary suction increases. The present system starts from saturated conditions (P_{c}= 0) and a meniscus water bridge is formed at capillary suction P_{c1}. Hence, at $P_{\mathrm{c}} = P_{\mathrm{c1}}$ the additional compressive inter-particle force ΔF is generated with a magnitude that lies between the bounding values of $\frac{4}{3}\pi\gamma r_{\text{part}}$ and $2\pi\gamma r_{\text{part}}$. As capillary suction further increases ($P_{\mathrm{c1}} < P_{\mathrm{c}}$), ΔF approaches the value of $2\pi\gamma r_{\text{part}}$ according to (3.65). If a wetting path is considered, starting from the reached condition of $P_{\mathrm{c1}} < P_{\mathrm{c}}$ the meniscus water bridge ceases to exist at $P_{\mathrm{c2}} < P_{\mathrm{c1}}$ due to hysteresis (see Section 2.3.1). Similar to the meniscus formation, ΔF reaches a value between the two bounding ones referred in (3.64) and (3.65) before the water meniscus bridge has disappeared. Therefore, it is justified to assume that ΔF is constant for any $P_{\mathrm{c}} = 2\pi\gamma r_{\text{part}}$ value as long as the meniscus water bridge is present (Wheeler et al., 2003).

To include the effect of the additional contact force ΔF in the mechanical model the formation of a meniscus water bridge must be considered. As shown in Figure 3.13b, two Voronoi polyhedra now replace the two spheres shown in Figure 3.13a. The polyhedra are presented smaller than they are in the model for a clearer view of the mechanical element that represents the contact of the two particles and the spheres and pipes that surround it. In calculating the value of ΔF within an individual mechanical element it is assumed that for the two particles that come in contact are equal spheres of radius equal to half the element's length l_{e}. Hence for (3.65), r_{part} is replaced by $l_{\mathrm{e}}/2$. As P_{c} increases in the transport network, the spheres are emptied of the wetting fluid. When all spheres surrounding the mechanical element are emptied, a wetting fluid meniscus bridge is assumed to be formed (Figure 3.13). Hence, an additional compressive force is added to the mechanical element as

$$\Delta F = \pi\gamma l_{\mathrm{e}} \tag{3.66}$$

3.6.3 Influence of mechanical response on transport

Only the pipe elements are influenced by the mechanical model, with the pipe radii changing when at least one of the surrounding mechanical elements exhibits plastic flow. The pipe radius is assumed to be linked to the mechanical element midpoint and its normal plastic displacements jump $\varepsilon_{\hat{n}\mathrm{p}} l_e$ produce an equivalent change of the cross-section circumference c_{circ} as

$$c_{\mathrm{circ}} = 2\pi r_{\mathrm{p}} = 2\pi r_{\mathrm{p0}} + \varepsilon_{\hat{n}\mathrm{p}} l_e \tag{3.67}$$

where r_{p0} is the initial pipe radius and r_{p} is the current pipe radius. The value of c_{circ} can only increase since the normal plastic displacement jump $\varepsilon_{\hat{n}\mathrm{p}} l_e$ can only be positive in this framework as it is evaluated based on the friction law presented in Section 3.5.4 that results only in positive normal plastic strains. Solving (3.68) for r_{p} the result is

$$r_{\mathrm{p}} = r_{\mathrm{p0}} + \frac{1}{2\pi} \varepsilon_{\hat{n}\mathrm{p}} l_e \tag{3.68}$$

For the general case where any of the three surrounding mechanical elements exhibits plastic strains, the pipe radius is evaluated as

$$r_{\mathrm{p}} = r_{\mathrm{p0}} + \frac{1}{2\pi} \sum_{i=1}^{3} \varepsilon_{\hat{n}\mathrm{p}i} l_{ei} \tag{3.69}$$

The influence of the mechanical model on transport is schematically presented in Figure 3.15. A pipe element with its corresponding spheres is presented along with the mechanical elements that surround it. The Voronoi polyhedra that correspond to the nodes of the mechanical elements are presented scaled down for a clearer visual representation. When plastic strains occur, the radius of the associated pipe increases in magnitude. The mechanical element that was presented to exhibit plastic flow in Figure 3.15 would affect all the pipe elements that surround it (see Figure 3.3a). These other pipe elements are not presented in Figure 3.15.

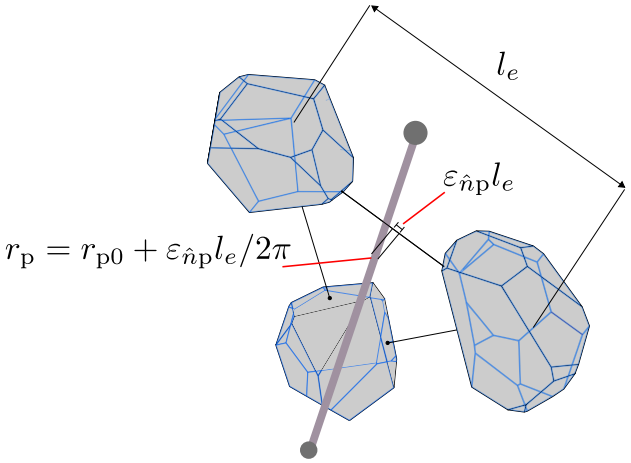

Figure 3.15: Schematic presentation of the influence of the mechanical changes on the transport model: plastic strains occur, the radius of the associated pipe elements increases by an amount of half of the product of the plastic strain times the mechanical element length.

3.6.4 Assumptions and simplifications

The coupled approach is based on the assumption that each mechanical contact is created by two perfectly spherical grains with equal radii. Also, when all the spheres surrounding a contact are filled with air, a water meniscus bridge is assumed to be created and an additional force is subjected to the contact (see Section 2.3.3). The additional force is assumed to be constant with varying capillary suction (see Section 2.3.3). From the transport network, only the pipes are affected by the mechanical model in case of plastic flow. Elastic deformations do not affect transport.

3.6.5 Model parameters

For the hydro-mechanical coupling, the input parameters are the same as those in the transport and mechanical models.

3.7 The periodic cell

3.7.1 Introduction

The micromechanical model described in Sections 3.1 to 3.6 was developed to investigate the hydro-mechanical behaviour of porous geomaterials at a constitutive level. Hence, the focus was on the behaviour at a material point based on the geomaterial microstructure, rather

than investigating boundary value problems. Therefore, cells subjected to Neumann or Dirichlet boundary conditions are not well suited since the boundaries influence their behaviour (Grassl and Jirásek, 2010). Additionally, the application of these boundary conditions implies the existence of defined boundaries where the microstructure would follow the boundary geometry. For instance, for the case of the present model discretisation, mechanical elements would be placed along the faces and the edges of a cell and transport elements would be perpendicular to the faces.

To solve the above implications, elements with Periodic Boundary Conditions (PBCs) can be applied. The formulation of the PBCs is developed here for elements that cross the boundaries, by extension of the 2D mechanical elements with PBCs presented in Grassl and Jirásek (2010) to 3D mechanical and transport lattice elements.

3.7.2 Transport element formulation

The periodic element presented in this section is the extension of the 2D mechanical periodic element presented in Grassl and Jirásek (2010) to a 3D periodic transport element. Let us consider a 3D periodic cell schematically presented in Figure 3.16 for the description of the 3D periodic transport element formulation. For this explanation, only two transport elements are presented out of a more complex network. The cell under consideration is highlighted with black edges and it has twenty six identical neighbouring cells. Only two out of the 26 neighbouring cells that share faces, edges and corners with the cell under consideration are presented in Figure 3.16 (shown with red edges). The common cell faces in Figure 3.16 are perpendicular to the global x axis.

Nodes I and J are located in the interior of the cell under consideration. Their periodic projections along the x axis are nodes I' and J', which lie outside the cell. The intersection points of the $I - J'$ and $I' - J$ elements with the boundaries of the periodic cell are presented with a circle and a cross in the plane of the boundary. The parts of the elements that lie within the cell boundaries are shown with dashed lines and those parts that lie outside the cell boundaries are shown by solid lines. The cell edges are aligned with the global orthogonal system. In general, node J' can be described by the result of the shift of node J by $k_{\mathrm{x}}a$ in the x-direction, $k_{\mathrm{y}}b$ in the y-direction, $k_{\mathrm{z}}c$ in the z-direction, where a, b and c are the edge lengths of the cell. The coefficients k_{x}, k_{y} and k_{z} are integers equal to -1 for a negative, 1 for a positive and 0 for no shift along the axis under consideration. In the present example $k_{\mathrm{y}} = k_{\mathrm{z}} = 0$ and $k_{\mathrm{x}} = \pm\ 1$. This is the same notation that was used in Section 3.1.

In the transport network, each node possess one degree of freedom, namely the capillary suction P_{c}. The values of P_{c} at the two ends of a transport element $I'J$ that crosses a cell

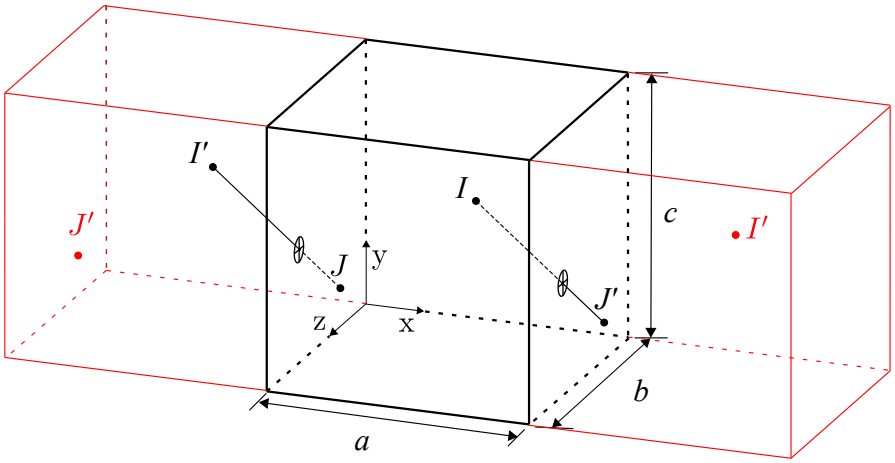

Figure 3.16: 3D periodic cell: main cell (black edges) and the 2 out of 26 neighbouring cells (red edges), periodic elements IJ' and $I'J$, the nodes I' and J' are the result of the shifting of nodes I and J by a length of a in the x direction.

boundary are evaluated with a transformation rule as

$$\begin{pmatrix} P_{I'} \\ P_J \end{pmatrix} = \mathbf{T}_{\mathrm{t}} \begin{pmatrix} P_I \\ P_J \\ \Delta P_{\mathrm{x}}/a \\ \Delta P_{\mathrm{y}}/b \\ \Delta P_{\mathrm{z}}/c \end{pmatrix} \tag{3.70}$$

where $\Delta P_{\mathrm{x}}/a$, $\Delta P_{\mathrm{y}}/b$ and $\Delta P_{\mathrm{z}}/c$ are the average capillary pressure gradients along the direction x, y and z respectively. Also $\mathbf{T}_{\mathrm{t}}$ is transformation matrix of size 2×5 and has the form

$$\mathbf{T}_{\mathrm{t}} = \begin{bmatrix} 1 & 0 & ak_{\mathrm{x}} & bk_{\mathrm{y}} & ck_{\mathrm{z}} \\ 0 & 1 & 0 & 0 & 0 \end{bmatrix} \tag{3.71}$$

When this rule is combined with (3.17) linking the capillary pressures of nodes to the reaction flow vector, if this involves image nodes, then the transformation matrix $\mathbf{T}_{\mathrm{t}}$ multiplies matrix $\boldsymbol{\alpha}_{\mathbf{e}}$ from the right. It follows from the duality that the internal forces must be multiplied by $\mathbf{T}_{\mathrm{t}}^{\mathrm{T}}$ from the left, before the evaluation of the equilibrium conditions. The conductivity matrix is evaluated as $\mathbf{T}_{\mathrm{t}}^{\mathrm{T}}\boldsymbol{\alpha}_{\mathbf{e}}\mathbf{T}_{\mathrm{t}}$ where the original conductivity matrix $\boldsymbol{\alpha}_{\mathbf{e}}$ is transformed from a 2×2 matrix to a 5×5 one. In evaluating the conductivity matrix at the internal reaction flow rate vector, the volume of each periodic element is halved since the volume of the periodic element appears only once in the cell region but there are two corresponding elements identified as falling partly within the basic cell (e.g. IJ' and $I'J$). The global conductivity matrix is assembled normally except for six rows and columns that relate the global degrees of freedom to its conjugate reaction flow rates. As a result, arbitrary combinations of average flux or gradients can be prescribed. Finally, the total number of unknown degrees of freedom is the

total number of the nodes located in the interior of the periodic cell plus three global degrees of freedom controlling the average flux or gradient in three directions.

3.7.3 Mechanical element formulation

The periodic mechanical element presented in this section is the extension from 2D to 3D of the periodic mechanical element presented in Grassl and Jirásek (2010). When the cell is subjected to an average strain field, the transformation to give the translations of a node lying outside the cell is

$$u' = u + ak_{\mathrm{x}}E_{\mathrm{x}} + ck_{\mathrm{z}}E_{\mathrm{zx}} + bk_{\mathrm{y}}E_{\mathrm{yx}} \tag{3.72}$$

$$v' = v + bk_{\mathrm{y}}E_{\mathrm{y}} + ck_{\mathrm{z}}E_{\mathrm{yz}} \tag{3.73}$$

$$w' = w + ck_{\mathrm{z}}E_{\mathrm{z}} \tag{3.74}$$

where the translation presented without and with the prime symbol are those of the nodes located within and outside the cell, respectively. Furthermore, E_{x}, E_{y} and E_{z} are the average normal strains in the x, y and z direction, respectively and E_{yz}, E_{zx} and E_{yx} are the average engineering shear strains. Note that the contributions of the average shear strains E_{zx} and E_{yx} has been included only in the displacements in the x direction and the contribution of E_{yz} has been included only in the displacement in the y-direction. This is justified by the arbitrariness of the rigid body rotation of the entire cell (Grassl and Jirásek, 2010). It is assumed that the two faces of the cell perpendicular to z axis do not rotate, whereas the other four faces of the cell are free to rotate. Finally one node of the lattice is fully fixed in order to prevent rigid body rotation and translation.

Making use of (3.72), (3.73) and (3.74) and of the relation for the rotations, $\phi_J = \phi_{J'}$, $\theta_J = \theta_{J'}$ and $\omega_J = \omega_{J'}$ the transformation rule giving the translations and rotations of the two ends I and J' of a mechanical element IJ' crossing a cell boundary can be set up as

$$\begin{pmatrix} \mathbf{u}_I \\ \mathbf{u}_{J'} \\ \mathbf{r}_I \\ \mathbf{r}_{J'} \end{pmatrix} = \mathbf{T_m} \begin{pmatrix} \mathbf{u}_I \\ \mathbf{u}_J \\ \mathbf{r}_I \\ \mathbf{r}_J \\ \mathbf{E}_{\text{AVE}} \end{pmatrix} \tag{3.75}$$

where $\mathbf{u}_I$, $\mathbf{r}_I$, $\mathbf{u}_J$, $\mathbf{r}_J$, $\mathbf{u}_{J'}$ and $\mathbf{r}_{J'}$ are the translational and rotational vectors of nodes I, J and J', respectively (Grassl and Jirásek, 2010). The vector $\mathbf{E}_{\text{AVE}}$ contains the average engineering strains

$$\mathbf{E}_{\text{AVE}} = \begin{pmatrix} E_{\text{x}} \\ E_{\text{y}} \\ E_{\text{z}} \\ E_{\text{yz}} \\ E_{\text{zx}} \\ E_{\text{yx}} \end{pmatrix} \tag{3.76}$$

The transformation matrix $\mathbf{T}_{\text{m}}$ is of size 12×18 and has the form

$$\mathbf{T}_{\text{m}} = \begin{bmatrix} \mathbf{I} & \mathbf{0} & \mathbf{k} \\ \mathbf{0} & \mathbf{I} & \mathbf{0} \end{bmatrix} \tag{3.77}$$

where $\mathbf{I}$ and $\mathbf{0}$ are the 6×6 identity and zero matrices, respectively. The sub-matrix $\mathbf{k}$ is the 6×6 matrix that contains transformation of the nodal displacements due to the average engineering strains which is in sub-matrix form

$$\mathbf{k} = \begin{bmatrix} \mathbf{0} & \mathbf{0} \\ \mathbf{k}_{21} & \mathbf{k}_{22} \end{bmatrix} \tag{3.78}$$

In (3.78), $\mathbf{0}$ is the 3×3 zero matrix and the other two sub-matrices are

$$\mathbf{k}_{21} = \begin{bmatrix} ak_{\text{x}} & 0 & 0 \\ 0 & bk_{\text{y}} & 0 \\ 0 & 0 & ck_{\text{z}} \end{bmatrix} \tag{3.79}$$

and

$$\mathbf{k}_{22} = \begin{bmatrix} 0 & ck_{\mathrm{z}} & bk_{\mathrm{y}} \\ ck_{\mathrm{z}} & 0 & 0 \\ 0 & 0 & 0 \end{bmatrix} \tag{3.80}$$

When the rule in (3.75) is combined with (3.33) linking the displacements of nodes to the discontinuities, and this includes image nodes, then the transformation matrix $\mathbf{T}_{\mathrm{m}}$ multiplies matrix $\mathbf{B}$ from the right. It follows from the duality that the internal forces must be multiplied by $\mathbf{T}_{\mathrm{m}}^{\mathrm{T}}$ from the left, before the evaluation of the equilibrium conditions. Hence, the original 12×12 stiffness matrix $\mathbf{K}$ of the non-periodic element is now transformed to the 18×18 matrix $\mathbf{T}_{\mathrm{m}}^{\mathrm{T}}\mathbf{K}\mathbf{T}_{\mathrm{m}}$. By applying the transformation rule on (3.45), the new stiffness matrix is evaluated. Here, it is presented in sub matrix form as

$$\mathbf{T}_{\mathrm{m}}^{\mathrm{T}}\mathbf{K}\mathbf{T}_{\mathrm{m}} = \begin{bmatrix} \mathbf{K}_{11} & \mathbf{K}_{12} & \mathbf{K}_{11}\mathbf{k} \\ \mathbf{K}_{21} & \mathbf{K}_{22} & \mathbf{K}_{21}\mathbf{k} \\ \mathbf{k}^{\mathrm{T}}\mathbf{K}_{11} & \mathbf{k}^{\mathrm{T}}\mathbf{K}_{12} & \mathbf{k}^{\mathrm{T}}\mathbf{K}_{11}\mathbf{k} \end{bmatrix} \tag{3.81}$$

In evaluating the global stiffness matrix and the internal forces the volume of each periodic element is halved since the volume of the periodic element appears only once in the cell region whereas there are two identical periodic elements crossing the cell boundaries (IJ' and $I'J$). This volume halving is an extension of the periodic element formulation presented in Grassl and Jirásek (2010) which took the total volume of the periodic elements into account. The global stiffness matrix is assembled normally except for six rows and columns that relate the global degrees of freedom to its conjugate reaction forces. As a result, average stresses or strains can be prescribed at the global node. Finally, the total number of unknown degrees of freedom is six times the number of nodes lying within the cell boundaries.

3.7.4 Hydro-mechanical coupling

As explained in Section 3.2, the mechanical and transport elements are placed along the edges of the Delaunay or Voronoi network that possess at least one node located within the periodic cell. Additionally, it was described in Section 3.6 that for the coupling, each element requires information from the elements placed along the edges of its associated facet. However, the associated facet may have one or more edges where both its nodes are located outside the cell. Hence, there are no elements placed along this edge of the facet. The solution of this problem is presented in this section.

Let us reconsider the simple 2D mechanical and transport networks presented in Figure 3.4b and 3.4c, respectively. The Delaunay edge where the mechanical element $I'J$ is placed (Figure 3.4b) possesses a dual Voronoi edge with both its nodes M'' and N'' located outside the cell. Therefore, no element is placed along this edge as presented in Figure 3.4c. In order to access information from the transport element located on its dual edge, the element MN' (Figure 3.4c) is used since M'' is the result of the shift of node M and N'' and N' are both results of the shift of N. Similarly, the transport element MN' which requires information from the mechanical element $I''J''$, accesses the information from the mechanical element IJ'. For the case of the mechanical elements this approach is well suited because the Periodic Boundary Conditions applied are based on an average gradients with zero spatial derivatives. Hence, all mechanical elements that possess node pairs that are results of shifts of the same pair of nodes experience the same strain. Similar arguments apply for the transport elements, where elements that possess node pairs that are results of shifts of the same pair of nodes experience the same gradient of capillary suction.

A 3D example of a mechanical network is presented in Figure 3.17a and the facets associated to each mechanical element are presented in Figure 3.17b. Transport elements lie along all edges. However, no new transport elements are placed along the edges whose nodes lie totally outside the cell. Instead, for edges whose both nodes lie outside the cell, transport elements that correspond to edges with one or both nodes inside the cell are considered. The later elements are the result from the periodic displacement of the nodes of the edges that lie outside the cell according to (3.1). Similarly, Figure 3.18a shows the corresponding dual transport network and Figure 3.18b shows the facets associated to each transport element. Mechanical elements lie along all edges. However, no new transport elements are placed along the edges whose nodes lie totally outside the cell. Instead, for edges whose both nodes lie outside the cell, mechanical elements that correspond to edges with one or both nodes inside the cell are considered. By comparing the geometries presented in Figures 3.17a and 3.18b, it can be observed that the geometry of the mechanical model (Figure 3.17) is different from that of the associated set of facet edges required by the transport model for coupling purposes (because the latter involves additional edges). Similar conclusions can be deduced for the transport model by comparison of Figures 3.18b and 3.17a.

3.8 Implementation

3.8.1 Introduction

Implementation was integrated in the finite element code OOFEM (Object Orientated Finite Element Method) (Patzák, 2012). The implementation of the coupled transport and mechan-

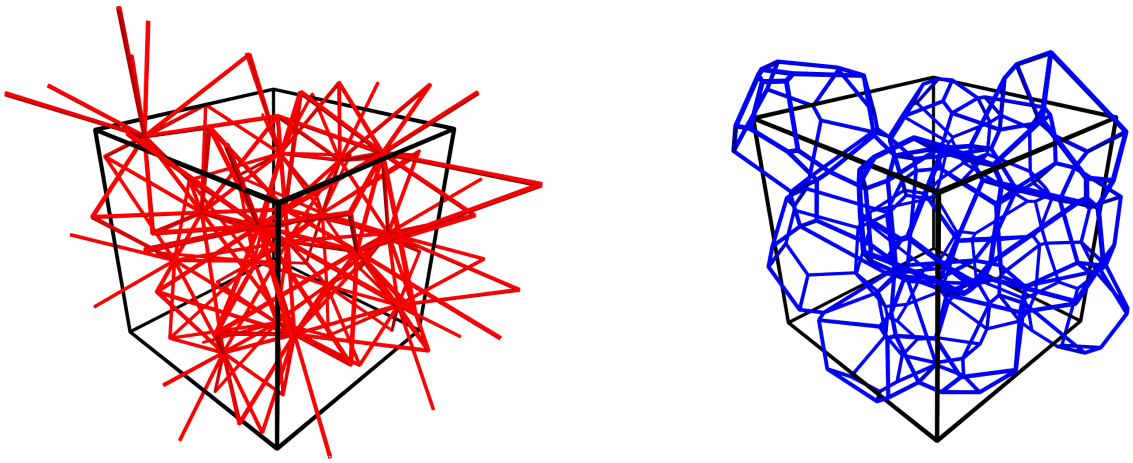

(a) (b)

Figure 3.17: 3D mechanical model including elements crossing the boundaries: (a) mechanical lattice and (b) edges of associated facets.

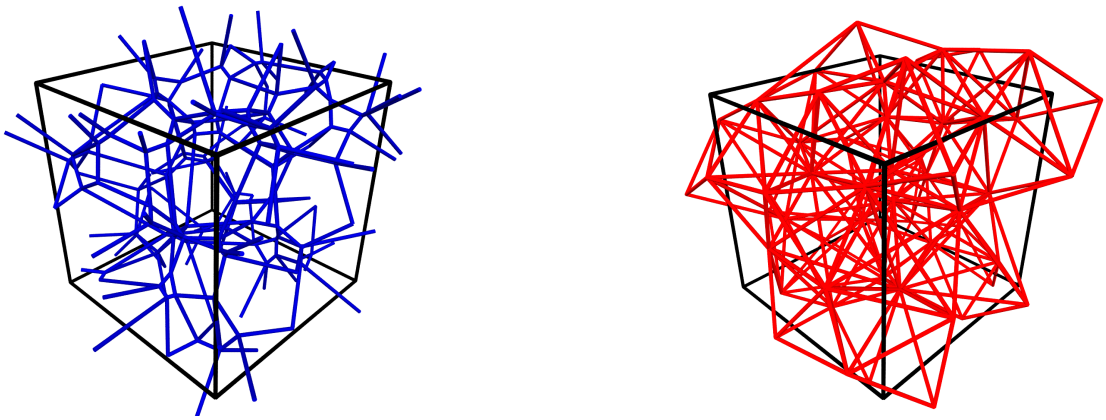

(a) (b)

Figure 3.18: 3D transport model including elements crossing the boundaries: (a) transport network and (b) edges of associated facets.

ical approach is presented in this section. The network initiation, fluid configuration and conductivity evaluation are described in detail for the transport model. For the mechanical model, the implementation of the friction law and the global structural solution are described. Finally, the coupling approach is explained.

3.8.2 Transport

The transport problem is solved as a stationary problem. At each step $h+1$ of an analysis, the driving variable is the target capillary suction $P_{\mathrm{c}}^{\mathrm{T}(h+1)}$. For each $P_{\mathrm{c}}^{\mathrm{T}(h+1)}$, the configuration of the drying and wetting fluids is chosen based on an algorithm presented in this section. Then, the degree of saturation S_{r}, is evaluated according to (3.16) presented in Section 3.4.4.

For the conductivity evaluation, the configuration of the fluids is fixed and the network is subjected to a notional uniaxial gradient of capillary suction. The gradient is characterised as notional since it is assumed that it does not produce any changes to the fluid configuration (which is not true for real conditions) and hence any value of pressure gradient can be chosen for the evaluation of cell conductivity using (2.4). The resulting network flow rate is computed as the reaction total flow in the direction in which the uniaxial gradient was applied.

Due to the the absence of boundaries and the shielding effect that prevents the generation of realistic retention and conductivity curves if drying or wetting commences from a single sphere, a special treatment of the network initiation is required (Section 3.4.3). The general concept of this process is to find appropriate spheres within the network that are going to be used as sources of either the wetting or drying fluid. The number of these spheres m_{seed} is a chosen proportion of the total number of spheres. These spheres are referred to as seeding spheres. For simulation of a wetting process from initially "dry" conditions, the network begins with all its spheres filled with wetting fluid except for one. Spheres are then filled with drying fluid one by one. The sphere chosen to fill with drying fluid each time, amongst all the spheres in the network, is the one connected to a drying fluid filled neighbour that has the lowest value of emptying capillary suction according to (3.12) (where r in (3.12) is taken as the radius of the connecting pipe as described in Section 3.4.3). Once a number m_{seed} of spheres remain filled with wetting fluid, the seeding process is completed. The remaining spheres still filled with wetting fluid are the seeding spheres for a subsequent wetting process.

During the wetting process, the sphere chosen to fill next with wetting fluid is the one connected to a wetting fluid filled neighbour that has the highest value of filling capillary suction according to (3.12) (where r in (3.12) is taken as the radius of the sphere about to be filled, as described in Section 3.4.3). The wetting process is terminated when a number m_{seed} of spheres are left filled with drying fluid. These would be the seeding spheres for simulation of any subsequent drying process from a "fully wet" condition.

The implementation of the initiation process is described in detail in the present section.

For this purpose, five quantities are assigned at each sphere.

1. A flag that determines whether the sphere is filled with wetting fluid or drying fluid, i.e. 0 when filled with wetting fluid and 1 when filled with drying fluid.

2. The total number of neighbouring spheres N_{n}.

3. The number of these neighbours that are filled with the wetting fluid N_{wn}.

4. The minimum capillary suction value (P_{cD}) that the sphere can be filled with drying fluid determined by the radius of the largest pipe connecting it to a neighbouring sphere filled with drying fluid filled spheres.

5. The capillary suction value (P_{cW}) for which the sphere would be filled with wetting fluid, determined by the radius of the sphere under consideration.

In the beginning of the analysis, the above quantities are assigned as described below. All but one spheres are considered to be filled with the wetting fluid, hence a flag value equal to 0 is assigned for each of them. The drying fluid filled sphere serves the purpose of the first seeding sphere and a flag equal to 1 is assigned. At all spheres, the values of N_{n} and P_{cW} are assigned. Additionally, a very large value for P_{cD} is initially assigned at each sphere. This is done because P_{cD} cannot be determined for the majority of spheres, since they are not available to be filled with drying fluid. For each sphere the quantity $N_{\text{wn}} = N_{\text{n}}$ is set. Both these values can not be less than zero. Throughout the analysis and the initiation process the values of N_{n} and P_{cW} of each sphere are invariant. The tracking of the pipe filling is not needed since it does not play an explicit role in determining the process of emptying or filling of spheres.

After setting all the aforementioned initial values, the seeding process begins. The neighbours of the first seeding sphere are identified and the value of their N_{wn} is decreased by one. Figure 3.19 presents a schematic 2D representation of the initial seeding sphere A and its neighbours B, C, D and E connected through pipes 1, 2, 3 and 4, respectively. All spheres in the network have a coordination number equal to four. The blue and white spheres represent the wetting and drying fluid filled ones, respectively. The P_{cD} values of B, C, D and E are changed from their initial very large value to that corresponding to pipes that connect them to sphere A.

All spheres with $N_{\text{wn}} < N_{\text{n}}$ and their phase condition flag equal to 0 are now candidates to fill with drying fluid at the next step of the initiation process. Hence, spheres B, C, D, and E in Figure 3.19 are the only candidates at the first step of the initiation. The sphere with the lowest P_{cD} value fills with drying fluid next. Hence, sphere E fills with drying fluid since pipe 4 has the largest radius amongst all the other connected ones. The flag value for sphere E therefore switches to 1.

Figure 3.20 shows sphere E, at the second step of the analysis, with its four neighbour spheres A, F, G and H. The N_{wn} values of each neighbour of sphere E are decreased by one. New paths for drying fluid to flow and potentially fill the neighbours of sphere E are now available. Therefore, the values of P_{cD} already assigned to spheres A, F, G and H are compared to the drying capillary suction value due to the new available pathways through pipes 4, 7, 5 and 6, respectively. If the capillary suction value corresponding to the new pathway is lower than the

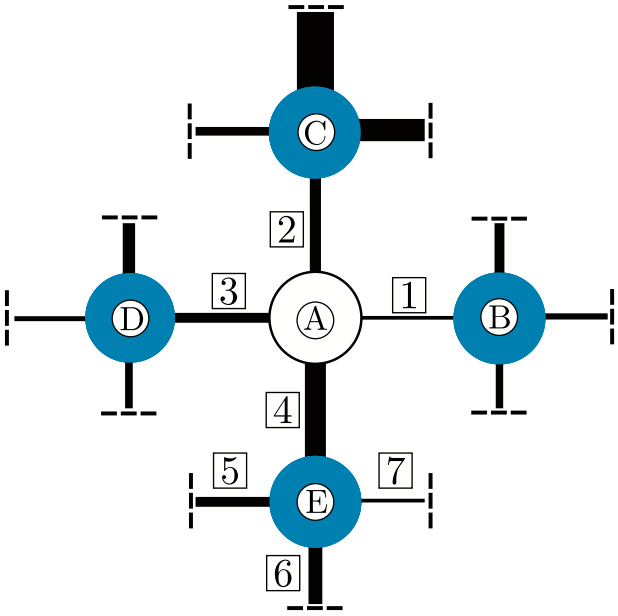

Figure 3.19: Schematic presentation of a sub-pore network: drying fluid filled sphere A and wetting fluid filled ones B, C, D and E and numbered pipes.

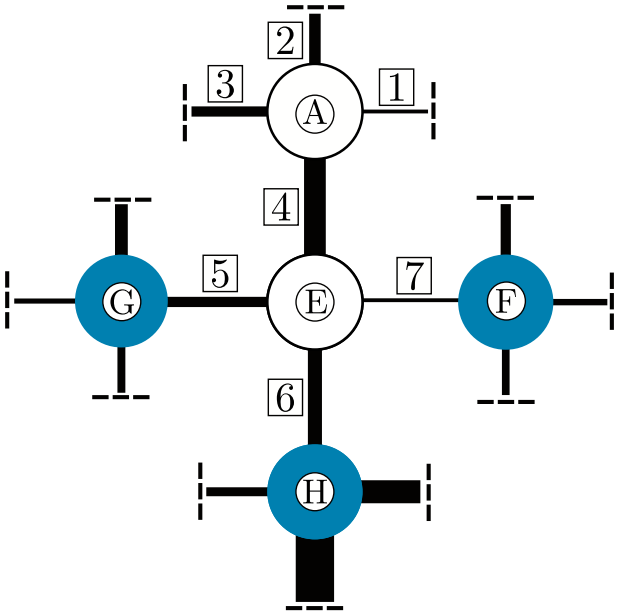

Figure 3.20: 2D schematic presentation of a sub-pore network connected to the one presented in Figure 3.19: drying fluid filled spheres A and E, wetting fluid filled ones G, F and H and numbered pipes.

previously assigned one, then P_{cD} is assigned this new value.

This process is continued until the entire cell is considered to be dry i.e. until the number of wetting fluid filled spheres are equal to the selected seeding number m_{seed}. This is done in a number (m - m_{seed}) sphere emptying events, each involving filling of an individual sphere with drying fluid. At each event, the sphere with the lowest value of P_{cD} amongst the candidate spheres is the one chosen to fill with drying fluid.

Once the drying process is completed, in the case that the user chooses to start an analysis from wet conditions, the cell is then subjected to wetting. During wetting, a similar process to the one previously described is performed. At each of a total of $m-2m_{\text{seed}}$ sphere filling event all the spheres of the network are checked to see whether they are candidates to be the next one for filling with wetting fluid. This check requires the sphere to be currently filled with drying fluid (flag $= 1$) and for it to be connected to a wetting fluid filled neighbour ($N_{\text{wn}} > 0$). For each individual sphere filling event, the sphere that fulfils the aforementioned criteria and has the highest P_{cW} value is the one that fills with wetting fluid.

At each step of the analysis, the user is able to determine the increment of capillary suction of the transport network. The value of capillary suction resulting from the chosen increment at an arbitrary step $(h+1)$ of the analysis is denoted as $P_{\text{c}}^{\text{T}(h+1)}$ which will be referred from now on as target capillary suction. For a fluid configuration resulting from the previous step (h), the wetting fluid filled sphere with the lowest drying capillary suction P_{cD} value and connected to a drying fluid filled one, determines the value P_{cDmin}. Also, at the same step, the drying fluid filled sphere with the highest wetting capillary suction value P_{cW} and connected to a wetting fluid filled sphere determines the value max P_{cWmax}. For the configuration to be stable, the relation below should hold

$$P_{\text{cWmax}} < P_{\text{c}}^{\text{T}(h+1)} < P_{\text{cDmin}} \tag{3.82}$$

When (3.82) holds, no filling of spheres with drying or wetting fluid occurs. However, when (3.82) does not hold, a new configuration should be searched until (3.82) is fulfilled. When $P_{\text{c}}^{\text{T}(h+1)} < P_{\text{cWmax}}$ the drying fluid filled sphere with $P_{\text{cW}} = P_{\text{cWmax}}$ is subjected to drying. After this sphere filling with wetting fluid, a new P_{cWmax} value is evaluated since the sphere for which its $P_{\text{cW}} = P_{\text{cWmax}}$ is now filled with wetting fluid. Similarly, when $P_{\text{cDmin}} < P_{\text{c}}^{\text{T}(h+1)}$ a sphere is subjected to wetting and a new P_{cDmin} is found. After each filling with wetting or drying fluid of a sphere, (3.82) is checked once more. If (3.82) is not fulfilled, another sphere is chosen to be filled with wetting fluid for $P_{\text{c}}^{\text{T}(h+1)} < P_{\text{cWmax}}$ or drying fluid for $P_{\text{cDmin}} < P_{\text{c}}^{\text{T}(h+1)}$. Therefore, for a given $P^{\text{T}(h+1)}$, more than one sphere changes can occur.

The description of the above process assumes that $P_{\text{cWmax}} < P_{\text{cWmin}}$ and also that a configuration that fulfils (3.82) can be found. However, due to the random assignment of spheres and pipes, both statements might not hold at a step $(h+1)$. For resolving these problems different rules are applied to determine the configuration at step $(h+1)$.

When $P_{\text{cDmin}} < P_{\text{cWmax}}$ the type of fluid filling of spheres in the network is the same as the last one performed in the previous trial sphere filling. In the case that the previous trial involved a sphere filling with wetting fluid, the next sphere filling will be with wetting fluid as well.

Reverse arguments apply if the previous trial involved a sphere filling with drying fluid. If the very first configuration search at step $(h+1)$ involves the condition $P_{\text{cDmin}} < P_{\text{cWmax}}$, then the choice of the fluid that is intruding is the same as that done for the last sphere that was filled in the previous step (h).

Another issue that might arise is that of having configurations that repeat at the same step $(h+1)$ i.e. the pair of spheres that correspond to P_{cWmax} and P_{cDmin} repeat throughout a configuration search. In this case the search of the configuration would infinitely continue without fulfilling (3.82). Hence, when a configuration is reached for the second time, the search is stopped.

All aforementioned rules for finding the fluid configuration for a target capillary suction is presented in pseudo code in Algorithm 1.

3.8.3 Mechanical

The stress-strain law is defined as

$$\boldsymbol{\sigma}^{(h)} = \mathbf{D}_{\text{el}}(\boldsymbol{\varepsilon}^{(h)} - \boldsymbol{\varepsilon}_{\text{p}}{}^{(h)}) \tag{3.83}$$

and the yielding function is (3.50), presented in Section 3.5.4.

To solve the mechanical analysis, the displacement method is implemented. At the h-th step of the analysis, trial nodal displacements are applied to a mechanical element that correspond to a total strain $\varepsilon^{(h)}$ and the internal stresses must be evaluated. Initially, a trial stress is evaluated as $\boldsymbol{\sigma}^{(tr)} = \mathbf{D}_{\text{el}}(\boldsymbol{\varepsilon}^{(h)} - \boldsymbol{\varepsilon}_{\text{p}}^{(h-1)})$ where $\mathbf{D}_{\text{el}}$ is the elastic stiffness tensor and $\boldsymbol{\varepsilon}_{\text{p}}$ is the vector of plastic strains evaluated at the previous step of the analysis. When the trial stress violates the yield condition i.e. $f(\boldsymbol{\sigma}^{(tr)}) > 0$ then plastic flow is exhibited. The term trial is used because it is unknown if plastic flow occurs during the initial nodal displacements. If that is the case, the plastic strains must be evaluated and the trial stress should be adjusted so that the element stress vector is admissible. In this work, the evolution of plastic strains is governed by an associated flow rule in the form of (3.51), presented in Section 3.5.4.

The flow rule in a discrete form is

$$\boldsymbol{\varepsilon}_{\text{p}}^{(h)} - \boldsymbol{\varepsilon}_{\text{p}}{}^{(h-1)} = \Delta\lambda^{(h)} \boldsymbol{f}_{\boldsymbol{\sigma}} \tag{3.84}$$

Algorithm 1. Stable fluid configuration algorithm.

1. for number of spheres = 1, 2, ... m
2. find P_{cDmin} and P_{cWmax}
3. **if** $P_{\text{cWmax}} < P_{\text{c}}^{\text{T}(h+1)} < P_{\text{cDmax}}$
4. Exit
5. **else**
6. **if** the spheres that determine P_{cDmin} and P_{cWmax} have already been checked before in the current configuration search
7. Exit
8. **else**
9. **if** $P_{\text{cWmax}} < P_{\text{cDmin}}$
10. **if** $P_{\text{c}}^{\text{T}(h+1)} < P^{\text{W}}$
11. go to 17.
12. **else**
13. go to 14.
14. **end**
15. **else**
16. **if** previous sphere that was filled with fluid that the drying one **then**
17. go to 14.
18. **else**
19. go to 17.
20. **end**.
21. **end**
21. **end**
21. **end**
22. Perform drying of the most critical sphere
23. **if** $m_{\text{w}} = m_{\text{seed}}$
24. Exit
25. **else**
26. go to 1.
27. **end**
28. Perform wetting of the most critical sphere
29. **if** $m - m_{\text{w}} = m_{\text{seed}}$
30. Exit
31. **else**
32. go to 1.
33. **end**

When plastic flow occurs at the current step the stress conditions can be evaluated by substituting (3.84) in (3.83), which results in

$$\boldsymbol{\sigma}^{(h)} = \mathbf{D}_{\text{el}}(\boldsymbol{\varepsilon}^{(h)} - \boldsymbol{\varepsilon}_{\text{p}}{}^{(h-1)}) - \Delta\lambda^{(h)}\mathbf{D}_{\text{el}}\boldsymbol{f}_{\boldsymbol{\sigma}} \tag{3.85}$$

and then by substituting the trial stress in the first term of the right hand side of (3.85) and readjusting

$$\boldsymbol{\sigma}^{(h)} + \Delta\lambda^{(h)}\mathbf{D}_{\text{el}}\boldsymbol{f}_{\boldsymbol{\sigma}} = \boldsymbol{\sigma}^{(tr)} \tag{3.86}$$

where $\boldsymbol{\sigma}^{(tr)}$ is the trial stress vector evaluated as

$$\boldsymbol{\sigma}^{(tr)} = \mathbf{D}_{\text{el}}(\boldsymbol{\varepsilon}^{(h)} - \boldsymbol{\varepsilon}_{\text{p}}{}^{(h-1)}) \tag{3.87}$$

(3.86) and (3.50) must be fulfilled simultaneously. When the yield function is non-linear a Newton-Raphson algorithm must be applied to solve the non-linear set of equations. This is not necessary for the present model. Therefore, the plastic multiplier can be evaluated at once as

$$\Delta\lambda^{(h)} = \frac{\boldsymbol{f}_{\boldsymbol{\sigma}}^{T}\boldsymbol{\sigma}^{(tr)}}{\boldsymbol{f}_{\boldsymbol{\sigma}}^{T}\mathbf{D}_{\text{el}}\boldsymbol{f}_{\boldsymbol{\sigma}}} \tag{3.88}$$

and

$$\boldsymbol{\sigma}^{(h)} = \boldsymbol{\sigma}^{(tr)} - \Delta\lambda^{(h)}\mathbf{D}_{\text{el}}\boldsymbol{f}_{\boldsymbol{\sigma}} \tag{3.89}$$

It can be observed that for this simple constitutive model the trial stress is returned onto the plastic surface along the direction of the $\mathbf{D}_{\text{el}}\boldsymbol{f}_{\boldsymbol{\sigma}}$ vector.

An additional case of stress conditions must be examined. In Figure 3.12, the vector resulting from the multiplication of $\boldsymbol{f}_{\boldsymbol{\sigma}}$ and the stiffness matrix $\mathbf{D}_{\text{el}}$ at $\sigma_{\hat{n}} = 0$ is presented as $\mathbf{D}_{\text{el}}(\boldsymbol{f}_{\boldsymbol{\sigma}})_{\sigma_{\hat{n}}=0}$. In case $\boldsymbol{\sigma}^{(tr)}$ lies on the semi-infinite plane enclosed in the acute angle between axis $\sigma_{\hat{n}}$ and the vector $\mathbf{D}_{\text{el}}(\boldsymbol{f}_{\boldsymbol{\sigma}})_{\sigma_{\hat{n}}=0}$ the above algorithm cannot be used to evaluate the stress according to (3.89). To solve this issue, the stresses are returned to the origin and the strain

increment is considered to be fully plastic and is added to the plastic vector. This case is known as vertex return (Grassl and Jirásek, 2006).

3.8.4 Coupled approach

A staggered approach is used to solve the coupled hydro-mechanical problem. Throughout an analysis, the transport and mechanical models are solved separately. At the beginning of each step, each of the two models receives the required information from the other model. For instance, at step number $h+1$ the mechanical model accesses the required coupling information from the transport model solution at step h. Based on this, the mechanical model is then solved. The transport model is solved in the same manner. The two models continue to exchange information until the analysis is completed. A schematic representation of the staggered approach is presented in Figure 3.21. The information passed to the mechanical and transport models are presented with black and grey arrows, respectively.

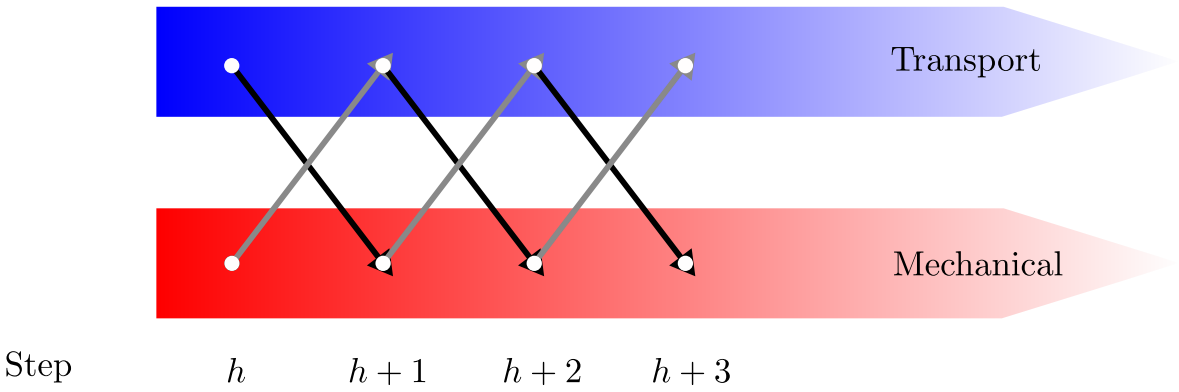

Figure 3.21: Staggered solution: at a step of an analysis, each problem is solved based on the previous step results of its dual one.

For the transport model, at the beginning of a new step each element receives the normal plastic strain of each mechanical element that surrounds it. Thereafter, the radius of each pipe element is evaluated according to (3.69), as described in Section 3.6.3 . Then, the new configuration of the fluids is identified according to the process described in Section 3.8.2 and the transport problem is then solved separately to the mechanical one. The pipes that possess surrounding mechanical elements with one or both nodes located outside the cell boundaries receive the information from elements with both nodes located in the interior of the cell as described in Section 3.7.4.

Similarly, the mechanical model receives information describing the configuration of the fluids from the transport model from the previous step. Then, a search is performed for the fluid filling the spheres surrounding each mechanical element. Subsequently, a force is added

to the mechanical elements that are solely surrounded by air filled spheres according to (3.66), to represent the influence of a meniscus water bridge (see Section 3.6.2).

Chapter 4

Model verification

4.1 Transport model

The transport model has been developed to compute the conductivity and fluid retention of a geomaterial containing a network of voids. The verification of the correct implementation for the evaluation of these two quantities is presented in this section. Initially the conductivity results are verified for saturated conditions by comparing network model results for a regular network of pipes of equal length and cross-sectional area to corresponding analytical results. Then, the evaluation of retention curve was verified for the case study of random networks containing spheres of single size and pipes of single size.

4.1.1 Conductivity

An analytical solution for the arrangement of pipes with equal radii placed along the edges of a Kelvin cell is presented. A Kelvin cell is the polyhedron obtained from a Voronoi tessellation dual to a Delaunay Body Centred Cubic (BBC) arrangement as presented in Figure 4.1. The edge length of the BCC is denoted as l_{BCC}. The centroid of the cell is indicated by the open circle. This network is part of an infinite arrangement of identical cells.

In general, the average conductivity of a cell k_{CELL} can be determined from

$$q_{\text{CELL}} = k_{\text{CELL}} \frac{\Delta p_{\text{f}}}{l_{\text{CELL}}} \tag{4.1}$$

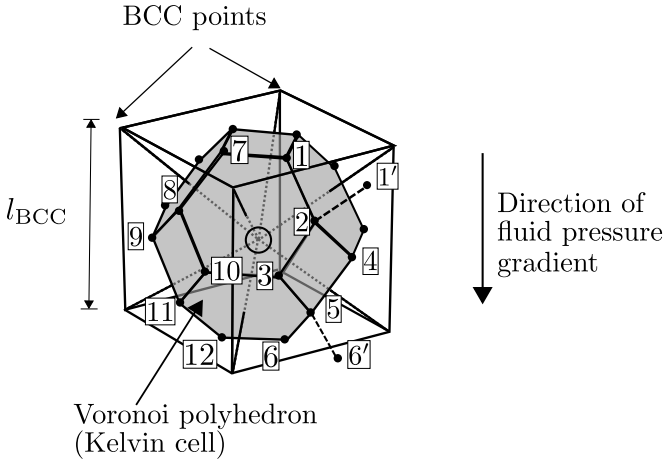

Figure 4.1: Body Centred Cubic cell of edge length l_{BCC} and its enclosed Kelvin cell.

Table 4.1: Standard physical input parameters.

Physical parameters	Value	Units	Reference
Liquid water density ρ	1000	kg/m^3	Daugherty and Franzini (1977)
Saturated gas fluid density ρ_0	0.01724	kg/m^3	Mayhew and Rogers (1976)
Dynamic viscosity μ	0.001002	Pa s	Daugherty and Franzini (1977)
Temperature T	293	K	Daugherty and Franzini (1977)
Gas universal constant R	8.314	J/mol/K	Daugherty and Franzini (1977)
Gas molecular weight M	0.018	kg/mol	Daugherty and Franzini (1977)
Surface tension γ	0.072	N/m	Daugherty and Franzini (1977)
Water molecular diffusivity D_{v}	2.3×10^{-5}	m^2/s	Haghi (2003)
Contact angle θ	0	$^\circ$	Delage (2005)

where $\Delta p_{\mathrm{f}}/l_{\mathrm{CELL}}$ [kg m^{-2} s^{-2}] is a pressure gradient applied across the cell between two opposite cell faces, q_{CELL} [kg m^{-2} s^{-1}] is the mass flow rate per unit area in the direction of the applied pressure gradient and k_{CELL} [s] is the conductivity of the cell. In this case, l_{CELL} corresponds to l_{BCC}.

For all transport analyses in the present verification chapter the physical parameters were chosen according to Table 4.1, except that $\gamma = 1$ N/m was used for the value of surface tension. In addition, the input parameters for the pipe radii distribution were $\mathrm{COV}^{\mathrm{p}} = 0$ and $r_{\mathrm{pm}} = 10^{-6}$ m. When $\mathrm{COV}^{\mathrm{p}} = 0$, all pipes have the same radius, hence they all have the same conductivity k_{pipe} (see (3.19)).

Due to the specific network geometry all element lengths are equal and all elements were chosen to have equal radii creating an isotropic network. Furthermore, flow occurs only due to a gradient of capillary pressure. Hence, no flow occurs along pipe elements that are perpendicular to the direction of the pressure gradient because the fluid pressures at both ends of the pipe are equal. Consequently, the network is divided into four disconnected sub-networks which start from one face of the cell and end at the opposite face (where the normal to both of these faces is in direction of the pressure gradient). The pipes connecting

nodes 1, 2, 3, 4, 5 and 6 in Figure 4.1 form one such sub-network (spanning between nodes 1 and 6), with this sub-network shown in 2D form in Figure 4.2. The pipes connecting nodes 7, 8, 9, 10, 11 and 12 in Figure 4.1 form a second such sub-network. Note that those two sub-networks are effectively disconnected, because there is no flow along pipes 1-7, 3-10 or 6-12, because each of these three linking pipes is perpendicular to the applied gradient of fluid pressure.

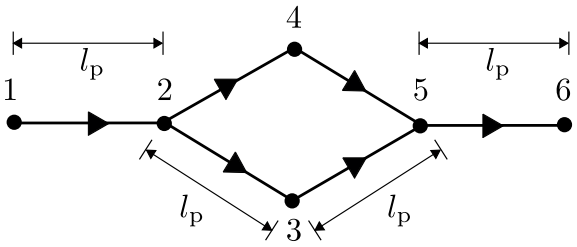

Figure 4.2: Equivalent pipe network: one of the two sub-networks shared with a neighbouring cell presented in a single plane of the continuum corresponding to one Voronoi polyhedron.

Pipes 1-2 and 5-6 in Figures 4.1 and 4.2 are only involved in carrying flow within the single sub-network involving nodes 1, 2, 3, 4, 5 and 6. However, pipes 2-3, 3-5, 2-4 and 4-5 lie on one of the side faces of the BCC cell shown in Figure 4.1, and these pipes also form part of the BCC cell. This partner sub-network, spanning between nodes 1' and 6' (see Figure 4.1) involves pipes connecting nodes 1', 2, 3, 4, 5 and 6'. Hence only half of the cross-sectional area of each of the pipes 2-3, 3-5, 2-4 and 4-5 is available for the flow carried by the first sub-network. As a consequence the mass flow rate Q within a single sub-network is given by

$$Q = Ak_{\mathrm{pipe}}\frac{P_6 - P_1}{4l_\mathrm{p}} \tag{4.2}$$

where A and k_{pipe} are the pipe element cross-sectional area and conductivity respectively and l_p is the length of individual pipe (all pipes forming the Kelvin cell are all of the same length). When the pipes are liquid filled the pipe conductivity is equal to k_ℓ and when they are gas filled it is equal to k_g according to (3.19) and (3.27), respectively.

With four sub-networks within each BCC cell, the total mass flow rate across the cell is given by $4Q$ and hence the flow rate per unit area of cell force q_{CELL} is given by

$$q_{\mathrm{CELL}} = \frac{4Q}{l_{\mathrm{BCC}}^2} = \frac{Ak_{\mathrm{pipe}}(P_6 - P_1)}{l_{\mathrm{BCC}}^2 l_\mathrm{p}} \tag{4.3}$$

Comparing (4.3) with (4.1) shows that the cell conductivity k_{CELL} is given by

$$k_{\mathrm{CELL}} = \frac{Ak_{\mathrm{pipe}}}{l_{\mathrm{BCC}} l_\mathrm{p}} \tag{4.4}$$

Note that the geometry of a Kelvin cell means that

$$l_{\mathrm{p}} = \frac{\sqrt{2}}{4} l_{\mathrm{BCC}} \tag{4.5}$$

For the present verification the BCC used has $l_{\mathrm{BCC}} = 7 \times 10^{-5}$ m that has a corresponding pipe element length $l_{\mathrm{p}} \approx 2.45 \times 10^{-5}$ m. The conductivities calculated by (4.4) are $k_{\mathrm{CELL}} = 2.28 \times 10^{-10}$ s when all pipes exhibit a liquid filled conductivity and 5.37×10^{-18} s when all pipes exhibit a gas filled conductivity. The same values were computed by the model. Therefore, the evaluation of the conductivity is correctly implemented for this type of regular network.

4.1.2 Fluid retention

The fluid retention aspect of the transport model was verified by performing analyses of random networks with all spheres of a single size and all pipes of a single size. This simple test was chosen to verify the correct implementation of the evaluation of the fluid retention network, as the model should predict emptying of all pores at a single value of capillary suction during a drying path and filling of all pores at a single (but different) value of capillary suction during wetting. The physical input parameters chosen in all cases are presented in Table 4.1 except the parameter of the surface tension that was chosen to be $\gamma = 1$ N/m.

The parameters defining the geometry of the random network, minimum distance of vertices d_{min}, the periodic cell edge length l_{CELL}, the number of spheres m and the number of seeding spheres m_{seed}, are presented in Table 4.2. The same geometry was used for all analyses. Three different combinations of pipe and sphere radii distribution were used (Table 4.3), referred to as cases a, b and c. The capillary suction values that correspond to the mean values of the pipe and sphere radii according to (3.12) are also presented in Table 4.3 denoted as $P_{\mathrm{c}}^{r_{\mathrm{pm}}}$ and $P_{\mathrm{c}}^{r_{\mathrm{sm}}}$, respectively.

The values presented in Tables 4.2 and 4.3 were chosen to present length scales at which capillary forces occur. However, they were chosen arbitrarily only for the verification of the fluid retention implementation since they do not match any specific material microstructure.

For all three cases, lognormal size distributions were used for both pipes and spheres, defined by the mean r_{m} and coefficient of variation COV, with $r_{\mathrm{pm}} \leq 0.1 r_{\mathrm{sm}}$. In all cases COV $= 0$ was taken for both spheres and pipes, meaning that all pipes were of a single radius (r_{pm}) and all spheres were of a single radius (r_{sm}). Each analysis began with all spheres filled with

Table 4.2: Random network input parameters.

	d_{min} [m]	l_{CELL} [m]	m	m_{seed}
Values	1.5×10^{-5}	1.05×10^{-4}	1436	14

Table 4.3: Transport model input parameters for three different cases.

Case	COV$^{\text{p}}$	COV$^{\text{s}}$	r_{pm} [m]	$P_{\text{c}}^{r_{\text{pm}}}$ [MPa]	r_{sm} [m]	$P_{\text{c}}^{r_{\text{sm}}}$ [MPa]
a			1×10^{-6}	2	1×10^{-5}	0.2
b	0	0	5×10^{-6}	0.4	5×10^{-5}	0.04
c			3×10^{-5}	0.0667	3×10^{-4}	0.00667

wetting fluid except for the dry seeding spheres, as explained in Section 3.8.2. Subsequently, the network was subjected to drying until all spheres were filled with the drying fluid except the wet seeding spheres. The network was then subjected to wetting until all spheres but the dry seeding ones were filled with wetting fluid. The number of dry and wet seeding spheres was chosen as 1% of the total number of spheres. Since the scaling approach presented in Section 3.4.4 was used, the values of degree of saturation in the results presented in this chapter vary between 0.01 and 0.99.

The results of the model simulations are presented in Figure 4.3. Since all pipes are of equal size, as capillary suction increases the full network will automatically dry (from $S_{\text{r}} = 0.99$ to $S_{\text{r}} = 0.01$ when the target suction passes the value $P_{\text{c}}^{r_{\text{pm}}}$ corresponding to the radius of the pipes. The same concept applies to the wetting process, with S_{r} increasing from 0.01 to 0.99 when the target capillary suction passes the value $P_{\text{c}}^{r_{\text{sm}}}$ corresponding to the radius of the spheres. During both drying and wetting, very small changes of target capillary suction were applied to the network, to capture the abrupt change in the degree of saturation S_{r} of the network. The results for the degree of saturation are presented in Figure 4.3. It can be observed that for each of the three cases the network results show complete drying and wetting at P_{c} values that correspond to the radii of the pipes and spheres as expected.

The above test indicates that the procedure for determining the configuration of wetting and drying fluids at a particular value of P_{c} (i.e. which spheres are filled with wetting fluid and which sphere are filled with drying fluid) presented in Section 3.8.2 is correctly implemented, since all spheres (except the seeding spheres) filled or emptied at the expected values target capillary suction. This means that the process of filling or emptying spheres does not stop at the first sphere that has to fill or empty but it continues until a stable configuration is found (or until only seeding spheres remain). Also the values of P_{c} at which all spheres filled or emptied for a wetting path or a drying path were equal to those corresponding to r_{pm} and r_{sm}, respectively. This behaviour, was observed for all input cases. Therefore the correct implementation of the retention evaluation of the network was verified.

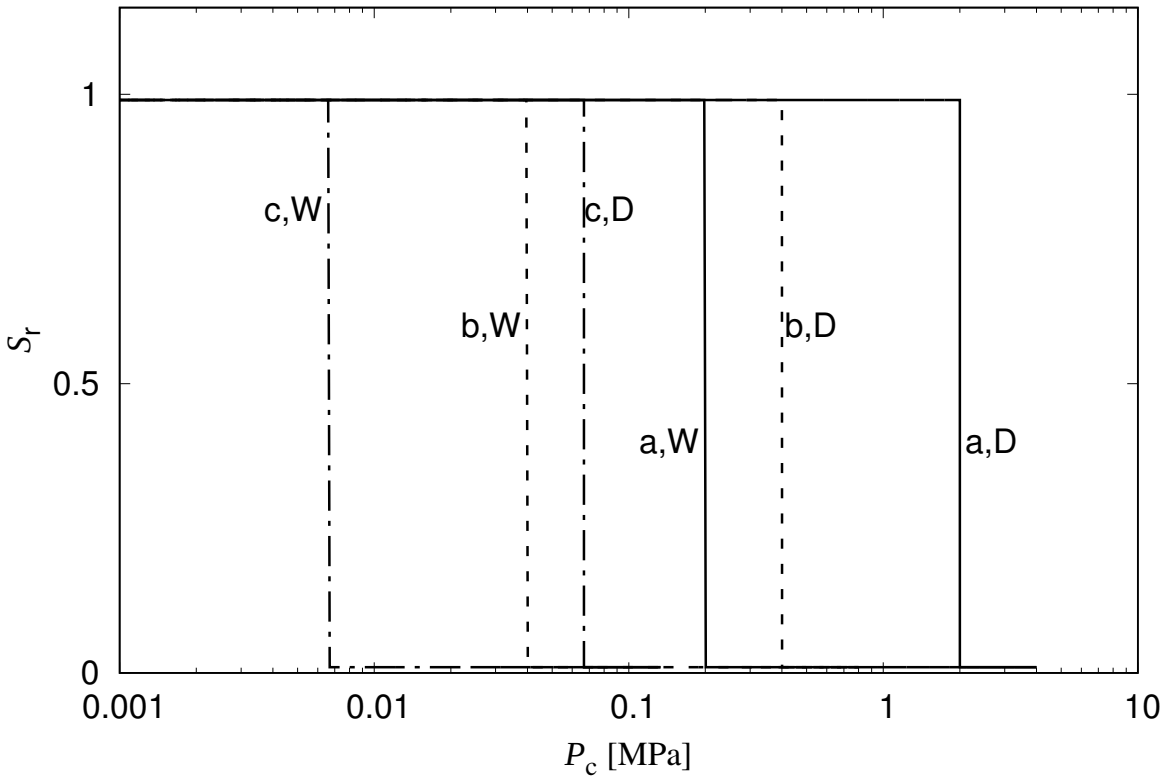

Figure 4.3: Verification of fluid retention: degree of saturation of wetting fluid S_r versus suction P_c. Here, D refers to drying and W to wetting.

4.2 Mechanical model

The elastic and plastic behaviour of the mechanical model was verified through comparison of the numerical results with analytical solutions for Face Centred Cubic (FCC) cell structures (see Figure 4.4) of identical spherical particles presented in the literature (Wang and Mora, 2008; Thornton, 1979). These comparisons verified the correct implementation of the new 3D periodic and non periodic lattice elements and the friction law.

4.2.1 Elastic behaviour

The elastic behaviour of the model was verified by comparing the numerical results to the analytical expressions in Wang and Mora (2008) for an FCC arrangement of identical rigid spheres with contacts represented by linear springs. The analytical expressions for the macroscopic elastic moduli of the FCC arrangements were deduced by Wang and Mora (2008) by differentiating with respect to each strain the elastic strain energy density stored in the elementary arrangement of sphere for an FCC structure formed by periodically repeating a basic FCC cell.

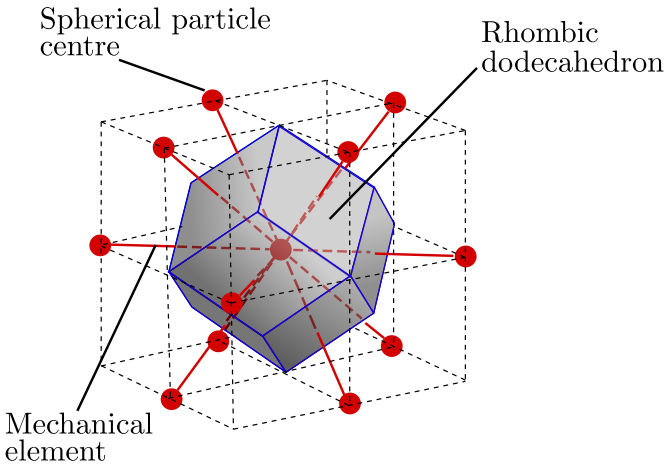

Figure 4.4: Rhobic dodecahedron presented in grey: result of the Voronoi tessellation of an FCC structure presented with red lines and filled circles.

For an FCC structure, each spherical particle is in contact with twelve neighbours. If the domain is subjected to a dual Delaunay/Voronoi tessellation using the centres of the spherical particles as the Delaunay tetrahedra vertices, a Voronoi tessellation of rhombic dodecahedra is generated (Figure 4.4). These Voronoi polyhedra are regular with twelve equal faces. Therefore, each spherical particle is idealised by a rhombic dodecahedron. Each dodecahedron possesses a centroid that coincides with the centre of a spherical particle. The line elements that connect the centre of a spherical particle to the centres of the other particles that it is in contact with, are perpendicular to the dodecahedron faces. The contact point between two of the rigid spherical particles is that at the centre of the corresponding dodecahedron face and this dodecahedron face is tangential to both spherical particles. From the above tessellation, only the mechanical part was used for the verification (the transport elements that would lie along the dodecahedron edges were not used). The model described in Section 3.5 was used for the mechanical interaction between the neighbouring particles.

The analytical expressions proposed by Wang and Mora (2008) for the evaluation of the macroscopic elastic Young's modulus, shear modulus and Poisson's ratio of an FCC spherical structure were based on a specific choice of the orientation of the structure. Views of the FCC structure aligned with the chosen y, x and z axes are shown in Figure 4.5. It can be seen that the FCC structure appears the same whether viewed along x, y or z axes, but it would, for example, appear different if viewed at 45 ^{o} to the x and y axes. Hence, this is an anisotropic structure. The FCC structure is known to have "cubic anisotropy" such that it has 3 independent elastic contacts (rather than the two independent constant of an isotropic elastic material).

The expressions proposed by Wang and Mora (2008) relate the macroscopic Young's modulus E_{macro}, macroscopic Poisson's ratio ν_{macro} and macroscopic shear modulus G_{macro} to the element length l_{e}, element cross-section area A_{mech} (where $A_{\text{mech}} = \pi r_{mech}^2$), element normal modulus E and ratio γ_1 of element tangent modulus to element normal modulus

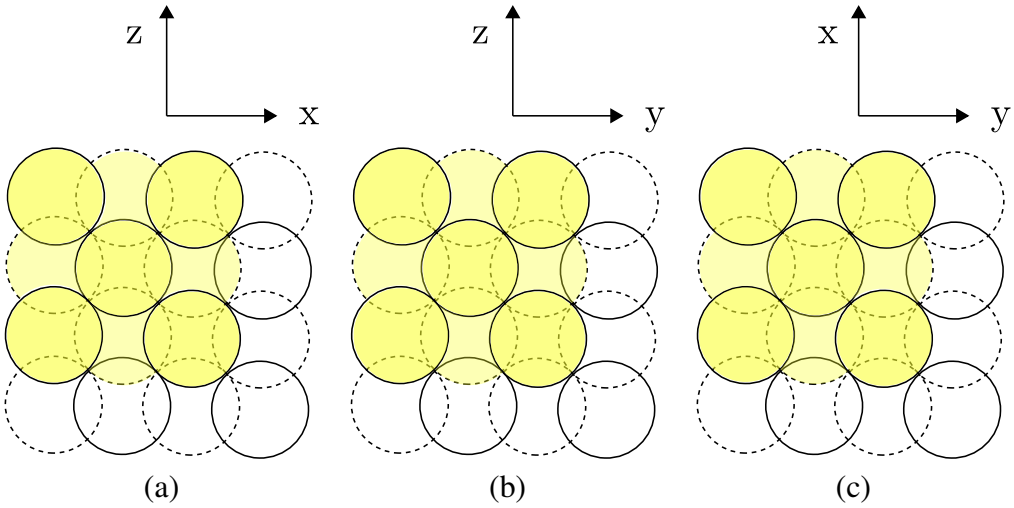

Figure 4.5: Views of the FCC structure along the chosen Cartesian global axes used for the analytical solution presented in Wang and Mora (2008): (a) along y, (b) along x and (c) along z.

$$E_{\text{macro}} = \frac{2\sqrt{2}EA_{\text{mech}}(1+3\gamma_1)}{l_{\text{e}}^2(3+\gamma_1)},\ \nu_{\text{macro}} = \frac{1-\gamma_1}{3+\gamma_1},\ G_{\text{macro}} = \frac{\sqrt{2}EA_{\text{mech}}(1+\gamma_1)}{2l_{\text{e}}^2} \tag{4.6}$$

The chosen global axes and part of an infinite 3D FCC arrangement of spherical particles are presented in Figure 4.6a. Given the anisotropic nature of the FCC structure, it is important to note that the macroscopic elastic moduli given in (4.6) refer to the x, y and z axes, so that $E_{\text{macro}} = E_{\text{xx}} = E_{\text{yy}} = E_{\text{zz}}$, $\nu_{\text{macro}} = \nu_{\text{xy}} = \nu_{\text{yz}} = \nu_{\text{zx}}$ and $G_{\text{macro}} = G_{\text{xy}} = G_{\text{yz}} = G_{\text{zx}}$. Symbols E_{xx}, E_{yy} and E_{zz} are the Young's moduli of the FCC structure corresponding to normal loading on the x, y and z directions respectively, for the given orientation of the structure, not to be confused with the average strains E_{x}, E_{y} and E_{z} presented in (3.76). In order to choose the smallest unit cell configuration that is periodic and aligned with the chosen axes, cut spheres must be taken into account, as shown in Figure 4.6b, which shows a periodic cell consisting of sphere segments. The black lines represent the edges of the fictitious boundaries of the periodic cell. The small black spheres represent the centres of the spherical particles presented in grey colour. All spherical particles are cut. The spheres with their centres on the faces of the periodic cell are half spheres, whereas those with their centres on the vertices of the periodic cell are an eighth of a spherical particle. When the cell is repeated in all directions, it forms an infinite FCC structure.

The mechanical elements used in the present model represent the contacts between the spherical particles. The resulting network is presented in Figure 4.7. The green lines represent the elements which lie on the faces of the periodic cell and the pink lines are the element which lie within the cell volume. The element nodes are presented with black spheres. In evaluating the stiffness matrix and internal forces in the mechanical lattice model, the volume

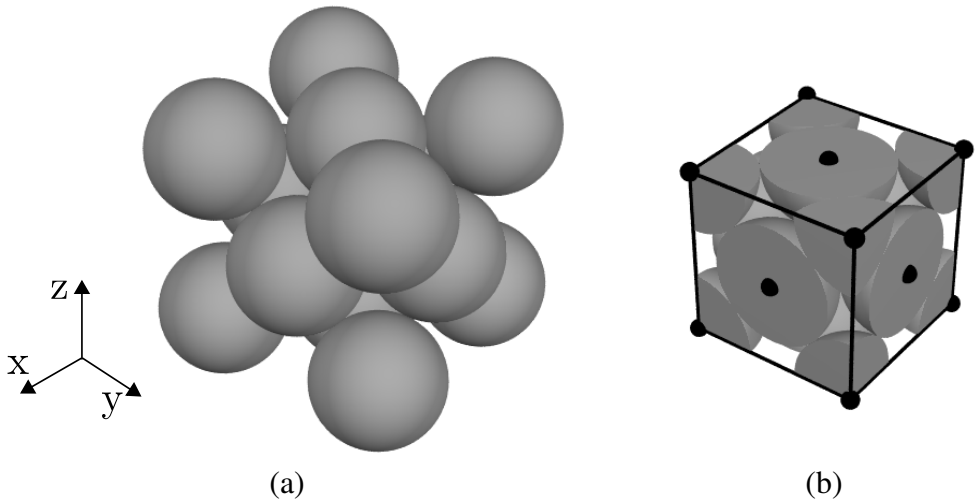

Figure 4.6: 3D FCC arrangement: (a) global axes and 3D FCC arrangement of spherical particles for verification of the elastic model and (b) periodic cell for the FCC structure.

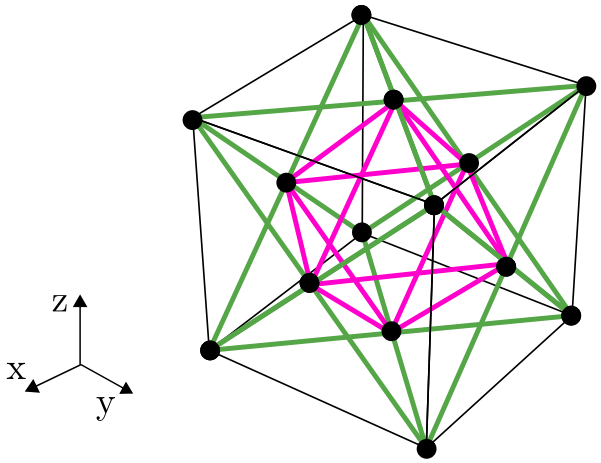

Figure 4.7: FCC periodic cell: the green lines represent the lattice elements which lie on the periodic cell faces and pink lines represent the lattice elements which lie within the periodic cell value by Wang and Mora (2008).

of elements that lie on the faces of the periodic cell are halved, as described in Section 3.7.3.

The input parameters used for all the mechanical verifications are presented in Table 4.4. The parameter values are not chosen to reproduce any material behaviour but rather to compare numerical and analytical results. The element length was chosen to produce a periodic cell with edge length of 1 m. Also, the radius of the cross-sectional area was chosen to give to a cross-sectional area of 1 m^2. The tangent of the friction angle was used as input for the verification of the plastic model in Section 4.2.2. The formulae presented in (4.6) were developed by Wang and Mora (2008) based on the assumption of zero rotations of the spheres due to the uniform strains that are assumed. The application of the PBCs does not imply uniform strain across each periodic cell. Therefore, very high values of element rotational stiffnesses must be used in order to obtain zero rotations. Thus, γ_2 was set to a very high value (see Section 3.7.3).

Table 4.4: Input parameters for the mechanical verification

Parameters	E	γ_1	γ_2	l_e	r_{mech}	COV^{mech}	$\tan\phi$
Values	1	1	10^{+7}	$\sqrt{2}/2$	$\sqrt{1/\pi}$	0	0.3
Units	N/m^2			m	m		

For varying γ_1, E_{macro} and ν_{macro} were evaluated by subjecting the periodic cell to a normal strain ε_{xx}, with the cell free to strain in y and z directions with E_{macro} ν_{macro} then evaluated as

$$E_{\text{macro}} = \frac{\Delta\sigma_{\text{xx}}}{\varepsilon_{\text{xx}}} \tag{4.7}$$

and

$$\nu_{\text{macro}} = -\frac{\varepsilon_{\text{yy}}}{\varepsilon_{\text{xx}}} = -\frac{\varepsilon_{\text{zz}}}{\varepsilon_{\text{xx}}} \tag{4.8}$$

where $\Delta\sigma_{\text{xx}}$ is the normal stress increment in the x direction which is evaluated as the ratio of the average reaction force increment in the x direction at the global node (see Section 3.7.3) over total area of the cell face perpendicular to the x axes i.e. $0.5l_{\text{e}}^2$. Also, ε_{xx} is the normal strain evaluated as the ratio of the global nodal displacement in the x direction to the edge cell edge length parallel to x axis. Similar arguments apply for the evaluation of ε_{yy} and ε_{zz} where the global nodal displacement and cell edge that are considered parallel to the y and z, respectively. In all cases ε_{yy} and ε_{zz} were equal. The direction of the strains is along the axes of the coordinate system presented on Figure 4.7. Due to the symmetry of the structure, the results are irrespective of whether the strains were applied about x, y or z axes.

G_{macro} was then evaluated by applying a shear strain ε_{zx} with G_{macro} then given by

$$G_{\text{macro}} = \frac{\Delta\sigma_{\text{zx}}}{\varepsilon_{\text{zx}}} \tag{4.9}$$

where $\Delta\sigma_{\text{zx}}$ is the shear stress increment evaluated as the ratio of reaction force increment of the global node corresponding to an average shear strain E_{zx} (see (3.76) in Section 3.7.3) over the average shear strain $\varepsilon_{\text{zx}} = E_{\text{zx}}$ that is evaluated as the ratio of the global node displacement related to the average strain E_{zx} over the cell edge length that is parallel to z axis.

The comparison of numerical and analytical results for E_{macro}/E, ν_{macro} and G_{macro}/E are presented in Figures 4.8, 4.9 and 4.10, respectively. It can be observed that there is an exact match between numerical and analytical results for all the macroscopic properties.

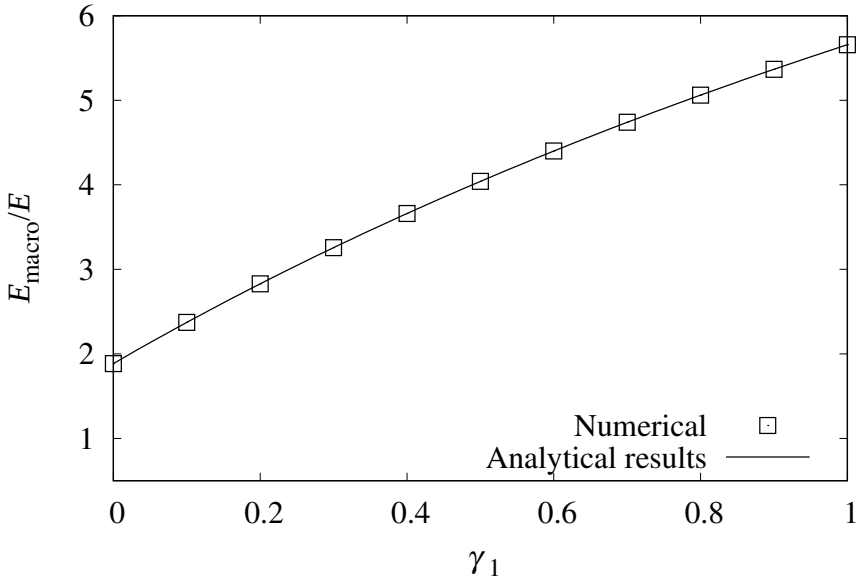

Figure 4.8: Comparison of the numerical to the analytical results: ratio of macroscopic Young's modulus to element normal modulus E_{macro}/E versus ratio γ_1 of element tangent modulus to element normal modulus.

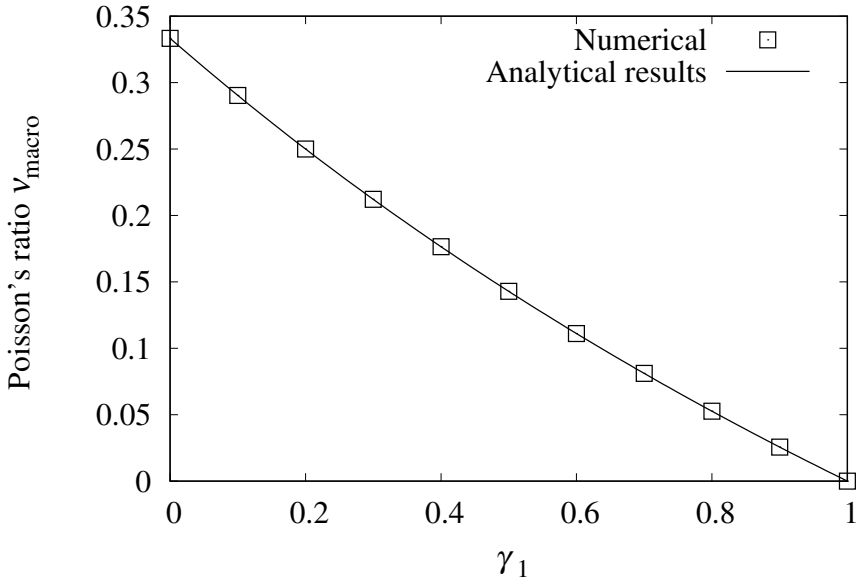

Figure 4.9: Comparison of the numerical to the analytical results: macroscopic Poisson's ratio ν_{macro} versus the ratio γ_1 of element tangent modulus to element normal modulus.

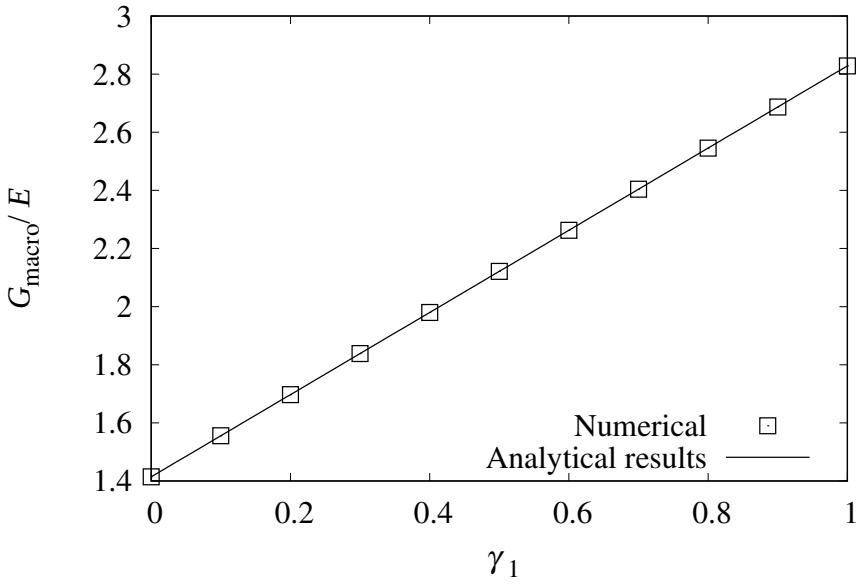

Figure 4.10: Comparison of the numerical to the analytical results: ratio of macroscopic shear modulus to element normal modulus G_{macro}/E versus the ratio γ_1 of element tangent modulus to element normal modulus.

In Wang and Mora (2008) the same comparisons for E_{macro}/E and ν_{macro} with results of classical DEM simulations of an FCC structure of equally sized spheres were presented. Neumann boundary conditions were used and more than 2500 spheres were required to obtain a good match between numerical and analytical results. Due to the Periodic Boundary Conditions developed in the present work, only 8 nodes are required to obtain an exact match. Furthermore, this is the first time that a comparison of numerical to analytical G_{macro} results were presented in the literature.

4.2.2 Plastic behaviour

Plastic behaviour was verified by comparing the numerical results with the analytical solution for the failure of FCC structures of identical spherical particles under triaxial conditions in Thornton (1979). The analytical solution is based on a different orientation of the FCC structure than for the elastic verification. The new orientation is obtained by rotating the global coordinate system presented in Figures 4.5 and 4.6 around the z axis by an angle of 45^o. Views of the FCC structure of spherical particles based on the new global axes orientation are presented in Figures 4.11a, b and c. It can be observed that the spherical particle arrangement is the same when viewed along the x and y axes but different when viewed along the z axis. All arrangements are different from those in Figure 4.5.

The chosen global axes and part of an infinite 3D arrangement of spherical particles are presented in Figure 4.12a, with the smallest unit cell configuration that is periodic and aligned

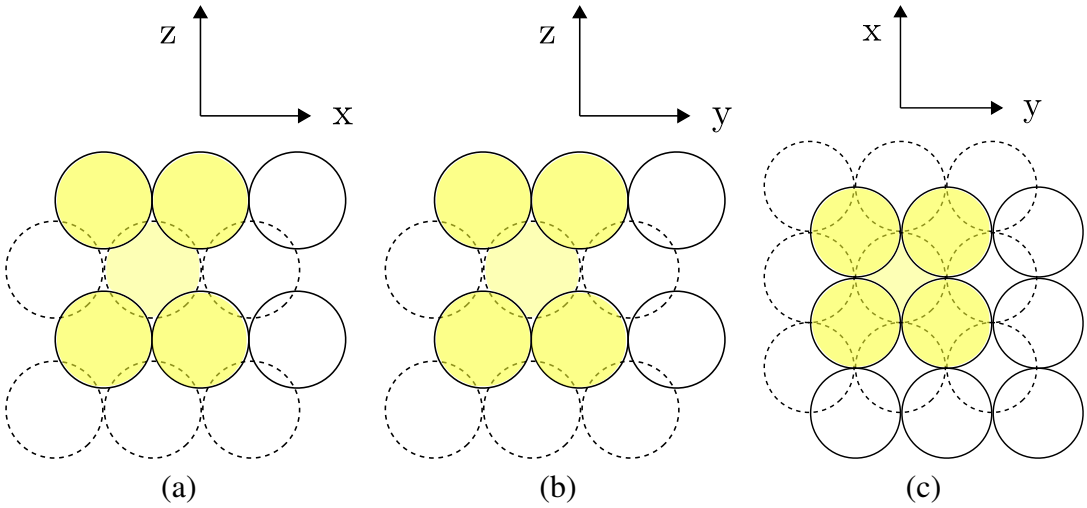

Figure 4.11: Views of the FCC structure along the chosen Cartesian global axes used for the analytical solution presented in Thornton (1979): (a) along y, (b) along x and (c) along z.

with the chosen axes shown in Figure 4.12b. This unit cell involves a central particle and eight segments of further spherical particles (each segment consisting of one eighth of sphere, each with its centre at a vertex of the unit cell). The four upper sphere segments are in contact with each other and with the central spherical particle but are not in contact with the four lower sphere segments. Hence, the cell is not cubic. The edges parallel to the x and y axis are equal to twice the spherical particle radius, whereas the edges parallel to the z axis are equal to $2\sqrt{2}$ times the spherical particle radius.

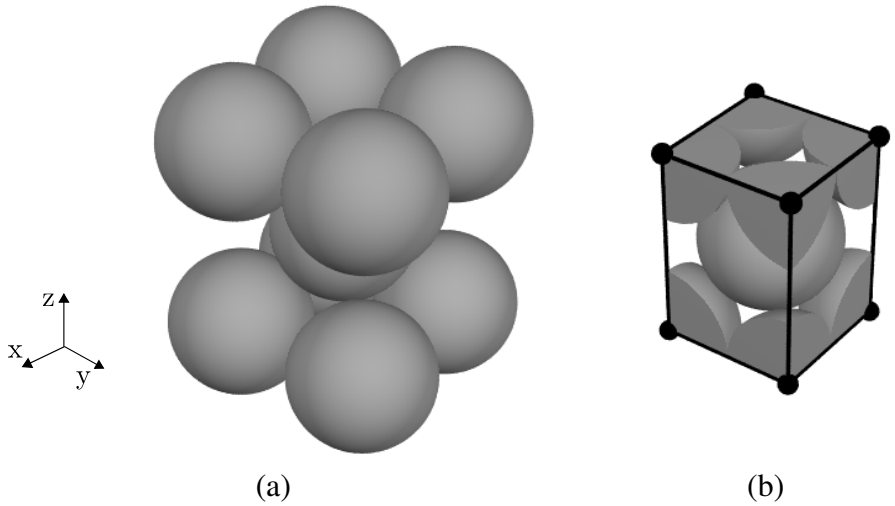

Figure 4.12: 3D FCC arrangement: (a) global axes and 3D FCC arrangement of spherical particles for verification of the plasticity model and (b) periodic cell for the FCC structure.

The corresponding periodic cell of the model is presented in Figure 4.13. The faces of the periodic cell are presented with a light grey colour in order to create a visual impression of the mechanical elements that cross these boundaries. The point at which the elements cross the boundaries are marked with a cross inscribed in a circle. These crossing elements represent the contacts that the central sphere shares with the central spheres in four adjacent periodic

cells. Since only one out of the two spheres that create the contact lies within the periodic cell, the volume of each of these four elements is halved when evaluating the stiffness matrix and internal forces in the mechanical lattice model. Furthermore, for the four mechanical elements joining the four upper vertices of the periodic cell and the four mechanical elements joining the four lower vertices of the cell, the volumes of each are quartered when evaluating the stiffness matrix and internal forces (because each of these elements is shared between four periodic cells). It can be observed from Figures 4.12 and 4.13 that a different cell structure than the one used in Figure 4.6 and 4.7 was constructed for the present choice of orientation of global axes.

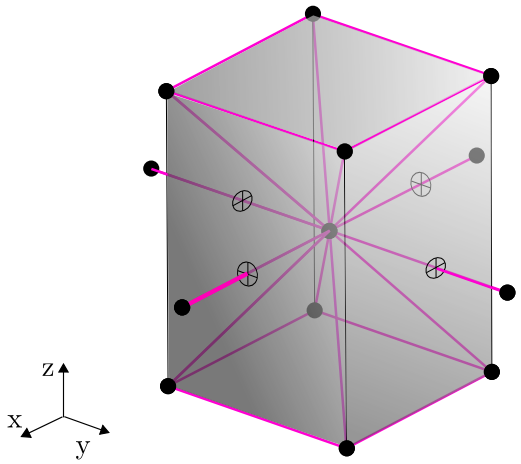

Figure 4.13: Periodic cell for verification of the plasticity model: the mechanical elements are presented in pink, the nodes with black discs and the cell faces in light grey.

The choice of the global axes is based on the orientation of the strain increment tensor applied during failure of the FCC spherical arrangement in Parkin (1965). This strain increment tensor applied by Parkin (1965) is given by

$$\mathrm{d}\boldsymbol{\varepsilon}_{\mathrm{macro}} = \begin{bmatrix} \mathrm{d}\varepsilon_{\mathrm{xx}} & \mathrm{d}\varepsilon_{\mathrm{xy}} & \mathrm{d}\varepsilon_{\mathrm{xz}} \\ \mathrm{d}\varepsilon_{\mathrm{yx}} & \mathrm{d}\varepsilon_{\mathrm{yy}} & \mathrm{d}\varepsilon_{\mathrm{yz}} \\ \mathrm{d}\varepsilon_{\mathrm{zx}} & \mathrm{d}\varepsilon_{\mathrm{zy}} & \mathrm{d}\varepsilon_{\mathrm{zz}} \end{bmatrix} = \begin{bmatrix} 2\psi & 0 & 0 \\ 0 & 2\mathrm{o} & 0 \\ 0 & 0 & -\psi - \mathrm{o} \end{bmatrix} \tag{4.10}$$

where $\mathrm{d}\boldsymbol{\varepsilon}_{\mathrm{macro}}$ is the strain increment tensor, $\boldsymbol{\varepsilon}_{\mathrm{macro}}$ is the macroscopic strain tensor of the cell and $\psi + \mathrm{o} = 1$. All the non zero terms are principal strains. The major principal is strain aligned with the z axis and is equal to a unit compressive strain $(\psi + \mathrm{o})$. Tensile strains are applied in both x and y directions and volumetric strain $(\mathrm{d}\varepsilon_{\mathrm{xx}} + \mathrm{d}\varepsilon_{\mathrm{yy}} + \mathrm{d}\varepsilon_{\mathrm{zz}})$ is +1 (unit tensile volumetric strain). Failure is defined as the case in which one of the contacts is lost. Yielding does not automatically lead to failure of the structure since plastic flow can occur while elements experience compressive stresses (see Figure 3.12) that means that contacts are preserved. At this point, the system of spheres exhibits a perfect plastic behaviour. Based on the incremental strain tensor the average macroscopic stress tensor of the cell was then

evaluated by Thornton (1979) under the assumption of perfectly rigid spheres and all contacts are located at the original FCC sphere configuration, i.e. no sliding nor elastic displacement occurred before failure. For the case that the incremental strain tensor at failure coincides with the average macroscopic stress tensor of the cell at failure, i.e. no shear stress is applied, the macroscopic stress tensor proposed by Thornton (1979) predicts failure at an infinite number of possible values of stresses at ratios of normal stresses as

$$\frac{\sigma_{zz}}{\sigma_{yy}} = \frac{-2 - 2\frac{(\psi + o)tan\phi}{\Theta}}{-1 + 2o\frac{tan\phi}{\Theta}} \tag{4.11}$$

and

$$\frac{\sigma_{xx}}{\sigma_{yy}} = \frac{-1 + 2\psi\frac{tan\phi}{\Theta}}{-1 + 2o\frac{tan\phi}{\Theta}} \tag{4.12}$$

where Θ is defined as

$$\Theta = \sqrt{\frac{3}{2}(\psi^2 + o^2) + \psi o} \tag{4.13}$$

The network geometry in Figure 4.13 and the input parameters in Table 4.4 were used for the verification of the mechanical model with plastic behaviour. The cell was analysed under two conditions. For transversely isotropic strain conditions $\psi = o = 0.5$ and the incremental strain tensor takes tha form

$$d\varepsilon_{macro} = \begin{bmatrix} 1 & 0 & 0 \\ 0 & 1 & 0 \\ 0 & 0 & -1 \end{bmatrix} \tag{4.14}$$

and for plane strain $\psi = 1$ and $o = 0$ and the incremental strain tensor takes the form

$$d\varepsilon_{macro} = \begin{bmatrix} 2 & 0 & 0 \\ 0 & 0 & 0 \\ 0 & 0 & -1 \end{bmatrix} \tag{4.15}$$

Table 4.5: Normal stress ratio during failure comparisons for the transversely isotropic strain case.

	Numerical	Analytical
σ_{zz}/σ_{yy}	3.7143	3.7143
σ_{xx}/σ_{yy}	1.0000	1.0000

Table 4.6: Normal stress ratio during failure comparisons for the plane strain case.

c	Numerical	Analytical
σ_{zz}/σ_{yy}	4.9063	4.8812
σ_{xx}/σ_{yy}	2.0064	1.9604

In each case, the cell was subjected to a combination of normal strains according to (4.10). The numerical results from the mechanical lattice model are compared to the analytical ones from Thornton (1979) from in the form of stress ratios in Tables 4.5 and 4.6 for transversely isotropic strain conditions and plane strain conditions, respectively.

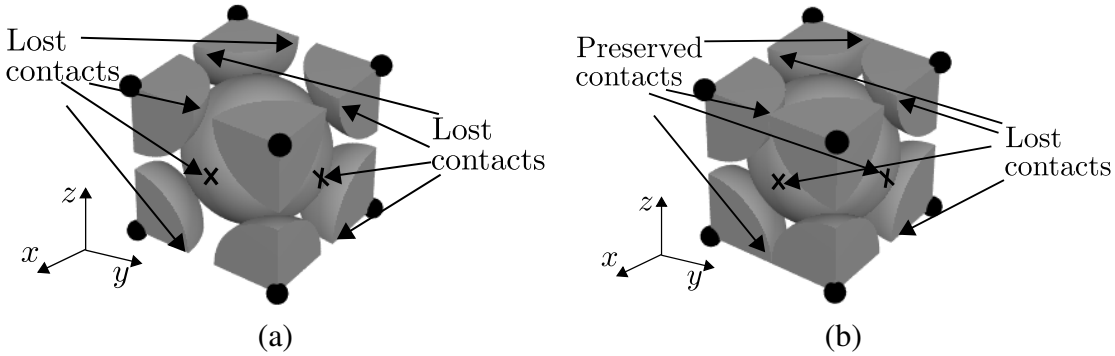

Figure 4.14: The failure mechanism of the FCC structure of spherical particles: (a) transversely isotropic strain case and (b) plane strain case.

4.3 Coupled model

The coupling of the transport and mechanical models was verified by two benchmarks. The first test demonstrates the correct implementation of the influence of the transport model on the mechanical response and the second one was used to verify the inverse effect. In both cases, a mechanical lattice corresponding to a cubic arrangement of equal spherical particles was used that has a dual cubic arrangement of pipes and spheres in the transport model. The input parameters for the mechanical part are presented in Table 4.4 and for the transport part the physical input parameters are presented in Table 4.1 and the pipe and sphere radii distribution inputs are in Table 4.3 for case a with $r_{pm} = 1 \times 10^{-6}$ m.

4.3.1 Influence of meniscus water bridges on macroscopic mechanical properties

A simple network was used to verify the correct implementation of the influence of the transport model on the mechanical model. A mechanical lattice corresponding to a cubic arrangement of equal spherical particles was used. The resulting transport network was also a cubic arrangement of spheres and pipes. A 3D representation of this dual cubic arrangement is presented in Figure 4.15a which is a part of an infinite arrangement. The dual cubic structure is a Voronoi/Delaunay tessellation when hexahedra are used instead of tetrahedra for the Delaunay tessellation.

Since all the spherical particles are identical, all the void arrangements throughout the structure are also identical. Therefore, in the transport model idealisation where the voids between the spherical particles are represented by spheres and the narrower throats are represented by pipes, all spheres have the same radius r_{sm} and all pipes have the same radius r_{pm} (the sphere radius is larger than the pipe radius). Hence, the infinite network can be reduced to a periodic cell such as the one presented in Figure 4.15b. The periodic cell consists of one spherical particle, twelve pipe elements and segments of eight spheres (voids). The pipe elements are placed along the edges of the periodic cell and only a quarter of their volume is taken into account in evaluating the conductivity matrix and the internal reaction flows. The spheres of the transport model are placed on the vertices of the periodic cell and only one eighth of their volume is taken into account in evaluating degree of saturation. The spherical particle interacts with six neighbouring spherical particles, through six mechanical contacts, one at each face of the cell. Since each contact is shared between two cells, the volumes of the six corresponding mechanical elements are halved when evaluating the stiffness matrix and the internal forces.

The equivalent dual network of a periodic cell is presented in Figure 4.16. The mechanical elements are presented with pink lines and their nodes with black discs. The transport elements are presented with blue lines and their nodes with green discs. The mechanical elements cross the boundaries of the periodic cell, having half their length outside the cell. Both transport and mechanical elements have a length equal to the length of the cell edges which is equal to twice the radius of the spherical particles.

For the verification exercise, the transport network was initially filled with wetting fluid. In the mechanical model, all strains were prescribed as zero as capillary suction P_{c} was varied. The mechanical elements used were elastic, therefore no detachment of a contact was observed upon tension. This is a special case for which there is no need of seeding spheres for drying and wetting.

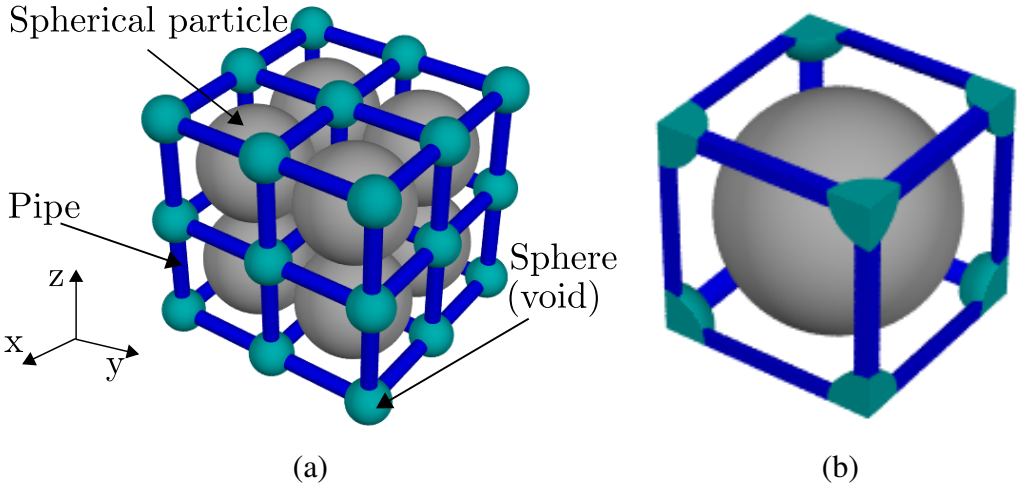

Figure 4.15: A cubic arrangement of spherical particles and their coupled surrounding pipes and spheres: (a) as part of an infinite structure and (b) the periodic cell of a cubic arrangement of spherical particles coupled to transport pipes and spheres.

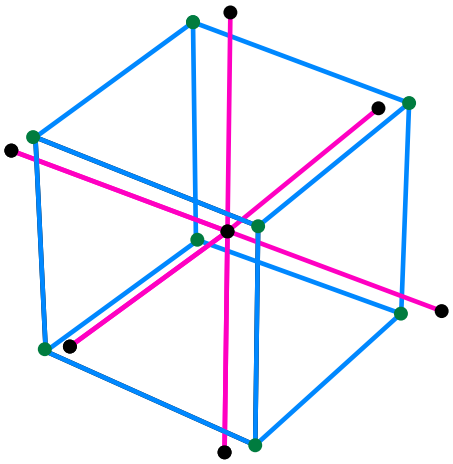

Figure 4.16: The periodic coupled cell: mechanical elements presented in pink and transport elements in blue.

The network was first subjected to a drying path. As capillary suction P_c increased, no additional force is exerted on the mechanical elements while the spheres remain filled with wetting fluid (this is a major assumption concerning the present model as previously explained in Section 3.6.2). When the magnitude of P_c reached a value corresponding to application of (3.12) with r as the radius of the pipe elements, all sphere segments are filled with drying fluid simultaneously. Beyond this point, an additional compressive force was applied to all particle contacts i.e. to every mechanical element, to represent the formation of meniscus water bridges at particle contacts as described in Section 3.6.2. The value of this force is $2\pi\gamma r_{\text{part}}$ as presented in Section 3.6, where r_{part} is the particle radius.

The change of the normal stresses ($\sigma_{xx} = \sigma_{yy} = \sigma_{zz}$) is presented in Figure 4.17. On the vertical axis, the normal stresses are presented as σ_{ii} (no summation). Hysteresis of the stress increase with suction change is observed as a consequence of the fluid retention hysteresis.

The expected stress variation is marked with a dashed line. Since the area of the cell is $4r_{\text{part}}^2$ and due to the strain restriction (all average strains of the cell were prescribed as zero) an increase of the cell normal stresses of a value of $0.5\pi\gamma/r_{\text{part}}$. The model results are equal to those predicted analytically.

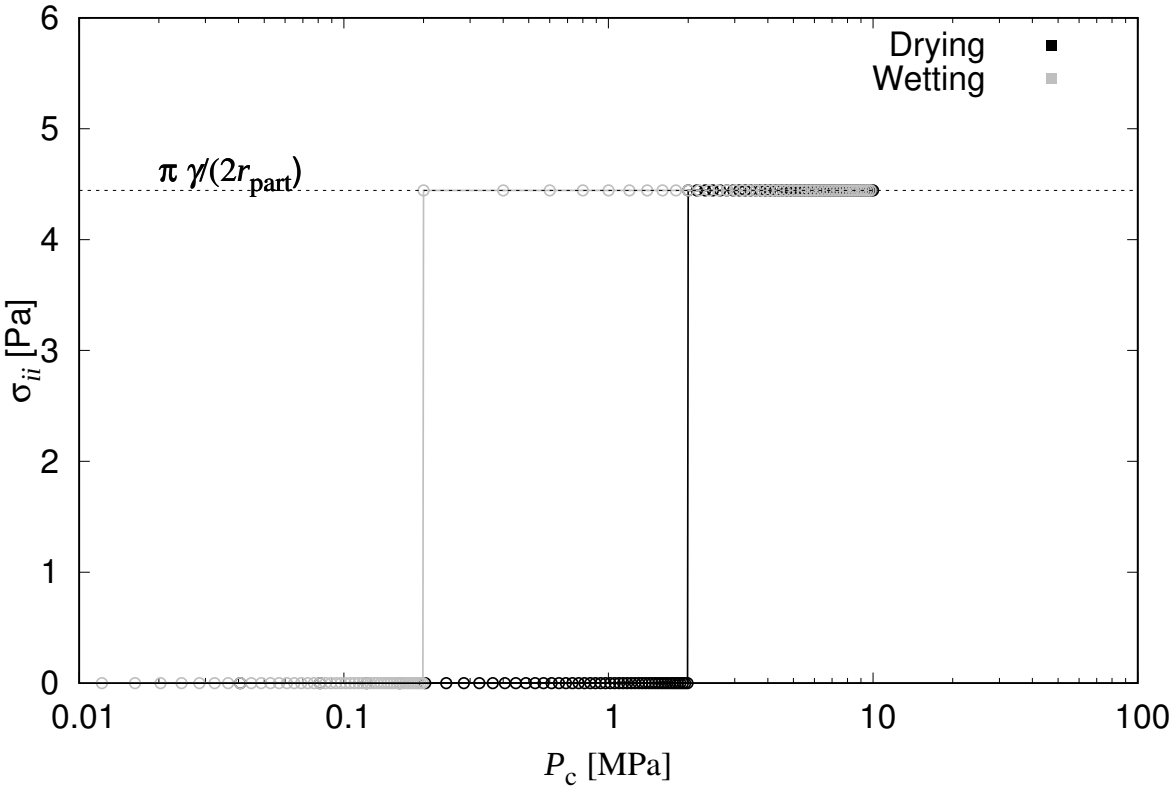

Figure 4.17: Influence of transport model on mechanical response for a periodic cubic arrangement subjected to a drying and wetting path: normal stress σ_{ii} versus capillary suction P_{c}.

Equivalent results of a similar test with arbitrary input parameters is schematically presented in Figure 4.18 in the case that the major assumption of the present model would not be considered, i.e. the fluid pressure is now considered to act on the particle and hence on the mechanical elements. Initially, the test cell is fully wet and subjected to 0 capillary suction P_{c} (point A in Figure 4.18). Then, the cell is subjected to a drying path by incrementally increasing P_{c} until all spheres are instantly filled with air (point B). Since air pressure is assumed to be 0, water pressure is equal to the capillary suction value. Hence, the cell normal stress σ_{ii} increases with P_{c} with an inclination of 45^o because all spheres and pipes surrounding the particle are filled with water and hence all water pressure is transmitted the mechanical elements. When P_{c} reaches a value that allows for air to enter spheres and a meniscus water bridge is generated, the extra force on the particle contacts due to its generation is $2\pi\gamma r_{\text{part}}$ as presented in Section 3.6. Furthermore, the effect of water pressure on the particles is terminated since now air fills the spheres and pipes where its pressure is assumed to be 0. Thereafter, σ_{ii} instantly increases to a value of $\pi\gamma/(2r_{\text{part}})$ (point C) as explained in the numerical results presented above in Figure 4.17. Capillary suction P_{c} is

then increased to point D and σ_{ii} is constant since the model assumes that the inter-particle force is constant once the meniscus water bridge is formed. Once reached point D, the cell is subjected to a wetting path by incrementally decreasing P_c. As long as the spheres are filled with drying fluid, σ_{ii} is constant as explained above. Once P_c reaches a value that allows water to enter the spheres (point E), σ_{ii} instantly decreases to a value where it is equal to P_c (point F). Similar to the numerical results presented in Figure 4.17, points E and F are on a lower P_c value than points B and C due to fluid retention hysteresis.

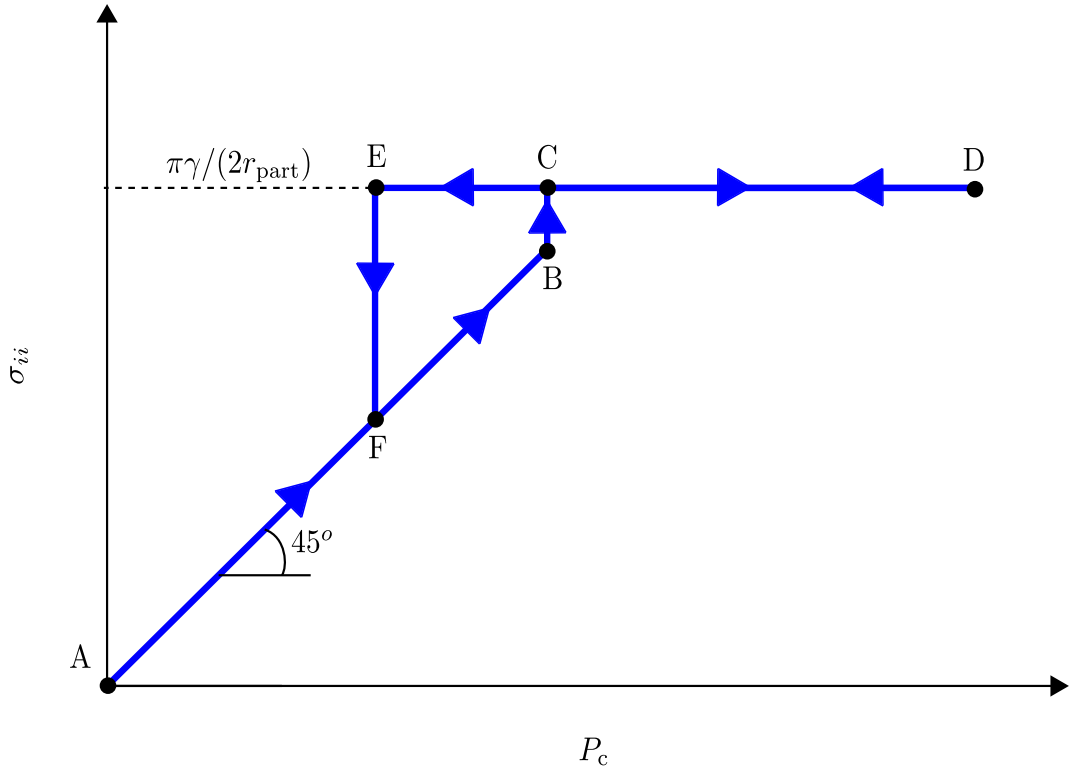

Figure 4.18: Schematic presentation of influence of transport on mechanical response when fluid pressure is considered to act on the particles: normal stress σ_{ii} versus capillary suction P_c.

It should be mentioned that there could be cases where the combination of surface tension, cell geometry and mechanical element normal modulus would result to an inter-particle force generated due to a meniscus water bridge formation that is less than P_c related to the sphere drying. In that case, points C, D and E would lie below the line of 45^o degrees and reverse arguments for the cell normal stress σ_{ii} change would apply, after filling the spheres with air.

4.3.2 Influence of plastic strains on macroscopic transport properties

For the verification of the influence of mechanical model on the transport network, the same cubic arrangement as the one in Figure 4.16 was used, with input parameters for

the mechanical and transport models given in Tables 4.4 and 4.3 case a, respectively. The mechanical material response used here was elasto-plastic. The capillary suction value applied on the cell was equal to zero so that the material remained saturated with wetting fluid. The mechanical cell was initially unloaded. The initial conductivity of the cell was determined in the network model from (4.1) the periodic cell conductivity k_{CELL} is related to the pipe conductivity k_{pipe} by

$$k_{\text{CELL}} = \frac{k_{\text{pipe}} A_{\text{pipe}}}{A_{\text{CELL}}} \tag{4.16}$$

For the initial case, where all spheres and pipes are filled with the wetting fluid, k_{pipe} is given by (3.19) and hence the predicted cell conductivity is given by

$$k_{\text{CELL}} = \frac{\rho}{\mu} \frac{r_{\text{p}}^4}{8 l_{\text{p}}^2} \tag{4.17}$$

Inserting the relevant values in (4.17), the predicted initial value of cell conductivity k_{cell} was 7.7×10^{-19} s, and this was exactly reproduced by the transport model.

At the next step of the analysis, a tensile strain of 0.1 was applied in the y direction of the global axes. This tensile strain produced a separation at the contacts represented by mechanical elements is parallel to the y axis. No shear occurred at the contacts and therefore the material exhibited only plastic flow in the normal (y) direction where the plastic strains were equal to the total strain. The only elements that exhibited plastic strains were those parallel to the y axis. Hence, the cross-sections of the transport elements parallel to the y axis were unaffected by the plastic strains, since all their surrounding mechanical elements were unstrained. The configurations of mechanical elements that surround a transport element parallel to the y axis, x axis and z axis are presented in Figures 4.19a, b and c, respectively. The pipe element cross-sections are presented with a light blue disc and the mechanical elements with pink colour. The transport elements that are affected by the mechanical changes are those that are not parallel to the y axis. For these transport elements parallel to the x and z axes two out of four surrounding mechanical elements exhibit plastic strains. Therefore, the new radius of the cross-section was evaluated using the procedure set out in Section 3.6.3

$$r_{\text{p}} = r_{\text{p0}} + \frac{1}{2\pi} \sum_{i=1}^{4} \varepsilon_{\hat{n}\text{p}i} l_{ei} \tag{4.18}$$

Equation (4.18) is slightly different to (3.69), given in Section 3.6.3 as the number of me-

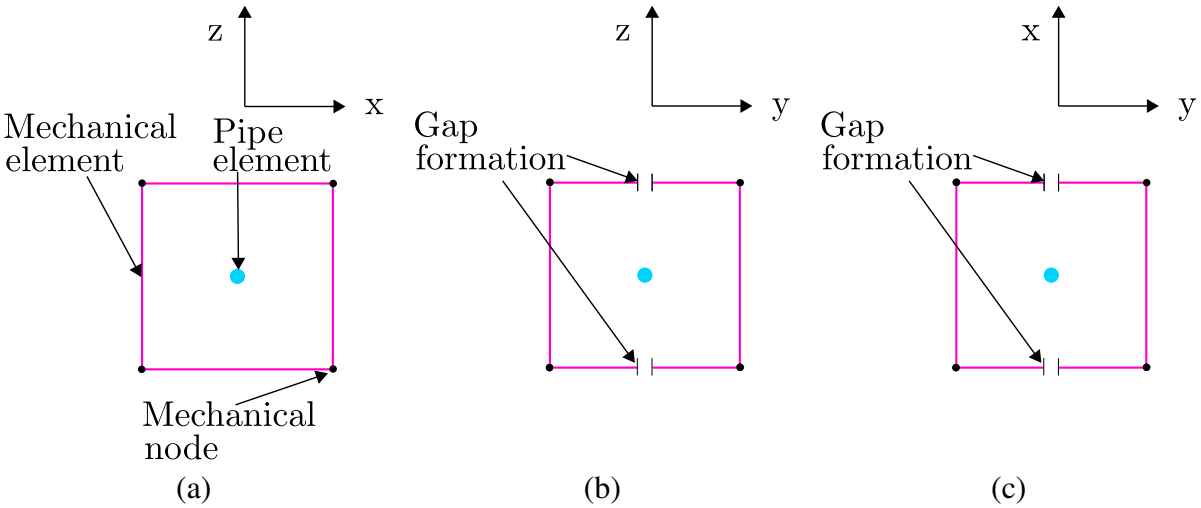

Figure 4.19: Individual pipe elements with their surrounding mechanical elements presented after the strain is applied to the periodic cell: (a) pipe element in y direction, (b) pipe element in x direction and (c) pipe element in z direction.

chanical elements surrounding each transport element was 4 for the regular cubic network of Figures 4.15 and 4.16, whereas it is 3 for the random dual Voronoi/Delaunay tessellation assumed in Section 3.6.3.

Based on the above, the expected new values of k_{CELL} for flow in the x or z directions increased to to 1.9765×10^{-1} s whereas the value of k_{CELL} for flow in the y direction should remain unchanged at 7.7×10^{-19} s. This was recovered by the model results, thus verifying correctness of the model implementation. It should be noted that the increase of conductivity by 17 orders of magnitude emerge from the combination of very small pipe radius $r_{\text{pm}} = 10^{-6}$ m (Table 4.3 for case a) and a mechanical element length $l_e = \sqrt{2}/2$ m (Table 4.4) which results to an large increase of the radius according to (4.18) and then magnified by its exponentiation to the power of four, since the pipes were exhibiting a liquid filled conductivity k_{l} according to the combination of (3.18) and (3.19).

4.4 Discussion

The implementation of the new model was verified through a series of tests. The comparison of the macroscopic conductivity and elastic constant of regular cells with corresponding analytical solutions verified the correctness of the implementation of periodic and non-periodic elements. Also, the retention cases of random networks with all spheres having a single radius and all pipes having a single radius was verified by comparing with simple theoretical predictions. Finally, the correct coupling of the transport and the mechanical approaches was confirmed by two simple tests on cubic networks.

Chapter 5

Parametric investigation of the transport model

5.1 Introduction

The investigation presented in this chapter is focused on the influence of the transport input parameters on the changes of the degree of saturation S_{r} and conductivity k_{CELL} with capillary suction P_{c}. More specifically, the conductivity and retention curves are computed for different means and coefficients of variation of the pipe and sphere radii lognormal distributions. For each curve, 100 cells with the same sphere and pipe distributions were analysed for changing P_{c}. For each value of P_{c}, the degree of saturation and conductivity were computed and the average values for all cells were calculated and presented in the curves.

Figures 5.1 and 5.2 show the retention and conductivity results respectively from the transport model for the case where the input parameters were taken from Table 5.1. Furthermore, standard physical input parameters from Table 4.1 were chosen, except that $\gamma = 1$ N/m was used for the value of surface tension. This γ value was chosen for an easier evaluation of the approximate position of retention and conductivity curves with respect to P_{c} by substituting γ and the mean sphere or mean pipe radius into (3.12). In addition, the cell edge length was taken as 4×10^{-3} m giving $l_{\mathrm{CELL}}/d_{\mathrm{min}} = 7.14$ that resulted in networks with number of spheres, and hence number of degrees of freedom, of approximately 1500 for each realisation.

The transport model input parameters presented in Table 5.1 were chosen to produce pipe and sphere radii of orders of magnitude that capillary phenomena can occur. However, these values were not chosen to match a specific porous geomaterial microstructure. Hence, the values were arbitrarily chosen and used only to serve the purpose of the investigation of the

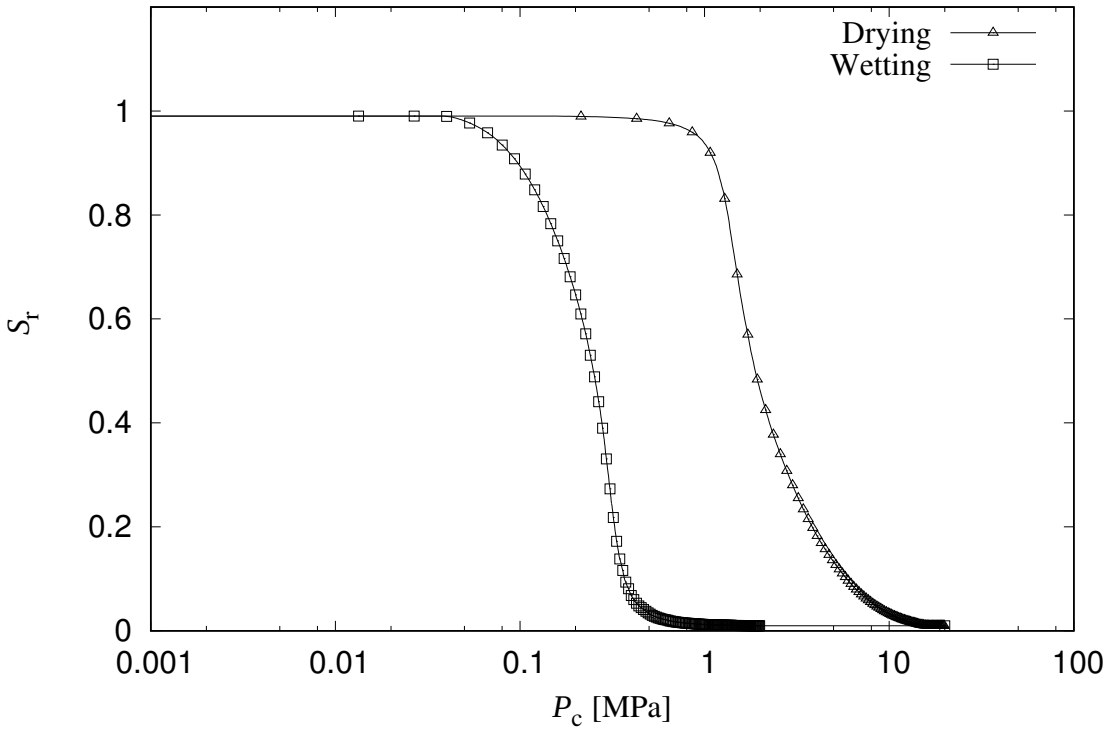

Figure 5.1: Retention curves for drying and wetting: degree of saturation S_r versus capillary suction P_c for the input parameters presented in Table 5.1 and standard physical input parameters from Table 4.1, except that $\gamma = 1$ N/m.

influence of the sphere and pipe size distribution parameters on the cell conductivity and retention behaviour. Additionally, the values of $r_\mathrm{p}^\mathrm{min}$ and $r_\mathrm{s}^\mathrm{min}$ were chosen to match minimum pore radius a meniscus of water can be formed (Bažant and Bazant, 2012).

It can be observed that the network transport model presented in Section 3.4 is able to capture the macroscopic retention and conductivity hysteresis presented in Section 2.2.1.

Table 5.1: Network input parameters

Network parameter	value	units
Minimum distance of Delaunay points d_min	5.6×10^{-4}	m
Mean of pipe radii distribution r_pm	10^{-6}	m
COV of pipe radii distribution COV^p	1	
Minimum pipe radius $r_\mathrm{p}^\mathrm{min}$	1.35×10^{-9}	m
Maximum pipe radius $r_\mathrm{p}^\mathrm{max}$	2×10^{-3}	m
Mean of sphere radii distribution r_sm	10^{-5}	m
COV of sphere radii distribution COV^s	1	
Minimum sphere radius $r_\mathrm{s}^\mathrm{min}$	1.35×10^{-9}	m
Maximum sphere radius $r_\mathrm{s}^\mathrm{max}$	2×10^{-3}	m

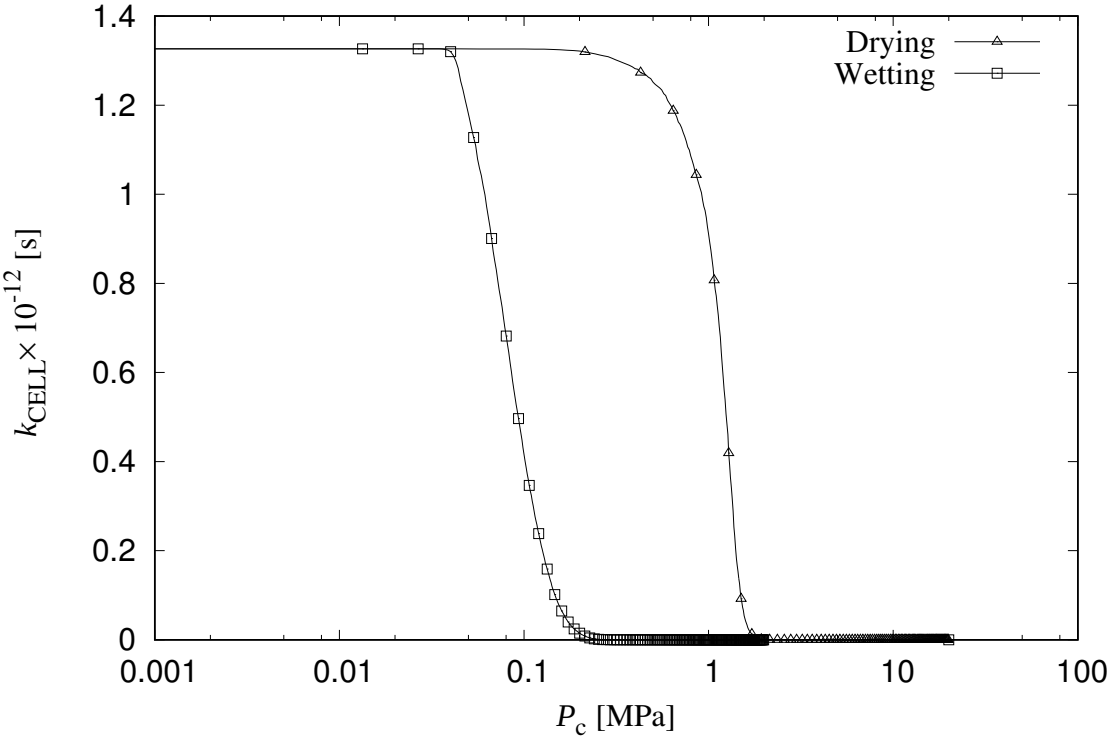

Figure 5.2: Conductivity curves for drying and wetting: conductivity k_{CELL} versus capillary suction P_{c} for the input parameters presented in Table 5.1 and standard physical input parameters from Table 4.1, except that $\gamma = 1$ N/m.

5.2 Influence of sphere radii distribution on fluid retention and conductivity

The influence of the sphere (pore) radii distribution on the retention and conductivity is presented. For constant pipe radii distribution, the sphere radii distribution influences only the wetting behaviour of the network, because the drying behaviour is governed entirely by the pipe radii distribution and the network connectivity if the pore volume scaling approach described in Section 3.4.4 is applied. Therefore, only the wetting curves are presented. For all analyses the input parameters are presented in Table 5.1 except for the individual parameter under investigation in each parametric study. The edge length is $l_{\mathrm{CELL}} = 4 \times 10^{-3}$ m.

Two types of study were performed. For the first one, the same value of mean sphere radius r_{pm} was used throughout and the coefficient of variation of the sphere radius $\mathrm{COV}^{\mathrm{s}}$ was varied as 0.2, 0.5, 1, and 2. In the second case, $\mathrm{COV}^{\mathrm{s}}$ was kept constant equal to 1 and r_{pm} was varied as 10^{-5}, 10^{-4}, and 10^{-3} m. For each combination, 100 analyses were performed each with a different network geometry and different pore and pipe radii realisations.

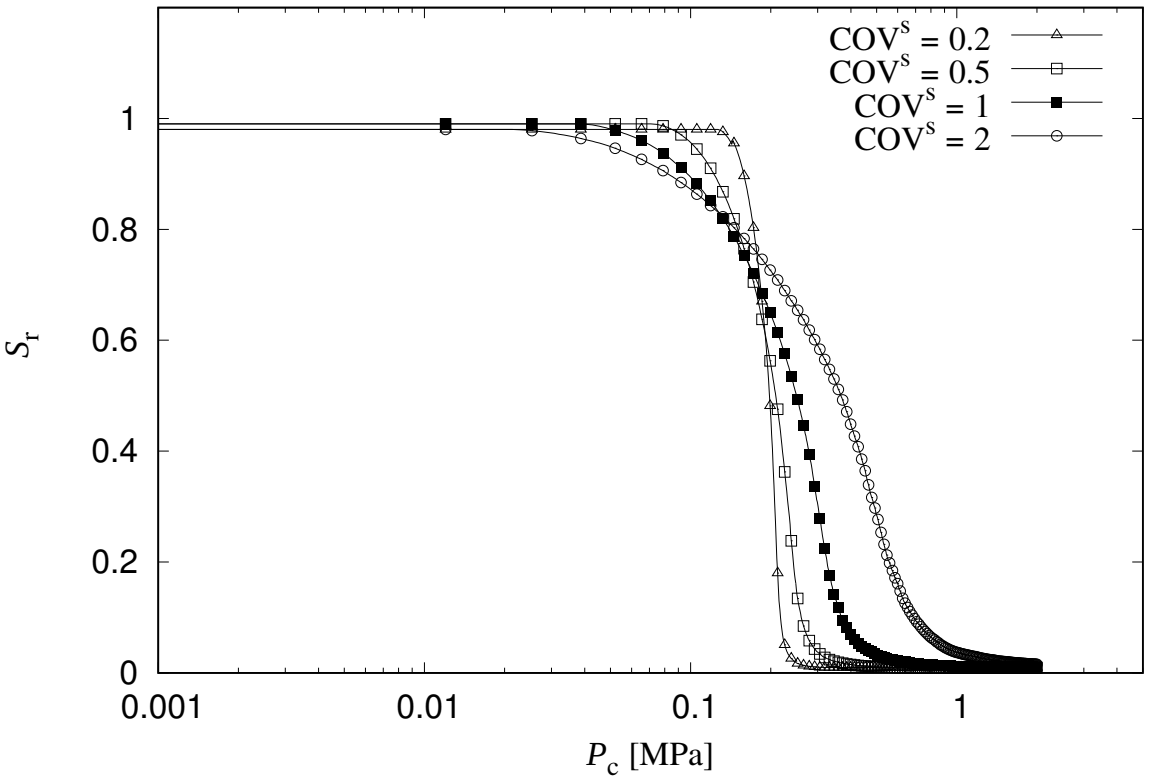

Figure 5.3: Retention curves for wetting process: degree of saturation S_{r} versus capillary suction P_{c} for varying coefficient of variation of sphere radius $\mathrm{COV}^{\mathrm{s}}$ and constant mean sphere radius $r_{\mathrm{sm}} = 10^{-5}$ m.

5.2.1 Influence of $\mathrm{COV}^{\mathrm{s}}$

Retention curves are presented in Figure 5.3 for the case where r_{pm} was kept constant and $\mathrm{COV}^{\mathrm{s}}$ was varied. The curves approximately intersect at $P_{\mathrm{c}} = 0.2$ MPa, which is the capillary suction that corresponds to $r_{\mathrm{sm}} = 10^{-5}$ m according to (3.12), with surface tension as $\gamma = 1$ N/m. As $\mathrm{COV}^{\mathrm{s}}$ increases, the retention curve becomes less steep, i.e. it covers a wider range of capillary suction values. This is expected behaviour as the sphere radii distribution spectrum widens.

The network model results presented in Figure 5.3 can be qualitatively compared to results of an idealised network with perfect connectivity where all unfilled spheres would be candidates for filling at every step of the analysis, and hence spheres would be filled in exact sequence of increasing size. This case can be described by converting the Cumulative Distribution Function used as input to a retention curve, since each sphere represents the same volume when the pore volume scaling approach described in Section 3.4.4 is used. For the same input parameters, the results of the idealised network are presented in Figure 5.4. The same qualitative behaviour as the one presented for the network model is observed.

The comparison of the idealised case with the network model results is presented in Figure 5.5

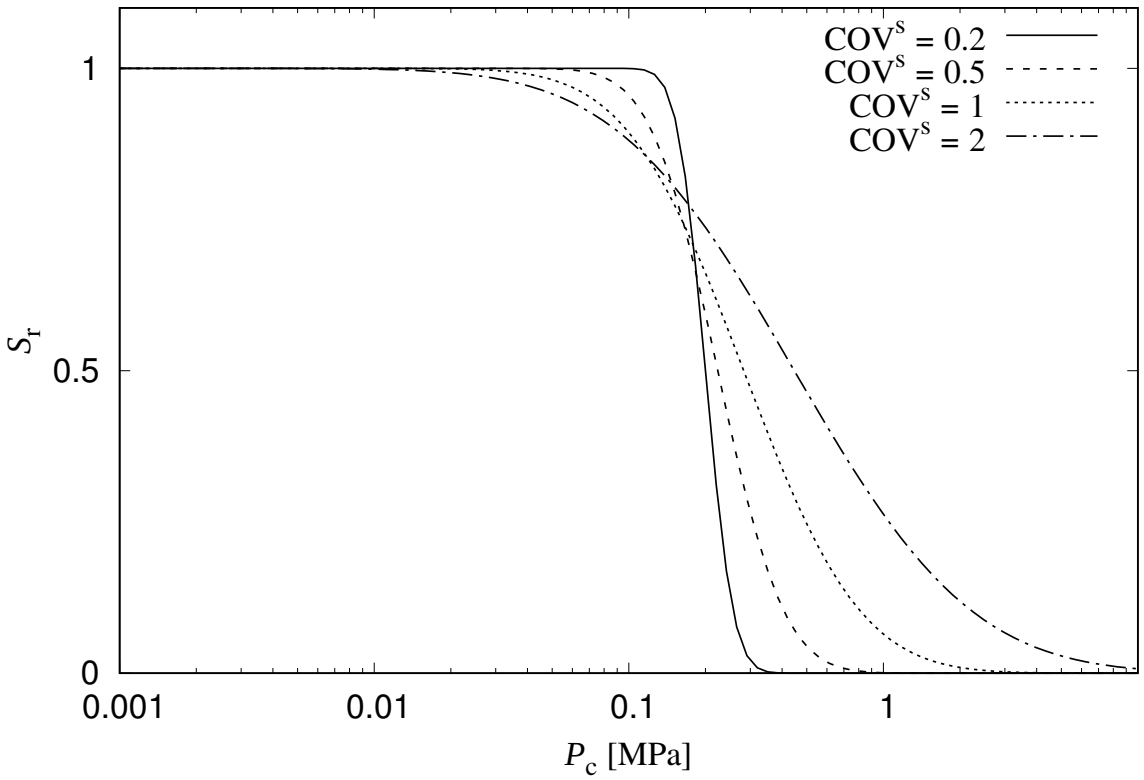

Figure 5.4: Retention curves for wetting process in idealised network with perfect connectivity: degree of saturation S_{r} versus capillary suction P_{c} for varying coefficient of variation of sphere radius $\mathrm{COV}^{\mathrm{s}}$ and constant mean sphere radius $r_{\mathrm{sm}} = 10^{-5}$ m.

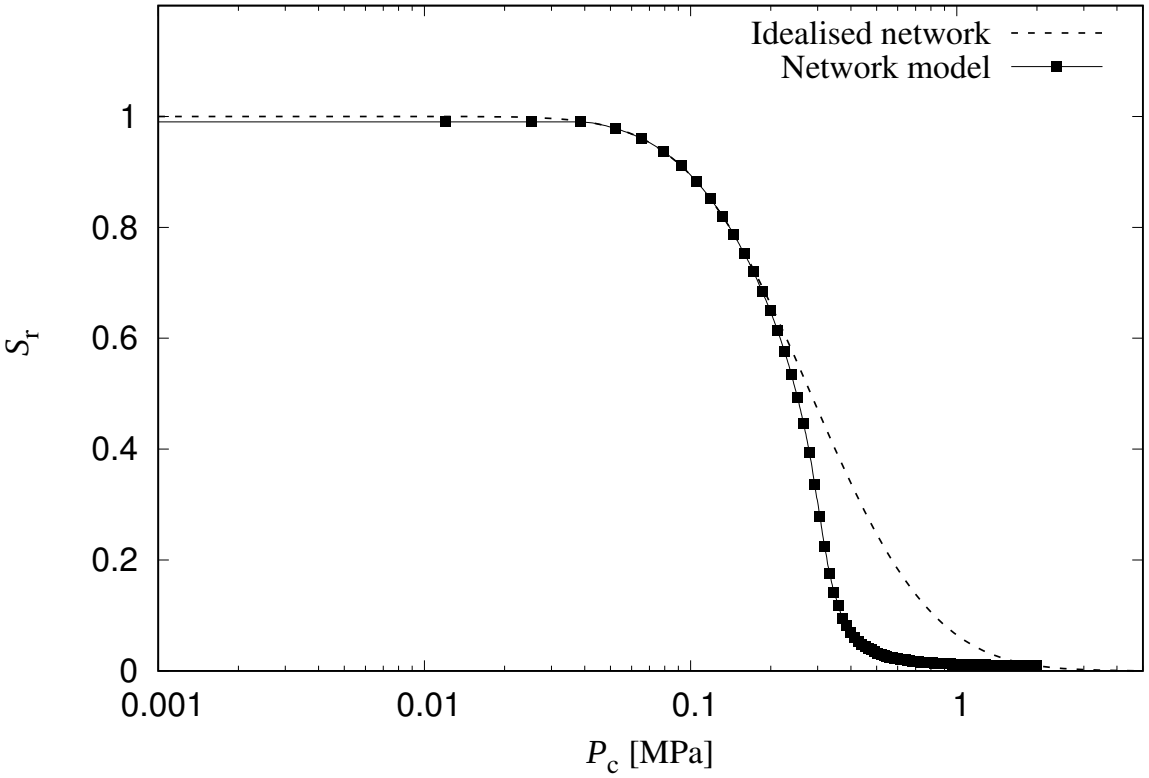

Figure 5.5: Comparison of retention curves from network model and from idealised network with perfect connectivity for wetting process: degree of saturation S_r versus capillary suction P_c for coefficient of variation of sphere radius $\text{COV}^s = 1$ and constant mean sphere radius $r_{sm} = 10^{-5}$ m.

for $\text{COV}^s = 1$. At high values of P_c, the network model predicts lower values of degree of saturation S_r than the idealised network. This is observed because spheres that would be available to fill with wetting fluid in the idealised network, are blocked by larger unfilled spheres (shielding) in the network model. As more spheres fill with wetting fluid and the degree of saturation increases, this shielding effect reduces and from about $S_r = 0.5$ the results from the network model match those from the idealised network. For networks with higher connectivity, the retention curve would be closer to the idealised one for the full range of capillary suction values.

The variation of conductivity k_{CELL} with capillary suction P_c for varying COV^s is presented in Figure 5.6. Since the pipe radii distribution is the same for all cases, the value of k_{CELL} for saturated conditions (where the curves reach the upper value plateau) would be expected to be the same for all cases. This is approximately true, although the results in Figure 5.6 for $\text{COV}^s = 1$ show a higher average value of saturated k_{CELL} than for other values of COV^s. This is presumably simply a consequence of a different set of random network geometries since the difference between the standard deviations of the cases with highest k_{CELL} for $S_r = 0.99$ ($\text{COV}^s = 1$ and $\text{COV}^s = 0.5$) is of 17.5% (standard deviation of k_{CELL} for $\text{COV}^s = 1$ is 2.02×10^{-13} s and for $\text{COV}^s = 0.5$ is 1.67×10^{-13} s). For unsaturated conditions, the

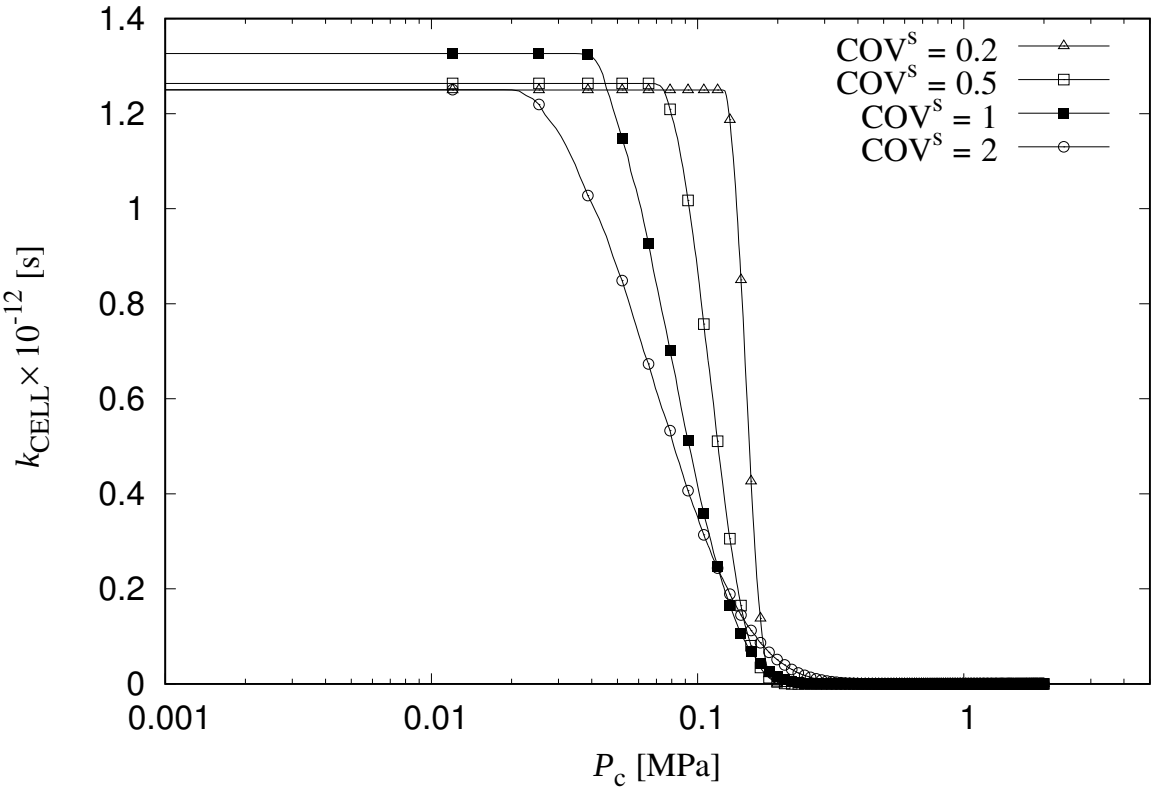

Figure 5.6: Conductivity curves for wetting process: cell conductivity k_{CELL} versus capillary suction P_{c} for varying coefficient of variation of sphere radius COV$^{\text{s}}$ and constant mean sphere radius $r_{\text{sm}} = 10^{-5}$ m.

conductivity predictions would be expected to be significantly affected by COV$^{\text{s}}$ and this is what is observed in Figure 5.6. This can be explained by an inspection of Figure 5.3. When S_{r} is between 0.01 and 0.99, for the same capillary suction the four curves for four different values of COV$^{\text{s}}$ present different values of S_{r}. For the case of a curve having S_{r} greater than the other, it means that more spheres are filled with the wetting fluid. Therefore, more pipes are filled with wetting fluid and the conductivity is higher. For this reason, the conductivity at any value of P_{c} is highest for the case giving the highest S_{r}. At high values of P_{c} (approximately $P_{\text{c}} > 0.2$ MPa) the conductivity is therefore larger for larger values of COV$^{\text{s}}$ whereas for low values of P_{c} (approximately $P_{\text{c}} < 0.2$ MPa) the reverse phenomenon is presented.

5.2.2 Influence of r_{sm}

The retention curve for COV$^{\text{s}} = 1$ and varying r_{sm} is presented in Figure 5.7. The shape of the curves is preserved since the horizontal axis is presented with a log scale. There is a transition of the curves to lower capillary suction values with increasing r_{sm}. The transition is determined by the P_{c} value that corresponds to the r_{sm} value of each curve.

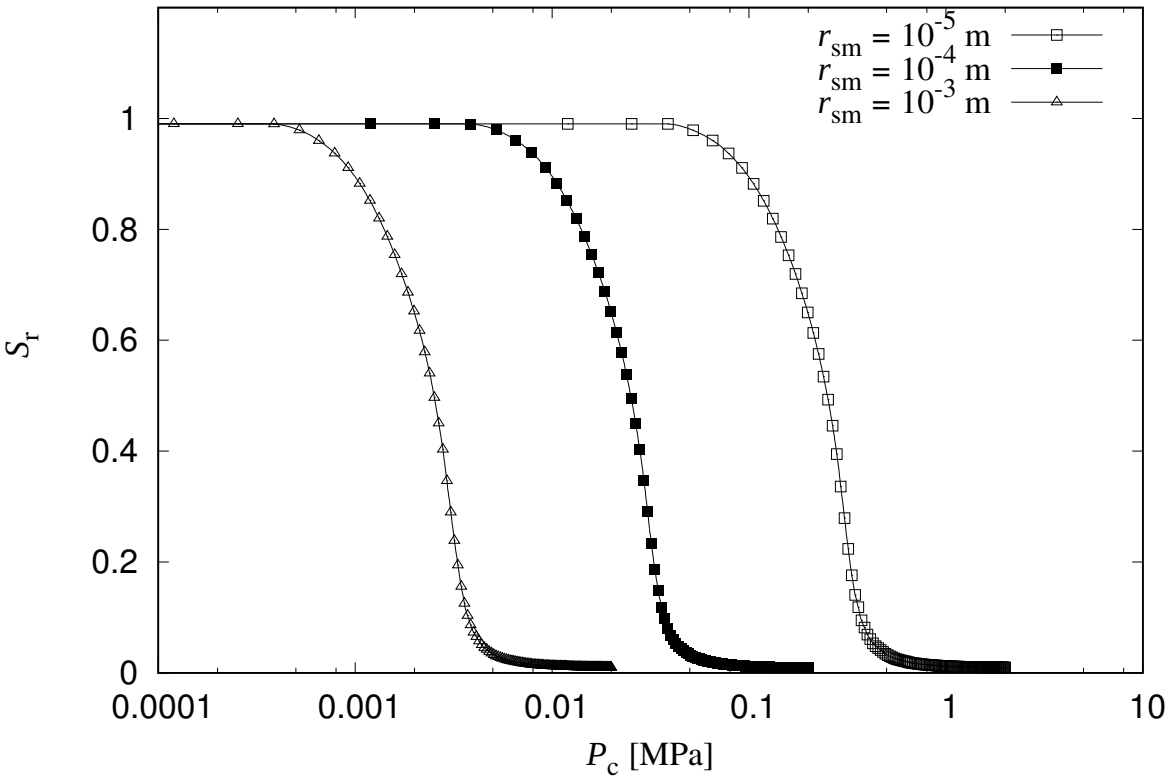

Figure 5.7: Retention curves for wetting process: degree of saturation S_{r} versus capillary suction P_{c} for varying mean sphere radius r_{sm} and constant $\mathrm{COV}^{\mathrm{s}} = 1$.

The results of the variation of conductivity with varying capillary suction for the same input combinations are presented in Figure 5.8. Since the pipe radii distributions are the same for all cases, k_{CELL} is roughly the same for saturated conditions in all cases (the results for $r_{\mathrm{sm}} = 10^{-5}$ m, $\mathrm{COV}^{\mathrm{s}} = 1$ again show a slightly higher saturated value for k_{CELL} than other cases, as Figure 5.6, and this is presumably simply a random consequence of a different set of random network generations). In Figure 5.8, the curve shapes are similar for the three values of r_{sm} and they show the same translation as seen in the corresponding retention curves. This is expected behaviour, since for networks with the same pipe radii distributions for the same S_{r} values the same pipes are going to be filled with wetting fluid. Therefore, the same conductivities are evaluated for the same S_{r} values as presented in Figure 5.9, which shows a unique curve when k_{CELL} is plotted against S_{r} rather than against P_{c}.

It should be noted that the rough equality of the cell conductivity k_{CELL} for the three mean sphere radius values for saturated conditions in Figure 5.8 and for the same degree of saturation S_{r} in Figure 5.9 emerges from the use of the same pipe radius distributions in all three cases. In the case that different pipe distributions were used, different k_{CELL} values would be evaluated at the same S_{r}.

The sets of pipes filled with wetting fluid are $S_{\mathrm{r}} \approx 0.01$, 0.5 and 0.99 are presented in Figures 5.10, with the corresponding sets of pipes filled with drying fluid shown in Figure 5.11.

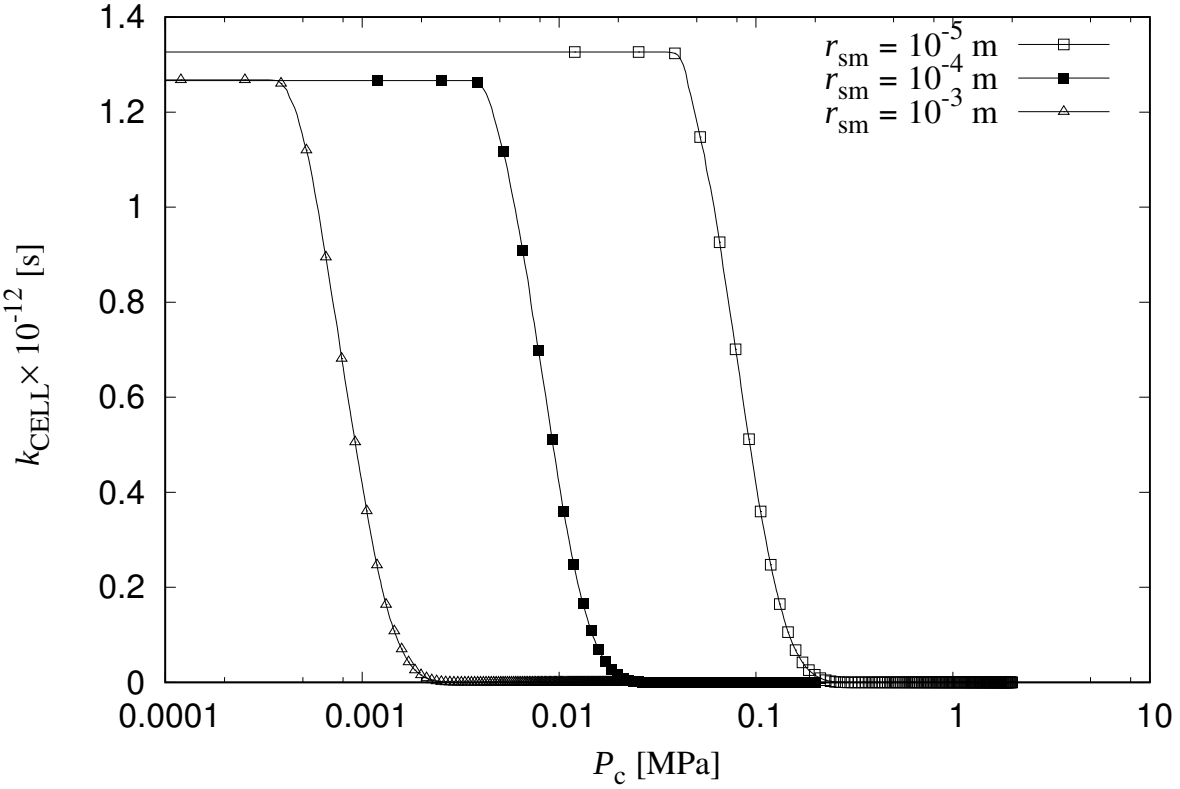

Figure 5.8: Conductivity curve for wetting process: cell conductivity k_{CELL} versus capillary suction P_{c} for varying mean sphere radius r_{sm} and constant $\mathrm{COV}^{\mathrm{s}} = 1$.

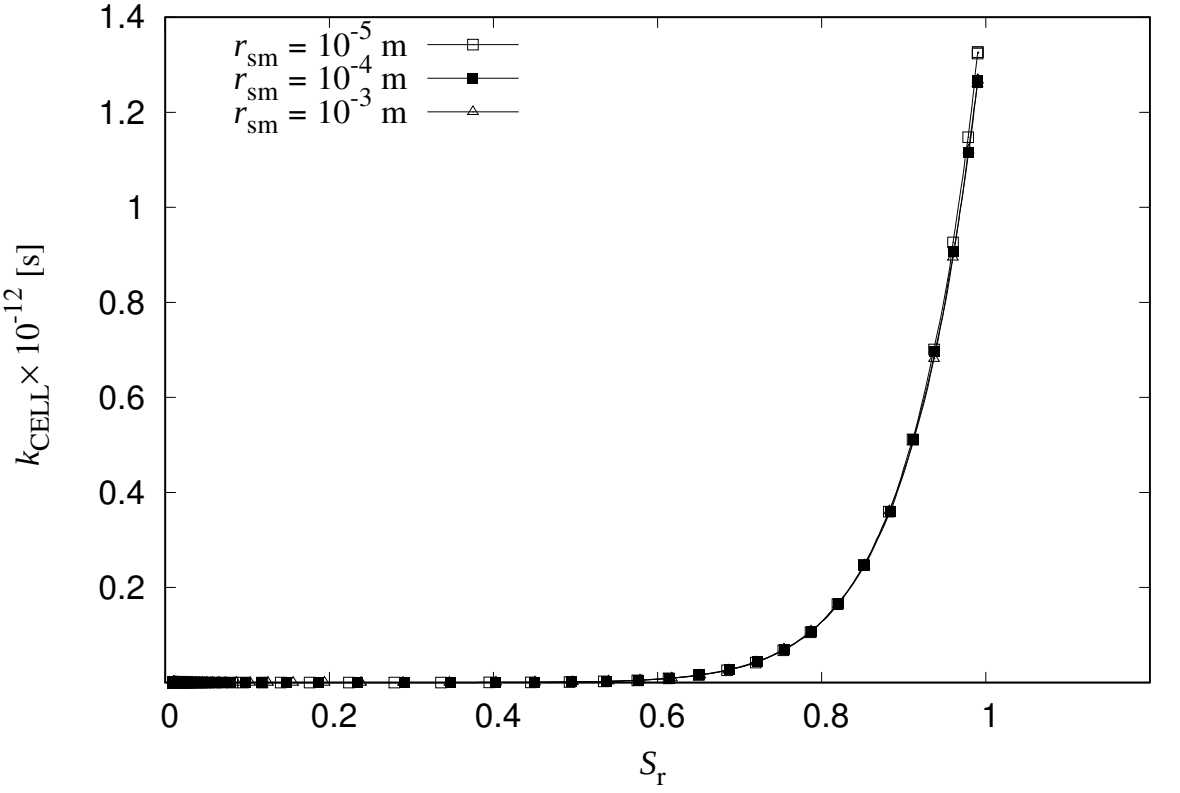

Figure 5.9: Conductivity curve for wetting process: cell conductivity k_{CELL} versus saturation S_{r} for varying mean sphere radius r_{sm} and constant $\mathrm{COV}^{\mathrm{s}} = 1$.

As S_r increases the number of pipes filled with wetting fluid increases and the number of pipes filled with drying fluid decreases. For $S_r \approx 0.5$, the network contains many more pipes filled with drying fluid than with wetting fluid (Figures 5.10b and 5.11b). This is reflected in the results presented in Figure 5.9 where the value of k_{CELL} is still very low for $S_r \approx 0.5$ compared to the value for $S_r \approx 0.99$.

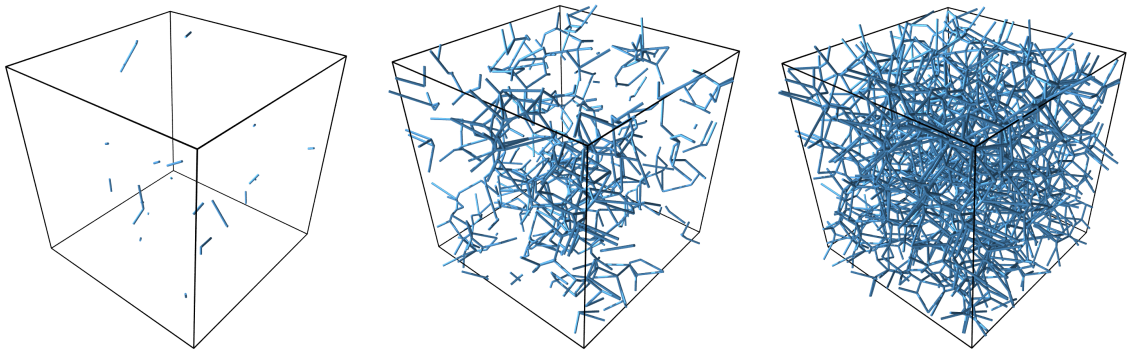

(a) (b) (c)

Figure 5.10: Pipes filled with wetting fluid: (a) $S_r \approx 0.01$, (b) $S_r \approx 0.5$ and (c) $S_r \approx 0.99$.

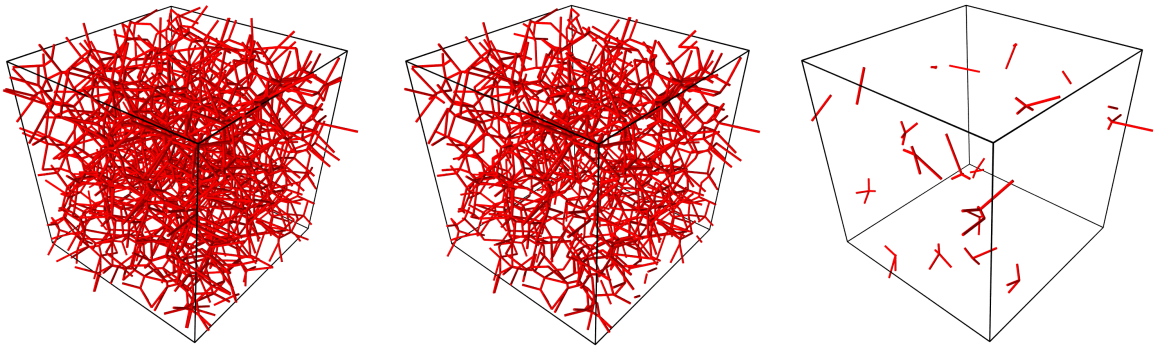

(a) (b) (c)

Figure 5.11: Pipes filled with drying fluid: (a) $S_r \approx 0.01$, (b) $S_r \approx 0.5$ and (c) $S_r \approx 0.99$.

5.3 Influence of pipe radii distribution on retention and conductivity

The influence of the pipe radii distribution on the retention and conductivity is presented in this section. In the present model with the pore volume scaling approach described in Section 3.4.4, when the sphere radii distribution is kept constant, the wetting retention behaviour of the network is not affected by varying the pipe radii distribution. However, the conductivity during drying is affected by the pipe radii distribution. Therefore, only drying analyses are presented here. Similarly to the previous section, the input parameters presented in Table 5.1 are used as base input, with the standard physical parameters given in Table 4.1, except for $\gamma = 1$ N/m. Two types of variation were investigated. For the first one, the same mean pipe

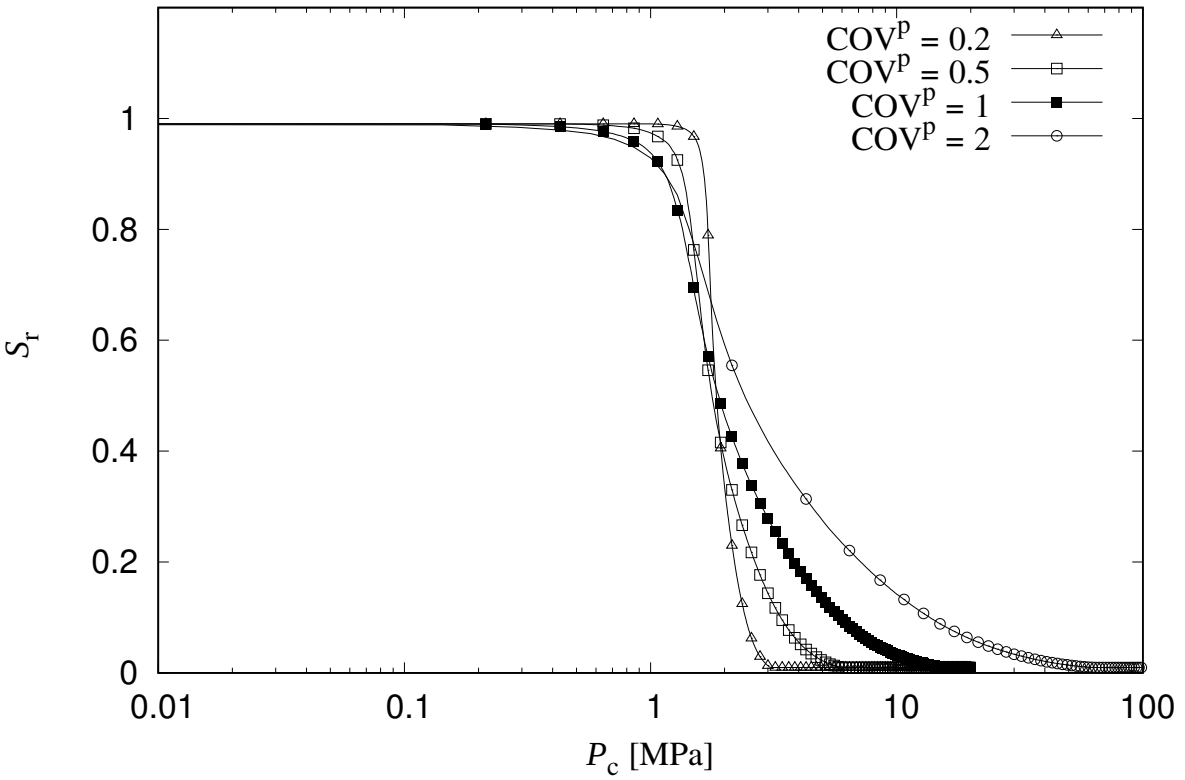

Figure 5.12: Retention curves for drying process: degree of saturation S_{r} versus capillary suction P_{c} for varying coefficient of variation of pipe radius $\mathrm{COV}^{\mathrm{p}} = 0.2$, 0.5, 1, 2 and constant mean pipe radius $r_{\mathrm{pm}} = 10^{-6}$ m.

radius $r_{\mathrm{pm}} = 10^{-6}$ m was used throughout and the coefficient of variation of pipe radius $\mathrm{COV}^{\mathrm{p}}$ was varied as 0.2, 0.5, 1, and 2. In the second variation type, $\mathrm{COV}^{\mathrm{p}}$ was kept constant equal to 1 and r_{pm} was varied as 10^{-6}, 10^{-7} and 10^{-8} m.

5.3.1 Influence of $\mathrm{COV}^{\mathrm{p}}$

Figure 5.12 presents the drying retention curves for different values of $\mathrm{COV}^{\mathrm{p}}$. The behaviour of the curves is similar to that for the wetting case presented in Figure 5.3. The curves approximately intersect at $P_{\mathrm{c}} \approx 2$ MPa which is the value of capillary suction that corresponds to $r_{\mathrm{pm}} = 10^{-6}$ m according to (3.12) if $\gamma = 1$ N/m is used. This is expected since the capillary suction values for which a sphere is filled with drying fluid is determined by the radius of the entry pipe. As $\mathrm{COV}^{\mathrm{p}}$ increases the retention curve becomes less steep, and this means that for $P_{\mathrm{c}} < 2$ MPa, S_{r} decreases with increasing $\mathrm{COV}^{\mathrm{p}}$, whereas for $P_{\mathrm{c}} > 2$ MPa, S_{r} increases with increasing $\mathrm{COV}^{\mathrm{p}}$ is observed.

In Figure 5.13, the network model results for $r_{\mathrm{pm}} = 10^{-6}$ m and $\mathrm{COV}^{\mathrm{p}} = 1$ are compared to that of an idealised network where pipes are filled with drying fluid in an exact sequence of

decreasing pipe radius (at the value of P_c corresponding to that pipe radii) and each pipe gives access to an identical pore volume (e.g. if each pipe provided access to a single sphere of standard volume). This comparison is equivalent to the one presented in Figure 5.5 for the case of wetting (but this time the idealised case uses the pipe radii distribution, rather than sphere radii distribution).

Four main regions can be distinguished for the comparison of the network model to the idealised network results. The first two regions are the region of fully dry conditions ($S_r \approx 0.01$ for the network results) and the region of fully wet conditions ($S_r \approx 0.99$ for the network results) where the two networks have the expected difference of $S_r \approx 0.01$. The third region is where the degree of saturation of the network model is greater the degree of saturation of the idealised network. Finally, the fourth region is where the degree of saturation of the network model is lower than the degree of saturation of the idealised network.

Focus is now given to the third and fourth regions. As explained above, each sphere of the idealised network is connected to the same drying fluid filled sphere through one pipe that is of different radius for each sphere. Therefore, when the idealised network starts to dry while capillary suction increases, each sphere is filled with drying fluid at the capillary suction that corresponds to its pipe radius. In the beginning of the drying process of the network model from saturated conditions ($S_r \approx 0.01$), wetting fluid filled spheres are connected to drying fluid filled spheres through pipes that would allow for the drying fluid filled sphere at higher capillary suction values than the one applied. Therefore, in the beginning of the drying process the shielding effect is responsible for the network degree of saturation being greater than that of the idealised network, i.e. third region. As capillary suction increases, more spheres are filled with drying fluid. This has a double effect on the retention behaviour of the network model. Firstly, spheres that where previously connected to wetting fluid filled spheres are now connected to drying fluid ones. Secondly, wetting fluid filled spheres that were previously connected to drying fluid filled spheres might find new routes to drying fluid through other pipes that have potentially larger radii than the previous drying fluid connecting pipes. The second effect can produce a cascade effect where more than a sphere fills with drying fluid for a capillary suction change (Haines' jump). After a certain capillary suction, the network model possesses more spheres than the idealised network that are connected to drying fluid with pipes of radii that would allow for drying fluid to be filled in the connected spheres at lower capillary suction than the one applied. Therefore, the network model degree of saturation is less than that of the idealised network, i.e. fourth region.

The evolution of conductivity for varying capillary suction for different $\mathrm{COV}^{\mathrm{p}}$ is presented in Figure 5.14. For saturated conditions (maximum conductivity of each curve), k_{CELL} decreases with increasing $\mathrm{COV}^{\mathrm{p}}$. This behaviour can be attributed to the fact that for higher $\mathrm{COV}^{\mathrm{p}}$ more small radius pipes are generated in the cell and these narrower pipes create bottlenecks in the overall flow which reduce the overall conductivity.

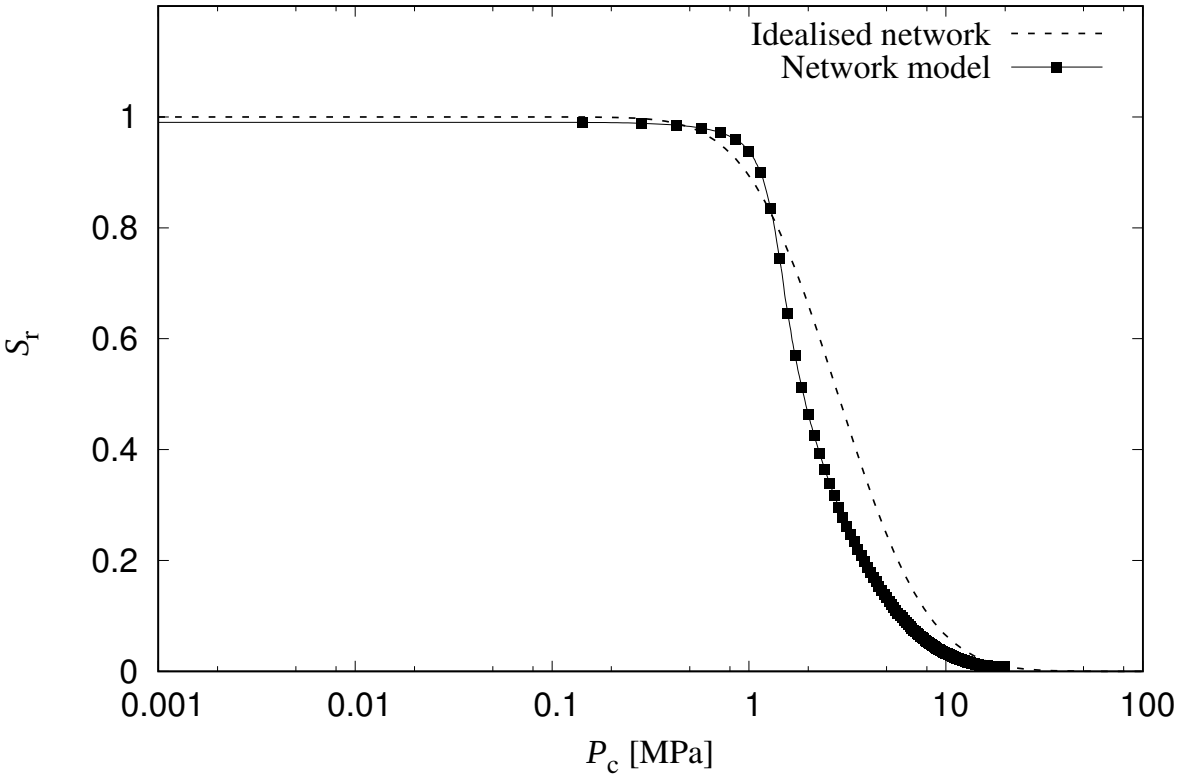

Figure 5.13: Comparison of drying retention curves from network model and an idealised network: degree of saturation S_r versus capillary suction P_c for $r_{pm} = 10^{-6}$ m and $COV^p = 1$.

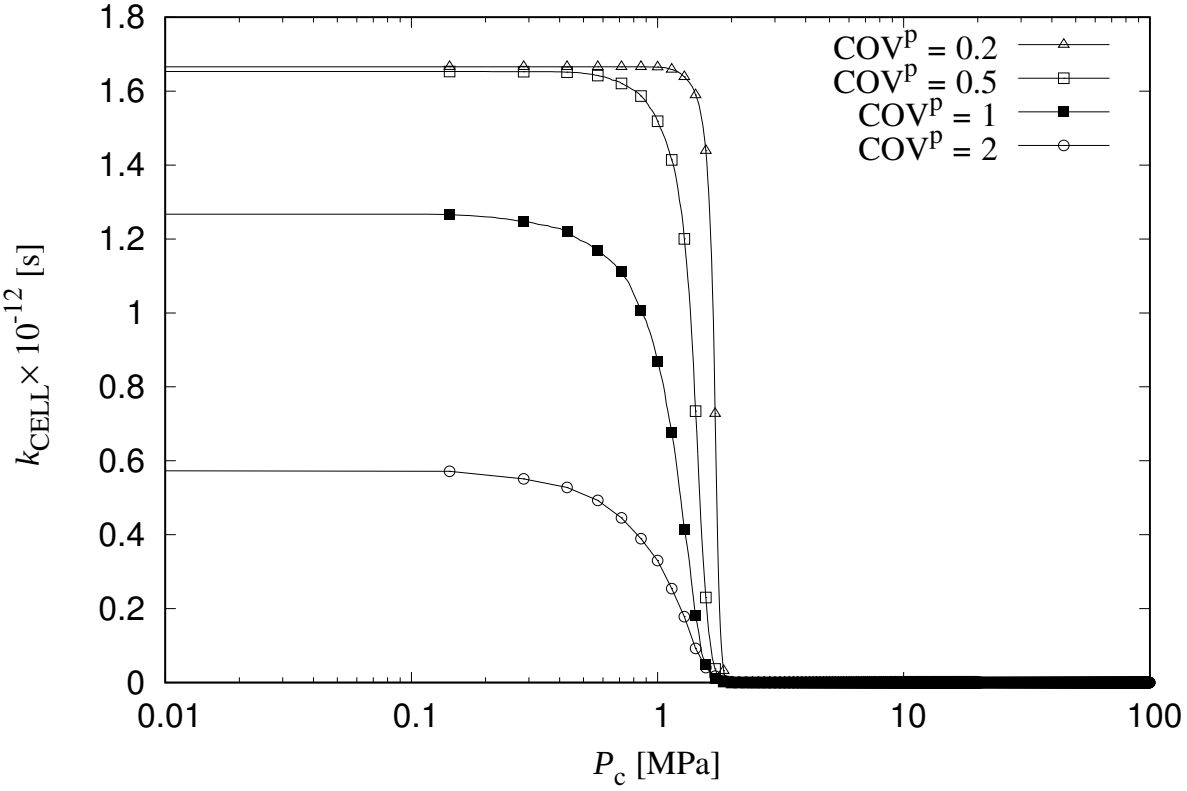

Figure 5.14: Conductivity curves for drying process: cell conductivity k_{CELL} versus capillary suction P_c for varying COV^p and constant $r_{pm} = 10^{-6}$ m.

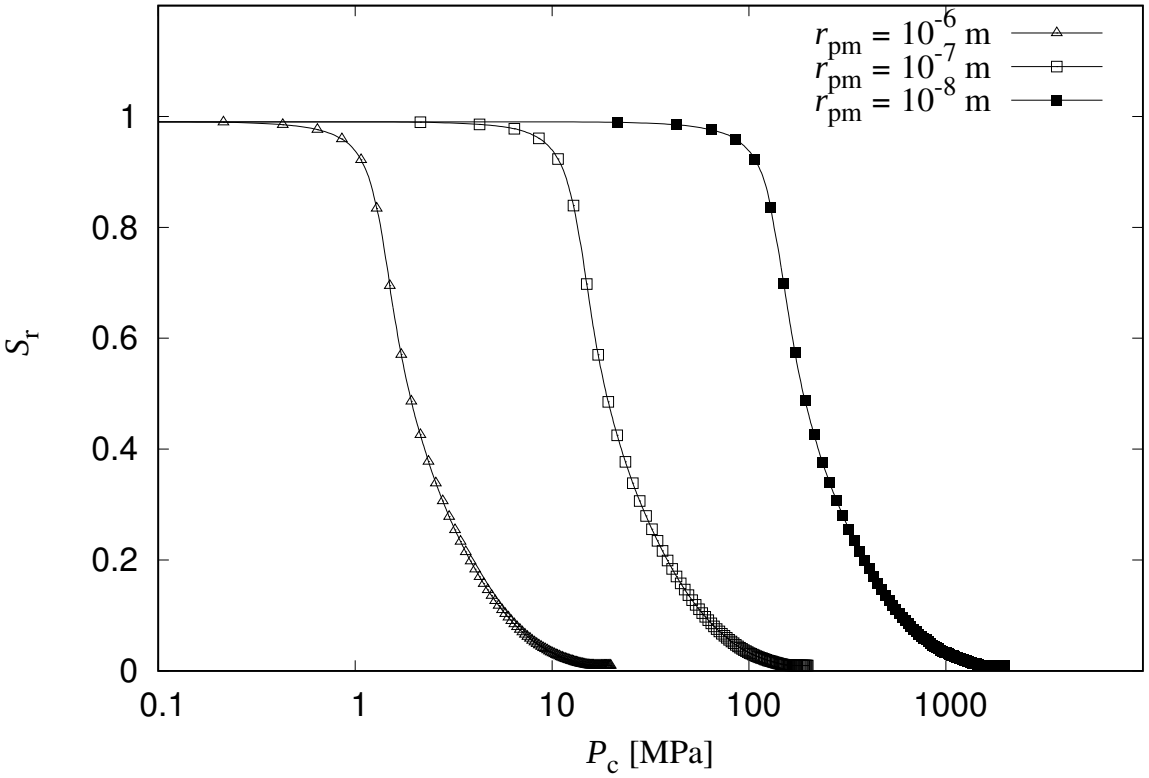

Figure 5.15: Retention curves for drying process: degree of saturation S_{r} versus capillary suction P_{c} for varying r_{pm} and constant $\mathrm{COV}^{\mathrm{p}} = 1$.

5.3.2 Influence of r_{pm}

Drying retention curves for different values of r_{pm} and constant $\mathrm{COV}^{\mathrm{p}} = 1$ are presented in Figure 5.15. The shapes of the curves are the same because the P_{c} axis is presented on a log scale. As the r_{pm} value decreases the curves translate to higher values of P_{c}. The translation equal to the change of the P_{c} value that corresponds to the r_{pm} values of the two curves. Hence, the transition of the curve with $r_{\mathrm{pm}} = 10^{-6}$ m (that correspond to a capillary suction of 2 MPa) to that with $r_{\mathrm{pm}} = 10^{-7}$ m (that corresponds to a capillary suction of 20 MPa) is a factor of 10 on all P_{c} values.

The variation of conductivity during drying is presented in the $k_{\mathrm{CELL}} - P_{\mathrm{c}}$ space in Figure 5.16 for different values of r_{pm} and constant $\mathrm{COV}^{\mathrm{p}} = 1$. The values of k_{CELL} are presented on a log scale, due to the great variations of conductivity values. Typical s-shaped conductivity curves are presented. As r_{pm} decreases, three different effects are seen in Figure 5.16: a reduction in the "saturated" conductivity (at low values of P_{c}); a reduction in the "dry" conductivity (at high values of P_{c}); and an increase in the P_{c} values over which the conductivity falls from the saturated values to the dry value. The saturated conductivity of the cell in Figure 5.16 is proportional to r_{pm} raised to a power 4, so that when r_{pm} decreases from 10^{-6} m to 10^{-8} m, k_{CELL} changes by a factor of 10^{-8}. This can be explained by (3.19), where the conductivity of

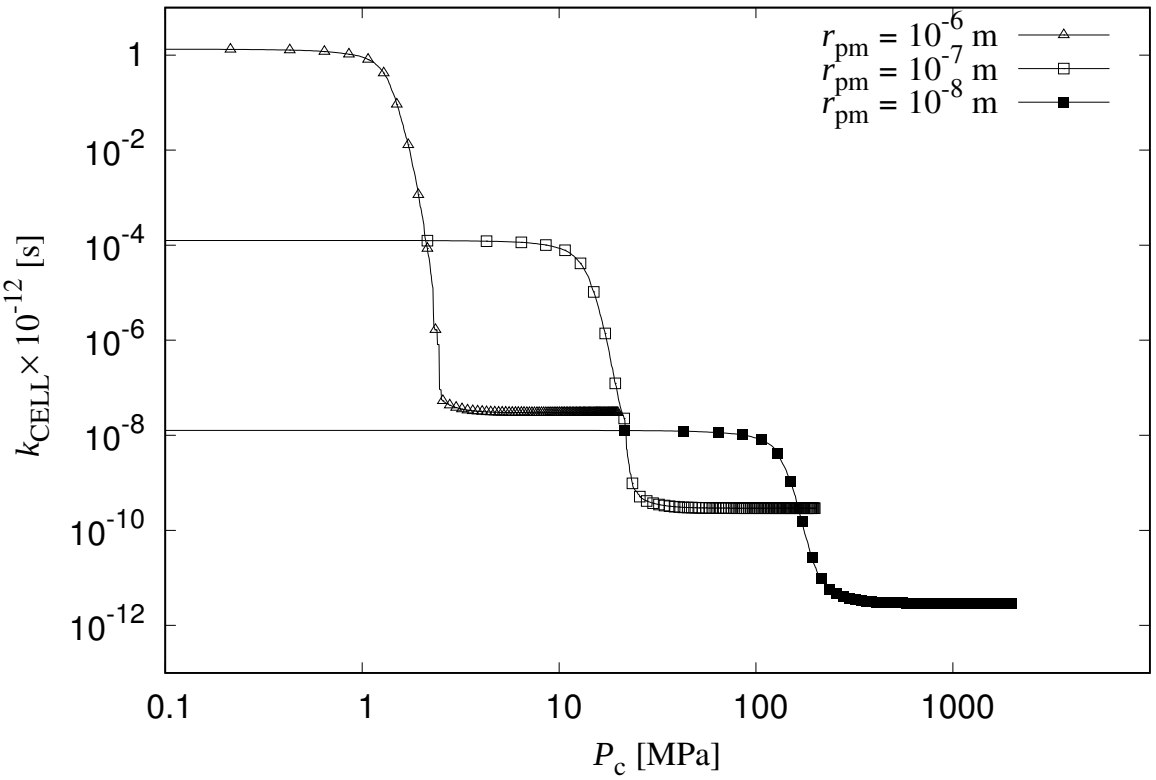

Figure 5.16: Conductivity curves for drying process: cell conductivity k_{CELL} versus capillary suction P_{c} for varying r_{pm} and constant $\mathrm{COV}^{\mathrm{p}} = 1$.

each individual liquid filled pipe varies with the pipe radius squared, so that (allowing for the fact that the cross-section area of the pipe also varies with the radius squared) the flow rate through each pipe varies with the pipe radius raised to the power 4 (see (2.15) and (2.16)). On the other hand, for dry conditions the cell conductivity in Figure 5.16 scales with r_{pm} raised to a power of 2. For instance when r_{pm} decreases from 10^{-6} m to 10^{-8} m the conductivity of the cell for dry conditions change by a factor of 10^{-4}. This can be explained by (3.27) which shows that when a pipe is filled with gas fluid, the vapour conductivity of the pipe is independent of the pipe radius and hence (allowing for the fact that cross-section area of the pipe varies with the radius squared) the vapour flow rate through each pipe varies with the pipe radius raised to a power 2. Since for dry conditions almost all pipes are filled with gas, the same scaling effect is presented for the overall cell conductivity.

5.4 Discussion

The comparison of the fluid retention behaviour of the network model to idealised networks can be used to understand the limitations of mercury intrusion (drying, since mercury is the drying fluid in an air-mercury system) and extrusion (wetting) porosimetry tests to generate retention curves and infer pore size distributions (Matthews et al., 1995). Mercury

intrusion and extrusion porosimetry tests are often used to determine the pipe and sphere size distributions. For the intrusion test, it is assumed that pipes are filled with drying fluid in an exact sequence of decreasing pipe radius (low connectivity) similar to the idealised network considered for the results presented in Figure 5.13. On the other hand, for extrusion it is assumed that all spheres are perfectly connected, similar to the idealised network considered for the results presented in Figure 3.19. As discussed before it is not clear that these two arrangements exclude each other. Different pore networks are tacitly considered for the intrusion and the extrusion retention curves. Furthermore, shielding, Haines' jumps and connectivity are not taken into account. However, in the present section it was shown that idealised networks with intermediate connectivities, where Haines' jump and shielding occur, present different retention behaviour than the idealised networks with infinite connectivity (for wetting) and almost disconnected (for drying) (Figures 5.5 and 5.13). Hence, it is not sufficient to perform mercury intrusion and extrusion porosimetry tests for an accurate measure of the pipe and sphere size distributions (Diamond, 2000).

Furthermore, it was shown in Figure 5.16 that for the same porosity (since the sphere size distribution is constant) the cell conductivity scale with mean pipe radius in the power of four for saturated conditions ($S_{\mathrm{r}} = 0.99$) similar to the scaling of a single liquid filled pipe (see (3.19) and (3.18)). Moreover, for dry conditions ($S_{\mathrm{r}} = 0.01$) the cell conductivity was shown to scales with mean pipe radius in the power of two for saturated conditions similar to the scaling of a single vapour filled pipe (see (3.27) and (3.18)). However, this relationship is not true for the case of real particulate materials where the pipe length and sphere radii increase with the particle size increase. Therefore, for the same cell size, less pipes and spheres would be present as the pipe mean would increase since larger particles would allow for larger pipe radii. This effect results in a cell conductivity scaling at a lower rate than predicted by the network model for an increase of the mean pipe radius. Hence, for using the network model to investigate fluid conductivity through particulate material, an appropriate particle size and therefore pipe lengths should chosen.

Chapter 6

Influence of cell size on retention, conductivity, Young's modulus and Poisson's ratio

6.1 Introduction

The network model proposed in Section 3.4 involves an idealisation of the microstructure of a porous geomaterial with a statistical distribution of sphere sizes, representing the pores, and a statistical distribution of pipe radii, representing the narrower throats. For chosen sphere and pipe radii distributions, each cell generation results in a different microstructure, because the generation of sphere locations and sphere and pipe radii is random (Sections 3.1 to 3.3). Therefore, each cell generation presents a different retention and conductivity behaviour. For a series of analyses, all with the same size of cell, the mean and the COV can be evaluated for a property of interest, such as degree of saturation S_{r}, conductivity k_{CELL}, Young's modulus E_{macro} and Poisson's ratio ν_{macro}. It has been reported that for saturated conditions, as the cell size increases the COV of the property of interest decreases (Zhang et al., 2000). A cell size that is large enough to produce very small COV values of the quantity of interest, is said to be a Representative Volume Element (RVE). This means that for each cell generation of that size, the quantity of interest will not change significantly. This happens because as the cell size increases, more information of the chosen distributions is introduced and the differences of the microstructure between cells become less significant. Hence, a single cell of that size can adequately represent the chosen microstructure.

In Sections 6.2 and 6.3 the influence of cell size on S_{r} and k_{CELL} is investigated for unsaturated conditions. For this, three cell sizes with ratios $l_{\mathrm{CELL}}/d_{\mathrm{min}} = 3$, 5 and 10 were chosen, and

100 cells were generated for each cell size. The analysis of each cell began from an almost saturated condition at $S_r \approx 0.99$ (with only one seeding sphere filled with drying fluid, as described in Section 3.4.3) and then the cell was fully dried (to $S_r \approx 0.01$) and fully wetted again (to $S_r \approx 0.99$) by changing P_c. For each target value of P_c, the values of S_r and k_{CELL} were evaluated for each cell (as described in Section 3.4 and 3.8.2). Then a mean and a COV of each quantity was evaluated. The results of the above analyses are presented, to show the influence of cell size on fluid retention and then on conductivity.

In Section 6.4, the influence of cell size on E_{macro} and ν_{macro} is investigated for two different sets of input. Four cell sizes of l_{CELL}/d_{min} = 3, 5, 10 and 20 were subjected to a uniaxial strain and E_{macro} and ν_{macro} were evaluated, as described in Section 3.5 and 4.2.1. Finally, the results for ν_{macro} from the cells involving irregular networks were compared to analytical results for regular FCC networks presented in the literature.

6.2 Fluid retention

The input parameters used for the investigation of the influence of cell size on fluid retention are presented in Table 5.1 and standard physical input parameters from Table 4.1 were used, except that $\gamma = 1$ N/m. Three different cell sizes were investigated, corresponding to $l_{CELL}/d_{min} = 3$, 5 and 10, where l_{CELL} is the edge length of the cell and d_{min} is the minimum distance between vertices for the domain tessellation. For each cell size, one hundred different realisations were performed each with its own network geometry and sphere and pipe radii generations. The number of degrees of freedom for $l_{CELL}/d_{min} = 10$, that is the largest problem analysed, was approximately 4.2×10^2 for each realisation. For each realisation, the network was initiated at $S_r \approx 0.99$ (with a previous wetting stage to set up seeding cells), dried to $S_r \approx 0.01$, and then wetted back to $S_r \approx 0.99$. The drying and wetting processes were performed by incrementally increasing and decreasing the capillary suction P_c, respectively. At each value of applied P_c, S_r was evaluated. For each value of P_c, the mean and COV of S_r were then calculated from the 100 realisations with the same cell size.

In Figure 6.1, means of S_r during the drying path are plotted against P_c for the three cell sizes. The curves of the means of S_r for the three cell sizes are almost indistinguishable. Hence, for $l_{CELL}/d_{min} \geq 3$ there is a small influence of cell size on the mean values of S_r during drying. However, there is a strong influence of the cell size on the COV of S_r drying as shown in Figure 6.2 for intermediate S_r values. For increasing cell size, the COV decreases. This trend indicates that an RVE exists for fluid retention during drying. For $l_{CELL}/d_{min} = 10$, the maximum COV of S_r has dropped to a small value (approximately 0.025), suggesting that a cell of this size can be considered as an RVE.

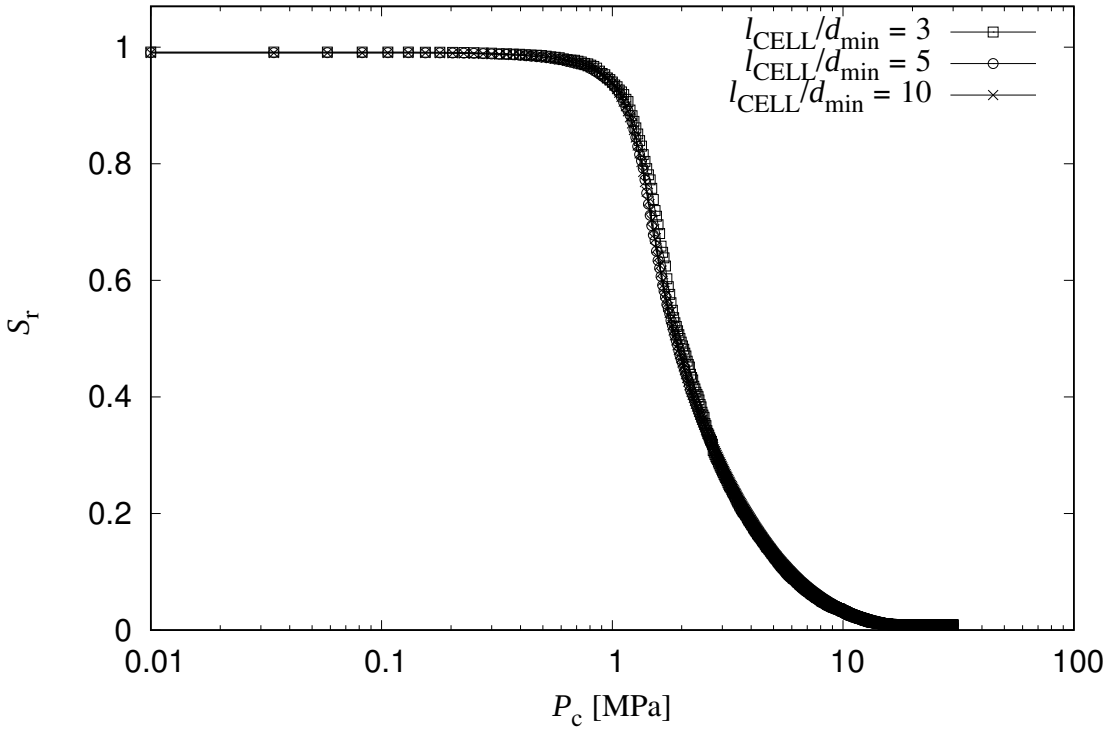

Figure 6.1: Influence of cell size on retention during drying: mean degree of saturation S_r versus capillary suction P_c for 100 realisations for $l_{CELL}/d_{min} = 3$, 5 and 10.

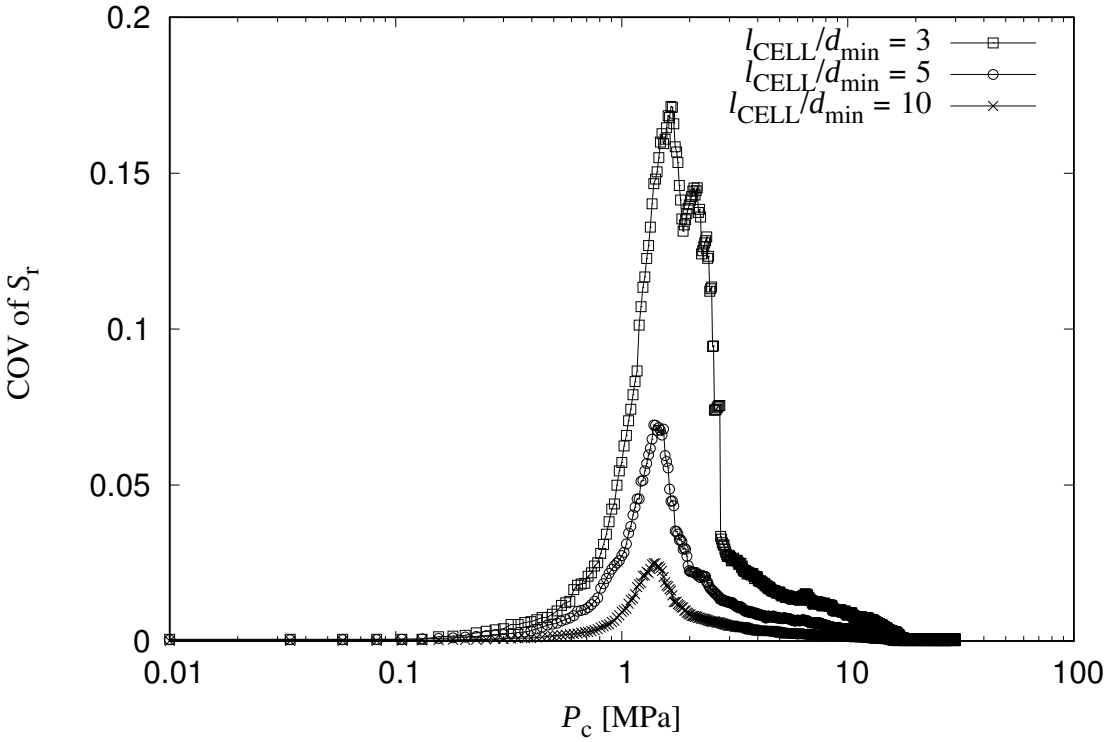

Figure 6.2: Influence of cell size on retention during drying: coefficient of variation of degree of saturation (COV of S_r) versus capillary suction P_c for 100 realisations for $l_{CELL}/d_{min} = 3$, 5 and 10.

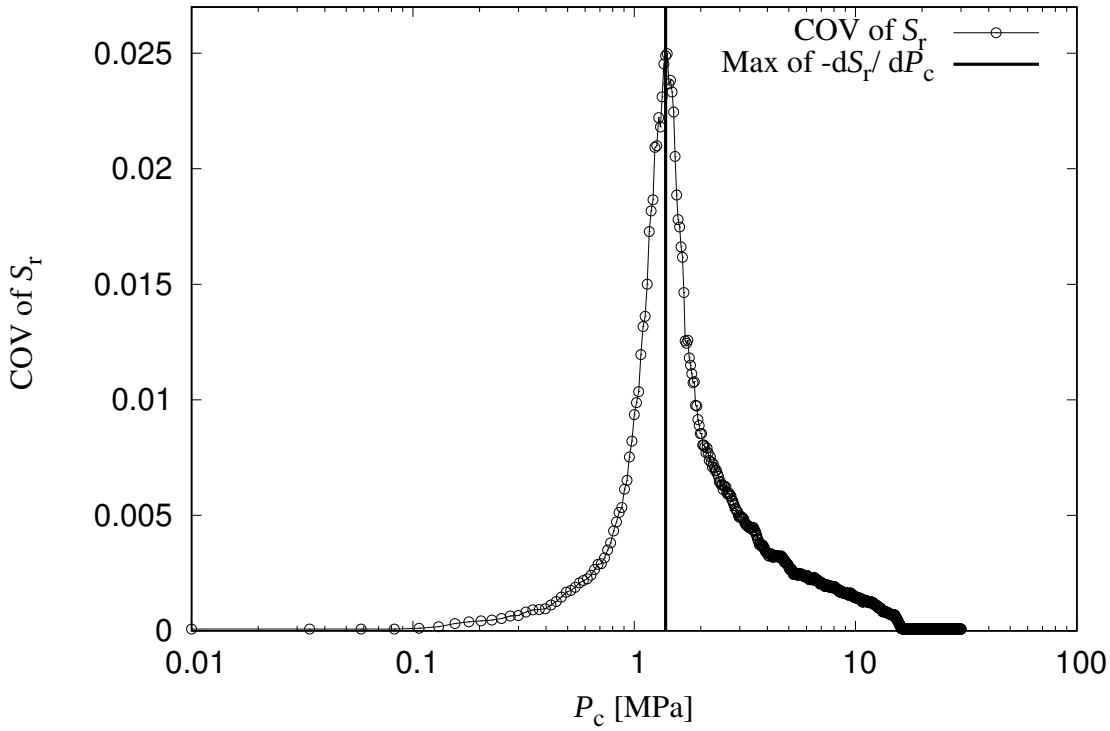

Figure 6.3: Influence of cell size on retention during drying: COV of S_r versus capillary suction P_c for $l_{CELL}/d_{min} = 10$, with vertical line indicating the value of P_c corresponding to the maximum negative gradient of the mean retention curve.

The results of the COV of S_r for the case with $l_{CELL}/d_{min} = 10$ are re-plotted to a larger scale in Figure 6.3. Also shown in Figure 6.3 (by a solid vertical line) is the value of P_c corresponding to the maximum negative gradient of the plot of mean S_r against P_c from Figure 6.1. As might be expected, the peak of the COV curve exactly coincides with the point of maximum gradient on retention curve.

For wetting path, retention curves of mean S_r versus P_c for three different cell sizes are shown in Figure 6.4. Similar to the drying case, the mean S_r is not strongly affected by the cell size for $l_{CELL}/d_{min} \geq 3$. The variation of COV of S_r during wetting for the various cell sizes is presented in Figure 6.5. Similar behaviour to the drying case can be observed. The strong reduction in COV with increasing cell size indicates again that an RVE exists, and the low maximum values of COV (approximately 0.025) for $l_{CELL}/d_{min} = 10$ again indicates that a cell of this size can be considered as an RVE for retention behaviour.

Again, as expected, the peak of the COV curve occurs at the value of P_c corresponding to the maximum negative gradient of mean retention curve (Figure 6.6).

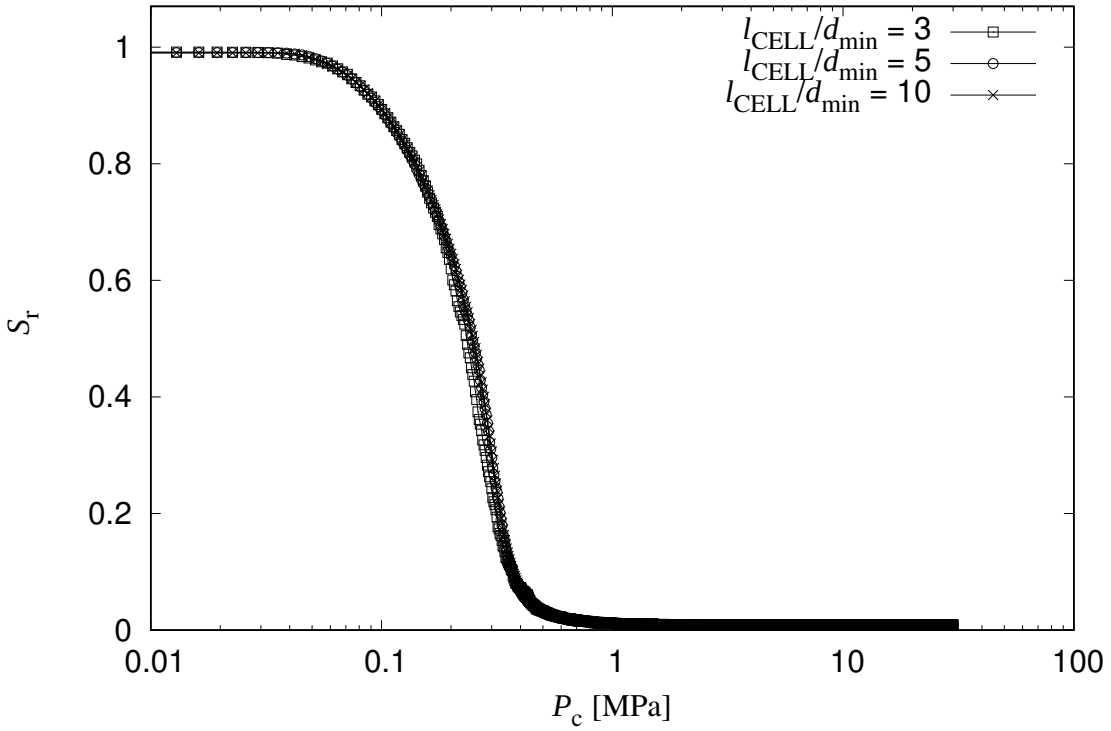

Figure 6.4: Influence of cell size on retention during wetting: mean degree of saturation S_r versus capillary suction P_c for 100 realisations for $l_{CELL}/d_{min} = 3$, 5 and 10.

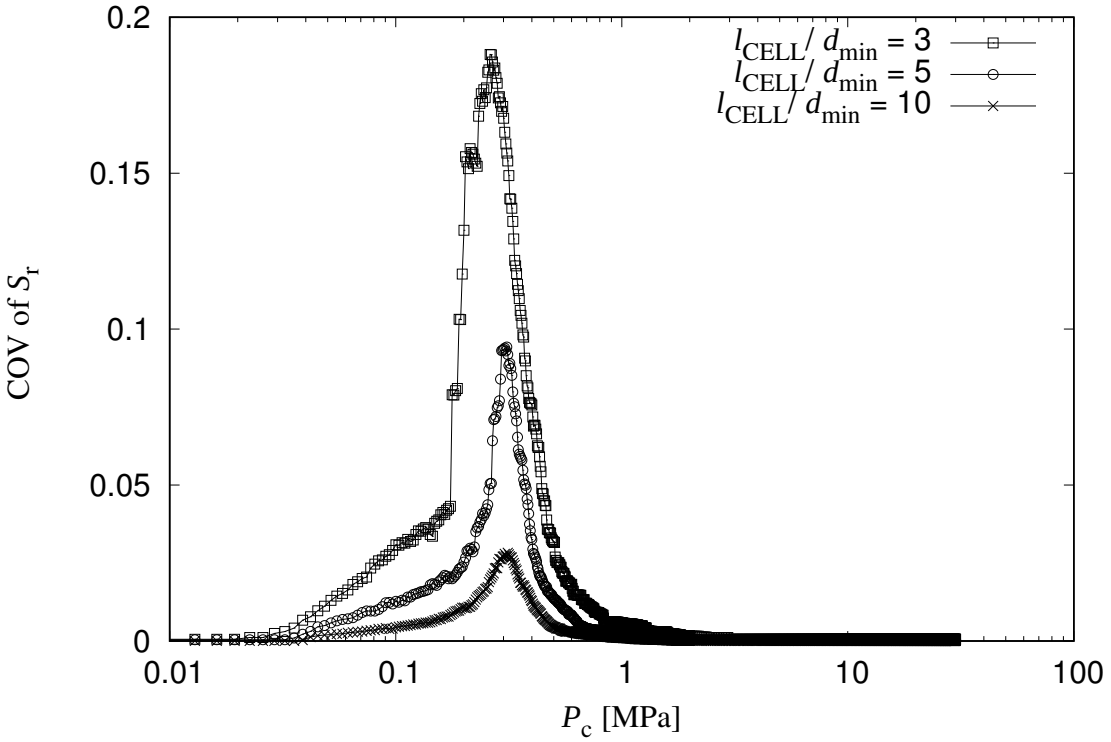

Figure 6.5: Influence of cell size on retention during wetting: coefficient of variation of degree of saturation S_r (COV of S_r) versus capillary suction P_c for 100 realisations for $l_{CELL}/d_{min} = 3$, 5 and 10.

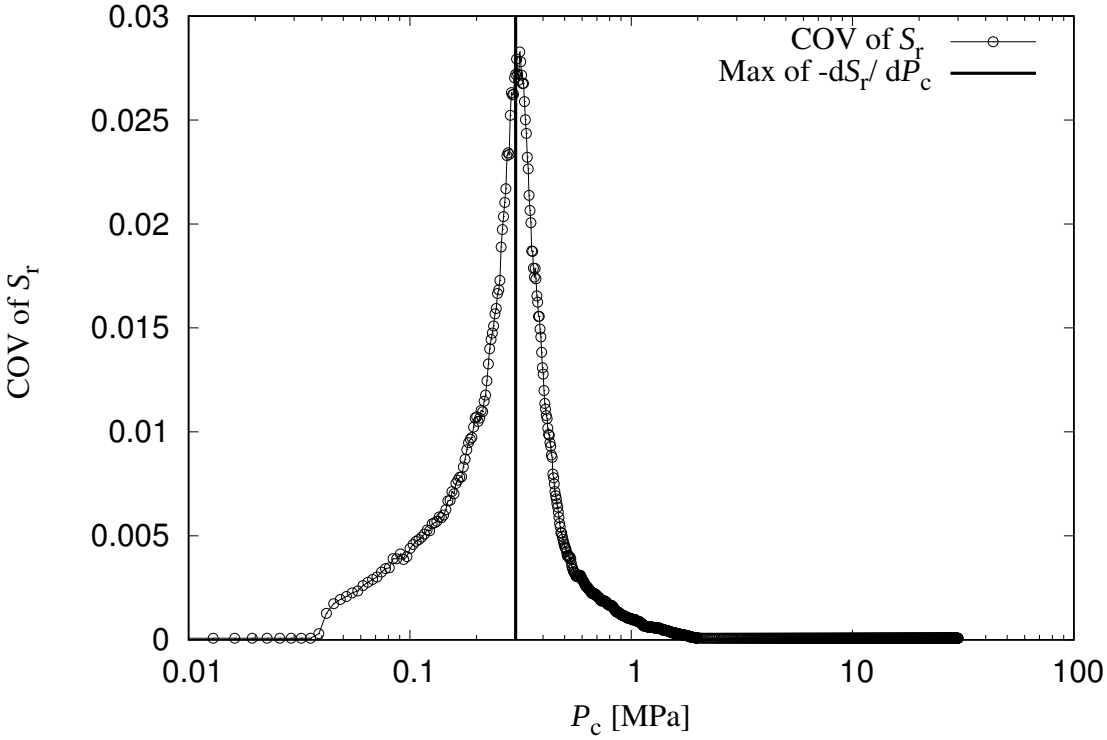

Figure 6.6: Influence of cell size on retention during wetting: COV of S_r versus capillary suction P_c for $l_{CELL}/d_{min} = 10$ with vertical line indicating the value of P_c corresponding to the maximum negative gradient of the mean retention curve.

6.3 Conductivity

The influence of cell size on the mean and standard deviation of the conductivity for a constant degree of saturation of $S_r \approx 0.99$ was initially investigated. Then, the conductivity curves for unsaturated conditions for drying and wetting were determined.

For each value of P_c, the cell conductivity k_{CELL} was evaluated as

$$k_{CELL} = \frac{Q_{CELL}}{l_{CELL} \Delta p_f} \tag{6.1}$$

where Q_{CELL} is the fluid mass flow rate through a cell face perpendicular to the pressure gradient and l_{CELL} is the cell edge length.

Two types of analyses were performed for each cell size. In the first type, for each cell size, the same Voronoi network geometry was used for all 100 realisations. Then, for each cell realisation different sphere and pipe radii were assigned to the unchanged vertices and edges of the network. For the second type of analyses, each cell realisation involved a different Voronoi network geometry, as well as different sphere and pipe radii generation. The first and second

types of analyses are referred to as constant geometry and varying geometry, respectively. For $S_r = 0.99$, the evaluations are presented both for constant geometry and for varying geometry. In both cases, the sphere and pipe radii distributions and value of d_{min} presented in Table 5.1 were used. Five different cell sizes were investigated with $l_{CELL}/d_{min} = 3$, 5, 10, 20 and 30. For each cell size, 100 pipe and sphere radii generations were analysed. For the case of $l_{CELL}/d_{min} = 30$, the number of degrees of freedom was approximately 108×10^3 for each realisation. Other approaches such as Lattice-Boltzmann Method or Finite Volume Method would require a multiple of the above degrees of freedom to evaluate the conductivity of a network with the same size.

Figure 6.7 presents the variation of the mean of k_{CELL} with the normalised cell size l_{CELL}/d_{min} for the cases of constant geometry and varying geometry. The error bars show $\pm$ one standard deviation. In both cases, the standard deviation decreases with increasing cell size. Also, for all five values of l_{CELL}/d_{min}, the mean and standard deviation are very similar for constant geometry case and the varying geometry case. In order to have a better comparison, the COV of k_{CELL} versus the normalised cell size $l_{CELL}/d_{min}$is shown for the two cases in Figure 6.8. Both cases present similar behaviour and values of COV for increasing cell sizes. The decreasing COV with increasing cell size is an expected behaviour, because increasing size means that, more statistical information is included and therefore there is less difference in the overall behaviour from cell to cell.

Furthermore, it is expected that the mean of k_{CELL} for $S_r \approx 0.99$ should converge to a finite value as l_{CELL}/d_{min} approaches infinity. Therefore, the size of an RVE regarding the mean of k_{CELL} for $S_r \approx 0.99$ should be the minimum cell size for which the mean k_{CELL} is equal to the mean k_{CELL} for a cell of infinite size (l_{CELL}/d_{min} approaches infinity). The same statement is true for d_{min}/l_{CELL} approaching zero. Figure 6.9 presents the change of the mean of k_{CELL} for $S_r \approx 0.99$ for decreasing d_{min}/l_{CELL} ratio. It can be observed that for a varying geometry, the mean has converged for $d_{min}/l_{CELL} = 1/20$ since it presents the same mean as that of the cell size of $d_{min}/l_{CELL} = 1/30$. For constant geometry, the mean k_{CELL} does not indicate to be converged yet since it continues to decrease as d_{min}/l_{CELL} decreases.

For smaller cell sizes the mean k_{CELL} of varying geometry networks are larger than those of constant geometry, whereas for larger cell sizes inverse statements apply. However, for the same cell size change, the inclination of the varying geometry curve is larger than the constant geometry curve. Therefore, varying geometry cells produce a mean k_{CELL} that converges faster than that of the constant geometry cells. Furthermore, COV of k_{CELL} of varying geometry is lower for all cell sizes as shown in Figure 6.8. In the case of constant geometry, at each cell realisation pipes with different radii but the same length are presented. Therefore, the only factor that influences the mean of k_{CELL} is the varying assignment of the radii to unchanged pipe locations. On the other hand, in the varying geometry case, each pipe radii realisation is assigned to a completely different network geometry. Therefore, relatively significant changes

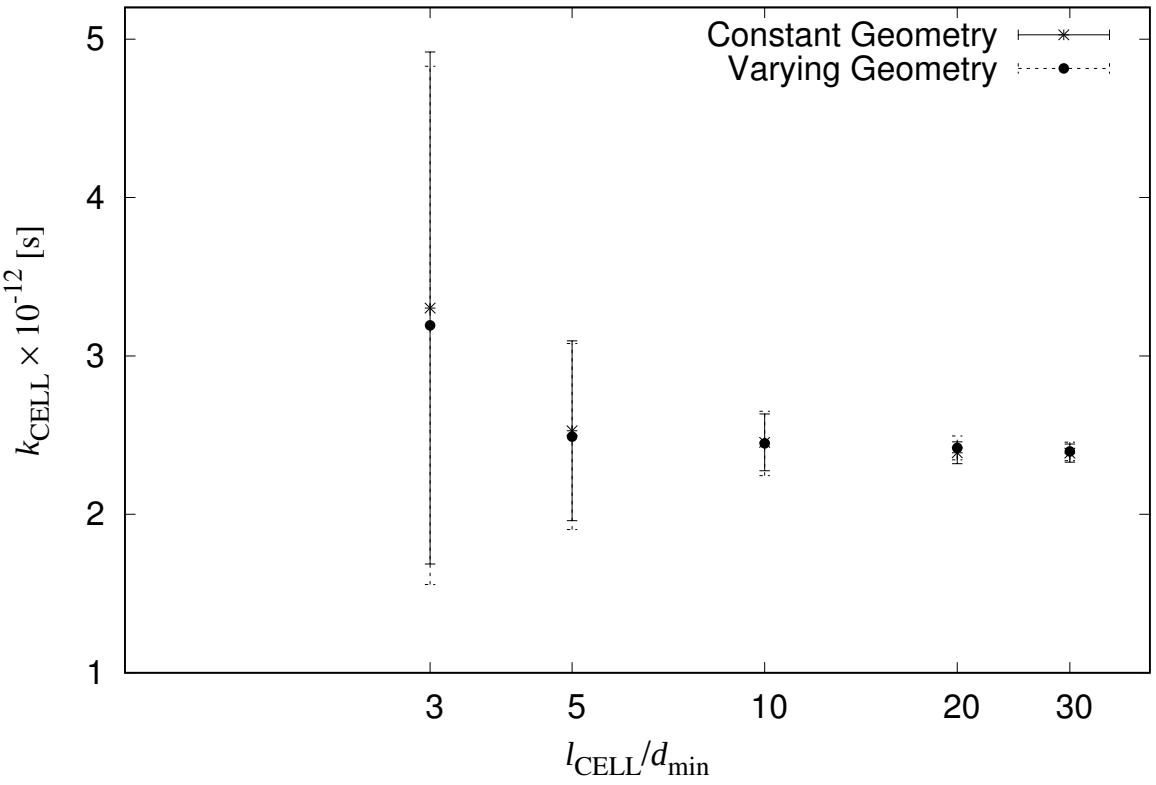

Figure 6.7: Influence of cell size on conductivity for $S_{\mathrm{r}} \approx 0.99$: conductivity k_{CELL} versus $l_{\mathrm{CELL}}/d_{\mathrm{min}}$, the symbols represent the mean of 100 realisations and the error bars show $\pm$ one standard deviation.

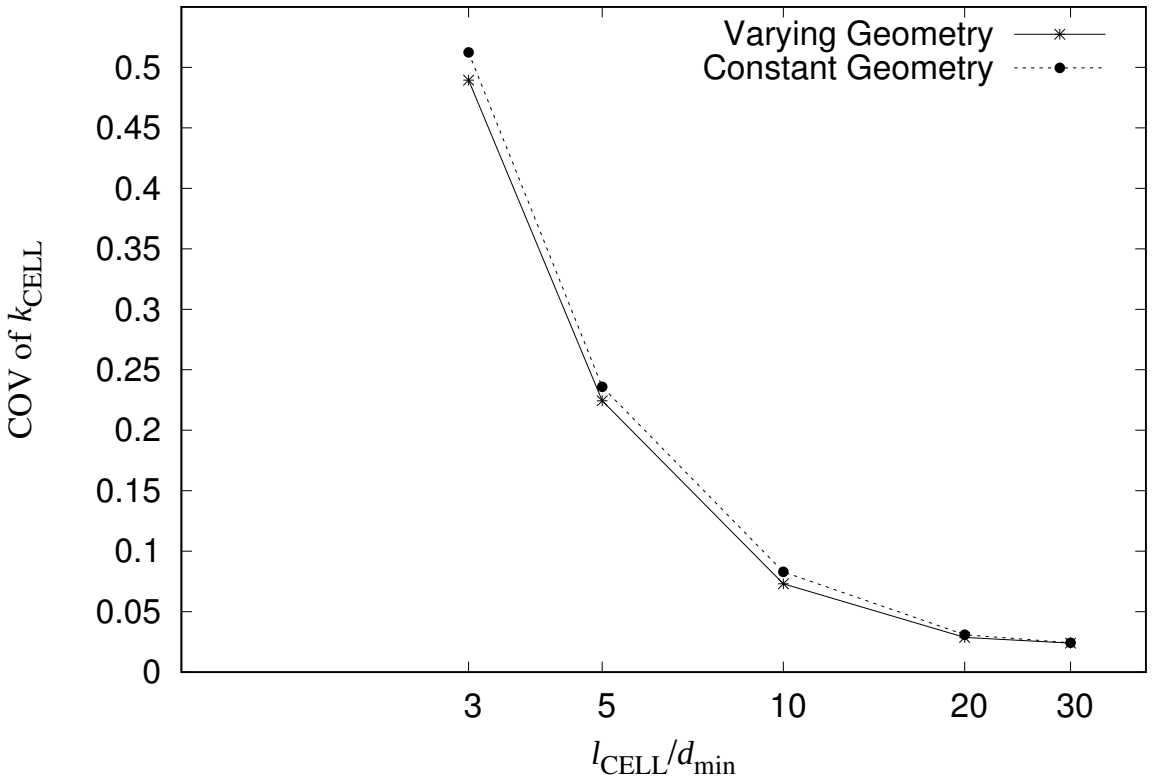

Figure 6.8: Influence of cell size on conductivity for $S_{\mathrm{r}} \approx 0.99$: COV of k_{CELL} versus $l_{\mathrm{CELL}}/d_{\mathrm{min}}$.

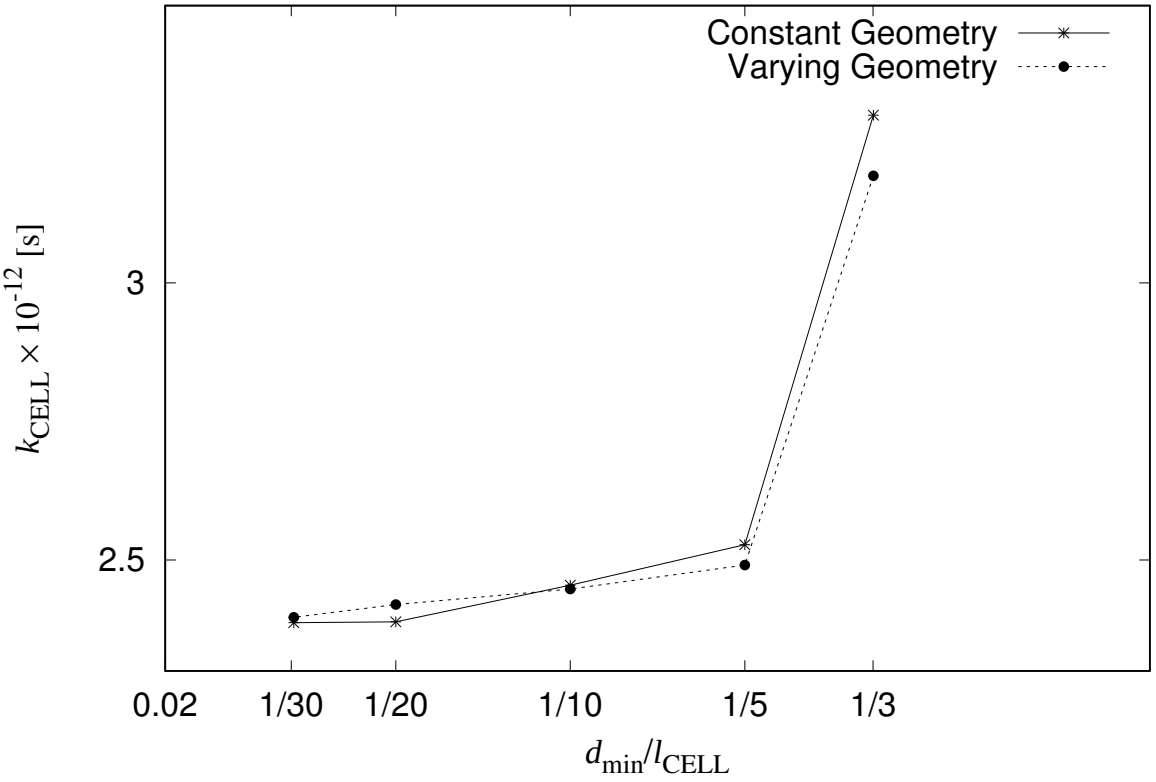

Figure 6.9: Influence of the cell size on the conductivity for $S_r \approx 0.99$: cell conductivity k_{CELL} versus inverse of cell edge length over the minimum distance of the vertices d_{min}/l_{CELL}.

of conductivity occurring for new pipe radii realisations in constant geometry cells might be compensated by generating new network geometries for new pipe radii realisations. It is expected that for larger cell sizes the mean k_{CELL} would of constant geometry networks will be equal to the varying one since the same pipe radii distribution and the same d_{min} is used in both cases. For unsaturated conditions, the mean and COV of k_{CELL} were evaluated for $l_{CELL}/d_{min} = 3$, 5, and 10 for varying geometry, as part of the same analyses as those presented in Section 6.2. For each value of P_c the conductivity of the cell was evaluated. For each value of P_c and each cell size the mean and COV of k_{CELL} were evaluated for 100 realisations. The mean value of k_{CELL} is plotted against P_c, for drying (increasing capillary suction) in Figure 6.10. As the cell size increases, the conductivity curves come closer. For P_c values that correspond to almost saturated conditions, i.e. for low capillary suction values, the mean k_{CELL} decreases with increasing cell size as expected from the previous saturated analysis (Figure 6.7).

Figure 6.11 presents the same results as those presented in Figure 6.10, but in a log-log plot. It can be seen that for lower k_{CELL} values there are differences of orders of magnitude between the mean conductivities for the same P_c for the three cell sizes. This is not observed in almost saturated conditions ($S_r = 0.99$) where k_{CELL} are of the same order of magnitude for all cell sizes. These high differences could be attributed to the effect of percolation which is the stage at which a continuous path of wetting fluid in the direction of the gradient applied that

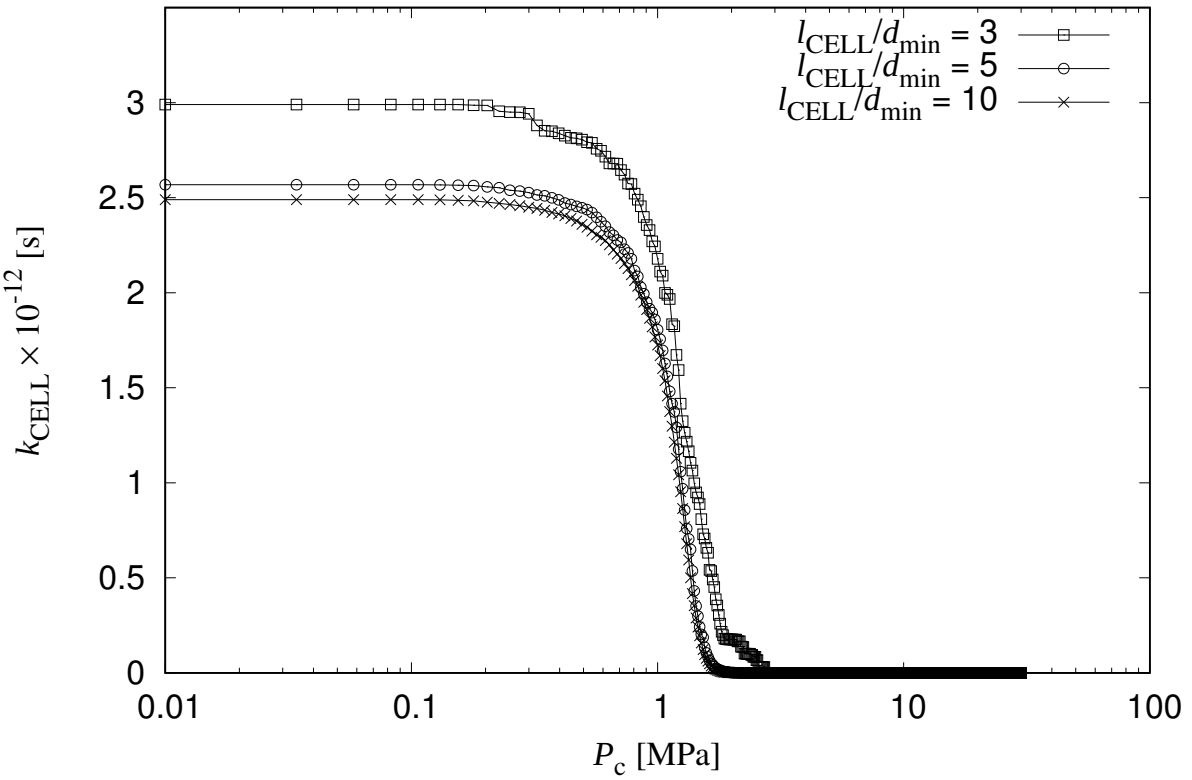

Figure 6.10: Influence of cell size on mean conductivity during drying: conductivity k_{CELL} versus capillary suction P_{c} for 100 realisations for $l_{\text{CELL}}/d_{\text{min}} = 3$, 5 and 10.

connects opposite faces is formed.

The COV of k_{CELL} versus P_{c} is presented in Figure 6.12. Generally, the COV of k_{CELL} at any given value of P_{c} decreases with increasing cell size, as expected. Furthermore, it can be observed that for almost saturated conditions (low values of P_{c}), the COV of k_{CELL} is larger than that for almost dry conditions (high values of P_{c}), because the flow rate along a single pipe in dry conditions is determined by the square of the pipe radius whereas for the saturated case it is determined by the fourth power of the pipe radii (see (3.18), (3.27) and (3.19)).

The variation of the mean value of k_{CELL} with P_{c} during wetting is shown in Figure 6.13 for $l_{\text{CELL}}/d_{\text{min}} = 3$, 5 and 10. For increasing cell size, the mean value of k_{CELL} decreases, although the change from one cell size to another is generally less than during drying (compare Figure 6.13 with Figure 6.10.

Figure 6.14 presents the same results as those presented in Figure 6.13 but in a log-log plot. A similar behaviour to that of the drying process for the change of mean of k_{CELL} curves with increasing cell size. It can be seen that for lower k_{CELL} values there are differences of orders of magnitude between the mean conductivities for the same P_{c} for the three cell sizes. This is not observed in almost saturated conditions ($S_{\text{r}} = 0.99$) where k_{CELL} are of the same order of magnitude for all cell sizes.

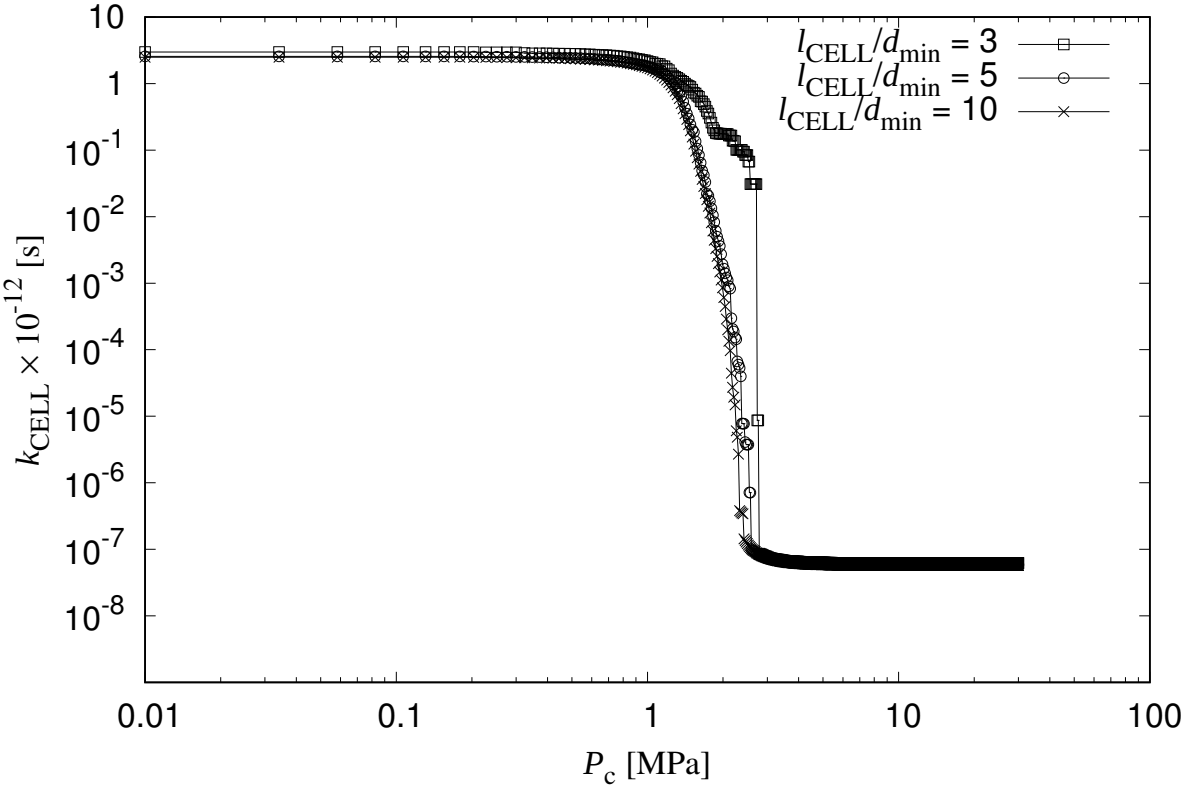

Figure 6.11: Influence of cell size on mean conductivity during wetting: conductivity k_{CELL} (in log scale) versus capillary P_c for 100 realisations for $l_{\text{CELL}}/d_{\text{min}} = 3$, 5 and 10.

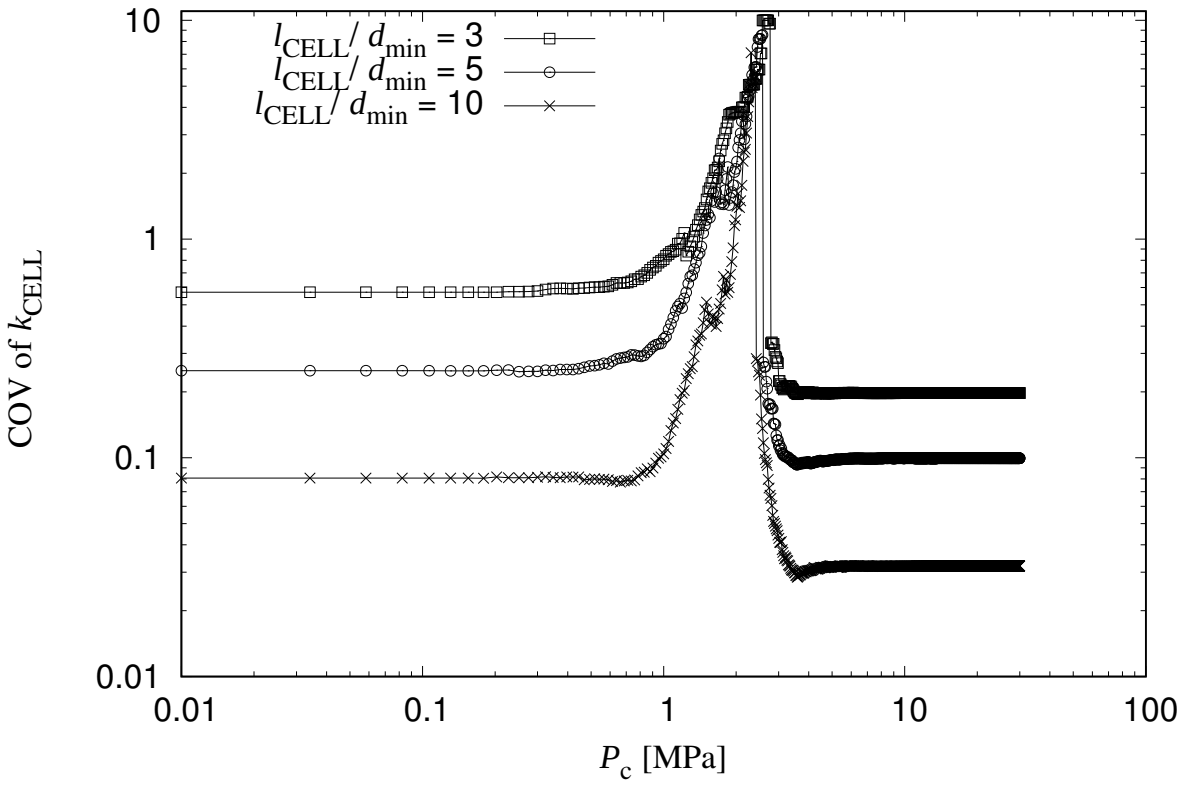

Figure 6.12: Influence of cell size on conductivity during drying: COV of k_{CELL} versus capillary suction P_c for 100 realisations for $l_{\text{CELL}}/d_{\text{min}} = 3$, 5 and 10.

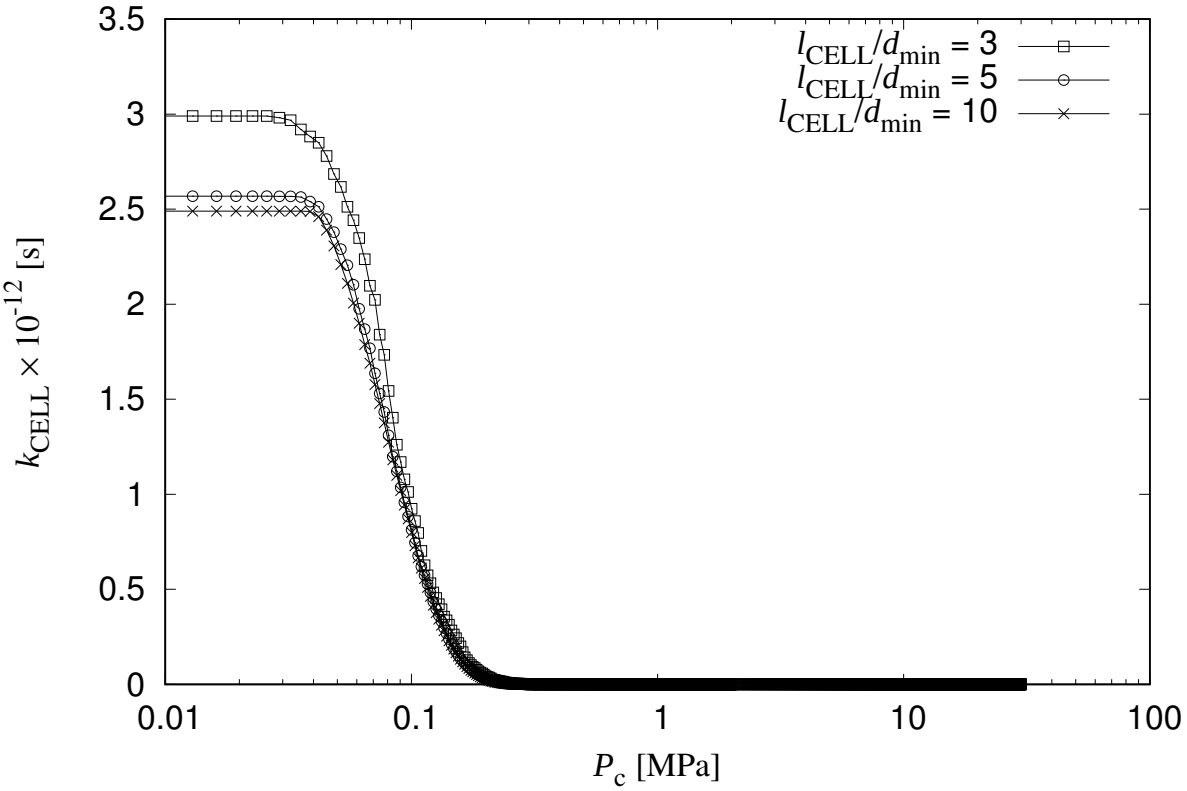

Figure 6.13: Influence of cell size on mean conductivity during wetting: conductivity k_{CELL} versus capillary P_c for 100 realisations for $l_{\text{CELL}}/d_{\text{min}} = 3$, 5 and 10.

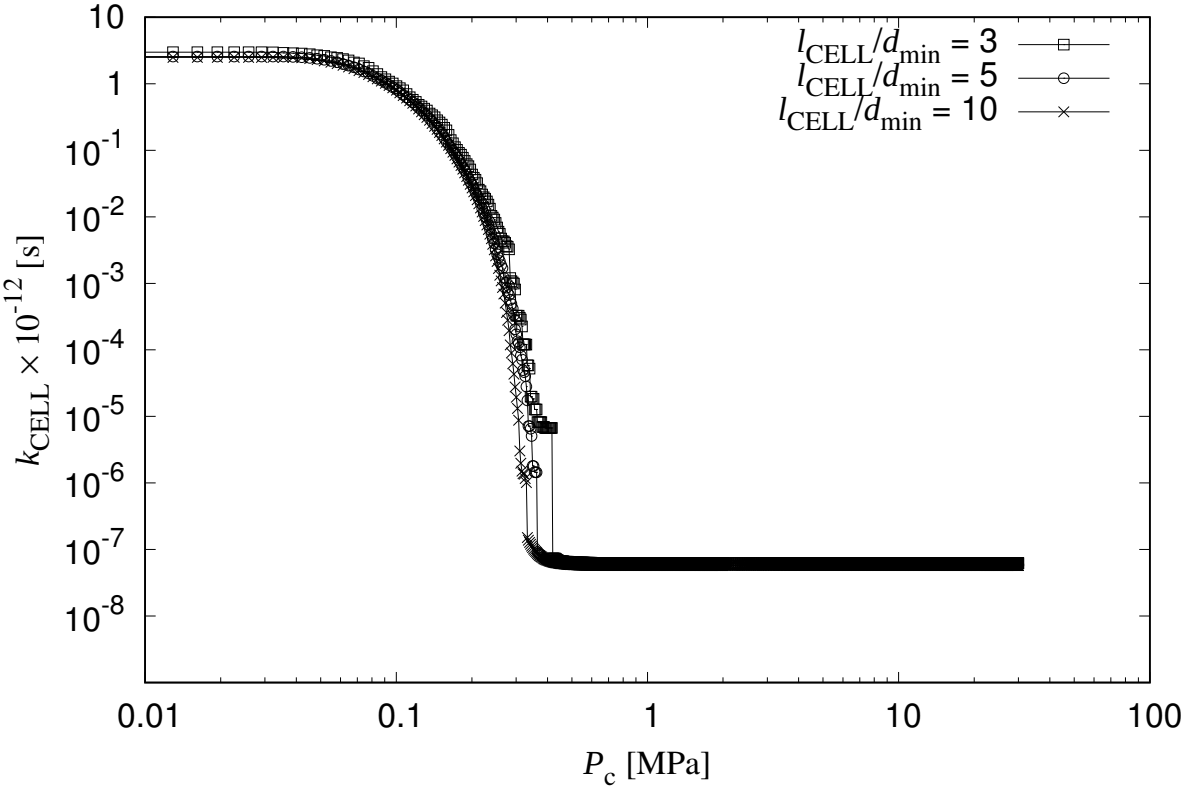

Figure 6.14: Influence of cell size on mean conductivity during wetting: conductivity k_{CELL} (in log scale) versus capillary P_c for 100 realisations for $l_{\text{CELL}}/d_{\text{min}} = 3$, 5 and 10.

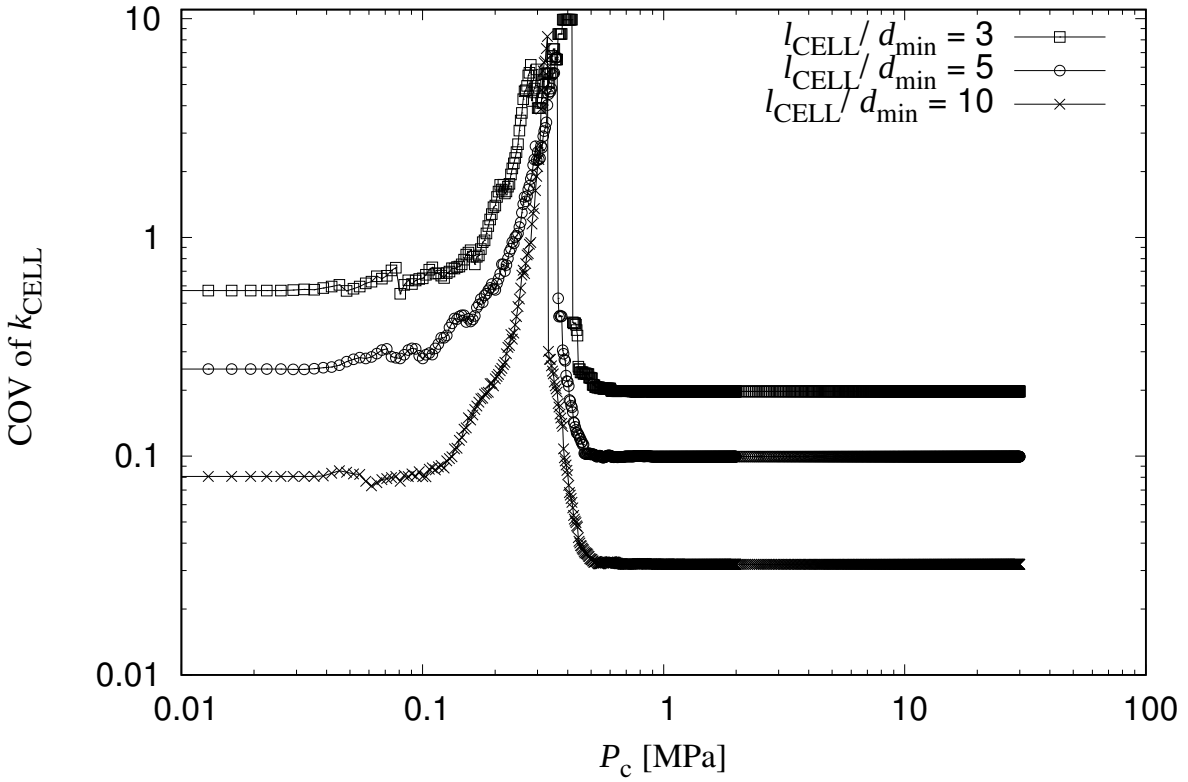

Figure 6.15: Influence of cell size on conductivity during wetting: COV of k_{CELL} versus capillary suction P_{c} for 100 realisations for $l_{\text{CELL}}/d_{\text{min}} = 3$, 5 and 10.

The variation of the COV of k_{CELL} during wetting, is presented in Figure 6.15 for $l_{\text{CELL}}/d_{\text{min}} = 3$, 5 and 10. Similar behaviour to that presented during drying is observed.

From Figures 6.12 and 6.15, it can be observed that both for drying and wetting curves there is a narrow range of P_{c} over which the COV of k_{CELL} is very large. This could be interpreted that over this narrow range of P_{c} there is no size of cell that gives an RVE. Reason for this is apparent when k_{cell} is plotted versus P_{c} in a log-log plot. For the range of P_{c} where high values of COV occur, cells can be seen that exhibit k_{cell} with difference of orders of magnitude. Outside this narrow range of P_{c} with large COVs, the COV of k_{cell} for $l_{\text{CELL}}/d_{\text{min}} = 10$ is low. Therefore, this cell size can be thought to be used as an RVE.

6.4 Young's modulus and Poisson's ratio

The influence of cell size on the Young's modulus E_{macro} as well as the influence of the mechanical element ratio of the tangential to the normal modulus γ_1 on Poisson's ratio ν_{macro} are investigated. Four cell sizes of $l_{\text{CELL}}/d_{\text{min}} = 3$, 5, 10 and 20 were used with $d_{\text{min}} = 1 \times 10^{-3}$ m which is different than the one used in Sections 6.2 and 6.3. For each analysis a uniaxial strain ε_{11} is applied and the lateral and shear component are kept zero. The

macroscopic Young's modulus E_{macro} is evaluated as the ratio of the reacting stress σ_{11} over the applied strain ε_{11}. The element normal modulus was chosen arbitrarily as $E = 31.5$ MPa. Furthermore, the ratio of the element tangent modulus to the element normal modulus was chosen as $\gamma_1 = 1$. Also, ratio of the element rotational modulus to the element normal modulus was chosen as $\gamma_2 = 1$. Additionally, the influence of the mechanical element cross-section radius distribution on the macroscopic Young's modulus E_{macro} of the cell and the macroscopic Poisson's ratio ν_{macro} was investigated. For this, the sum of all element volumes was kept constant equal to 80 $\%$ of the total cell volume for two mechanical radii distributions with $\text{COV}^{\text{mech}} = 0$ and $\text{COV}^{\text{mech}} = 1$. By means of a trial and error process to obtain the mean radii values for which the sum of all element volumes would be 80 $\%$ of the total cell volume the following results were obtained. For $\text{COV}^{\text{mech}} = 0$, $r_{\text{mechm}} = 1.92 \times 10^{-4}$ m which corresponds to a network with all elements having the same cross-section. For $\text{COV}^{\text{mech}} = 1$, $r_{\text{mechm}} = 1.4 \times 10^{-4}$ m which results in a network, where the cross-section of elements vary.

The results are presented in Figure 6.16. Each case is presented according to the COV^{mech} values used. The error bars present $\pm$ the standard deviation of the results and the mean is presented by the symbols used. The standard deviation of E_{macro} reduces as the cell volume increases, which is an expected behaviour since for an elastic material, for increasing cell size the cell behaviour approximates that of an RVE.

It can be observed that E_{macro} for $\text{COV}^{\text{mech}} = 0$ is roughly double than that for $\text{COV}^{\text{mech}} = 1$. This can be explained by the concept of line elements in series. When the network is subjected to a uniaxial loading, the significant forces are forming a force chain on the direction of the load. Therefore, these forces are carried by chains of elements. Each chain is working similar to a chain of elements in series and the overall structure behaves as parallel chains formed by elements in series.

For a series of elements, the overall chain stiffness is strongly affected by the elements with the lowest stiffness. For the parallel chains, the total stiffness is the sum of the stiffness of each individual chain. In the case of $\text{COV}^{\text{mech}} = 0$, almost all elements posses the same stiffness. However, for $\text{COV}^{\text{mech}} = 1$ the stiffnesses of the elements vary. Therefore, for the latter case, the overall stiffness of each chain is determined by the elements with low stiffness as which is lower than that of the elements in the case of $\text{COV}^{\text{mech}} = 0$. This happens because for the two distributions the element lengths are roughly the same, but some cross-sections can be small for $\text{COV}^{\text{mech}} = 1$. Therefore, the chains of elements for the cells with $\text{COV}^{\text{mech}} = 1$ present a lower stiffness. Thus, the overall E_{macro} is lower as well.

The evolution of the Poisson's ratio ν_{macro} for varying γ_1 was investigated for the two cases for $l_{\text{CELL}}/d_{\text{min}} = 20$. The input parameters used are the same as those presented above. For each $\gamma_1 = 0$, 0.2, 0.4, 0.6, 0.8 and 1, one hundred network and radii realisations were performed. For each cell a uniaxial strain ε_{11} was applied with keeping all lateral and shear

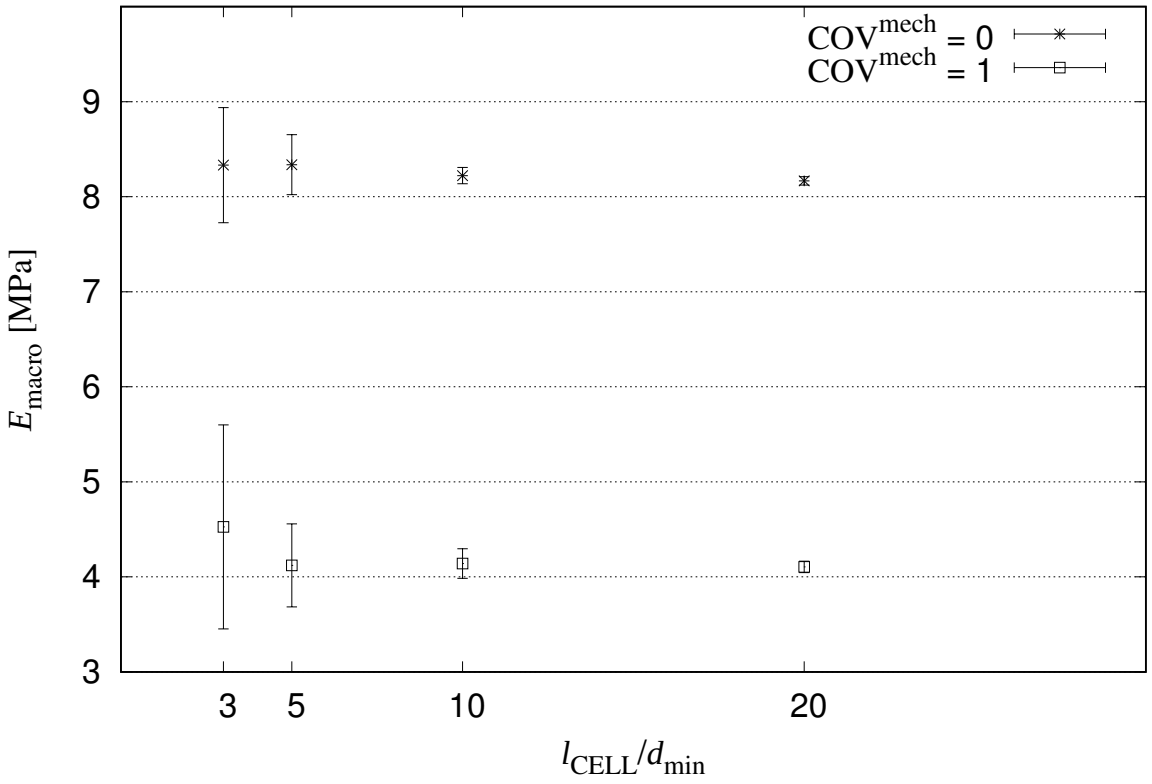

Figure 6.16: Influence of the cell size on Young's modulus: Young's modulus E_{macro} versus the ratio of the cell edge length to the minimum vertices distance $l_{\text{CELL}}/d_{\text{min}}$, the mean is presented with symbols and the error bars present $\pm$ one standard deviation for $\text{COV}^{\text{mec}} = 0$ and 1.

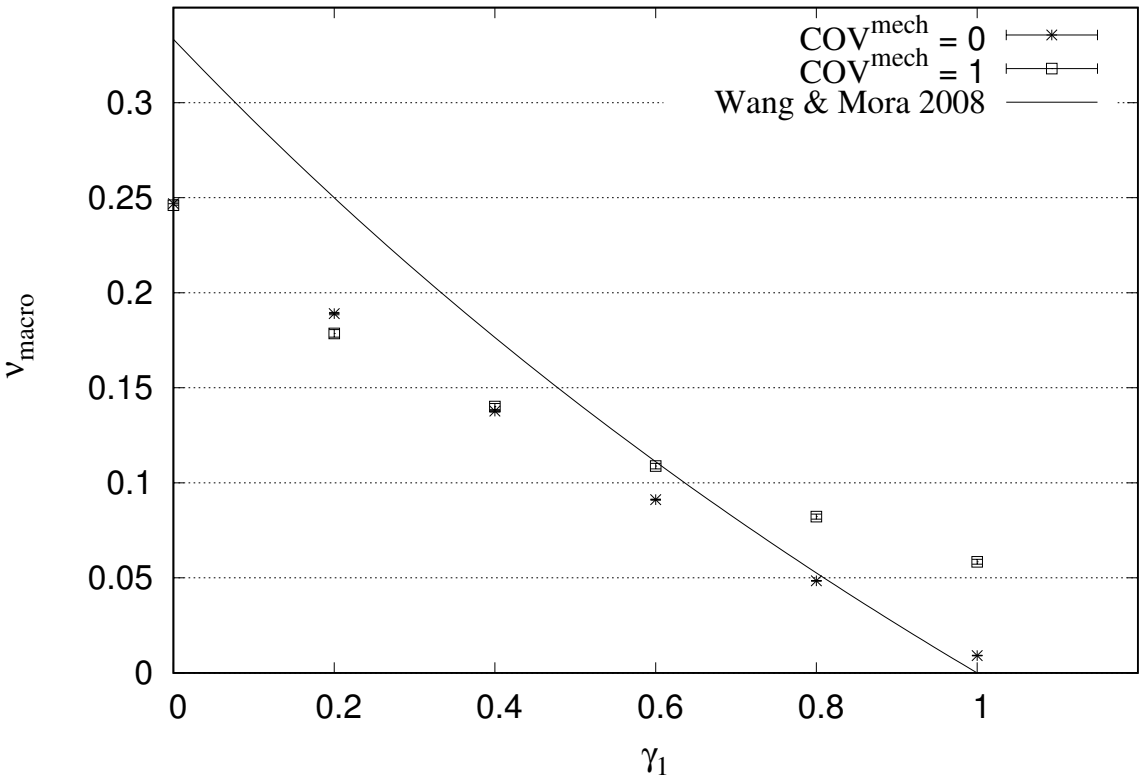

Figure 6.17: Influence of γ_1 on Poisson's ratio: Poisson's ratio ν_{macro} versus the normal to the shear modulus ratio γ_1 for $l_{\text{CELL}}/d_{\text{min}} = 20$, $\text{COV}^{\text{mec}} = 0$ and 1.

stress components equal to zero. Then, the mean of the resulting lateral strains was used to evaluate ν_{macro} of each cell. For each γ_1, the mean and standard deviation of the total number of realisations was evaluated.

The results are presented in Figure 6.17 in comparison with the analytical results presented in Wang and Mora (2008) for the FCC network. For the majority of γ_1 values, the Poisson's ratio for the random cases is less than the analytical expression. For $\gamma_1 = 0$ and 0.2 the results for $\text{COV}^{\text{mech}} = 1$ lie below those for $\text{COV}^{\text{mech}} = 1$. For higher values the reverse effect is presented, and the difference is consistently increasing for increasing γ_1. However, the results for $\gamma_1 = 0$ to 0.4 are very close still, for higher γ_1 the difference increases significantly. The variance of the element stiffness for $\text{COV}^{\text{mech}} = 1$ presents a strong influence on Poisson's ratio for $\gamma_1 = 1$. For $\gamma_1 = 0$ and 1, ν_{macro} results in values close to those of the continuum based approach reported in the literature.

The similarity in the results of ν_{macro} for $\gamma_1 = 0$ for the two COVs can be attributed to the fact that the elements cannot uptake any shear load. Therefore, for an elastic material with $\gamma_1 = 0$, for a prescribed normal strain the element nodes will move to a configuration where all elements exhibit no shear stress. Therefore, identical networks with high degree of indeterminacy and different cross-section areas will result in exactly the same strain field for the same normal strain applied. Therefore, for $\gamma_1 = 0$ the same ν_{macro} in any Delaunay

network is obtained.

Moreover, the random networks do not present $\nu_{\text{macro}} = 0$ for $\gamma_1 = 1$ as the case of an FCC network because in these analyses rotations are allowed ($\gamma_2 = 1$). Separate analyses of random networks with very high values of γ_2 resulted to $\nu_{\text{macro}} = 0$. However, a $\nu_{\text{macro}} = 0$ for $\gamma_2 = 1$ would be recovered if the dual Voronoi faces would be used as cross-sections and then applied a Rigid Body Spring Model (Berton and Bolander, 2006). Furthermore, the difference in the ν_{macro} for $\gamma_1 = 1$ between the two random networks is due to the difference in the area distributions. Since, the elements can now transfer shear forces, the nodes displace differently according to elements' shear stiffness. Therefore, for the same normal strain applied, a different displacement field of the nodes will result in a different distribution of shear and normal stresses in the elements.

The relationship between E_{macro} and γ_1 in (4.6) for an FCC structure proposed in Wang and Mora (2008), involves the element cross-section area A_{mech} and the element length l_{e}. However, the relationship for ν_{macro} in (4.6) that does not involve any element parameters. For the FCC structure the element lengths and the element cross-sections are equal. However, this is not the case for random networks used in the present section. The results of a random mechanical network with $\text{COV}^{\text{mech}} = 0$ were chosen for a comparison with the results from the analytical expression of (4.6). For this network, all elements have the same cross-section $A_{\text{mech}} = \pi r_{\text{mech}}^2 = 1.158 \times 10^{-7}$ m^2. The element length in (4.6) was chosen to be equal to the minimum distance allowed in the random network $l_e = d_{\text{min}} = 10^{-3}$ m. The numerical results of the present mechanical random networks to the analytical results of Wang and Mora (2008) are presented in Figure 6.18. The differences of the results are due to the difference in element arrangement between the random and the FCC structure, the variation of element lengths in random networks in contrast with constant lengths in FCC structures and finally with choice of $\gamma_2 = 1$ that allows the nodes to rotate rather than the assumption of no rotations made for evaluating (4.6).

6.5 Discussion

The investigation of the influence of the cell size on retention and conductivity for varying capillary suction was presented. A computationally efficient RVE size for the retention behaviour of a transport material was found for $l_{\text{SVE}}/d_{\text{min}}$ = 10. The increase and then decrease of COV of S_{r} with P_{c} increase was attributed to the change of the negative derivative of degree of saturation with respect to capillary suction $-\text{d}S_{\text{r}}/\text{d}P_{\text{c}}$. The COV of S_{r} increases with an increase of $-\text{d}S_{\text{r}}/\text{d}P_{\text{c}}$.

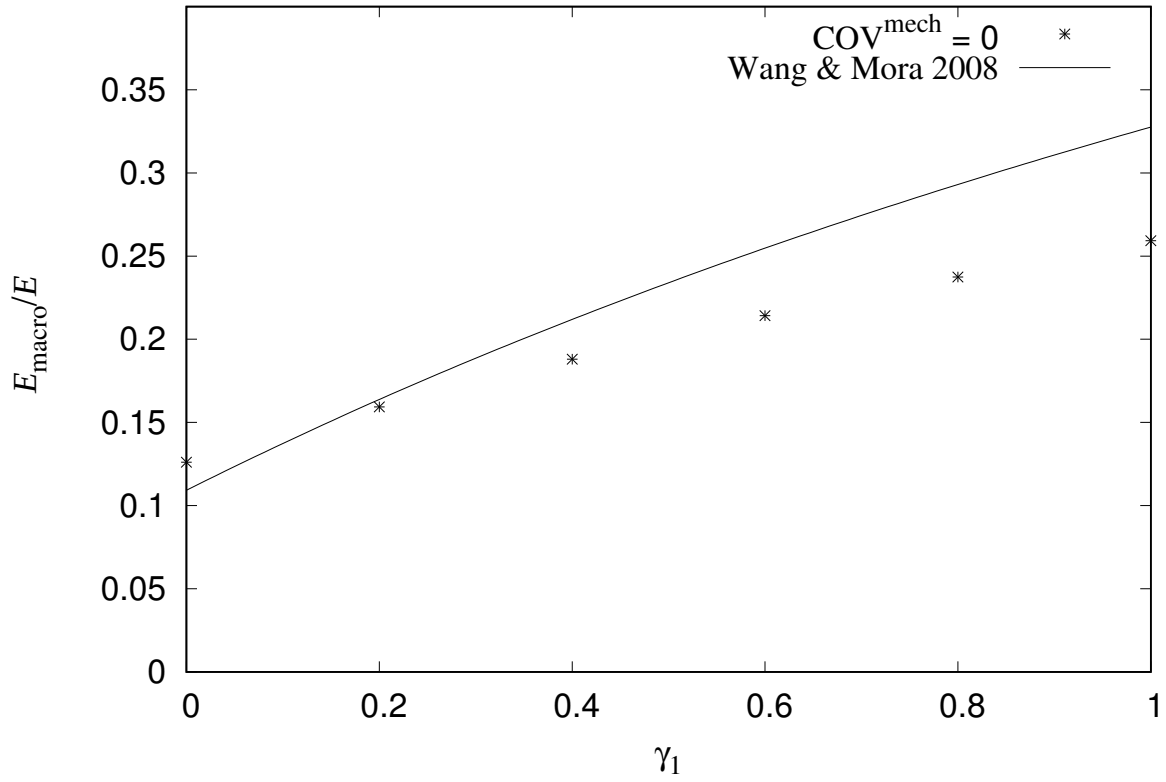

Figure 6.18: Influence of γ_1 on E_{macro}/E: the ratio of macroscopic Young's modulus to the element normal modulus E_{macro}/E versus the normal to the shear modulus ratio γ_1 for cell size of $l_{\text{CELL}}/d_{\text{min}} = 20$, for the numerical results $\text{COV}^{\text{mech}} = 0$ and results based on Wang and Mora (2008).

The influence of cell size on cell conductivity k_{CELL} for almost saturated conditions ($S_{\text{r}} \approx 0.99$) for constant and varying network geometries was also investigated. It was found that the mean of k_{CELL} for varying geometry converges to a constant value at smaller cell sizes than for the constant geometry cells. It was suggested that this effect could be attributed to less significant changes of cell conductivity when new geometries and new pipe radii realisations are combined. More investigation is needed to verify this hypothesis.

For unsaturated conditions, for the majority of the range of P_{c}, very low values of COV of k_{CELL} were found. For a range of very low conductivities, the COV of k_{CELL} was found to be very high. This behaviour was attributed to the fact that for the same value of P_{c} for which high values of COV of k_{CELL} is observed there can be cells that exhibit conductivities of differences higher than an order of magnitude. Such high differences can be observed between the means of k_{CELL} when plotted against P_{c} in a log-log scale (Figures 6.11 and 6.14). These high differences could be attributed to the effect of percolation which is the stage at which a continuous path of wetting fluid in the direction of the gradient applied that connects opposite faces is formed.

The RVE size was also investigated for the mechanical cell in elastic conditions. It was found that the RVE size is the cell with edge length to minimum node distance radio $l_{\text{CELL}}/d_{\text{min}} = 20$. Furthermore, an investigation was performed for the influence of mechanical element cross-section distribution on the macroscopic elastic cell properties E_{macro} and ν_{macro} for elements with the same normal modulus. It was found that for two distributions chosen to result to the same target of sum of the volumes of all elements, the distribution with lower COV^{mech} presents higher E_{macro} values. For values of γ_1 between 0 and 0.4, the cells with the two distributions presented similar values of ν_{macro} that are deviating for higher values of γ_1. For $\gamma_1 = 0$, the resulting ν_{macro} is solely dependent on the network geometry and not on element area or element normal modulus. For $\gamma_1 = 1$ the difference between the analytical and the numerical results was attributed to differences in the assumption of rotation of nodes. Additionally, the size of the RVE is not influenced by the mechanical element cross-section distribution.

Chapter 7

Influence of microstuctural changes on conductivity, porosity and degree of saturation

7.1 Introduction

There are many materials that exhibit microstructural changes when they are filled with water. For instance, compacted bentonite can show reduction of inter-aggregate pore volumes when it is wetted under confined conditions, due to the wetting-induced swelling of the individual aggregate caused by repulsive forces developed between the montmorillonite platelets (Delage et al., 2006). Another example is concrete, for which its pore volume reduces due to the solid hydration products generated in the presence of water (Hall et al., 1995; Martys and Ferraris, 1997).

In the present chapter a simple approach to represent pore volume changes is proposed where sphere and pipe radii change due to wetting but do not change continuously in time. Here, the transport network is not coupled with the mechanical network. In order to take into account the mechanical changes occurring in porous geomaterial under confined conditions due to presence of water (Delage et al., 2006), it is assumed that pipe radii and sphere radii reduce when they are filled with water.

The model description is presented in Section 7.2. Thereafter, the investigation of k_{CELL}, S_{r} and n evolution during wetting are presented in Sections 7.3 and 7.4. In both cases, numerical results for saturated conditions are compared to analytical ones. Finally, the results are further discussed.

7.2 Pipe and sphere size evolution due to particle swelling

In the present section, water and air are going to be used instead of wetting and drying fluid due to the particular application considered. When a void is filled with water, the surrounding solid phase expands. If this expansion is constrained, the void volume decreases. In Figure 7.1a a 2D cross-section of a sphere or pipe is schematically presented. The solid that surrounds the sphere or pipe of initial radius r_0 is presented with dark grey colour. The extra volume that the solid will occupy after its expansion, once the sphere or pipe is filled with water, is presented with the hatched area and the sphere or pipe has now a radius $(1-\alpha)r_0$.

The influence of the wetting induced swelling of the bentonite aggregates and the resulting reduction of pore spaces is considered by instantly reducing the radius of any pipes and spheres that fill with water. The change of either the sphere or pipe radii r is described by the expression as a function of capillary suction

$$r = \begin{cases} \left[H(P_{\mathrm{c}}) - (H(P_{\mathrm{c}}) - H(P_{\mathrm{c}} - P_{\mathrm{c0}}))\alpha\right] r_0 & \forall \;\; (1-\alpha)r_0 \geq r_{\mathrm{min}} \\ H(P_{\mathrm{c}})r_0 + (H(P_{\mathrm{c}}) - H(P_{\mathrm{c}} - P_{\mathrm{c0}}))r_{\mathrm{min}} & \forall \;\; (1-\alpha)r_0 < r_{\mathrm{min}} \end{cases} \tag{7.1}$$

where r_0 is the radius of the pipe or sphere when filled with air, $H()$ is the Heaviside function, r_{min} is the minimum radius possible that a pipe or sphere can be reduced to and α is a dimensionless coefficient that reduces the radius when the pipe or sphere fills with water at a capillary suction P_{c0}. A schematic representation of the change of r for varying P_{c} as described in (7.1) is presented in Figure 7.1b. The pipe or sphere under consideration starts from dry conditions, hence from high P_{c} values, having a radius of r_0. At P_{c} = P_{c0}, the void fills with water and its radius instantly reduces to a value of $(1-\alpha)r_0$ and remains constant during further capillary suction decrease.

7.3 Conductivity evolution

The evolution of conductivity was investigated for varying α. The network began from an almost dry condition ($S_{\mathrm{r}} \approx 0.01$) and capillary suction P_{c} was then progressively decreased. For each decrease of P_{c}, the wetting fluid enters some spheres previously filled with drying fluid based on their original radius since their radii change only after the wetting fluid enters. Therefore, for the same network sphere and pipe generation the wetting fluid will enter spheres

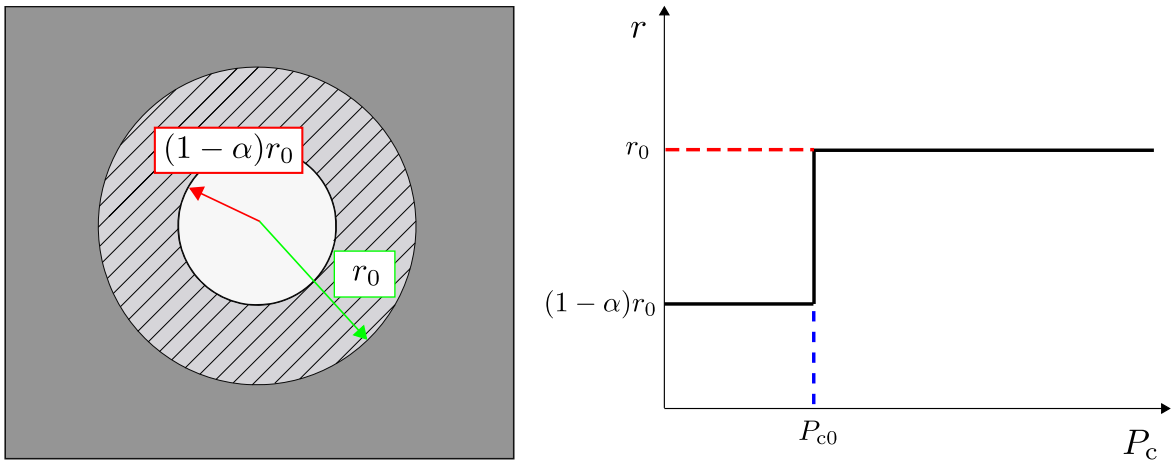

(a) (b)

Figure 7.1: Microstructural evolution: (a) schematic presentation of the radius change from r_0 to $(1-\alpha)r_0$ of a water filled sphere or pipe and (b) graph presenting the change of radius of either a pipe or a sphere when water filled or emptied at capillary suction P_{c0}.

in the same sequence during wetting for any value of α, and the values of P_c at which a given sphere wets is independent on the value of α.

The cell size was determined by the ratio l_{CELL}/d_{min}= 7.14 with all remaining network parameters given in Table 4.1 and Table 5.1 but having a surface tension of 1 N/m. For each value of α an identical set of 100 different network realisations was analysed. The evolution of conductivity from almost dry ($S_r \approx 0.01$) to almost saturated ($S_r \approx 0.99$) conditions is presented in Figure 7.2 for different α values. On the vertical axis in Figure 7.2, the conductivity is presented as the ratio of the mean network conductivity k_{CELL} evaluated for the given P_c and α value divided by the mean network conductivity for almost saturated conditions ($S_r \approx 0.99$) for α = 0 denoted as $k_{CELL,0}$. In the present case $k_{CELL,0}$ is equal to 1.33×10^{-12} s.

For almost saturated conditions ($S_r \approx 0.99$), $k_{CELL}/k_{CELL,0}$ ratio can be analytically evaluated. All analyses have the same COV^p and r_p prior to wetting. Almost all the pipes are filled with wetting fluid, hence the flow rate along each pipe is a function of the pipe radius to the power of four (see (3.18) and (3.19)). Therefore, for almost saturated conditions, the network conductivity is a function of the mean pipe radius to the power of four i.e. $k_{CELL} = \xi r_{pm}^4$, where ξ is a constant parameter. For a microstructurally evolving material in almost saturated conditions, the mean radius is reduced to approximately $(1-\alpha)r_{pm}$ and the COV^p remains approximately unchanged (these statements would be precise if every sphere radius decreased $(1-\alpha)$ times its initial radius i.e. if there were no seeding spheres and no spheres where the radius reduction was restricted by r_{min}). From the above it can be deduced that for the almost saturated condition the ratio $k_{CELL}/k_{CELL,0} \approx (1-\alpha)^4$. This is verified by comparing these ratios for the almost saturated condition to the above analytical expression in Figure 7.3. The numerical and analytical results present a good match.

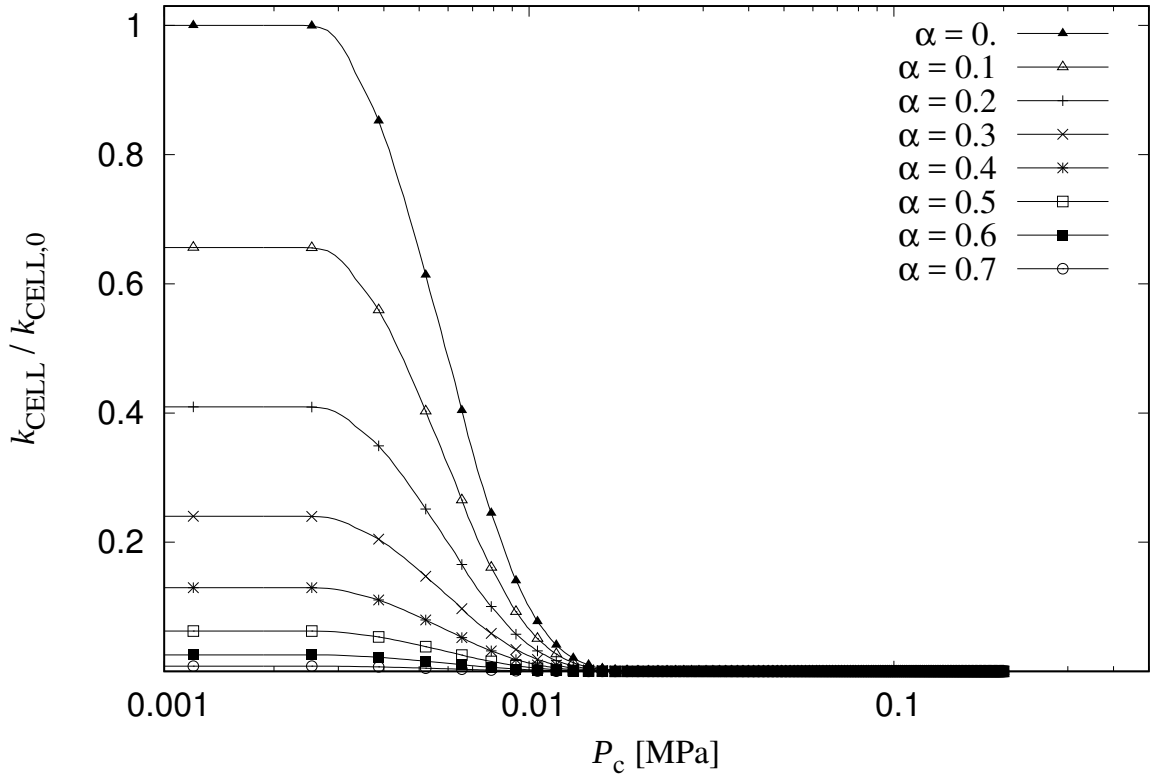

Figure 7.2: Conductivity evolution for wetting process: conductivity ratio $k_{\text{CELL}}/k_{\text{CELL,0}}$ versus capillary suction P_{c} for varying radius reduction factor α.

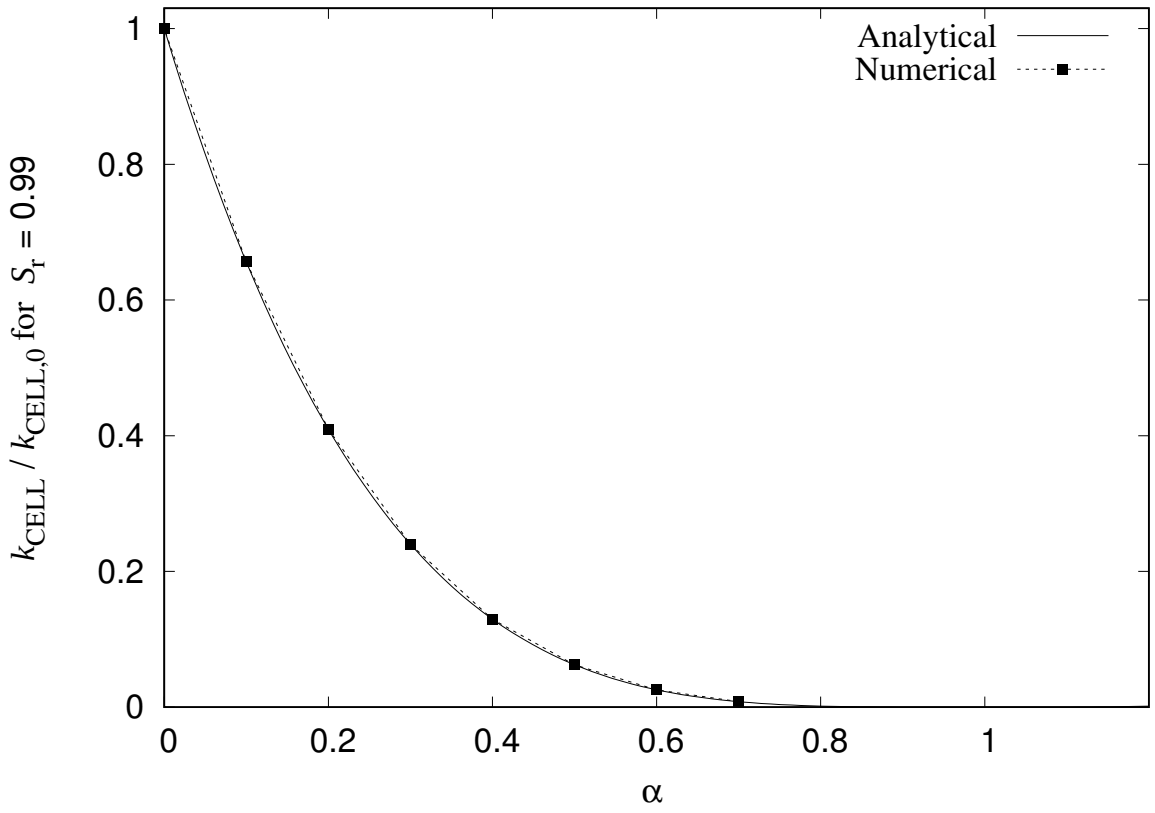

Figure 7.3: Comparison of the analytical to the numerical results for $S_{\text{r}} = 0.99$: conductivity ratio $k_{\text{CELL}}/k_{\text{CELL,0}}$ versus radius reduction factor α.

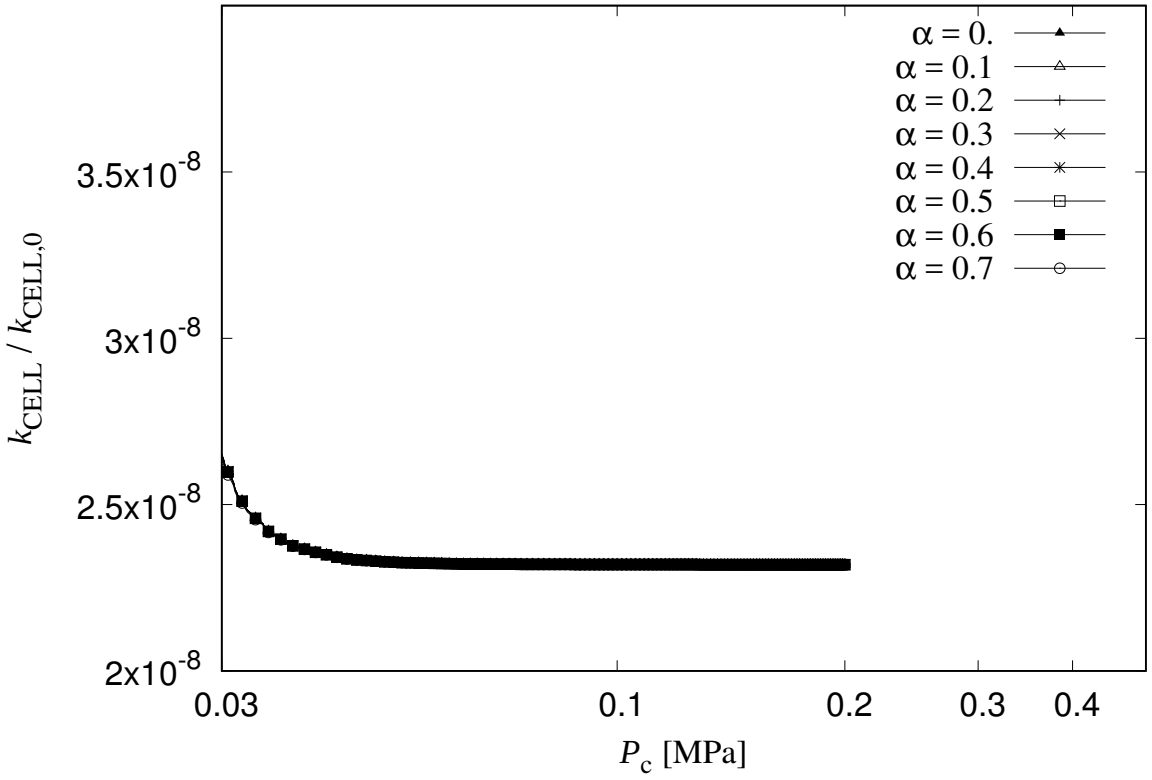

Figure 7.4: Zoom of Figure 7.2 for high values of P_{c}.

For almost dry conditions ($S_{\mathrm{r}} \approx 0.01$), almost all pipes are filled with the drying fluid which is gas in this case. Therefore, very few pipe radii are changed and the overall conductivity is dominated by the gas fluid filled pipes. Since in all cases the same pipe radii distribution input parameters are used, the mean conductivities for almost dry conditions should be almost the same for all values of α. This behaviour can be observed in Figure 7.4 which is a zoom-in to the $k_{\mathrm{CELL}}/k_{\mathrm{CELL},0}$ values presented in Figure 7.2 for high P_{c} values. All cases present a similar conductivity in the almost dry condition, as expected.

7.4 Porosity and saturation evolution

The evaluation of the porosity and the degree of saturation for a microstructurally evolving porous material is based on the pore volume scaling technique presented in Section 3.4.4. When a sphere is filled with wetting fluid, its radius reduces according to (7.1). In the network model, the pore volume scaling approach described in Section 3.4.4 means that each sphere represents a number N of pores, such that when all spheres are at their initial radius, each sphere represents the same volume of pores. The value of N is therefore given by

$$N = \left(\frac{r_{\text{sm0}}}{r_{\text{s0}}} \right)^3 \tag{7.2}$$

where r_{s0} is the initial radius of the individual sphere and r_{sm0} is the mean sphere radius when all spheres are at their initial radius. When a sphere is filled with wetting fluid, the number of pores N that the sphere represents is unchanged but the volume of the pores represented is reduced. The volume of pores V_{v} represented by an individual sphere is now given by

$$V_{\text{v}} = N \frac{4}{3} \pi r_{\text{s}}^3 = \frac{4}{3} \pi \frac{r_{\text{sm0}}^3 r_{\text{s}}^3}{r_{\text{s0}}^3} \tag{7.3}$$

where r_{s} is the current radius of the sphere, which will be less than the initial radius r_{s0} if the sphere is filled with wetting fluid and if $\alpha > 0$. The porosity n is therefore given by

$$n = \frac{4\pi r_{\text{sm0}}^3}{3 l_{\text{CELL}}^3} \sum_{i=1}^{m} \left(\frac{r_{\text{s}}}{r_{\text{s0}}} \right)^3 \tag{7.4}$$

where m is the number of spheres within the cell. From the above, and comparing (7.4) with (3.15), it can be understood that the porosity n decreases as the material is wetted (as P_{c} decreases).

The evolution of microstructure also effects the evolution of S_{r}. When a sphere is filled with wetting fluid and its volume changes, it now represents a different fraction of the total void volume. Hence the degree of saturation S_{r} is given by

$$S_{\text{r}} = \frac{\sum_{i=1}^{m_{\text{w}}} \left(\frac{r_{si}}{r_{\text{s0}i}} \right)^3}{\sum_{i=1}^{m} \left(\frac{r_{si}}{r_{\text{s0}i}} \right)^3} \tag{7.5}$$

where the summation in the numerator of (7.5) involves only those spheres filled with wetting fluid (where m_{w} is the number of spheres filled with wetting fluid).

Note that, in determining the porosity n and degree of saturation S_{r} through (7.4) and (7.5), only the capillary scale pores represented by spheres in the network model are considered. This means that for a material such as bentonite, the calculated values of n and S_{r} provide only the capillary scale porosity and degree of saturation and do not include the smaller

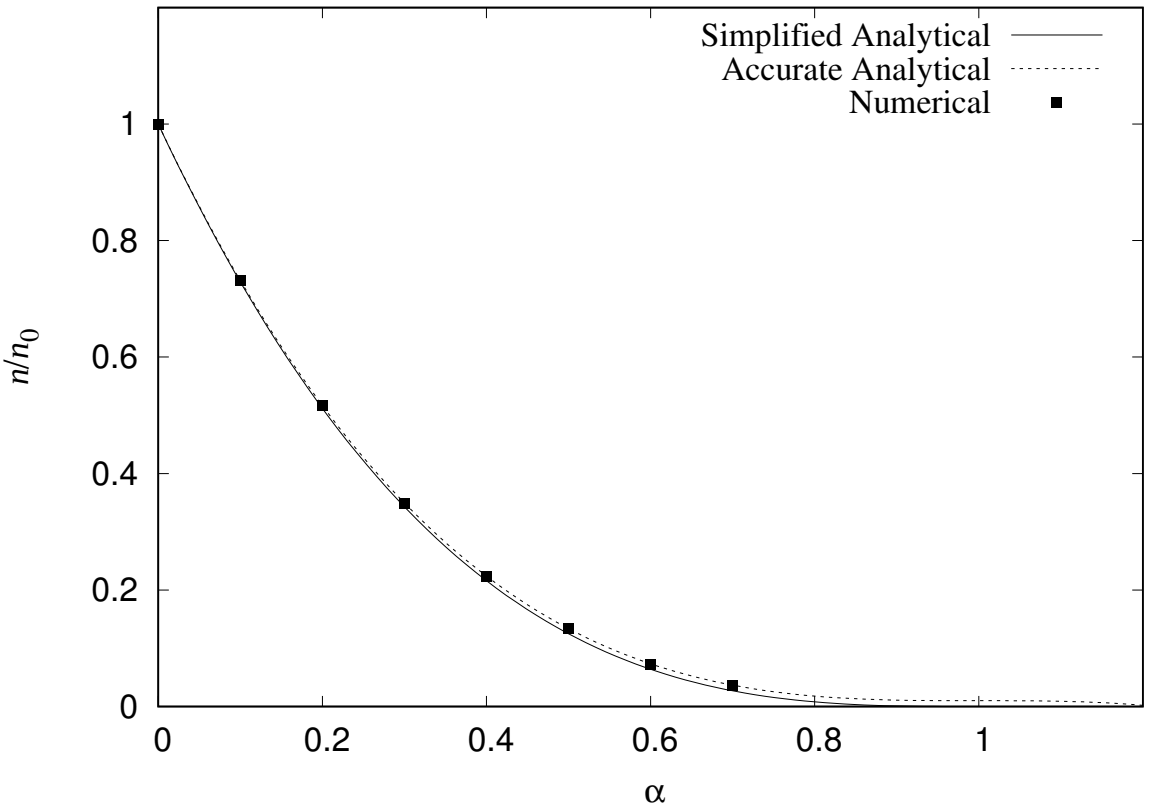

Figure 7.5: Comparison of numerical and analytical results for almost saturated conditions ($m_{\mathrm{w}}/m \approx 0.99$): ratio of the current porosity n divided by the initial porosity n_0 versus radius reduction factor α.

scale intra-aggregate void volume. This intra-aggregate void volume (and the corresponding volume of intra-aggregate wetting fluid volume) will increase during a wetting process, as the bentonite aggregates take in water and expand.

The variation of porosity n with decreasing capillary suction for various α values is presented in Figure 7.6. The porosity evolution is presented in terms of the ratio of the current porosity n divided by the initial porosity n_0, i.e. the porosity before the initiation of wetting. For each volume of P_{c}, the porosity decreases with increasing α. Ignoring seeding spheres and ignoring any influence of spheres where the reduction of radius is restricted by r_{min} the value of n/n_0 should tend to $(1-\alpha)^3$ in the almost saturated condition ($m_{\mathrm{w}}/m \approx 0.99$). Figure 7.5 shows the numerical results for $m_{\mathrm{w}}/m \approx 0.99$ compared against this analytical expression. Note that the numerical values of n/n_0 are greater than the analytical expression for high values of α. This is due to the disproportionate effect of the small number of seeding spheres still filled with drying fluid. Although those seeding spheres only account for 1% of the total void volume if the remaining 99% of spheres have dramatically reduced in volume when they wetted, i.e. if α is large. Allowing for these seeding spheres (but still ignoring the influence of any spheres where the reduction of radius is restricted by r_{min}), the value of n/n_0 in the almost saturated condition should be given by

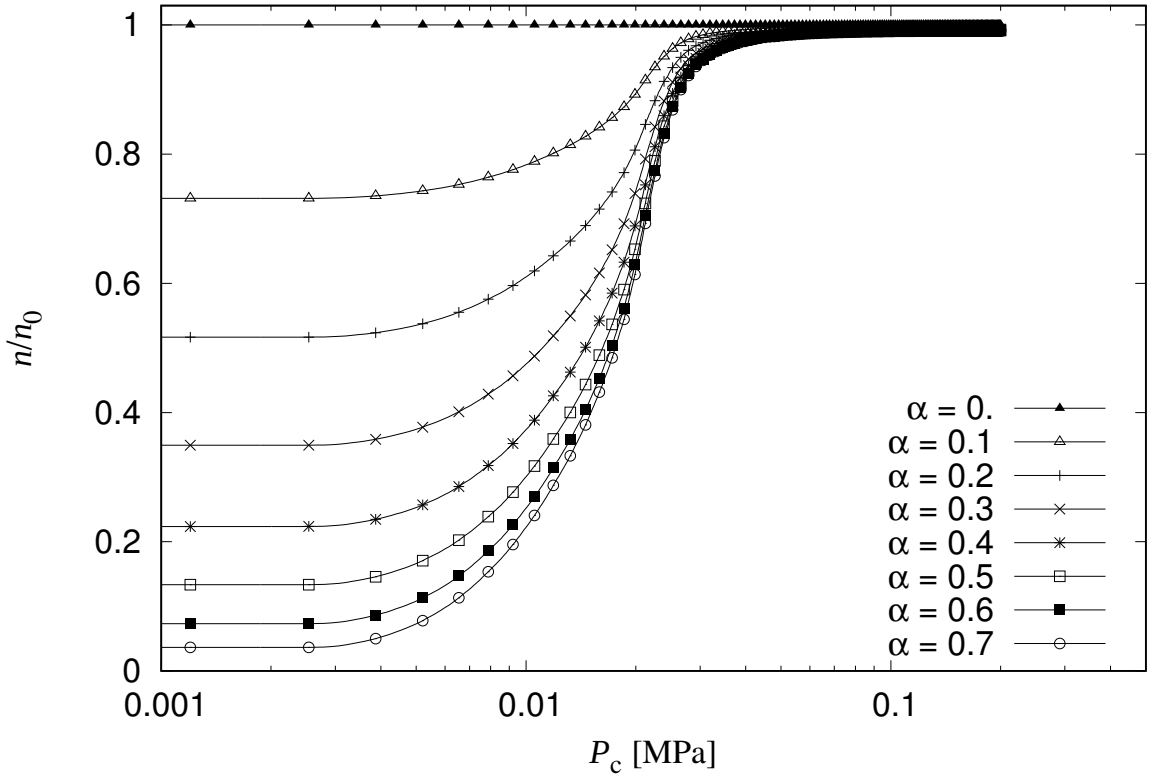

Figure 7.6: Porosity evolution for a wetting process: ratio of current to initial porosity ratio n/n_0 versus capillary suction P_c for varying radius reduction factor α.

$$\frac{n}{n_0} = \frac{(1-\alpha)^3(m - m_{\text{seed}}) + m_{\text{seed}}}{m} \tag{7.6}$$

where m_{seed} is the number of seeding spheres. In all analyses presented here, $m_{\text{seed}} \approx 0.01$ m. The analytical expression of (7.6) is also presented in Figure 7.5, which shows that the numerical results agree with this corrected analytical expression.

The evolution of the degree of saturation S_r with decreasing P_c for various α values is presented in Figure 7.7. It can be observed that for each value of P_c, the value of S_r decreases with increasing α. Also, for $\alpha > 0$, the final value of S_r (corresponding to $m_\mathrm{w}/m \approx 0.99$) is less than 0.99 and it decreases significantly with increasing α. Again this due to the disproportionate effect of the seeding spheres, which are still filled with drying fluid and therefore have not reduced in size, unlike the other 99% of spheres. Allowing for these seeding spheres (but ignoring the influence of any spheres where the radius reduction is restricted by r_{min}), the analytical expression for the value of S_r in the almost saturated condition (when only the seeding spheres are left filled with drying fluid) is given by

$$S_\mathrm{r} = \frac{(1-\alpha)^3(m - m_{\text{seed}})}{(1-\alpha)^3(m - m_{\text{seed}}) + m_{\text{seed}}} \tag{7.7}$$

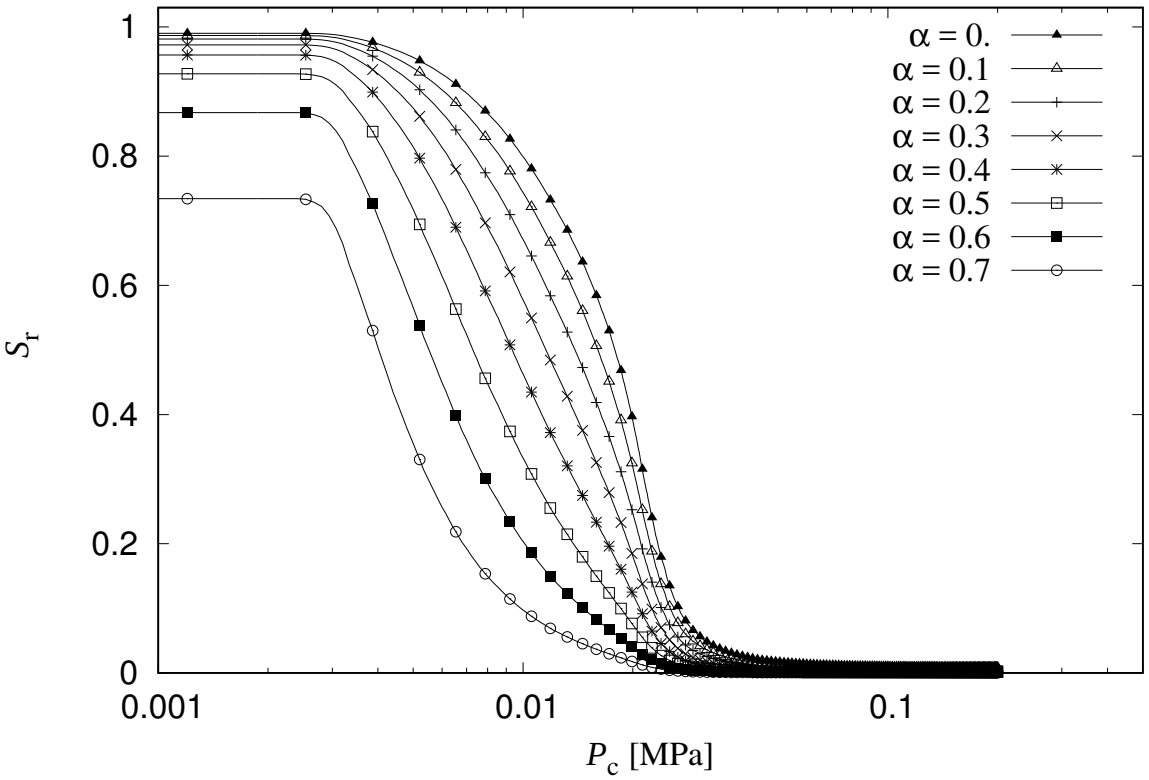

Figure 7.7: Retention curves for wetting process: degree of saturation S_r versus capillary suction P_c for varying radius reduction factor α.

Figure 7.8 shows the numerical results for the maximum value of S_r (corresponding to $m_w/m \approx 0.99$) plotted against α, together with the analytical expression of (7.6) confirming excellent agreement.

A zoom-in in to the high P_c section of Figure 7.7 is presented in Figure 7.9. This shows that the value of S_r in the almost dry condition (with $m_w/m \approx 0.01$) is dependent on the value of α, because the seeding spheres (filled with fluid) have already reduced in volume if $\alpha > 0$. Accounting for these seeding spheres (but ignoring the influence of any seeding spheres where the radius reduction is restricted by r_{min}) the analytical expression for the corresponding minimum value for S_r is

$$S_r = \frac{(1-\alpha)^3 m_{seed}}{(1-\alpha)^3 m_{seed} + (m - m_{seed})} \tag{7.8}$$

Figure 7.10 shows excellent agreement between the numerical results and the analytical expression of (7.8). The small differences presented in low values of α are evident because the scale on the S_r axis is very small ($S_r = 0.01$ for $\alpha = 0$) compared to results presented in Figure 7.8 where $S_r = 1$ for $\alpha = 0$.

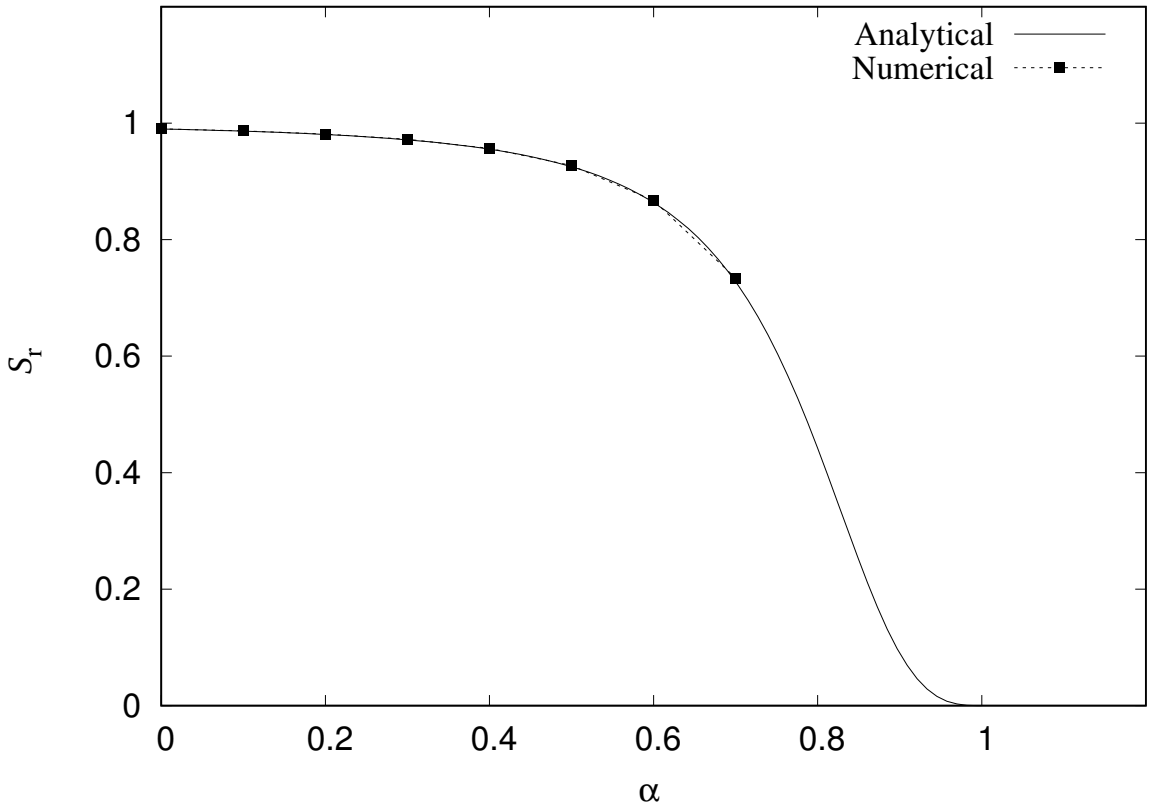

Figure 7.8: Comparison of numerical to analytical results for maximum saturation: degree of saturation S_r versus radius reduction factor α.

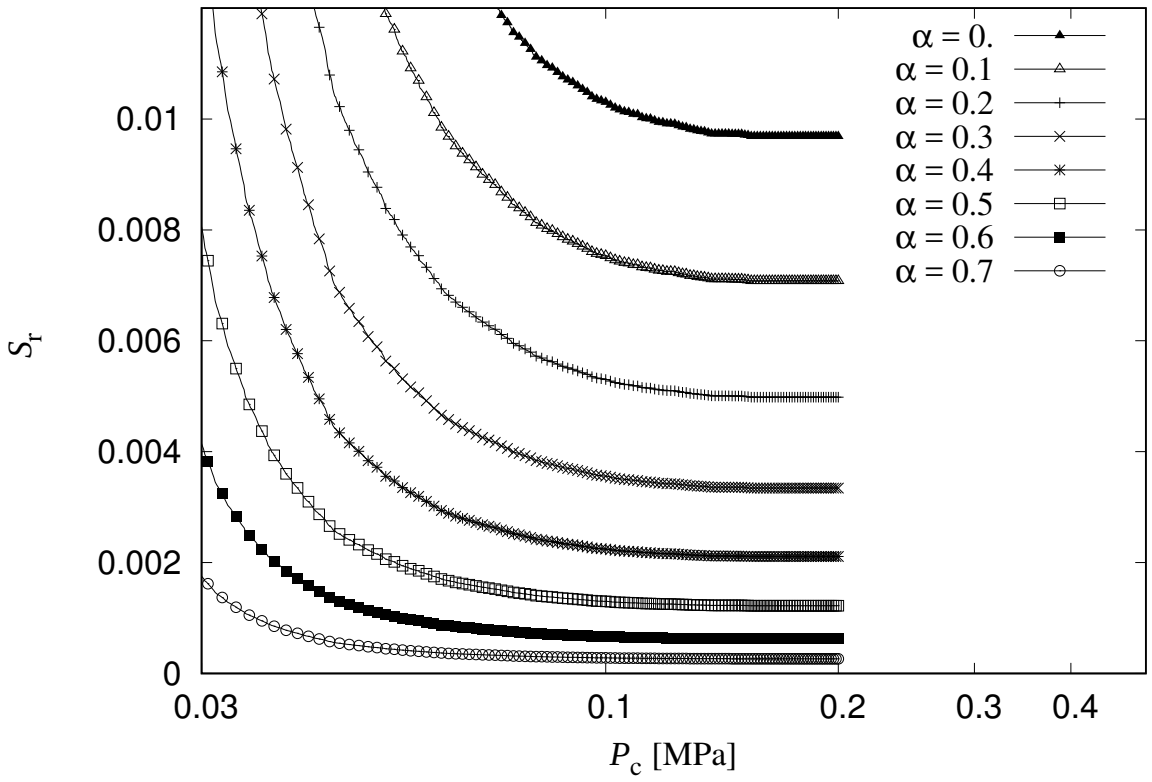

Figure 7.9: A zoom in Figure 7.7 for high P_c values.

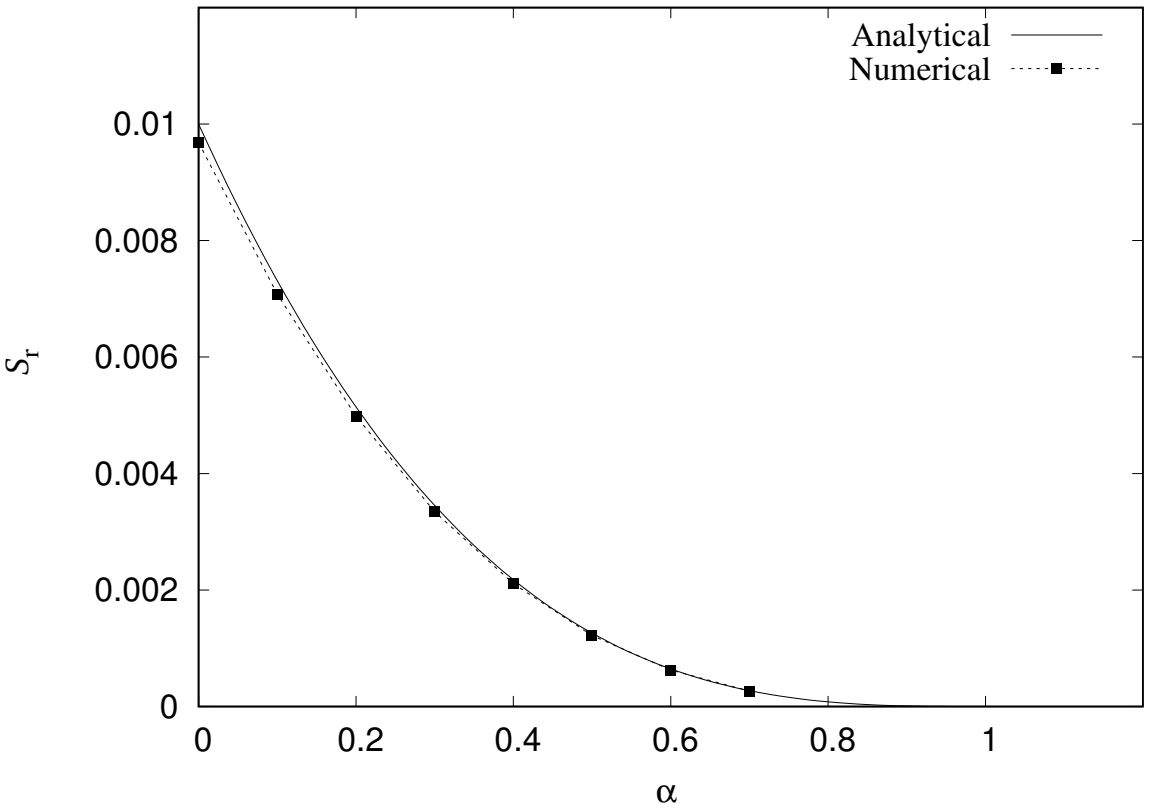

Figure 7.10: Comparison of numerical to analytical results for minimum saturation: degree of saturation S_{r} versus radius reduction factor α.

7.5 Discussion

An investigation was presented for the behaviour of the model for the simulation of the pore network changes of microstructurally evolving porous material. More specifically, the influence of parameter α, that is used for describing a microscopically evolving porous material, on the evolution of k_{CELL}, S_{r} and n was investigated. The results for m_{w}/m = 0.99 and 0.01 were verified through analytical expressions presented. For high P_{c} values, α does not influence k_{CELL} but for lower values of P_{c} a strong influence is observed. S_{r} and n are strongly influenced by the chosen value of α over all the P_{c} spectrum.

Additionally, it was shown in Figure 7.2 that conductivity increases monotonically with capillary suction decrease. However, this is not necessarily the case for conductivity evolution of bentonite under confined conditions (Wang et al., 2013). Athanasiadis et al. (2016) presented non-monotonical changes of cell conductivity during wetting based on an extension of the present work where the changes of the pipe and sphere diameters were coupled with mechanical changes of the dual mechanical network. The mechanical elements exhibited swelling (tensile) strains when at least one sphere located around them was wetted to simulate swelling induced wetting. Furthermore, the mechanical elements exhibited a simple elastic-plastic behaviour without hardening. Moreover, in Athanasiadis et al. (2016), a similar coupling of

the mechanical and transport network as those presented in Section 4.3.1 and Section 4.3.1, was used. In this work, pipe radii changes were associated to the plastic strains exhibited by the surrounding elements. Furthermore, the cell was subjected to wetting under confined conditions. As the cell was wetting, more mechanical elements were surrounded by at least a sphere filled with water presented swelling strains. Due to confinement, mechanical elements were compressed irrespective to the condition of their neighbouring spheres causing them to yield. Therefore, pipes that were not filled with water could change radius. Hence, it is concluded that the simple approach presented in this chapter, where pipe radii change only when they are filled with wetting fluid, is not sufficient to model non-monotonic conductivity changes with capillary suction decrease. The transport and mechanical networks have to be coupled, so that more complex phenomena are allowed to manifest, which then lead to the non-monotonic cell conductivity evolution.

Chapter 8

Calibration of transport model parameters and validation

8.1 Aim

In the previous chapters, the network model proposed in this thesis has been used to investigate the influence of pore scale phenomena on the evolution of macroscopic quantities such as relative permeability, degree of saturation. Here, a strategy to calibrate the model to predict macroscopic fluid retention is proposed. The aim of the calibration of the network model is to propose a method for the choice of pipe and sphere radii distributions to match easily obtainable experimental results for drying and wetting.

8.2 Strategy

The experimental results required for the calibration of the proposed network model are wetting and drying retention curves of the porous geomaterial of interest. The calibration procedure is divided into four steps:

1. Retention of wetting and drying experimental results are converted from the $S_{\mathrm{r}} - P_{\mathrm{c}}$ (Figure 8.1a) to the $S_{\mathrm{r}} - r$ (Figure 8.1b) space using the Young-Laplace equation in (3.12).

2. Pipe and sphere radii linear probability distribution functions are selected by performing a least square fit for the linear part of the experimental results in the $S_{\mathrm{r}} - r$ space for drying and wetting, respectively.

3. The minimum radii $r^{\mathrm{s}}_{\mathrm{min}}$ and $r^{\mathrm{p}}_{\mathrm{min}}$ resulting from the fitting are checked in order to consistent according to the expression

$$r^{\mathrm{s}}_{\mathrm{min}} \geq r^{\mathrm{p}}_{\mathrm{min}} > r_{\mathrm{min}} \tag{8.1}$$

   where r_{min} is the minimum pore radius that capillary suction is the dominant force acting on the fluid.

4. In case that (8.1) is not fulfilled, the radii distributions are refitted by applying constraints according to (8.1).

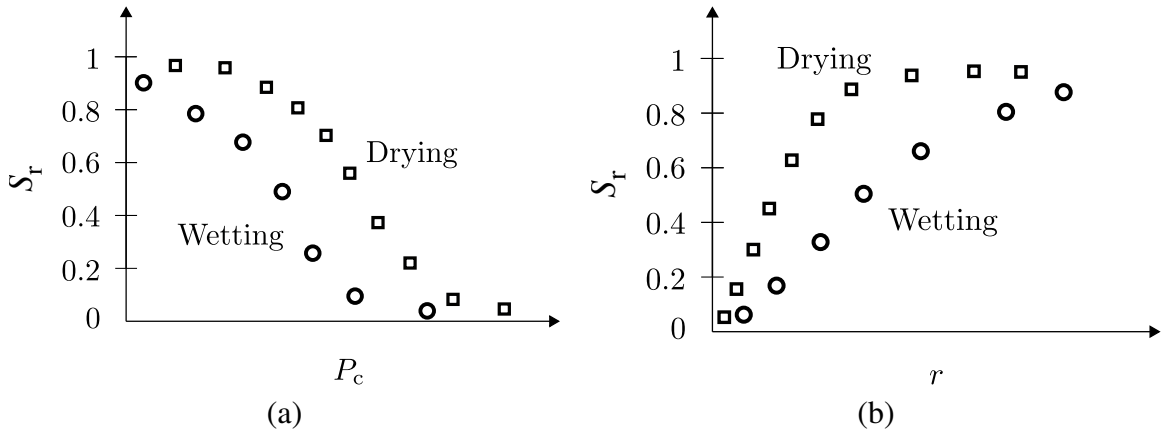

Figure 8.1: Network model calibration strategy: (a) schematic presentation of the wetting and drying retention curves in the degree of saturation S_{r} versus capillary suction P_{c} space and (b) the same retention curves presented in the degree of saturation S_{r} versus radius r space using the Young-Laplace equation.

The choice of using the wetting and drying retention curves for the calibration of the network model is closely linked to the scaling technique proposed in Section 3.4.4. The fact that each sphere represents the same volume of voids, means that the drying curve predicted by the network model (in $S_{\mathrm{r}} - P_{\mathrm{c}}$ space) depends upon only the distribution of pipe (throat) sizes and the network connectivity. It does not depend on the distribution of sphere (void) sizes. Similarly, the wetting curve predicted by the network model depends only on the distribution of sphere sizes and the network connectivity, i.e. it does not depend on the distribution of pipe sizes.

The second step of the calibration can result in two cases. A fitted line can intersect the horizontal axis at a value either less or greater than the minimum radius r_{min} for capillary pores. In Figures 8.2a and 8.2b the fitted line cases are schematically presented for very low values of S_{r} and r i.e. very close to the origin. Figure 8.2a presents the case where the fitted

line intersects the horizontal axis at a greater value than r_{min}. In this case, step 2 is completed. In Figure 8.2b, the case is presented in which the fitted line intersects the horizontal axis at a lower value than r_{min}. This case creates an inconsistency in the model since there are going to be either spheres or pipes that can be smaller than a the minimum radius where capillary forces are dominant in a pore. For resolving this inconsistency, a new fitting is required to be performed by enforcing the fitted line to intersect the horizontal axis at r_{min} (Figure 8.3a).

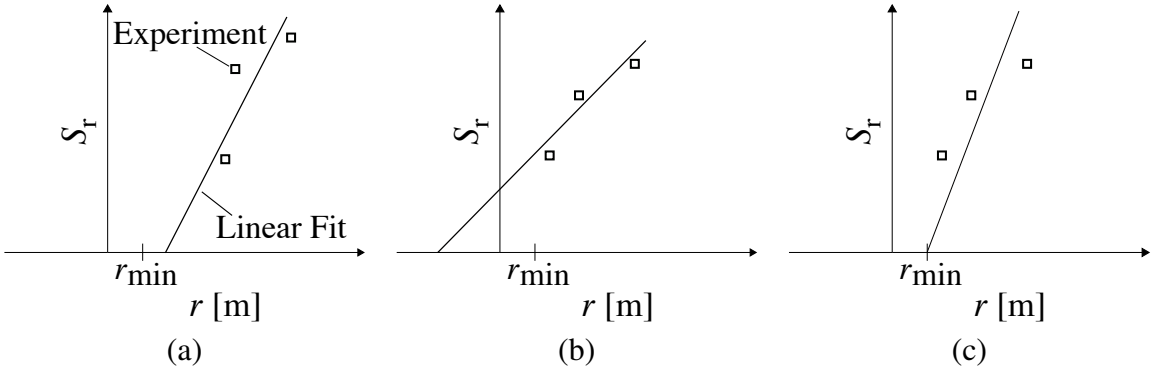

Figure 8.2: Network model calibration strategy: schematic presentation of the cases of the fitted to experimental results lines (a) the fitted line intersects the r axis at $r > r_{\text{min}}$, (b) the fitted line intersects the r axis at $r < r_{\text{min}}$ and (c) the fitted line is constricted to intersect the r axis at $r = r_{\text{min}}$.

After linear fits are performed, it must be checked whether the intersection with the radius axis of the sphere distribution is lower than the one of the pipe distribution (Figure 8.3a). If this is the case, yet another inconsistency is created in the model since this would mean that there would be small pores connected to throats that are larger in radius. Then, a fit is carried out with the additional constraint that the fitted lines for pipe and throat distributions intersect the r axis at the same point.

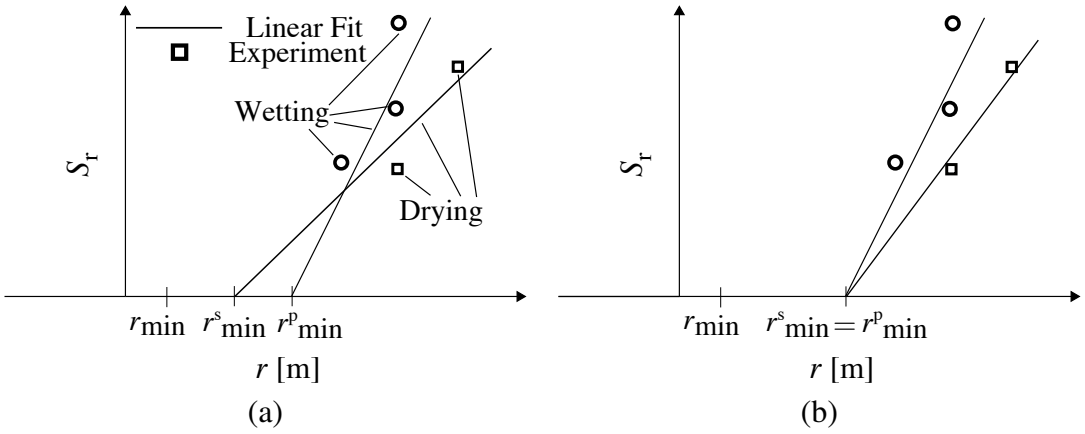

Figure 8.3: Network model calibration strategy: schematic presentation of the cases of the fitted to experimental results drying and wetting lines (a) the fitted lines intersects the r axis at $r^{\text{p}}_{\text{min}} < r^{\text{s}}_{\text{min}}$ and (b) the drying fitted line is constricted to intersect the r axis at $r^{\text{p}}_{\text{min}} = r^{\text{s}}_{\text{min}}$.

8.3 Comparison with experiments

For validation of the calibration technique, two sets of experimental results were needed. Firstly, experimental data of retention behaviour of a porous geomaterial during wetting and drying is required to determine the pore network input parameters according to the calibration approach proposed in Section 8.2. Secondly, experimental data of evolution of relative permeability of the same geomaterial during wetting and drying is required.

Since the present validation is done for transport networks whose geometry does not change in presence of a fluid, the above experimental data of a geomaterial that presents a rigid pore structure must be used. Soils present volume changes during wetting and drying and therefore changes in their pore structure (Alonso et al., 1990). Furthermore, concrete presents changes of pore spaces in the presence of water (Hall et al., 1995; Martys and Ferraris, 1997). However, rocks present the desired attributes required for the calibration technique validation.

The majority of experimental results found in the literature present either only one branch of the retention curve (either drying or wetting). Moreover, when permeability evolution data during drying and wetting are presented, no full retention behaviour is presented for the same geomaterial. The only data found in the literature regarding the same type of material was for Barea sandstone where drying and wetting retention information was presented by Matthews et al. (1995) and relative permeability evolution results for the same material was presented by Oak (1990) (numerical results could be compared only for drying due to trapping). It should also be mentioned that (to the authors knowledge) no network modelling work can be found in the literature that compares experimental results both for permeability and retention evolution.

The strategy presented in the previous section was applied to match experimental results presented in Matthews et al. (1995). Since the contact angle θ is 40^o measured from the side of air, mercury here is considered to be the drying fluid and air is the wetting fluid. Therefore, the degree of saturation S_{r} presented in this chapter is that of air. The surface tension of the mercury-air interface is considered to be $\gamma = 0.48$ N/m.

Mercury intrusion and extrusion data reported in Matthews et al. (1995) is presented in Figure 8.4 as points (squares) in the $S_{\mathrm{r}} - P_{\mathrm{c}}$ plane, since the mercury porosimety test involves the step wise pressure increase or decrease of mercury for intrusion and extrusion, respectively. For the present calibration strategy, the experimental data was back calculated to find the corresponding r values using the Young-Laplace equation and it is presented in Figure 8.5. Inspection of Figure 8.5 shows that the experimental plots of S_{r} against back-calculated value of r from (3.12) for both drying and wetting paths can each be approximated by a straight line, at least up to a certain value of S_{r}. For the drying curve this is true up to approximately

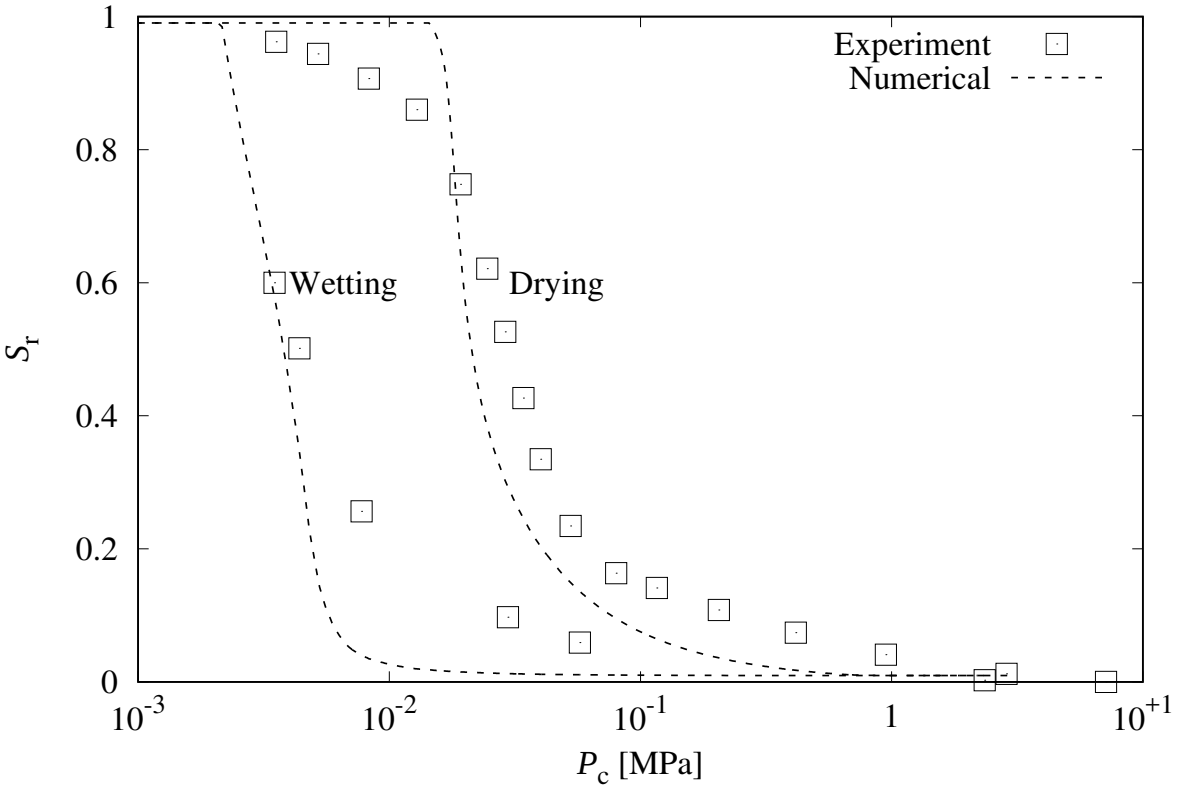

Figure 8.4: Comparison of the network retention to experimental results presented in Matthews et al. (1995): degree of saturation S_r versus capillary suction P_c.

S_r = 0.8 and for the wetting curve it is true up to the final experimental point (S_r = 0.6). Two best-fit straight lines were fitted to these parts of the two experimental sets of data, which are the curves with label "radii distribution" shown in Figure 8.5, to give an equation for the cumulative probability distribution of pipe or sphere sizes for input to the network model according to (3.9). Values of the coefficients a_{Lin} and b_{Lin} for pipes and spheres are given in Table 8.1. The linear cumulative probability distribution of (3.9) corresponds to a uniform probability distribution between a minimum radius of $b_{\text{Lin}}/a_{\text{Lin}}$ and a maximum radius of $(1 + b_{\text{Lin}})/a_{\text{Lin}}$, and a mean radius of $(1 + 2b_{\text{Lin}})/(2a_{\text{Lin}})$. With the values of a_{Lin} and b_{Lin} presented in Table 8.1, the pipe radii varied between 1.35×10^{-9} m and 5.00×10^{-5} m, the sphere radii varied between 1.35×10^{-9} m and 3.44×10^{-4} m and the mean sphere radius r_{sm} was 1.72×10^{-4} m.

Having defined the mean sphere radius r_{sm}, the values of l_{CELL} (the cell edge length) and d_{min} (the minimum distance between the randomly positioned points forming the Delaunay tessellation) were selected to give an appropriate number m of spheres within the cell and to match the reported porosity of the sandstone of 0.21. The values of l_{CELL} and d_{min} shown in Table 8.1 produced a cell containing 1560 spheres.

A series of 100 analyses was performed. The same network geometry was used for all 100 analyses, but different sphere and pipe radii generation and allocation were undertaken for

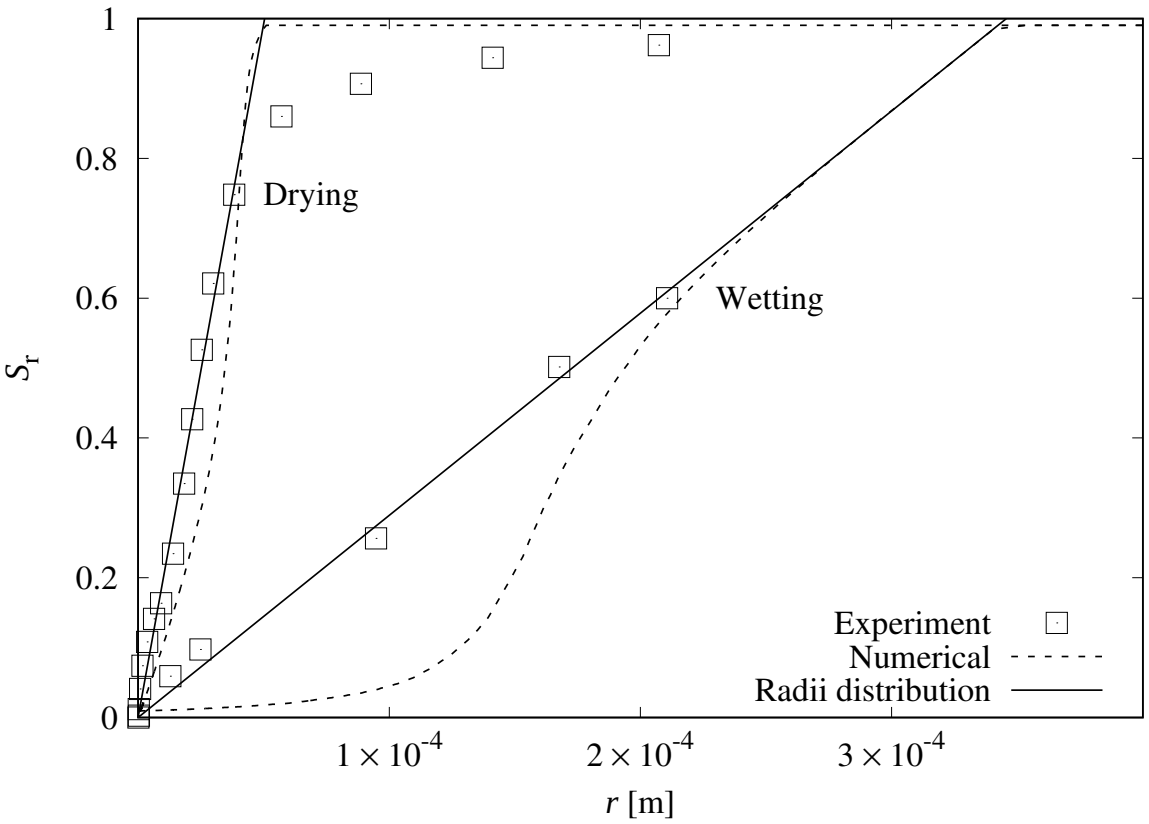

Figure 8.5: Comparison of the network retention to experimental results presented in Matthews et al. (1995): degree of saturation S_r versus radius r.

each analysis. The number of the seeding spheres used for the initiation procedure described in Section 3.8.2 was 1% of the total number of spheres, so that drying and wetting curves were simulated over a range of S_r from 0.99 to 0.01. The same increments of capillary suction were applied for all 100 analyses.

The dashed lines in Figure 8.4 show the results of the network model simulations in S_r-P_c space. Values of S_r represent the average from 100 analyses. Comparison with the experimental results shows that the network model simulation of the drying curve overestimates values of S_r at low values of P_c and underestimates values of S_r at high values of P_c. The network model simulation of the wetting curve underestimates values of S_r at all but the lowest experimental value of P_c.

The dashed lines in Figure 8.5 show the results of the network model simulations re-plotted in the space of S_r against back-calculated radius r (where (3.12) was used to convert values of P_c to corresponding values of r). Figure 8.5 provides insights into some of the mismatches between model simulations and experimental results in Figure 8.4.

In Figure 8.5, comparison of the network model simulations of S_r against back-calculated r with the cumulative probability distributions of spheres and pipes used as input for the network model (shown by the straight lines in Figure 8.5) highlights the influence of network

Table 8.1: Network calibration parameters.

Parameters	Values	Units
θ	40	^{o}
γ	0.48	N/m
a_{p}	2.0×10^{4}	m^{-1}
b_{p}	2.7×10^{-5}	
a_{s}	2.9×10^{3}	m^{-1}
b_{s}	3.9×10^{-6}	
d_{min}	0.756×10^{-3}	m
l_{CELL}	5.4×10^{-3}	m

connectivity on wetting and drying curves. For example, the network model simulation of the wetting curve predicts lower values of S_{r} than those corresponding to the cumulative probability distribution of sphere sizes, because network connectivity means that some smaller spheres cannot be intruded with the wetting fluid at the expected P_{c}, because access of the wetting fluid to these spheres is shielded by some larger spheres. As the degree of saturation increases, the network model simulation converges with the cumulative probability distribution of spheres, because this shielding effect reduces as more spheres are filled with the wetting fluid. This behaviour is aligned with the observations made in Section 5.2.1.

The model simulations in Figure 8.4 could be tuned to match better the experimental results by adjusting the values of some of the input parameters in Table 8.1. This would mean, however, that the method had reverted to no more than a curve fitting exercise. One significant point to emerge from Figure 8.4 is that the match achieved between model simulations and experimental results was better than in previous network model simulations (Athanasiadis et al., 2014) which did not use the pore volume scaling technique. Even though these earlier simulations included substantial tuning of input parameter values to try to achieve the best possible match, the drying curve would present an abrupt change of degree of saturation for small changes of capillary suction instead of the gradual degree of saturation changes presented in Figure 8.4. This provides encouraging evidence on the usefulness of the pore volume scaling technique.

Additionally, the model results were validated by comparing permeability results with water permeability experimental measurements. The sphere and pipe distribution used were the same as those for the mercury intrusion-extrusion test. An initially fully water saturated network that is invaded by gas until the cell is almost dried ($S_{\mathrm{r}} \approx 0.01$) and then water is allowed to inflow the network until $S_{\mathrm{r}} \approx 0.99$. The input parameters for the water and gas conductivity are presented in Table 8.1. No results of permeability tests was presented in Matthews et al. (1995). Therefore, experimental measurements of water permeability for Barea sandstone presented in Oak (1990) were used for the model validation since it is the same material as the one presented in Matthews et al. (1995).

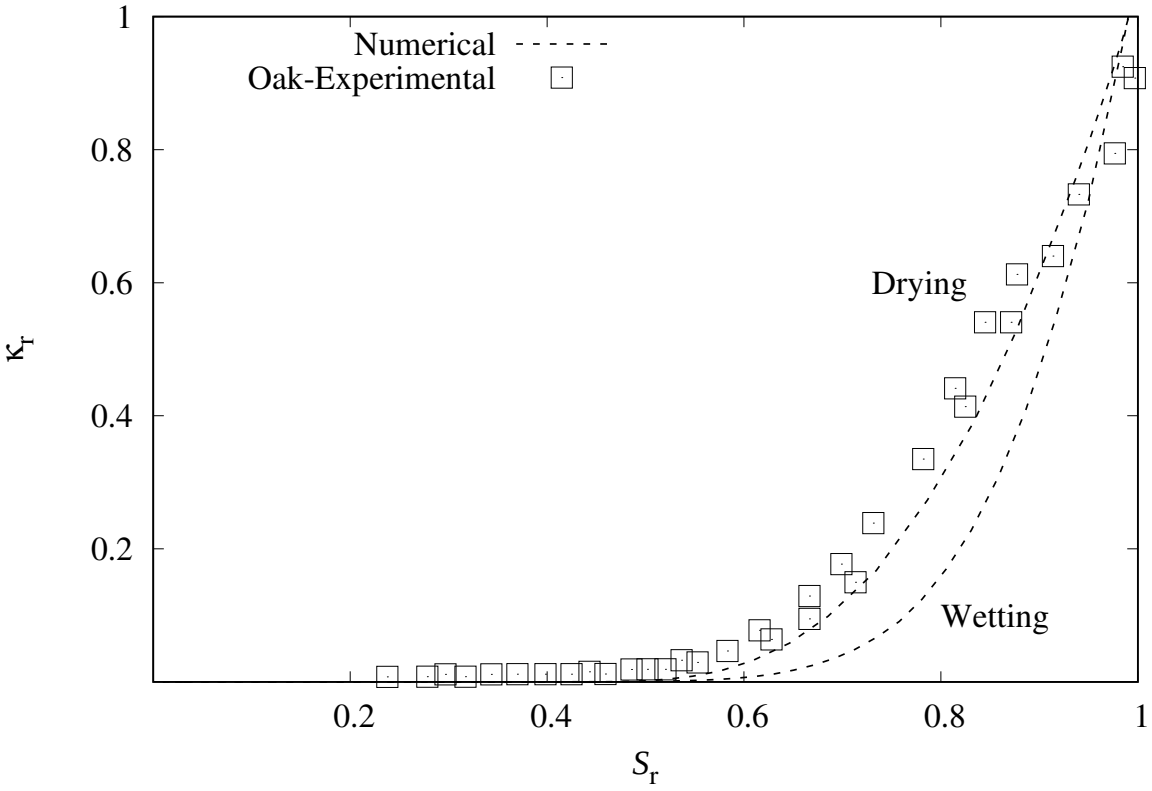

Figure 8.6: Comparison of network relative permeability to experimental results presented in Oak (1990): relative permeability κ_{r} versus saturation S_{r}.

The Barea sandstone water permeability tests were performed during the drying and wetting of a sample having oil as the drying fluid and water as the wetting one. The model can not capture the permeability of two fluids but only that of the wetting one. However, since the gas filled pipes contribute very low conductivity to the network, the gas filled pipes can be assumed to represent an oil filled one that creates a disconnection between the water filled pipes.

The change of relative permeability, κ_{r} with change of S_{r} are presented in Figure 8.6. Both the wetting and drying results of the numerical analysis are presented. Only the drying experimental results are presented since during wetting trapping occurs and κ_{r} can not increase more than 0.2. It can be observed that there is a good match between the experimental and numerical results in the κ_{r} - S_{r} space.

The intrinsic permeability in the experiments was about 9.87×10^{-13} m ^{2}. However, the average network permeability was 9.33×10^{-11} m ^{2} which is about one hundred times larger. This is an expected result since the the spheres that represent a cluster of equal volume voids assume that all the voids are perfectly connected with each other. As a result, the permeability in the model is expected to be higher than in the experiments.

8.4 Discussion

A calibration strategy to capture macroscopic fluid retention was presented. The model results emerging from the calibration process presents a very good match for the drying. For wetting, the deviation between the experimental and numerical results decrease with increasing S_{r}. The reason of this discrepancy is the strong influence of the sphere connectivity on the wetting retention curve. This could be overcome by adjusting the sphere distribution. However, the purpose of the calibration technique is not to present a simple curve fitting exercise but rather to propose a process to choose the model input parameters from the experimental results without using the network model.

The model and calibration results were validated by comparing the numerical permeability evolution to experimental results reported in the literature. Since the work that presented the experimental results used for the fluid retention calibration did not present any permeability tests, results from permeability experimental measurements on the same type of material reported in the literature were used. The model sphere and pipe radii distributions used were the same as those from a retention calibration. A good match was found for the drying curve in the $\kappa_{\mathrm{r}} - S_{\mathrm{r}}$ space. Since the permeability experimental results of wetting was reported only for $S_{\mathrm{r}} < 0.2$, no comparison was presented. The network permeability was found to be one hundred times more than the one presented in the experimental tests. This is owed to the fact that the connectivity of smaller spheres that each small sphere represents is overstated as discussed in Section 3.4.4. This does not undervalue the qualities of the model presented since the match of the relative permeabilities is good and by knowing the ratio of the network and the real material saturated permeabilities, an accurate prediction of the permeability evolution can be performed for unsaturated conditions.

Chapter 9

Conclusions and future work

9.1 Conclusions

A new framework for a hydro-mechanical network model for porous geomaterials has been presented. The aim of the present work was to investigate the macroscopic properties of retention, conductivity and mechanical response at the capillary pore scale of these type of materials. After the model was verified by comparison with analytical solutions, the influence of the model parameters on macroscopic transport response, and the influence of the cell size on the macroscopic properties was investigated by means of cells with Periodic Boundary Conditions. Also, a calibration strategy for choosing transport input parameters from easily obtainable experimental input has been proposed. The main conclusions of this study are presented here.

The implementation of the modelling framework in Chapter 3 has been shown to be correct by means of verification benchmark tests in Chapter 4. Computations of conductivity reproduced analytical solutions for a regular Body Centred Cubic (BCC) network of pipes of equal radii. Furthermore, the evaluation of the degree of saturation matched theoretical results for a spatially random network with spheres and pipes of the same radius, respectively, with the pipe radius being smaller than the one of the spheres. Analyses of elastic and plastic behaviour of the mechanical model for a Face Centred Cubic (FCC) network of mechanical elements with equal cross-section areas matched analytical results presented in the literature. Finally, the hydro-mechanical response of coupled mechanical and transport networks reproduced theoretical results.

The parametric study in Chapter 5 showed that mercury intrusion and extrusion porosimetry tests do not provide, on their own, enough information for determining the sphere and pipe

size distribution of porous geomaterials.

From the study of the influence of the size on macroscopic properties of the transport network, it was found that for all macroscopic properties, the mean converges to a representative value in Chapter 6. For large cell sizes, the cell size increase did not result in significant changes to the mean macroscopic values. Moreover, for the larger sizes, the standard deviations were found to be very close to zero for the main range of unsaturated conditions. Only for very low conductivities, large standard deviations were presented for a small range of capillary suction. This effect was attributed to the occurrence of percolation.

The influence of cell size on macroscopic Young's modulus E_{macro} and macroscopic Poisson's ratio ν_{macro} was investigated in Chapter 6. For large cell sizes, the means converged to representative values, while the standard deviations approached zero. Furthermore, the influence of mechanical element radii distribution on E_{macro} and ν_{macro} was presented. It was found that for the same target sum of element volumes, the RVE with an element radii distribution with lower COV^{mech} presents a higher E_{macro}. This was attributed to the fact that the RVE with lower COV^{mech} had less soft elements than that with a higher COV^{mech}.

The study on microstructural changes in Chapter 7 showed that the model can produce only monotonic changes of macroscopic transport properties for monotonically changing capillary suction. Selected model results matched analytical expressions.

The calibration strategy for the transport model proposed for the new scaling technique presented in Section 3.4.4 was applied to the analysis of mercury intrusion and extrusion porosimetry experiments presented in the literature. It was found that the connectivity of spheres influences strongly the evolution of the degree of saturation during wetting. The new scaling technique introduced in Chapter 3 captures a better retention behaviour than the standard pore network approach presented in Athanasiadis et al. (2014). The new calibration strategy provided a good match with experimental results for retention and relative permeability. However, intrinsic permeability was overestimated by two orders of magnitude. The model validation presented possibility to predict evolution of relative permeability during drying when the model is calibrated according to the technique proposed in Section 8.2.

Potential benefit to be gained by the framework proposed in this thesis, is to test validity of macroscopic constitutive models for conditions other than those applied to experiments whose results where used for the development of these models. Moreover, the framework can be used to identify key processes occurring at the capillary scale that are responsible for macroscopic behaviour observed at the continuum level that cannot be captured by means of laboratory tests.

9.2 Future work

The present model can be used as a basis for further investigations of the influence of micromechanical processes on macroscopic properties. In addition to hydro-mechanical coupling studied here, the effect of heat transfer can be modelled. For materials, such as bentonite and concrete, heat transfer is expected to strongly interact with hydro-mechanical processes.

A calibration technique for the input parameters of the mechanical model for Young's modulus and strength could be developed. Then, the mechanical as well as the coupled hydro-mechanical model could be further validated by comparing numerical results to those of experiments.

The coupled periodic boundary conditions for the structural and mechanical network developed in the framework of the first order computational homogenisation has the ability to be embedded in a nested finite element multiscale approach. In this way, the developed model could be used for the modelling of boundary value problems and not only to investigate the material point behaviour. Then, the model performance could be evaluated by means of large scale analyses.

Appendix A

List of publications

The list of publications arising from the research conducted for the completion of the present thesis is presented below

Journal article

I. Athanasiadis, S. Wheeler and P. Grassl. Network Modelling of the Influence of Swelling on the Transport Behaviour of Bentonite. *Geosciences*, 6(4), 2016.

Conference articles

I. Athanasiadis, S. J. Wheeler and P. Grassl. Network modelling of fluid retention behaviour in unsaturated soils. In *E3S Web Conf.*, 9, 11016, 2016.

P. Grassl and I. Athanasiadis. 3D Modelling of the Influence of Microcracking on Mass Transport in Concrete.In *Concreep 10*, Vienna, 2015.

I. Athanasiadis and S. Wheeler and P. Grassl. Modelling the Time Dependence of Transport Properties of Porous Materials. In *Concreep 10*, Vienna, 2015.

I. Athanasiadis, S. Wheeler, P. Grassl. Three-dimensional network modelling of the influence of microstructure on mass transport in unsaturated soils. In *Geomechanics from micro to macro*, pp. 901-906, 2014.

I. Athanasiadis , S. Wheeler, P. Grassl. Three-dimensional network modelling of the influence of microstructure of concrete on water transport. In *Computational Modelling of Concrete Structures (EURO-C)*, St. Anton am Arlberg, Austria, 2014.

I. Athanasiadis , S. Wheeler, P. Grassl. Lattice modelling of the micro-structure of porous materials for water transport. In *TRANSCEND Conference on Water Transport in Cementitious Materials*, Guildford, UK, 2013.

Bibliography

J. Ai, J. F. Chen, J. M. Rotter, and J. Y. Ooi. Assessment of rolling resistance models in discrete element simulations. *Powder Technology*, 206(3):269–282, 2011.

E. E. Alonso, A. Gens, and A. Josa. A constitutive model for partially saturated soils. *Géotechnique*, 40(3):405–430, 1990.

J. E. Andrade, K. W. Lim, C. F. Avila, and I. Vlahinic. Granular element method for computational particle mechanics. *Computer Methods in Applied Mechanics and Engineering*, 241: 262–274, 2012.

M. Andrew, B. Bijeljic, and M. J. Blunt. Pore-scale contact angle measurements at reservoir conditions using X-ray microtomography. *Advances in Water Resources*, 68:24–31, 2014a.

M. Andrew, B. Bijeljic, and M. J. Blunt. Pore-by-pore capillary pressure measurements using X-ray microtomography at reservoir conditions: Curvature, snap-off, and remobilization of residual CO2. *Water Resources Research*, 50(11):8760–8774, 2014b.

A. Anthoine. Derivation of the in-plane elastic characteristics of masonry through homogenization theory. *International Journal of Solids and Structures*, 32(2):137–163, 1995.

I. Athanasiadis, S. Wheeler, and P. Grassl. Three-dimensional network modelling of the influence of microstructure on mass transport in unsaturated soils. In *Geomechanics from Micro to Macro*, pages 901–906, 2014.

I. Athanasiadis, S. Wheeler, and P. Grassl. Network modelling of the influence of swelling on the transport behaviour of bentonite. *Geosciences*, 6(4), 2016.

S. Bakke and P. E. Øren. 3-d pore-scale modelling of sandstones and flow simulations in the pore networks. *Spe Journal*, 2(2):136–149, 1997.

C. A. Baldwin, A. J. Sederman, M. D. Mantle, P. Alexander, and L. F. Gladden. Determination and characterization of the structure of a pore space from 3D volume images. *Journal of Colloid and Interface Science*, 181(1):79–92, 1996.

J. P. Bardet and I. Vardoulakis. The asymmetry of stress in granular media. *International Journal of Solids and Structures*, 38(2):353–367, 2001.

Z. P. Bažant and M. Z. Bazant. Theory of sorption hysteresis in nanoporous solids: Part I Snap-through instabilities. *Journal of the Mechanics and Physics of Solids*, 60(9):1644–1659, 2012.

S. Berg, H. Ott, S. A. Klapp, A. Schwing, R. Neiteler, N. Brussee, A. Makurat, L. Leu, F. Enzmann, J. O. Schwarz, M. Kersten, S. Irvine, and M. Stampanoni. Real-time 3D imaging of Haines jumps in porous media flow. *Proceedings of the National Academy of Sciense of the United States of America*, 110(10):3755–3759, 2013.

S Berton and J. E. Bolander. Crack band model of fracture in irregular lattices. *Computer Methods in Applied Mechanics and Engineering*, 195(52):7172–7181, 2006.

M. A. Biot. General theory of three-dimensional consolidation. *Journal of applied physics*, 12(2):155–164, 1941.

A. W. Bishop. *The principles of effective stress*. Norges Geotekniske Institutt, 1960.

M. J. Blunt, B. Bijeljic, H. Dong, O. Gharbi, S. Iglauer, P. Mostaghimi, A. Paluszny, and C. Pentland. Pore-scale imaging and modelling. *Advance in Water Resources*, 51:197–216, 2013.

J. E. Bolander and S. Berton. Simulation of shrinkage induced cracking in cement composite overlays. *Cement and Concrete Composites*, 26:861–871, 2004.

J. E. Bolander and S. Saito. Fracture analyses using spring networks with random geometry. *Engineering Fracture Mechanics*, 61(5-6):569–591, 1998.

E. Y. Bormashenko. *Wetting of real surfaces*. De Gruyter Studies in Mathematical Physics. De Gruyter, Berlin, 2013.

R. H. Brooks and A. T. Corey. Hydraulic properties of porous media. *Hydrology Paper No. 3*, 1964.

H. J. Butt and M. Kappl. Normal capillary forces. *Advances in Colloid and Interface Science*, 146(1):48–60, 2009.

R. Campos, I. Barrios, and J. Lillo. Experimental CO2 injection: Study of physical changes in sandstone porous media using Hg porosimetry and 3D pore network models. *Energy Reports*, 1:71–79, 2015.

E. Catalano, B. Chareyre, and E. Barthelemy. Pore-scale modeling of fluid-particles interaction and emerging poromechanical effects. *International Journal for Numerical and Analytical Methods in Geomechanics*, 38(1):51–71, 2014.

I. Cavarretta, M. Coop, and C. O'Sullivan. The influence of particle characteristics on the behaviour of coarse grained soils. *Géotechnique*, 60(6):413–423, 2010.

E. M. Chapman, J. Yang, J. P. Crawshaw, and E. S. Boek. Pore scale models for imbibition of CO_2 analogue fluids in etched micro-fluidic junctions from micro-model experiments and direct LBM flow calculations. *Energy Procedia*, 37:3680–3686, 2013.

I. Chatzis and F. A. L. Dullien. Modelling pore structure by 2-D and 3-D networks with application to sandstones. *Journal of Canadian Petroleum Technology*, 16(1):97–100, 1977.

J. D. Chen and J. Koplik. Immiscible fluid displacement in small networks. *Journal of Colloid and Interface Science*, 108(2):304–330, 1985.

Y. P. Cheng, Y. Nakata, and M. D. Bolton. Discrete element simulation of crushable soil. *Géotechnique*, 53(7):633–641, 2003.

G. C. Cho, J. Dodds, and J. C. Santamarina. Particle shape effects on packing density, stiffness, and strength: Natural and crushed sands. *Journal of Geotechnical and Geoenvironmental Engineering*, 132(5):591–602, 2007.

J. Christoffersen, M. M. Mehrabadi, and S. Nemat-Nasser. A micromechanical description of granular material behavior. *Journal of Applied Mechanics*, 48(2):339–344, 1981.

D. M. Cole, L. U. Mathisen, M. A. Hopkins, and B. R. Knapp. Normal and sliding contact experiments on gneiss. *Granular Matter*, 12(1):69–86, 2010.

P. A. Cundall and O. D. L. Strack. A discrete numerical model for granular assemblies. *Géotechnique*, 29(1):47–65, 1979.

Y. F. Dafalias and L. R. Herrmann. Bounding surface formulation of soil plasticity. *Soil mechanics-transient and cyclic loads*, 10:253–282, 1982.

R. L. Daugherty and J. B. Franzini. *Fluid mechanics, with engineering applications*. Tokyo: McGraw-Hill Kogakusha, 7th edition, 1977.

P. G. De Gennes, F. Brochard-Wyart, and D. Quéré. *Capillarity and wetting phenomena: drops, bubbles, pearls, waves*. Springer Science & Business Media, 2004.

P. Delage. Thermo-hydro-mechanical issues in geo-materials: physical mechanisms and experimental determination. *ALERT Doctoral School 2015 Coupled and Multiphysics Phenomena*, pages 5–41, 2005.

P. Delage, D. Marcial, Y. J. Cui, and X. Ruiz. Ageing effects in a compacted bentonite: a microstructure approach. *Géotechnique*, 56(5):291–304, 2006.

A. Di Renzo and F. P. Di Maio. Comparison of contact-force models for the simulation of collisions in DEM-based granular flow codes. *Chemical Engineering Science*, 59(3): 525–541, 2004.

S. Diamond. Mercury porosimetry - An inappropriate method for the measurement of pore size distributions in cement-based materials. *Cement and Concrete Research*, 30(10): 1517–1525, 2000.

D. A. DiCarlo, J. I. G. Cidoncha, and C. Hickey. Acoustic measurements of pore-scale displacements. *Geophysical Research Letters*, 30(17), 2003.

H. Dong and M. J. Blunt. Pore-network extraction from micro-computerized-tomography images. *Physical Review E*, 80(3):036307, 2009.

J. Drelich, J. D. Miller, and R. J. Good. The effect of drop (bubble) size on advancing and receding contact angles for heterogeneous and rough solid surfaces as observed with sessile-drop and captive-bubble techniques. *Journal of Colloids and Interface Science*, 179 (1):37–50, 1996.

A. Drescher and G. De Josselin De Jong. Photoelastic verification of a mechanical model for the flow of a granular material. *Journal of the Mechanics and Physics of Solids*, 20(5): 337–340, 1972.

D. C. Drucker. Coulomb friction, plastivity, and limit loads. *Journal of Applied Mechanics-Transactions of the ASME*, 21(1):71–74, 1954.

D. C. Drucker and W. Prager. Soil mechanics and plastic analysis or limit design. *Quarterly of Applied Mathematics*, 10(2):157–165, 1952.

F. A. L. Dullien, F. S. Y. Lai, and I. F. MacDonald. Hydraulic continuity of residual wetting phase in porous media. *Journal of Colloid and Interface Science*, 109:201–218, 1986.

K. I. Eshiet, Y. Sheng, and J. Ye. Microscopic modelling of the hydraulic fracturing process. *Environmental Eearth Science*, 68(4):1169–1186, 2013.

T. P. Farmer and J. C. Bird. Asymmetric capillary bridges between contacting spheres. *Journal of Colloid and Interface science*, 454:192–199, 2015.

I. Fatt. The network model of porous media: I. Capillary pressure characteristics. *Transactions of the American Institute of Mining and Metallurgiacal Engineers*, 207:144–159, 1956.

A. Ferrari and I. Lunati. Inertial effects during irreversible meniscus reconfiguration in angular pores. *Advances in Water Resources*, 74:1–13, 2014.

B. Ferreol and D. H. Rothman. Lattice-Boltzmann simulations of flow through Fontainebleau sandstone. *Transport in Porous Media*, 20:3–20, 1995.

R. Fetzer and J. Ralston. Exploring defect height and angle on asymmetric contact line pinning. *Journal of Physical Chemistry C*, 115(30):14907–14913, 2011.

R. A. Fisher. On the capillary forces in an ideal soil; Correction of formulae given by W. B. Haines. *Journal of Agricaltural Science*, 16(3):492–505, 1926.

D. G. Fredlund and N. R. Morgenstern. Stress state variables for unsaturated soils. *Journal of Geotechnical and Geoenvironmental Engineering*, 103(ASCE 12919), 1977.

D. G. Fredlund and A. Q. Xing. Equations for the soil-water characteristic curve. *Canadian Geotechnical Journal*, 31(4):521–532, 1994.

D. G. Fredlund, N. R. Morgenstern, and R. A. Widger. Shear-strength of unsaturated soils. *Canadian Geotechnical Journal*, 15(3):313–321, 1978.

D. Gallipoli, S. J. Wheeler, and M. Karstunen. Modelling the variation of degree of saturation in a deformable unsaturated soil. *Géotechnique*, 53(1):105–112, 2003.

J. K. M. Gan, D. G. Fredlund, and H. Rahardjo. Determination of the shear-strength parameters of an unsaturated soil using the direct shear test. *Canadian Geotechnical Journal*, 25(3): 500–510, 1988.

X. Garcia, J. P. Latham, J. Xiang, and J. P. Harrison. A clustered overlapping sphere algorithm to represent real particles in discrete element modelling. *Géotechnique*, 59(9):779–784, 2009.

A. Gens and E. E. Alonso. A framework for the behaviour of unsaturated expansive clays. *Canadian Geotechnical Journal*, 29(6):1013–1032, 1992.

A. Genty and V. Pot. Numerical Simulation of 3D Liquid-Gas Distribution in Porous Media by a Two-Phase TRT Lattice Boltzmann Method. *Transport in Porous Media*, 96(2):271–294, 2013.

I. M. Gitman, H. Askes, and L. J. Sluys. Representative volume: existence and size determination. *Engineering Fracture Mechanics*, 74(16):2518–2534, 2007.

J. M. Golden. Percolation theory and models of unsaturated porous-media. *Water Resources Research*, 16(1):201–209, 1980.

P. Grassl and J. Bolander. Three-Dimensional Network Model for Coupling of Fracture and Mass Transport in Quasi-Brittle Geomaterials. *Material*, 9:782, 2016.

P. Grassl and M. Jirásek. Damage-plastic model for concrete failure. *International Journal of Solids and Structures*, 43(22-23):7166–7196, 2006.

P. Grassl and M. Jirásek. Meso-scale approach to modelling the fracture process zone of concrete subjected to uniaxial tension. *International Journal of Solids and Structures*, 47 (7):957–968, 2010.

P. Grassl, H. S. Wong, and N. R. Buenfeld. Influence of aggregate size and volume fraction on shrinkage induced micro-cracking of concrete and mortar. *Cement and Concrete Research*, 40(1):85–93, 2010.

D. V. Griffiths and G. G. W. Mustoe. Modelling of elastic continua using a grillage of structural elements based on discrete element concepts. *International Journal for Numerical Methods in Engineering*, 50(7):1759–1775, 2001.

G. Grimmett. *Percolation and disordered systems*. Springer, 1997.

J. M. Guedes and N. Kikuchi. Preprocessing and postprocessing for materials based on the homogenization method with adaptive Finite-Element methods. *Computer Methods in Applied Mechanics and Engineering*, 83(2):143–198, 1990.

A. K. Haghi. Factors effecting water-vapor transport through fibers. *Theoretical and Applied Mechanics*, 30:277–309, 2003.

W. B. Haines. Studies in the physical properties of soil V The hysteresis effect in capillary properties, and the modes of moisture distribution associated therewith. *The Journal of Agricultural Science*, 20(01):97–116, 1930.

C. Hall, W. D. Hoff, S. C. Taylor, M. A. Wilson, B. G. Yoon, H. W. Reinhardt, M. Sosoro, P. Meredith, and A. M. Donald. Water anomaly in capillary liquid absorption by cement-based materials. *Journal of Materials Science Letters*, 14(17):1178–1181, 1995.

R. Hamajima, T. Kawai, K. Yamashita, and M. Kusabuka. Numerical analysis of cracked and jointed rock mass. In *International conference on numerical methods in geomechanics*, pages 207–214, 1985.

M.H. Hasan. *Small strain elastic behaviour of unsaturated soil investigated by bender/extender element testing*. Ph.D. Thesis, University of Glasgow, Glasgow, UK, 2016.

H. J. Herrmann, A. Hansen, and S. Roux. Fracture of disordered, elastic lattices in two dimensions. *Physical Review B*, 39(1):637, 1989.

E. S. Hosseininia. Discrete element modeling of inherently anisotropic granular assemblies with polygonal particles. *Particuology*, 10(5):542–552, 2012.

K. Iwashita and M. Oda. Rolling resistance at contacts in simulation of shear band development by DEM. *Journal of Engineering Mechanics-ASCE*, 124(3):285–292, 1998.

J. E. B. Jennings and J. B. Burland. Limitations to the use of effective stresses in partly saturated soils. *Géotechnique*, 12(2):125–144, 1962.

G. R. Jerauld and S. J. Salter. Effect of pore-structure on hysteresis in relative permeability and capillary pressure: pore-level modeling. *Transport in Porous Media*, 5:103–130, 1990.

M. J. Jiang, S. Leroueil, and J. M. Konrad. Insight into shear strength functions of unsaturated granulates by DEM analyses. *Computers and Geotechnics*, 31(6):473–489, 2004.

M. J. Jiang, H. S. Yu, and D. Harris. A novel discrete model for granular material incorporating rolling resistance. *Computer and Geotechnics*, 32(5):340–357, 2005.

A. Johnson, I. M. Roy, G. P. Matthews, and D. Patel. An improved simulation of void structure, water retention and hydraulic conductivity in soil with the Pore-Cor three-dimensional network. *European Journal of Soil Science*, 54(3):477–489, 2003.

J. W. Ju. On Energy-based coupled elastoplastic damage theories - constitutive modeling and computational apsects. *International Journal of Solids and Structures*, 25(7):803–833, 1989.

L. M. Kachanov. Time of the rupture process under creep conditions. *Izvestia Akademii Nauk SSSR Otdelenie Tekhnicheskich Nauk*, 8:26–31, 1958.

T. Kawai. New discrete models and their application to seismic response analysis of structures. *Nuclear Engineering and Design*, 48(1):207–229, 1978.

T. Kawai. Some Consideration on the Finite-Element Method. *International Journal for Numerical Methods in Engineering*, 16:81–120, 1980.

W. R. Ketterhagen, R. Bharadwaj, and B. C. Hancock. The coefficient of rolling resistance (corr) of some pharmaceutical tablets. *International Journal of Pharmaceutics*, 392(1): 107–110, 2010.

M. A. Knackstedt, A. P. Sheppard, and M. Sahimi. Pore network modelling of two-phase flow in porous rock: the effect of correlated heterogeneity. *Advances in Water Resources*, 24: 257–277, 2001.

D. E. Knuth. The art of computer programming, vol. 2, seminumerical algorithms (2nd edition). *Software: Practice and Experience*, 12(9):883–884, 1982.

M. M. Kohonen, D. Geromichalos, M. Scheel, C. Schier, and S. Herminghaus. On capillary bridges in wet granular materials. *Physica A: Statistical Mechanics and its Applications*, 339(1):7–15, 2004.

V. Kouznetsova, M. G. D. Geers, and W. A. M. Brekelmans. Multi-scale constitutive modelling of heterogeneous materials with a gradient-enhanced computational homogenization scheme. *International Journal for Numerical Methods in Engineering*, 54(8):1235–1260, 2002.

V. Kouznetsova, W. A. M. Brekelmans, and F. P. T. Baaijens. An approach to micro-macro modeling of heterogeneous materials. *Computational Mechanics*, 27(1):37–48, 2001.

G. Kresse and J. Hafner. Ab initio molecular-dynamics simulation of the liquid-metal–amorphous-semiconductor transition in germanium. *Physical Review B*, 49(20):14251, 1994.

P. V. Lade and J. M. Duncan. Elastoplastic stress-strain theory for cohesionless soil. *Journal of the Geotechnical Engineering Division*, 101(10):1037–1053, 1975.

R. Lenormand and S. Bories. Description d'un mécanisme de connexion de liaisons destiné à l'étude du drainage avec piégeage en milieu poreux. *Comptes Rendus de l'Académie des Sciences*, 291:279–282, 1980.

R. Lenormand, C. Zarcone, and A. Sarr. Mechanisms of the displacement of one fluid by another in a network of capillary ducts. *Journal of Fluid Mechanics*, 135:337–357, 1983.

S. Leroueil and P. R. Vaughan. The general and congruent effects of structure in natural soils and weak rocks. *Géotechnique*, 40(3):467–488, 1990.

M. C. Leverett. Capillary behavior in porous solids. *Transactions of the American Institute of Mining and Metallurgical Engineers*, 142:152–169, 1941.

A. E. H. Love. *The mathematical theory of elasticity*. 1927.

J. Ma. Review of permeability evolution model for fractured porous media. *Journal of Rock Mechanics and Geotechnical Engineering*, 7(3):351–357, 2015.

M. M. MacLaughlin and D. M. Doolin. Review of validation of the discontinuous deformation analysis (DDA) method. *International Journal for Numerical and Analytical Methods in Geomechanics*, 30(4):271–305, 2006.

K. Maekawa, T. Ishida, and T. Kishi. *Multi-scale modeling of structural concrete*. CRC Press, 2008.

W. M. Mahmud and V. H. Nguyen. Effects of snap-off in imbibition in porous media with different spatial correlations. *Transport in Porous Media*, 64:279–300, 2006.

H. N. Man and X. D. Jing. Pore network modelling of electrical resistivity and capillary pressure characteristics. *Transport in Porous Media*, 41(3):263–285, 2000.

V. Mani and K. K. Mohanty. Effect of pore-space spatial correlations on two-phase flow in porous media. *Journal of Petroleum Science and Engineering*, 23:173–188, 1999.

A. Marchand, J. H. Weijs, J. H. Snoeijer, and B. Andreotti. Why is surface tension a force parallel to the interface? *American Journal of Physics*, 79(10):999–1008, 2011.

A. Marmur. Contact-angle hysteresis on heterogeneous smooth surfaces. *Journal of Colloid and Interface Science*, 168(1):40–46, 1994.

N. S. Martys and C. F. Ferraris. Capillary transport in mortars and concrete. *Cement and Concrete Research*, 27(5):747–760, 1997.

G. Mason. A model of the pore space in a random packing of equal spheres. *Journal of Colloid and Interface Science*, 35(2):279–287, 1971.

J. Massmann and D. F. Farrier. Effects of atmospheric pressures on gas-transport in the vadose zone. *Water Resources Research*, 28(3):777–791, 1992.

P. G. Matthews, C. J. Ridgway, and M. C. Spearing. Void space modeling of mercury intrusion hysteresis in sandstone, paper coating, and other porous media. *Journal of Colloid and Interface Science*, 171:8–27, 1995.

Y. R. Mayhew and G. F. C. Rogers. *Thermodynamic and transport properties of fluids*. Blackwell, 1976.

G. R. McDowell and M. D. Bolton. On the micromechanics of crushable aggregates. *Géotechnique*, 48(5):667–679, 1998.

C. Miehe and A. Koch. Computational micro-to-macro transitions of discretized microstructures undergoing small strains. *Archive of Applied Mechanics*, 72(4-5):300–317, 2002.

C. Miehe, J. Dettmar, and D. Zaeh. Homogenization and two-scale simulations of granular materials for different microstructural constraints. *International Journal for Numerical Methods in Engineering*, 83(8-9, SI):1206–1236, 2010.

F. Moebius and D. Or. Interfacial jumps and pressure bursts during fluid displacement in interacting irregular capillaries. *Journal of Colloid and Interface Science*, 377:406–415, 2012.

A. Mohamed and M. Gutierrez. Comprehensive study of the effects of rolling resistance on the stress–strain and strain localization behavior of granular materials. *Granular Matter*, 12(5):527–541, 2010.

K. K. Mohanty, H. T. Davis, and L. E. Scriven. Physics of oil entrapment in water-wet rock. *SPE Reservoir Engineering*, 2(01):113–128, 1987.

F. Moro and H. Bohni. Ink-bottle effect in mercury intrusion porosimetry of cement-based materials. *Journal of Colloid and Interface Science*, 246(1):135–149, 2002.

N. R. Morrow. Irreducable wetting-phase saturations in porous media. *Chemical Engineering Science*, 25:1799–1815, 1970.

N. R. Morrow. Physics and Thermodynamics of Capillary Action in Porous Media. *Industrial and Engineering Chemistry*, 62(6):32–56, 1970.

M. J. Oak. Three-phase relative permeability of water-wet berea. In *SPE/DOE Enhanced Oil Recovery Symposium*. Society of Petroleum Engineers, 1990.

M. Oda, J. Konishi, and S. Nemat-Nasser. Experimental micromechanical evaluation of strength of granular materials: effects of particle rolling. *Mechanics of Materials*, 1(4): 269–283, 1982.

A. Okabe, B. Boots, K. Sugihara, S. N. Chiu, and D. G. Kendal. *Spatial Tessellations: Concepts and Applications of Voronoi Diagrams, Second Edition*. Wiley Online Library, 2nd edition, 2000.

P. E. Øren, S. Bakke, and O. J. Arntzen. Extending predictive capabilities to network models. *SPE Journal*, 3(04):324–336, 1998.

M. Ortiz. A constitutive theory for the inelastic behavior of concrete. *Mechanics of Materials*, 4(1):67–93, 1985.

A. K. Parkin. On the strength of packed spheres. *Journal of the Australian Mathematical Society*, 5(04):443–452, 1965.

B. Patzák. An object-oriented simulation tool for advanced modeling of materials and structures. *Acta Polytechnica*, 52:59–66, 2012.

A. A. Pena, P. G. Lind, and H. J. Herrmann. Modeling slow deformation of polygonal particles using DEM. *Particuology*, 6(6):506–514, 2008.

N. Petrinic. *Aspects of discrete element modelling involving facet-to-facet contact detection and interaction*. 1996.

A. Poulovassilis. Hysteresis of pore water, an application of the concept of independent domains. *Soil Science*, 93(6):405–412, 1962.

A. Q. Raeini, B. Bijeljic, and M. J. Blunt. Numerical modelling of sub-pore scale events in two-phase flow through porous media. *Transport in Porous Media*, 101(2):191–213, 2014a.

A. Q. Raeini, M. J. Blunt, and B. Bijeljic. Direct simulations of two-phase flow on micro-CT images of porous media and upscaling of pore-scale forces. *Advances in Water Resources*, 74:116–126, 2014b.

P. C. Reeves and M. A. Celia. A functional relationship between capillary pressure, saturation, and interfacial area as revealed by a pore-scale network model. *Water Resources Research*, 32(8):2345–2358, 1996.

B. C. Rennie. On the strength of sand. *Journal of the Australian Mathematical Society*, 1(01): 71–79, 1959.

E. Romero, A. Gens, and A. Lloret. Water permeability, water retention and microstructure of unsaturated compacted boom clay. *Engineering Geology*, 54(1):117–127, 1999.

J. G. Roof. Snap-off of oil droplets in water-wet pores. *Society of Petroleum Engineers Journals*, 10(1):85–90, 1970.

K. H. Roscoe, A. Schofield, and A. Thurairajah. Yielding of clays in states wetter than critical. *Géotechnique*, 13(3):211–240, 1963.

A. V. Ryazanov, M. I. J. van Dijke, and K. S. Sorbie. Two-phase pore-network modelling: existence of oil layers during water Invasion. *Transport in Porous Media*, 80(1):79–99, 2009.

H. Saduki and J. G. M. van Mier. Meso-level analysis of moisture flow in cement composites using a lattice-type approach. *Materials and Structures*, 30:579–587, 1997.

T. D. Scheibe, E. M. Murphy, X. Chen, A. K. Rice, K. C. Carroll, B. J. Palmer, A. M. Tartakovsky, I. Battiato, and B. D. Wood. An analysis platform for multiscale hydrogeologic modeling with emphasis on hybrid multiscale methods. *Groundwater*, 53(1):38–56, 2015.

E. Schlangen and J. G. M. van Mier. Simple lattice model for numerical-simulation of fracture of concrete materials and structures. *Materials and Structures*, 25(153):534–542, 1992.

J. Schmatz, J. L. Urai, S. Berg, and H. Ott. Nanoscale imaging of pore-scale fluid-fluid-solid contacts in sandstone. *Geophysical Research Letters*, 42(7):2189–2195, 2015.

K. Senetakis, M. R. Coop, and M. C. Todisco. The inter-particle coefficient of friction at the contacts of Leighton Buzzard sand quartz minerals. *Soils and Foundations*, 53(5):746–755, 2013.

G. H. Shi. Discontinuous deformation analysis: a new numerical model for the statics and dynamics of deformable block structures. *Engineering computations*, 9(2):157–168, 1992.

R. T. Shield. On coulomb's law of failure in soils. *Journal of the Mechanics and Physics of Solids*, 4(1):10–16, 1955.

H. Shimizu, S. Murata, and T. Ishida. The distinct element analysis for hydraulic fracturing in hard rock considering fluid viscosity and particle size distribution. *International Journal of Rock Mechanics and Mining Science*, 48(5):712–727, 2011.

D. Silin and T. Patzek. Pore space morphology analysis using maximal inscribed spheres. *Physica A: Statistical Mechanics and its Applications*, 371(2):336–360, 2006.

J. C. Simo and J. W. Ju. Strain- and stress-based continuum damage models I. Formulation. *International Journal of Solids and Structures*, 23(7):821–840, 1987.

A. W. Skempton. In *Effective stress in soils, concrete and rocks*, pages 4–16. Proceeding of Conference on Pore Pressure and Suction in Soils Butterworth., 1961.

S. E. Stallebrass and R. N. Taylor. The development and evaluation of a constitutive model for the prediction of ground movements in overconsolidated clay. *Géotechnique*, 47(2): 235–253, 1997.

W. C. Sun, M. R. Kuhn, and J. W. Rudnicki. A multiscale DEM-LBM analysis on permeability evolutions inside a dilatant shear band. *Acta Geotechnica*, 8(5):465–480, 2013.

T. Sweijen, E. Nikooee, S. M. Hassanizadeh, and B. Chareyre. The Effects of Swelling and Porosity Change on Capillarity: DEM Coupled with a Pore-Unit Assembly Method. *Transport in Porous Media*, 113(1):207–226, 2016.

K. Terzaghi. *Erdbaumechanik auf bodenphysikalischer Grundlage*. Franz Deuticke, 1925.

C. Thornton. The conditions for failure of a face-centered cubic array of uniform rigid spheres. *Géotechnique*, 29(4):441–459, 1979.

C. Thornton. Numerical simulations of deviatoric shear deformation of granular media. *Géotechnique*, 50(1):43–53, 2000.

J. F. Thovert, J. Salles, and P. M. Adler. Computerized characterization of the geometry of real porous media: their discretization, analysis and interpretation. *Journal of Microscopy*, 170(1):65–79, 1993.

Y. Tor and S. Yoshida. Numerical simulation of nonlinear behaviors of two-dimensional block structures. *Computers & Structures*, 41(4):593–603, 1991.

C. D. Tsakiroglou and A. C. Payatakes. A new simulator of mercury porosimetry for the characterization of porous materials. *Journal of Colloid and Interface Science*, 137(2): 315–339, 1990.

C. D. Tsakiroglou and A. C. Payatakes. Effects of pore-size correlations on mercury porosimetry curve. *Journal of Colloid and Interface Science*, 146:479–494, 1991.

M. T. Van Genuchten. A closed-form equation for predicting the hydraulic conductivity of unsaturated soils. *Soil Science Society of America Journal*, 44(5):892–898, 1980.

K. Wang and W. C. Sun. A semi-implicit discrete-continuum coupling method for porous media based on the effective stress principle at finite strain. *Computer Methods in Applied Mechanics and Engineering*, 304:546–583, 2016.

Q. Wang, Y. J. Cui, Anh M. T., J. D. Barnichon, S. Saba, and W. M. Ye. Hydraulic conductivity and microstructure changes of compacted bentonite/sand mixture during hydration. *Engineering Geology*, 164:67–76, 2013.

Y. Wang and P. Mora. Macroscopic elastic properties of regular lattices. *Journal of the Mechanics and Physics of Solids*, 56(12):3459–3474, 2008.

Y. Wang, F. Alonso-Marroquin, and W. W. Guo. Rolling and sliding in 3-d discrete element models. *Particuology*, 23:49–55, 2015.

S. J. Wheeler, R. S. Sharma, and M. S. R. Buisson. Coupling of hydraulic hysteresis and stress-strain behaviour in unsaturated soils. *Géotechnique*, 53:41–54, 2003.

S. J. Wheeler, A. Naatanen, M. Karstunen, and M. Lojander. An anisotropic elastoplastic model for soft clays. *Canadian Geotechnical Journal*, 40(2):403–418, 2003.

S.J. Wheeler and V. Sivakumar. An elasto-plastic critical state framework for unsaturated soil. *Géotechnique*, 45(1):35–53, 1995.

D. Wilkinson and J. F. Willemsen. Invasion percolation: a new form of percolation theory. *Journal of Physics A: Mathematical and General*, 16(14):3365–3376, 1983.

J. H. Yin and J. Graham. Elastic viscoplastic modelling of the time-dependent stress-strain behaviour of soils. *Canadian Geotechnical Journal*, 36(4):736–745, 1999.

A. G. Yiotis, A. K. Stubos, A. G. Boudouvis, I. N. Tsimpanogiannis, and Y. C. Yortsos. Pore-network modeling of isothermal drying in porous media. *Transport in Porous Media*, 58:63–86, 2005a.

A. G. Yiotis, A. K. Stubos, A. G. Boudouvis, N. Tsimpanogiannis, and Y. C. Yortsos. Pore-network modeling of isothermal drying in porous media. In *Upscaling Multiphase Flow in Porous Media*, pages 63–86. Springer, 2005b.

D. Zhang, R. Zhang, S. Chen, and W.E. Soll. Pore scale study of flow in porous media: Scale dependency, REV, and statistical REV. *Geophysical Research Letters*, 27:1195–1198, 2000.